

UNIVERSITY OF LEEDS

# On topography and crystal nucleation

by

James Matthew Campbell

Submitted in accordance with the requirements for the  
degree of Doctor of Philosophy

in the  
School of Physics and Astronomy

March 2014



---

# Publications

1. Topographical control of crystal nucleation  
J. L. Holbrough, J. M. Campbell, F. C. Meldrum and H. K. Christenson  
*Crystal Growth & Design*, **2012**, 12(2), 750–755
2. Characterization of preferred crystal nucleation sites on mica surfaces  
J. M. Campbell, F. C. Meldrum and H. K. Christenson  
*Crystal Growth & Design*, **2013**, 13(5), 1915–1925

The candidate confirms that the work submitted is his own, except where work which has formed part of jointly authored publications has been included. The contribution of the candidate and the other authors to this work has been explicitly indicated below. The candidate confirms that appropriate credit has been given within the thesis where reference has been made to the work of others.

Section 4.2 and much of Section 3.1.6 are based on work from 1 above. Most experiments were performed by J. L. Holbrough, carried out under the supervision of H. K. Christenson, although all electron microscopy and the results presented in Figure 4.4 are my own.

Chapter 5 is largely based on work from 2 above. All experiments are my own, carried out under the supervision of H. K. Christenson.

Figures 4.5, 5.12, 5.16, 5.22, 5.26, 5.32, 5.33, 5.35, 5.36 and 6.1 are reproduced from 2 above, with permission from the publisher.

# Intellectual property

This copy has been supplied on the understanding that it is copyright material and that no quotation from the thesis may be published without proper acknowledgement.

© 2014 The University of Leeds and James Matthew Campbell.

The right of James Matthew Campbell to be identified as Author of this work has been asserted by him in accordance with the Copyright, Designs and Patents Act 1988.

# Acknowledgements

Endless thanks to everyone who's given me assistance, advice or just moral support.  
You know who you are.

## Abstract

The influence of topography on crystal nucleation is investigated, mostly with regards to nucleation from vapour but also regarding nucleation from the melt and from solution. Two mechanisms are discussed for acute features to promote nucleation: a thermodynamic reduction in the free energy barrier provided by a favourable geometry, and the formation of a confined condensate of a metastable phase which then transitions to the crystalline phase.

Organic compounds nucleating from vapour are used to demonstrate the efficacy of scratches and mineral steps as preferable nucleation sites. A study of various compounds on mica demonstrates that highly acute features provide the most favourable nucleation sites. High-magnification study of the growth of crystals from such features reveals the presence of small condensates prior to the appearance of bulk crystals, and the growth of these is studied quantitatively.

Ice is shown to have a similar nucleation site preference to the organic compounds, although no condensate was seen prior to bulk nucleation. Well-defined 100 nm-wide trenches were milled into silicon substrates and shown to have a great ability to direct ice nucleation.

The freezing of picolitre droplets of water was studied on smooth and roughened silicon, glass and mica substrates, and the roughening was shown to have little to no effect. Calcium carbonate growth and its dependence on topography was investigated, and found to be broadly anomalous and greatly dependent on surface chemistry.

# Contents

<b>Publications</b>	<b>iii</b>
<b>Intellectual Property</b>	<b>iv</b>
<b>Acknowledgements</b>	<b>v</b>
<b>Abstract</b>	<b>vi</b>
<b>List of Figures</b>	<b>xiii</b>
<b>List of Tables</b>	<b>xix</b>
<b>1 Introduction</b>	<b>1</b>
<b>2 Background and theory</b>	<b>3</b>
2.1 The basics . . . . .	3
2.1.1 Crystals . . . . .	3
2.1.2 Supersaturation and supercooling . . . . .	4
2.1.3 Crystal growth . . . . .	5
2.1.4 Surface energy and curvature . . . . .	6
2.2 Classical nucleation theory . . . . .	7
2.2.1 Homogeneous nucleation . . . . .	7
2.2.2 Heterogeneous nucleation . . . . .	8
2.2.3 Nucleation in surface features . . . . .	9
2.2.4 Nucleation kinetics . . . . .	12
2.2.5 Contact angles of liquids and crystals . . . . .	14
2.2.6 Crystal anisotropy and nucleation site geometry . . . . .	16
2.2.7 Contact line nucleation . . . . .	17
2.2.8 Beyond the classical theory . . . . .	17
2.3 Two-step nucleation . . . . .	18
2.3.1 Ostwald's step rule . . . . .	18
2.3.2 Capillary condensation . . . . .	18
2.3.3 Liquid-mediated nucleation from vapour . . . . .	19
2.4 Prior work . . . . .	20
2.4.1 Nucleation on rough surfaces . . . . .	20
2.4.2 Nucleation in pores . . . . .	21
2.4.3 Nucleation in manufactured features . . . . .	22
2.4.4 Nucleation in naturally-occurring features . . . . .	22

2.4.5	Two-step nucleation . . . . .	23
2.4.6	Simulations . . . . .	23
<b>3</b>	<b>Methods and materials</b>	<b>25</b>
3.1	Substrates . . . . .	25
3.1.1	Mica . . . . .	25
3.1.2	Other layered minerals . . . . .	26
3.1.3	Glass . . . . .	26
3.1.4	Silicon . . . . .	26
3.1.5	Substrate cleaning . . . . .	27
3.1.6	Diamond powder and scratching . . . . .	27
3.2	Compounds . . . . .	28
3.2.1	Compounds for crystallisation from vapour . . . . .	28
3.2.2	Compounds for freezing . . . . .	31
3.2.3	Compounds for crystallisation from solution . . . . .	31
3.3	Imaging techniques . . . . .	31
3.3.1	Optical microscopy . . . . .	31
3.3.2	Electron microscopy . . . . .	32
3.4	Temperature control and measurement . . . . .	33
3.4.1	Thermocouples . . . . .	33
3.4.2	Temperature control . . . . .	33
3.4.3	Liquid nitrogen cooling stage . . . . .	33
<b>4</b>	<b>On crystal nucleation from vapour</b>	<b>35</b>
4.1	Introduction . . . . .	35
4.2	Prior work with neopentanol and carbon tetrabromide . . . . .	36
4.2.1	Method . . . . .	36
4.2.2	Results . . . . .	37
4.3	Methods for room temperature nucleation . . . . .	39
4.3.1	Cell design . . . . .	39
4.3.2	Procedure . . . . .	39
4.3.3	Issues with saturation . . . . .	41
4.4	Methods for low temperature nucleation . . . . .	42
4.4.1	Cell designs for the liquid nitrogen stage . . . . .	42
4.4.2	Peltier-cooled cell . . . . .	44
4.4.3	Flow control and saturation . . . . .	45
4.4.4	Procedures . . . . .	46
4.5	General and miscellaneous observations . . . . .	47
4.5.1	Crystallisation behaviour by compound . . . . .	47
4.5.2	Nucleation density and repeatability . . . . .	49
4.6	Nucleation on rough surfaces . . . . .	52
4.6.1	Scratches . . . . .	52
4.6.2	Mica defects . . . . .	55
4.7	Nucleation on milled silicon . . . . .	56
4.7.1	Ion milling . . . . .	57
4.7.2	Reactive-ion etching . . . . .	60
4.8	Summary . . . . .	66



---

<b>5</b>	<b>On the identification of dominant nucleation sites on mica surfaces</b>	<b>67</b>
5.1	Introduction . . . . .	67
5.2	Techniques . . . . .	68
5.2.1	Crystal growth . . . . .	68
5.2.2	Site identification . . . . .	68
5.3	Early results . . . . .	69
5.4	On mica defects . . . . .	72
5.4.1	Common topographic features of mica surfaces . . . . .	72
5.4.2	Ambiguity . . . . .	76
5.5	Results by compound . . . . .	78
5.5.1	Carbon tetrabromide . . . . .	78
5.5.2	Camphor . . . . .	80
5.5.3	Norbornane . . . . .	84
5.5.4	Hexachloroethane . . . . .	86
5.6	Multiple compounds on identical substrates . . . . .	89
5.7	Aggregated results and conclusions . . . . .	93
5.8	Extension to ice . . . . .	96
5.8.1	Procedure . . . . .	96
5.8.2	Results . . . . .	97
5.9	Summary . . . . .	99
<b>6</b>	<b>On the nucleation of crystals from vapour in acute wedges</b>	<b>101</b>
6.1	Introduction . . . . .	101
6.2	Wedges, interference and condensates . . . . .	104
6.3	General results . . . . .	108
6.3.1	General observations by compound . . . . .	108
6.3.2	Miscellaneous results . . . . .	113
6.4	Repeatability . . . . .	114
6.4.1	Camphor . . . . .	114
6.4.2	Hexachloroethane . . . . .	115
6.4.3	Norbornane . . . . .	115
6.4.4	Pocket geometries . . . . .	117
6.5	Condensate size analysis . . . . .	118
6.6	Condensate growth of organic compounds . . . . .	122
6.6.1	Camphor . . . . .	122
6.6.2	Hexachloroethane . . . . .	122
6.6.3	Norbornane . . . . .	124
6.6.4	Solid or liquid condensates? . . . . .	125
6.6.5	Discussion . . . . .	128
6.7	Ice . . . . .	131
6.8	Summary . . . . .	134
<b>7</b>	<b>On ice nucleation from water</b>	<b>137</b>
7.1	Introduction . . . . .	137
7.2	Nucleation from microlitre volumes . . . . .	138
7.2.1	Prior work . . . . .	138
7.2.2	Experimental procedure . . . . .	139

7.2.3	Results and conclusions . . . . .	140
7.3	The creation of picolitre droplet arrays . . . . .	141
7.3.1	Introduction . . . . .	141
7.3.2	The formation of hydrophobic surfaces . . . . .	141
7.3.3	Ultra-violet patterning . . . . .	143
7.3.4	Drop formation . . . . .	144
7.3.5	Oil immersion . . . . .	146
7.4	Equipment and procedure . . . . .	148
7.4.1	The cell . . . . .	148
7.4.2	Substrate preparation . . . . .	149
7.4.3	Preparing the array . . . . .	150
7.4.4	Freezing and melting . . . . .	151
7.4.5	Analysis . . . . .	151
7.5	Results . . . . .	152
7.5.1	Coincidence thresholds . . . . .	152
7.5.2	Silicon . . . . .	153
7.5.3	Glass . . . . .	157
7.5.4	Mica . . . . .	157
7.6	Heterogeneous or homogeneous nucleation? . . . . .	160
7.6.1	The problem and the solution . . . . .	160
7.6.2	Procedure . . . . .	161
7.6.3	Results . . . . .	162
7.7	Extension to other liquids . . . . .	165
7.7.1	Dimethyl sulphoxide . . . . .	166
7.7.2	Formamide . . . . .	167
7.8	Summary . . . . .	167
<b>8</b>	<b>On the nucleation of calcium carbonate from solution</b>	<b>169</b>
8.1	Introduction . . . . .	169
8.1.1	On calcium carbonate . . . . .	169
8.1.2	On the nucleation of calcium carbonate . . . . .	170
8.1.3	On calcium carbonate and mica . . . . .	171
8.2	Techniques . . . . .	171
8.3	General observations . . . . .	173
8.3.1	Substrate pretreatment . . . . .	173
8.3.2	Concentration . . . . .	175
8.3.3	Crystal rings . . . . .	176
8.4	Growth on smooth and scratched surfaces . . . . .	178
8.4.1	Diamond powder scratching . . . . .	178
8.4.2	Crude scratches . . . . .	182
8.5	Growth on mica defects . . . . .	186
8.5.1	Pocket features . . . . .	186
8.6	Other substrates and compounds . . . . .	188
8.6.1	Calcium fluoride . . . . .	188
8.6.2	Other layered minerals . . . . .	191
8.7	Summary . . . . .	191

---

<b>9</b>	<b>Conclusions</b>	<b>195</b>
9.1	Nucleation from vapour . . . . .	195
9.2	Nucleation from the melt . . . . .	196
9.3	Nucleation from solution . . . . .	197
9.4	Grand conclusion . . . . .	197
	<b>Appendices</b>	<b>199</b>
<b>A</b>	<b>Nucleation free energy barrier in a conical pit</b>	<b>199</b>



# List of Figures

2.1	Optical micrographs: regular and dendritic growth of camphor . . . . .	6
2.2	Graph: nucleus free energy vs. radius . . . . .	8
2.3	Diagram: contact angle and surface energies . . . . .	9
2.4	Diagram: nucleus in a wedge . . . . .	10
2.5	Diagram: nucleation modes in a wedge or pit . . . . .	10
2.6	Graph: nucleation free energy barrier in a wedge . . . . .	11
2.7	Graph: nucleation free energy barrier in a conical pit . . . . .	13
2.8	Graph: nucleation free energy barrier in a conical pit compared to a wedge	13
2.9	Diagram: polymorph selectivity in wedge features . . . . .	16
2.10	Diagram: capillary condensate . . . . .	19
3.1	Optical and electron micrographs: diamond powder . . . . .	27
3.2	Electron micrographs: diamond-scratched mica surfaces . . . . .	28
3.3	Electron micrographs: diamond-scratched glass surfaces . . . . .	29
3.4	Electron micrographs: diamond-scratched silicon surfaces . . . . .	29
3.5	Graph: light intensity response of camera . . . . .	32
3.6	Diagram: liquid nitrogen cooling stage . . . . .	34
4.1	Diagram: sublimation cell used in early experiments . . . . .	36
4.2	Graphs: nucleation density of neopentanol and carbon tetrabromide on smooth and scratched glass and mica . . . . .	37
4.3	Graphs: induction times of neopentanol and carbon tetrabromide on smooth and scratched glass and mica . . . . .	38
4.4	Graph: induction times of neopentanol on smooth and scratched mica .	38
4.5	Diagram: sublimation cell for room temperature experiments . . . . .	40
4.6	Diagrams: first flow cell . . . . .	43
4.7	Diagram: second flow cell . . . . .	44
4.8	Diagram: Peltier cell . . . . .	45
4.9	Diagram: humidity control system . . . . .	46
4.10	Optical micrographs: crystals grown from vapour . . . . .	48
4.11	Graph: nucleation positions on scratched glass . . . . .	50
4.12	Optical micrographs: repeat neopentanol nucleation at a single site . . .	51
4.13	Graph: nucleation positions on smooth mica at high ramp rate . . . . .	52
4.14	Optical micrograph and graph: neopentanol in a rough mica scratch . .	53
4.15	Optical micrograph and graph: carbon tetrabromide in a rough mica scratch . . . . .	53
4.16	Optical micrograph: camphor nucleation in a rough glass scratch . . . .	54
4.17	Optical micrographs: neopentanol in diamond-grain scratches . . . . .	54

4.18	Optical micrographs: neopentanol on diamond-scratched mica . . . . .	54
4.19	Optical micrographs: carbon tetrabromide nucleation on mica defects . . . . .	55
4.20	Optical micrographs: crystals grown on mica defects . . . . .	56
4.21	Electron micrographs: ion-milled trenches in silicon . . . . .	57
4.22	Optical micrograph: ice grown on ion-milled silicon . . . . .	58
4.23	Optical micrographs: ice grown on ion-milled silicon . . . . .	59
4.24	Optical micrographs: camphor grown on ion-milled silicon . . . . .	60
4.25	Optical micrographs: ice crystals on ion-milled silicon . . . . .	61
4.26	Electron micrographs: reactive-ion etched trenches in silicon . . . . .	61
4.27	Optical micrograph: ice grown on reactive-ion etched silicon at -40 °C . . . . .	62
4.28	Optical micrographs: ice crystals on reactive-ion etched silicon (three minutes' etch) . . . . .	63
4.29	Optical micrographs: ice crystals on reactive-ion etched silicon (two minutes' etch) . . . . .	64
4.30	Graphs: site correlation on milled silicon substrates . . . . .	65
5.1	Optical and electron micrographs: nucleation site location in electron microscope . . . . .	69
5.2	Electron micrograph: carbon tetrabromide nucleation site . . . . .	70
5.3	Electron micrographs: carbon tetrabromide nucleation sites . . . . .	71
5.4	Electron micrographs: dominant carbon tetrabromide nucleation site . . . . .	71
5.5	Graph: first nucleation $\Delta T$ of carbon tetrabromide in several regions . . . . .	72
5.6	Diagram and electron micrograph: step edge geometry . . . . .	73
5.7	Diagram and electron micrograph: step overhang geometry . . . . .	73
5.8	Diagram and electron micrograph: hanging flake geometry . . . . .	74
5.9	Diagram and electron micrograph: pocket geometry . . . . .	74
5.10	Diagram and electron micrograph: loose flake geometry . . . . .	75
5.11	Diagram and electron micrograph: crack or split geometry . . . . .	75
5.12	Optical micrographs: interference fringes from mica defects . . . . .	76
5.13	Electron micrographs: carbon tetrabromide nucleation sites on substrate □ . . . . .	79
5.14	Electron micrograph: carbon tetrabromide nucleation site on substrate ■ . . . . .	79
5.15	Electron micrographs: carbon tetrabromide nucleation sites on substrate ○ . . . . .	79
5.16	Graph: temperature differences at carbon tetrabromide nucleation . . . . .	80
5.17	Electron micrographs: camphor nucleation sites on substrate □ . . . . .	81
5.18	Electron micrographs: camphor nucleation sites on substrate ■ . . . . .	81
5.19	Optical and electron micrographs: camphor nucleation sites on substrate ○ . . . . .	82
5.20	Electron micrograph: camphor nucleation site on substrate ● . . . . .	82
5.21	Electron micrograph: camphor nucleation site on substrate ▲ . . . . .	83
5.22	Graph: temperature differences at camphor nucleation . . . . .	83
5.23	Electron micrographs: norbornane nucleation sites on substrate ■ . . . . .	85
5.24	Electron micrographs: norbornane nucleation sites on substrate ○ . . . . .	85
5.25	Electron micrographs: norbornane nucleation sites on substrate Δ . . . . .	85
5.26	Graph: temperature differences at norbornane nucleation . . . . .	86
5.27	Electron micrographs: hexachloroethane nucleation sites on substrate ■ . . . . .	87
5.28	Electron micrographs: hexachloroethane nucleation sites on substrate ○ . . . . .	87
5.29	Electron micrograph: hexachloroethane nucleation site on substrate ● . . . . .	88
5.30	Electron micrographs: hexachloroethane nucleation sites on substrate Δ . . . . .	88

5.31	Electron micrographs: hexachloroethane nucleation sites on substrate ▲	88
5.32	Graph: temperature differences at hexachloroethane nucleation . . . . .	89
5.33	Electron micrographs: nucleation sites on substrate ◇ . . . . .	91
5.34	Electron micrographs: nucleation sites on substrate ◆ . . . . .	92
5.35	Graph: nucleation coincidence on substrates ◇ and ◆ . . . . .	93
5.36	Graph: nucleation site categorisation . . . . .	95
5.37	Optical micrographs: ice nucleation all along mica defects . . . . .	97
5.38	Electron micrograph: preferable ice nucleation site featuring overhangs	98
5.39	Electron and optical micrographs: favourable defect for ice nucleation .	98
5.40	Optical and electron micrographs: nucleation site of ice on mica defect .	99
5.41	Optical micrographs: nucleation site of ice in mica pockets . . . . .	99
6.1	Optical micrographs: camphor growth along a linear feature . . . . .	103
6.2	Diagram: interference in an acute wedge . . . . .	104
6.3	Optical micrographs: large pocket feature on mica . . . . .	105
6.4	Graph: height profile of mica wedge . . . . .	105
6.5	Diagram: interference in an acute wedge with condensate . . . . .	106
6.6	Optical micrograph: condensate in mica wedge . . . . .	106
6.7	Optical micrograph: wedge fringes in 532 nm light . . . . .	107
6.8	Optical micrograph: neopentanol condensate visible in darkfield illumination . . . . .	107
6.9	Optical micrographs: crystals grown in mica pockets . . . . .	109
6.10	Optical micrographs: hexachloroethane growth in mica wedge . . . . .	110
6.11	Optical micrographs: camphor growth in mica wedge . . . . .	110
6.12	Optical micrographs: neopentanol growth in mica wedge . . . . .	111
6.13	Optical micrographs: hexachloroethane growth in mica wedges . . . . .	112
6.14	Optical micrographs: norbornane growth in mica wedge . . . . .	112
6.15	Optical micrograph: norbornane growing from scratch in preference to pocket . . . . .	113
6.16	Graph: repeatability of camphor nucleation in pockets . . . . .	115
6.17	Graph: repeatability of hexachloroethane nucleation in pockets . . . . .	116
6.18	Graph: repeatability of norbornane nucleation in pockets . . . . .	116
6.19	Graph: repeatability of norbornane nucleation in pockets after equilibration	117
6.20	Diagram: pixel binning procedure . . . . .	119
6.21	Graphs: intensity curve correction and alignment . . . . .	120
6.22	Graph: explanation of condensate size analysis . . . . .	121
6.23	Graph: growth of camphor condensates at 0.5 °C/minute . . . . .	123
6.24	Graph: growth of camphor condensate at 0.1 °C/minute . . . . .	123
6.25	Graph: growth of hexachloroethane condensate at 0.5 °C/minute . . . . .	124
6.26	Graph: growth of hexachloroethane condensate at 0.1 °C/minute . . . . .	125
6.27	Graph: growth of norbornane condensates at 0.5 °C/minute . . . . .	126
6.28	Graph: growth of norbornane condensates at 0.1 °C/minute . . . . .	127
6.29	Optical micrographs: faceted confined condensate of camphor . . . . .	127
6.30	Optical micrographs: jagged confined condensate of norbornane . . . . .	128
6.31	Optical micrographs: ice growing in series of mica pockets . . . . .	132
6.32	Optical micrographs: ice growing in mica pocket at -37.0 °C . . . . .	133
6.33	Optical micrographs: ice growing in mica pocket at -38.3 °C . . . . .	133

6.34	Graph: intensity curves for ice growing in acute wedge . . . . .	134
7.1	Graph: freezing points of water on smooth and scratched silicon; prior work . . . . .	138
7.2	Diagram: cell used for microlitre drop freezing experiments . . . . .	139
7.3	Graph: freezing points of water on smooth and scratched silicon; own work . . . . .	140
7.4	Optical micrographs: frosting on silicon . . . . .	140
7.5	Diagram: chamber used for surface silanation . . . . .	143
7.6	Graph: water contact angles on treated silicon surfaces . . . . .	145
7.7	Optical micrographs: poor and good array formation on silicon . . . . .	146
7.8	Optical micrographs: array formation on glass and mica . . . . .	146
7.9	Optical micrographs: freezing event in an unimmersed array . . . . .	147
7.10	Optical micrographs: freezing events in immersed arrays . . . . .	147
7.11	Diagram: droplet freezing cell and cooling stage . . . . .	149
7.12	Optical micrographs: droplet array formation . . . . .	151
7.13	Optical micrographs: frozen and unfrozen droplets . . . . .	152
7.14	Graphs: drop freezing temperatures on smooth and scratched silicon (3 °C/minute) . . . . .	154
7.15	Graph: correlation of freezing points on "< 1 μm" scratched silicon (fast ramp) . . . . .	154
7.16	Graphs: drop freezing temperatures on smooth and scratched silicon (1 °C/minute) . . . . .	155
7.17	Graph: correlation of freezing points on "< 1 μm" scratched silicon (slow ramp) . . . . .	156
7.18	Graphs: drop freezing temperatures on smooth and pitted silicon . . . . .	157
7.19	Graphs: drop freezing temperatures on smooth and scratched glass . . . . .	158
7.20	Graphs: drop freezing temperatures on smooth and etched mica . . . . .	158
7.21	Graphs: drop freezing temperatures on smooth and scratched mica . . . . .	159
7.22	Graphs: drop freezing temperatures during two runs on scratched mica . . . . .	160
7.23	Graph: exponential decay of unfrozen water drops . . . . .	163
7.24	Graph: size dependence of droplet nucleation rate on silicon . . . . .	164
7.25	Graph: size dependence of droplet nucleation rate on glass . . . . .	164
7.26	Graph: size dependence of droplet nucleation rate on mica . . . . .	165
7.27	Optical micrographs: droplet arrays of other compounds . . . . .	166
7.28	Graph: size dependence of dimethyl sulphoxide drop nucleation temperature . . . . .	167
8.1	Electron micrograph and graph: calcite epitaxy on mica . . . . .	172
8.2	Optical micrographs: calcite, aragonite and vaterite on mica . . . . .	173
8.3	Optical micrographs: calcite on two sides of a piece of mica . . . . .	174
8.4	Optical micrograph: inhomogeneous calcite growth on mica . . . . .	174
8.5	Optical micrographs: effect of mica pretreatment on CaCO <sub>3</sub> growth . . . . .	175
8.6	Optical micrographs: effect of concentration on CaCO <sub>3</sub> growth . . . . .	176
8.7	Optical micrograph: calcite aggregate . . . . .	176
8.8	Optical micrographs: rings of calcite crystals . . . . .	177
8.9	Optical micrograph: calcite ring on immersed mica . . . . .	177
8.10	Optical micrograph: calcite ring on mica caused by condensed water . . . . .	178



---

8.11	Graph: CaCO <sub>3</sub> nucleation density on smooth and scratched silicon . . .	179
8.12	Graph: CaCO <sub>3</sub> nucleation density on smooth and scratched mica . . . .	179
8.13	Graphs: CaCO <sub>3</sub> nucleation density on smooth and scratched glass . . . .	181
8.14	Graphs: CaCO <sub>3</sub> nucleation density on smooth and "< 10 nm"-scratched glass . . . . .	181
8.15	Optical micrographs: CaCO <sub>3</sub> growing on glass scratches . . . . .	182
8.16	Electron micrographs: glass gouge edge . . . . .	183
8.17	Optical micrographs: calcium carbonate in scraped mica scratches . . . .	184
8.18	Optical micrographs: calcium carbonate in crushed mica scratches . . . .	185
8.19	Optical micrographs: calcium carbonate on mica defects . . . . .	187
8.20	Optical micrograph: calcite epitaxy on mica defect . . . . .	188
8.21	Optical micrographs: pocket features before and after possible CaCO <sub>3</sub> growth . . . . .	189
8.22	Optical micrograph: calcite growth in mica pocket . . . . .	190
8.23	Optical micrographs: CaF <sub>2</sub> growth on mica . . . . .	190
8.24	Optical micrographs: calcium carbonate epitaxy on lepidolite, biotite and vermiculite . . . . .	192
8.25	Optical micrographs: calcium carbonate growth on lepidolite, biotite and vermiculite defects . . . . .	193
8.26	Optical micrograph: calcite growth on biotite . . . . .	194
A.1	Diagram: modes of nucleation . . . . .	200



# List of Tables

3.1	Table of physical properties of compounds for crystallisation from vapour	30
3.2	Table of physical properties of further compounds for crystallisation from vapour . . . . .	30
3.3	Table of physical properties of liquids used for freezing . . . . .	31
4.1	Table of equilibrium $\Delta T$ for each compound . . . . .	41
5.1	Table of nucleation site categorisations by substrate . . . . .	94
6.1	Table showing critical radii and free energy barriers of nuclei of each compound from liquid and from vapour . . . . .	102
6.2	Table characterising geometries of mica pockets used for repeat runs . .	118
6.3	Table of estimated temperature differences required for crystal emergence from wedges . . . . .	129
6.4	Table listing condensate heights and temperature differences at bulk emergence . . . . .	130
7.1	Table of pattern dimensions used for surface patterning . . . . .	143
8.1	Table of calcium carbonate polymorph solubilities . . . . .	170



# Chapter 1

## Introduction

Nucleation is a fundamentally improbable process. Consider a glass of water, slightly below 0 °C. This is an example of a supercooled liquid, one cooled below its melting point, and thus has a tendency to freeze; i.e. the thermodynamically favourable phase is a crystal of ice, not liquid water. But the water cannot freeze spontaneously, it must first undergo a transition, and that transition must begin at some particular point or points in the glass.

The trouble is that no part of the water wants to be the first to freeze. Whilst it is true that freezing would be favourable for the glass as a whole, for each local cluster of water molecules, the favourable state is whatever matches that of their neighbours: i.e. staying liquid. For an ice crystal to grow, it must first reach a critical size; form a “nucleus” typically a few nanometres across and containing between tens and thousands of molecules depending on conditions. And the only way for this to happen is by spontaneous formation through random fluctuations of the molecules’ configuration. This is fundamentally improbable.

Hence, anything which can help the process, even only very slightly, can significantly increase its chances of occurring. The presence of a foreign surface, such as the wall of the glass or a contaminant in the water, may reduce the volume of the required nucleus if it forms in contact with it. Indeed, nucleation in bulk material away from foreign surfaces is likely to be rare in nature.

Also rare in nature are perfectly flat surfaces. The glass will be pitted and scratched on a microscopic scale, even the contaminant particles in the water are likely to have a rich surface topography. Just as nucleation on a surface can be more probable than nucleation in bulk water, nucleation in a concave surface feature can be more probable

than nucleation on a flat surface. Hence, nucleation of ice in our glass may be primarily determined by what happens in these geometrically favourable sites.

In this thesis I study the effect of surface geometry on crystal nucleation, both probing the extent and magnitude of its ability to enhance nucleation in various systems, and attempting to address questions of how and why the phenomenon occurs on a microscopic level.

Nucleation as a model for phase transitions is of wider application than for just describing ice freezing from water. As well as the freezing of liquids, it can be used to describe the formation of crystals from solution, of bubbles from fizzy liquids, of liquid drops condensing from gas, and of crystal growth directly from vapour. Here I focus primarily on this latter possibility, although I also consider the freezing of liquids and crystal growth from solution.

Chapter 2 lays out the theory of nucleation in and out of surface features, and also discusses some prior work of particular relevance. Chapter 3 introduces the materials employed and methods used throughout the thesis.

Chapters 4–6 present work studying crystal nucleation directly from vapour, using both ice and various organic compounds. Chapter 4 introduces the experiments and presents some general results. Chapter 5 presents a series of experiments intended to identify and characterise the most favourable nucleation sites on cleaved mineral surfaces. Chapter 6 presents a study of the microscopic mechanics of nucleation in highly acute wedges.

Chapters 7 and 8 contain accounts of experiments addressing similar questions in very different systems. Chapter 7 looks at the nucleation of ice from supercooled water drops. Chapter 8 explores the nucleation of calcium carbonate from a supersaturated solution.

Finally, Chapter 9 discusses the work as a whole and summarises the previous chapters.

## Chapter 2

# Background and theory

### 2.1 The basics

#### 2.1.1 Crystals

A crystal is a solid whose constituent molecules are arranged in an ordered lattice. It can be constructed by taking a simple unit cell containing one or more molecules and repeating this periodically in three dimensions.

One of the most noticeable consequences of this is that crystals tend to grow in regular faceted shapes. Different faces along different crystal planes have different arrangements of molecules at their surface. Some of these grow at faster rates than others, and those that grow slowest are left as facets whilst those that grow fastest grow into nonexistence. Each crystal has its own energetically favourable shape, which is not always trivially related to that of the unit cell.

A material in which all molecules are aligned in a single regular lattice is known as a single crystal. Other materials are constructed from many small single crystals, each oriented independently and separated by grain boundaries, these are known as polycrystalline materials. Other solid materials have no crystalline ordering at all, and are known as amorphous materials.

There are various ways of repeating a unit cell through space to generate a crystal. For example, taking a cubic unit cell and repeating it in three orthogonal directions generates a cubic crystal, whilst taking a unit cell shaped as a hexagonal prism and tiling this in three dimensions generates a hexagonal crystal. This thesis is largely not concerned with these distinctions and so they will not be explained in detail. However, we must consider that a single compound can potentially form more than one crystalline arrangement, or

even that both a crystalline phase and an amorphous phase may both be possibilities. These different phases of the same compound are known as polymorphs. One of these will generally be more energetically favourable than the others (the thermodynamically stable phase) but other polymorphs may nonetheless be effectively stable. Others may be short-lived and liable to transition to a more stable phase.

## 2.1.2 Supersaturation and supercooling

### Growth from vapour

Consider the surface of a liquid or solid in contact with a vapour. Molecules on the surface liberate themselves from the material through thermal excitation; there exists a flux of molecules away from the surface into the vapour. If there is a partial pressure  $p$  of the compound in the vapour phase, then there also exists a flux of molecules onto the surface as they collide and attach, this flux increasing with pressure. There exists a particular value of  $p$  at which there is an equilibrium between the two phases; this is the vapour pressure,  $p_0$ . If  $p > p_0$ , the liquid or solid grows. If  $p < p_0$ , it sublimates away.

The higher the temperature, the higher the flux of thermally liberated molecules from the surface, and so the higher the vapour pressure. At the melting point, the vapour pressures of a solid and a liquid of the same compound are equal; above the melting point the solid has a higher vapour pressure than the liquid, below the melting point the liquid has a higher vapour pressure than the solid.[1]

The saturation,  $S$ , is defined as

$$S = \frac{a}{a_0} \quad (2.1)$$

where  $a$  and  $a_0$  are the thermodynamic activity and equilibrium thermodynamic activity respectively. At low pressure this is approximated by [2]

$$S \approx \frac{p}{p_0}, \quad (2.2)$$

an approximation that will be used throughout the thesis. The system is in equilibrium when  $S = 1$ , at higher saturations the vapour is said to be supersaturated.

Supersaturation is the driving force behind nucleation from vapour. If a volume of solid or liquid forms from a supersaturated vapour, it experiences a reduction in free energy per unit volume  $\Delta G_V$  expressed as [3]

$$\Delta G_V = \frac{RT \ln S}{V_m} \quad (2.3)$$



where  $R$  is the gas constant,  $T$  the temperature and  $V_m$  the molar volume of the condensed phase.

### Nucleation from the melt

Unlike growth from vapour, when a crystal forms within its own liquid it does so by a change in the conformation of its molecules with very little change in density. The driving force in this case is supercooling below the compound's melting point,  $T_m$ . If  $\Delta T$  is the supercooling such that  $\Delta T = T_m - T$ , then the free energy loss upon freezing may be expressed as [3]

$$\Delta G_V = \frac{\rho \Delta H_{\text{fus}} \Delta T}{T_m} \quad (2.4)$$

where  $\rho$  is the density of the crystal and  $\Delta H_{\text{fus}}$  the enthalpy of fusion per unit mass.

### Nucleation from solution

Growth from solution is thermodynamically analogous to growth from vapour. As from vapour, a phase of disperse, disordered molecules (those in solution) aggregates to form a dense, ordered phase. As such, the free energy change upon crystallisation has a form identical to that of Equation 2.3: [3]

$$\Delta G_V = \frac{RT \ln S}{V_m}. \quad (2.5)$$

Here, however, the activity  $a$  and equilibrium activity  $a_0$  are approximated by  $c$  and  $c_0$  respectively, where  $c$  is the concentration of the compound in solution and  $c_0$  is the solubility of the material, i.e. the concentration with which a bulk crystal would be in equilibrium.

#### 2.1.3 Crystal growth

Crystals grow by the successive nucleation and growth of new crystal planes, growing layer by layer, often aided by lattice defects.[4] When the growth rate is very slow, at very modest supersaturation, crystals grow in regular geometric shapes, e.g. cubes, hexagonal prisms or octahedrons. At the limit of zero growth rate, these shapes tend towards the equilibrium shape dictated by the relative surface energies of their faces.

However, at higher supersaturations crystals tend to exhibit dendritic growth. This is the process whereby the structure branches out into narrow arms known as dendrites.

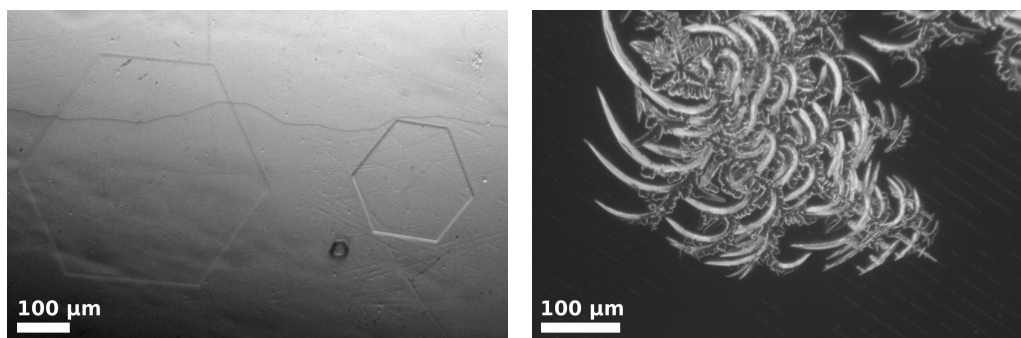


FIGURE 2.1: Optical micrographs showing large camphor crystals grown from vapour in differing conditions: (left) crystals grown on mica at 23 °C; (right) crystal grown on etched silicon at -5 °C.

The driving process behind this may be either diffusion, or the release of latent heat, or both: the tips of the dendrites receive the highest influx of molecules due to diffusion gradients, but they can also dissipate their latent heat the easiest. Figure 2.1 shows examples of both regular and dendritic growth styles for the same compound.

#### 2.1.4 Surface energy and curvature

The molecules at the edge of a solid or liquid are not in as energetically favourable a position as those in the bulk: they have fewer neighbouring molecules with which to form bonds. This is manifested as a surface free energy (or interfacial energy or surface tension) per unit area of interface,  $\gamma$ . Surface energies between two compounds or phases are determined by the ability of the molecules at the interface to bond to one another. By bonding, I refer either to chemical bonds, such as covalent or ionic bonds, or to weaker physical bonds, such as hydrogen or van der Waals bonds.

The vapour pressure of a solid or liquid is dependent on the curvature of its interface. If the vapour pressure over a flat interface is  $p_0$ , then the actual vapour pressure  $p'_0$  over a spherical interface is expressed by the Kelvin equation as [5]

$$\ln \frac{p'_0}{p_0} = \frac{2\gamma V_m}{RT r} \quad (2.6)$$

where  $r$  is the radius of curvature of the interface.  $r$  is defined as being positive for convex surfaces (e.g. the surface of a spherical drop) and negative for concave surfaces. Therefore the vapour pressure is higher over a convex surface and lower over a concave surface. Practically, this means that a small liquid droplet will evaporate unless the vapour is slightly supersaturated, and that a liquid with a concave interface (e.g. a meniscus in a narrow hydrophilic capillary) may be able to condense even in slightly undersaturated conditions.

Note that Equation 2.6 defines  $r$  as being the radius of curvature of a spherical surface. If instead we have a cylindrical surface, then we find [5]

$$\ln \frac{p'_0}{p_0} = \frac{\gamma V_m}{RT r}. \quad (2.7)$$

## 2.2 Classical nucleation theory

Classical nucleation theory was developed by Volmer,[6] based on earlier work by Gibbs.[7] It considers the formation of a nucleus of a new phase such that:

- the transformation of the old phase to the new has an accompanying free energy change per unit volume  $-\Delta G_V$ ;
- the formation of the new phase causes a new interface, with a cost in free energy  $\gamma$  per unit area;
- both  $\Delta G_V$  and  $\gamma$  are independent of the size of the nucleus and equal to the value for bulk material.

### 2.2.1 Homogeneous nucleation

For isotropic phases in the absence of a foreign surface, the most energetically favourable nucleus shape at any size is a sphere of radius  $r$ . Considering both volume and surface terms, this gives a total free energy change  $\Delta G$  where

$$\Delta G = 4\pi r^2 \gamma - \frac{4}{3}\pi r^3 \Delta G_V. \quad (2.8)$$

Figure 2.2 shows  $\Delta G$  as a function of  $r$ . It can be seen that further growth only becomes energetically favourable beyond a certain radius  $r^*$ , known as the critical radius. In order to reach this size it must surmount a free energy barrier  $\Delta G^*$ , which it must achieve by random fluctuations within the material. It can be shown that [3]

$$r^* = \frac{2\gamma}{\Delta G_V} \quad (2.9)$$

and

$$\Delta G^* = \frac{4}{3}\pi \gamma r^{*2} = \frac{16\pi \gamma^3}{3(\Delta G_V)^2}. \quad (2.10)$$

$\gamma$  is usually assumed to be independent of temperature, saturation etc. A suitable expression for  $\Delta G_V$  should be substituted from Section 2.1.2. Note that Equation 2.9

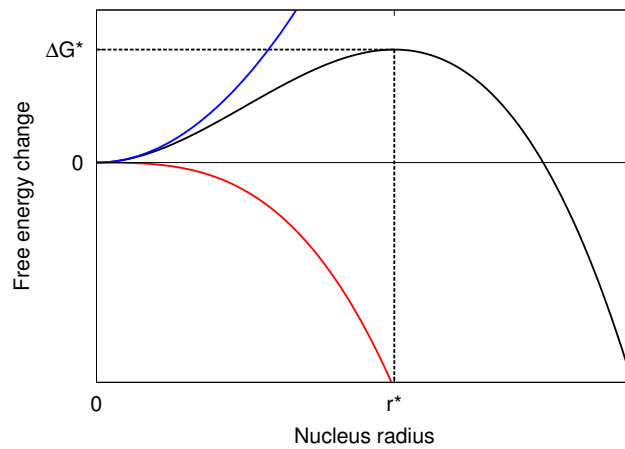


FIGURE 2.2: Graph showing the change in free energy accompanying formation of a nucleus of radius  $r$ , from Equation 2.8 (black line). The blue and red lines show the contributions from the surface area and volume, respectively.

can also be derived through the Kelvin effect (combining Equations 2.6 and 2.3); it is the radius at which the two phases are in equilibrium due to curvature effects, albeit an unstable equilibrium.

## 2.2.2 Heterogeneous nucleation

### Contact angles

The equilibrium shape taken by a small amount of a liquid placed on a solid substrate depends on three surface energies:  $\gamma_{sv}$ , the surface energy between the solid and the vapour;  $\gamma_{sl}$ , the surface energy between the solid and the liquid; and  $\gamma_{lv}$ , the surface energy between the liquid and the vapour. These are shown in Figure 2.3. If  $\gamma_{sv} - \gamma_{sl} > \gamma_{lv}$ , the liquid will spread across the surface. If  $\gamma_{sl} - \gamma_{sv} > \gamma_{lv}$ , the liquid will remain a spherical drop and not adhere to the surface. For any intermediate case, the drop will form a spherical cap with a contact angle  $\theta$  where [8]

$$\gamma_{lv} \cos \theta = \gamma_{sv} - \gamma_{sl}. \quad (2.11)$$

This concept applies equally for an isotropic solid in place of the liquid, and for a liquid in place of the vapour. The concept is not strictly valid for a crystal on a surface, as the angle which its faces make with the substrate is not trivially dependent upon its surface energies. However, the concept of a contact angle will continue to be used as a useful shorthand, and should be interpreted as the angle an isotropic phase, having the same surface energies, would make with the substrate.

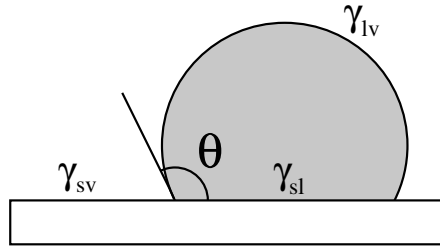


FIGURE 2.3: Illustration of surface energies and contact angle for a drop sitting on a flat surface.

### Flat heterogeneous nucleation

Continuing to use the  $\gamma_{sv}$ ,  $\gamma_{sl}$ ,  $\gamma_{lv}$  terminology of the previous section regardless of the particular phases involved, we find that nucleation can find no benefit from a foreign surface if  $\gamma_{sl} - \gamma_{sv} > \gamma_{lv}$  ( $\theta = 180^\circ$ ). If at the opposite extreme  $\gamma_{sv} - \gamma_{sl} > \gamma_{lv}$  ( $\theta = 0^\circ$ ), then the new phase will be able to grow from the surface without a nucleation barrier at all. For an intermediate contact angle, however, the critical nucleus will be a spherical cap such as that shown in Figure 2.3 having the same radius as in the homogeneous case. The critical free energy barrier to form such a nucleus can then be calculated to be proportional to the homogeneous free energy barrier  $\Delta G_{\text{hom}}^*$  but reduced by a shape factor  $Q(\theta)$  dependent only on the contact angle such that

$$\Delta G^* = Q(\theta)\Delta G_{\text{hom}}^* \quad (2.12)$$

where [3]

$$Q(\theta) = \frac{1}{4} (2 + \cos \theta) (1 - \cos \theta)^2. \quad (2.13)$$

### 2.2.3 Nucleation in surface features

#### Nucleation in a wedge

For the case of a wedge formed by two flat planes making an angle  $\varphi$ , as shown in Figure 2.4,  $\Delta G^*$  was first calculated by Chakraverty and Pound for the particular case of a  $90^\circ$  wedge,[9] and was then generalised for an arbitrary wedge angle by Sholl and Fletcher.[10] They found it to be proportional to the homogeneous free energy barrier but reduced by a factor  $Q_{\text{wedge}}(\theta, \varphi)$ , such that

$$Q_{\text{wedge}}(\theta, \varphi) = 1 - 2Q(180^\circ - \theta) \quad (2.14)$$

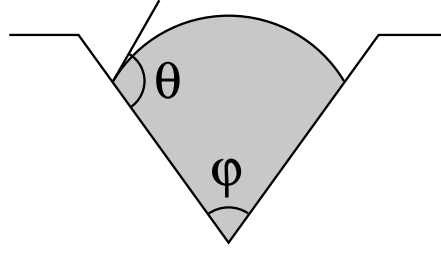


FIGURE 2.4: Illustration of a nucleus forming in a wedge or conical pit, showing the angles  $\theta$  and  $\varphi$ .

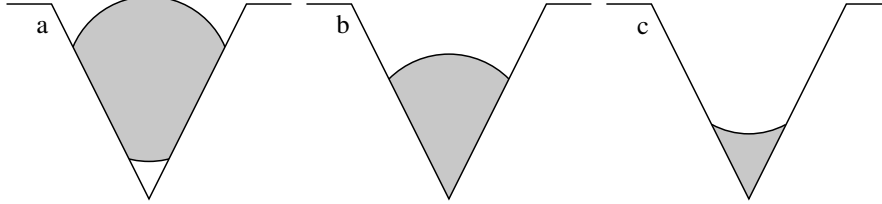


FIGURE 2.5: Illustration of a nucleus forming in a wedge or conical pit, showing three possible scenarios: (a)  $\theta \geq 90^\circ + \frac{\varphi}{2}$ ; (b)  $90^\circ - \frac{\varphi}{2} < \theta < 90^\circ + \frac{\varphi}{2}$ ; (c)  $\theta \leq 90^\circ - \frac{\varphi}{2}$ .

if  $\theta \geq 90^\circ + \frac{\varphi}{2}$ , where  $Q(x)$  is as defined in Equation 2.13. However if  $90^\circ - \frac{\varphi}{2} < \theta < 90^\circ + \frac{\varphi}{2}$  then

$$Q_{\text{wedge}}(\theta, \varphi) = \frac{1}{4\pi} \left( \cos \theta \sin^2 \theta \sin \Omega - \cos \theta (3 - \cos^2 \theta) \Omega + 4 \sin^{-1} \left( \sin \frac{\Omega}{2} \sin \frac{\varphi}{2} \right) \right) \quad (2.15)$$

where

$$\Omega = 2 \cos^{-1} \left( \cot \theta \cot \frac{\varphi}{2} \right). \quad (2.16)$$

Finally if  $\theta \leq 90^\circ - \frac{\varphi}{2}$  then  $Q_{\text{wedge}}(\theta, \varphi) = 0$ , and hence there is no nucleation barrier.

Figure 2.5 illustrates the three conditions. If  $\theta \geq 90^\circ + \frac{\varphi}{2}$  (Equation 2.14), i.e. a large contact angle and a narrow wedge, the favourable nucleation position is away from the wedge apex (as shown in Figure 2.5a) and  $\Delta G^*$  is independent of the wedge angle. If, however,  $90^\circ - \frac{\varphi}{2} < \theta < 90^\circ + \frac{\varphi}{2}$  (Equation 2.15), nucleation occurs at the apex of the wedge, as shown in Figure 2.5b, and  $\Delta G^*$  is dependent on both  $\theta$  and  $\varphi$ . Finally if  $\theta \leq 90^\circ - \frac{\varphi}{2}$ , then the new phase can grow from the wedge apex without a nucleation barrier, this condition dictating that it must have a concave interface as shown in Figure 2.5c.

Figure 2.6 plots Equations 2.14 and 2.15, plotting  $\frac{\Delta G^*}{\Delta G_{\text{flat}}^*}$  where  $\Delta G_{\text{flat}}^*$  is the equivalent critical free energy barrier on a flat plane. Several things are apparent:

1. the free energy barrier to nucleation in a wedge is always lower than that for a flat plane, therefore wedges should promote nucleation;

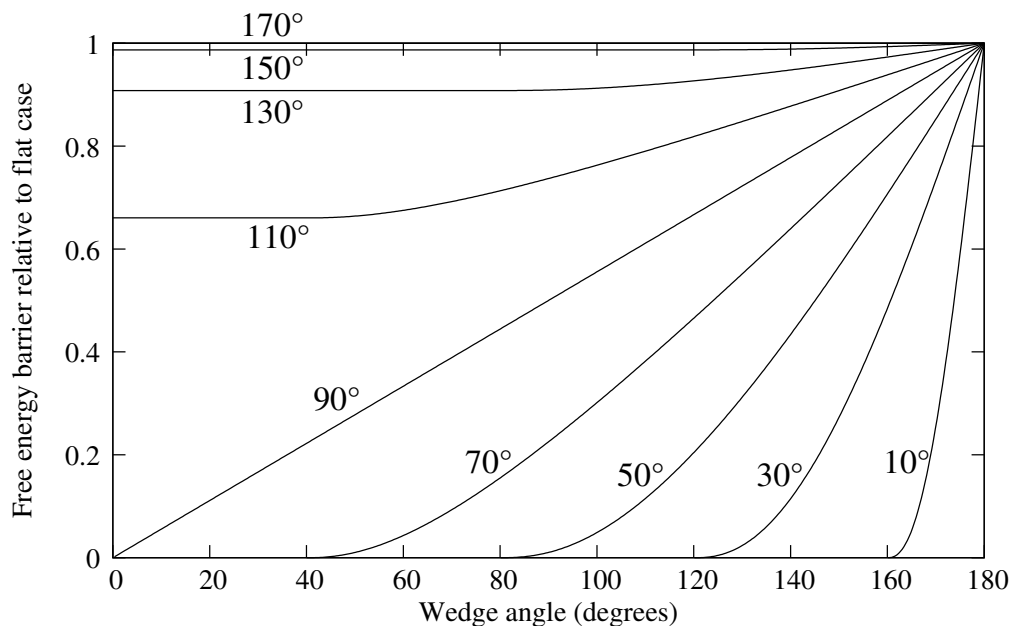


FIGURE 2.6: Graph showing free energy barrier calculations for a planar wedge made by Sholl and Fletcher. Values are relative to the free energy barrier of an equivalent nucleus on a flat plane. Each line represents a particular value of  $\theta$ . The line for

$$\theta = 170^\circ \text{ is indistinguishable from the line } \frac{\Delta G^*}{\Delta G_{\text{flat}}^*} = 1.$$

2. the nucleation free energy barrier decreases monotonically with decreasing wedge angle, therefore more acute wedges might be expected to provide more effective nucleation sites;
3. for lower contact angles, the free energy barrier is decreased more significantly below  $\Delta G_{\text{flat}}^*$ , therefore wedges are likely to be more effective for lower contact angle systems;
4. at contact angles above about  $150^\circ$ , there is very little benefit to nucleation in a wedge.

### Nucleation in a conical pit

A linear wedge provides a simple model for a one-dimensional surface feature such as a scratch, groove or step edge. Likewise a conical pit provides a model for a zero-dimensional feature such as a pit or sharp corner. I have used geometrical arguments to find  $\Delta G^*$  in a pit of angle  $\varphi$ , retaining the definition of  $\varphi$  shown in Figure 2.4 (see Appendix A for details).

Again,  $\Delta G^*$  is proportional to  $\Delta G_{\text{hom}}^*$  but reduced by a factor  $Q_{\text{cone}}(\theta, \varphi)$ . If  $\theta \geq 90^\circ + \frac{\varphi}{2}$ , then

$$Q_{\text{cone}}(\theta, \varphi) = Q\left(\theta + \frac{\varphi}{2} - 90^\circ\right) + Q\left(\theta - \frac{\varphi}{2} - 90^\circ\right) - \frac{1}{4} \cos^3\left(\theta + \frac{\varphi}{2}\right) \tan\left(90^\circ - \frac{\varphi}{2}\right) \left(1 - \left(\frac{\cos\left(\theta - \frac{\varphi}{2}\right)}{\cos\left(\theta + \frac{\varphi}{2}\right)}\right)^3\right) \quad (2.17)$$

whereas if  $90^\circ - \frac{\varphi}{2} < \theta < 90^\circ + \frac{\varphi}{2}$  then

$$Q_{\text{cone}}(\theta, \varphi) = Q\left(\theta + \frac{\varphi}{2} - 90^\circ\right) - \frac{1}{4} \cos^3\left(\theta + \frac{\varphi}{2}\right) \tan\left(90^\circ - \frac{\varphi}{2}\right). \quad (2.18)$$

Finally, as with a wedge geometry, if  $\theta \leq 90^\circ - \frac{\varphi}{2}$  then there is no free energy barrier to nucleation, as predicted by Fletcher.[11]

These three situations again correspond to those illustrated in Figure 2.5. That is, first, nucleation away from the apex when  $\theta \geq 90^\circ + \frac{\varphi}{2}$ , then nucleation at the apex when  $90^\circ - \frac{\varphi}{2} < \theta < 90^\circ + \frac{\varphi}{2}$  and finally growth without nucleation from the apex when  $\theta \leq 90^\circ - \frac{\varphi}{2}$ .

Figure 2.7 plots Equations 2.17 and 2.18, plotting  $\frac{\Delta G^*}{\Delta G_{\text{flat}}^*}$  where  $\Delta G_{\text{flat}}^*$  is the equivalent critical free energy barrier on a flat plane. Qualitatively it is similar to nucleation in a wedge, showing the same trends with varying  $\theta$  and  $\varphi$ . However the conical pit provides a lower free energy barrier to nucleation than a linear wedge for every value of  $\theta$  and  $\varphi$ . In particular the conical pit gives a significantly reduced free energy barrier at high contact angles where the wedge does not; at  $\theta$  about equal to  $150^\circ$ .

Figure 2.8 shows the ratio  $\frac{Q_{\text{cone}}}{Q_{\text{wedge}}}$  for a number of values of  $\theta$  as a function of  $\varphi$ . Here it can be clearly seen that the nucleation barrier in a cone is always less than that of a wedge of the same angle, and that the difference is much greater for small  $\varphi$  and small  $\theta$ .

## 2.2.4 Nucleation kinetics

Let us define the nucleation rate  $J$  in a system as the number of nucleation events per second. Using Boltzmann statistics, this can be related to the nucleation free energy barrier  $\Delta G^*$  by [3]

$$J = B \exp\left(-\frac{\Delta G^*}{k_B T}\right) \quad (2.19)$$

where  $k_B$  is the Boltzmann constant and  $B$  is a system-dependent constant.  $B$  may be thought of as the number of attempts to form a nucleus per unit time, and the exponential



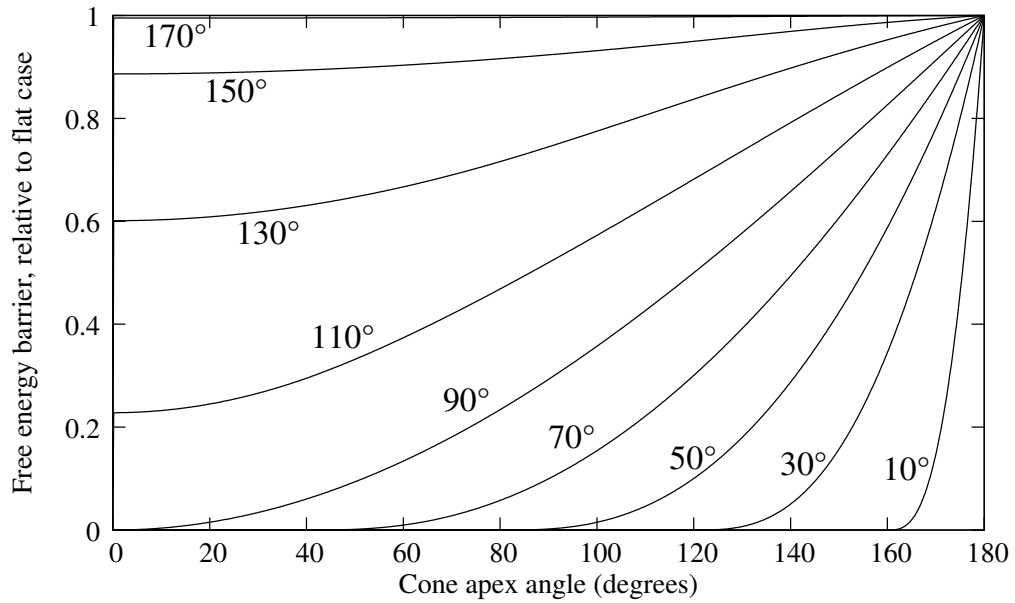


FIGURE 2.7: Graph showing free energy barrier calculations for a conical pit. Values are relative to the free energy barrier of an equivalent nucleus on a flat plane. Each line represents a particular value of  $\theta$ .

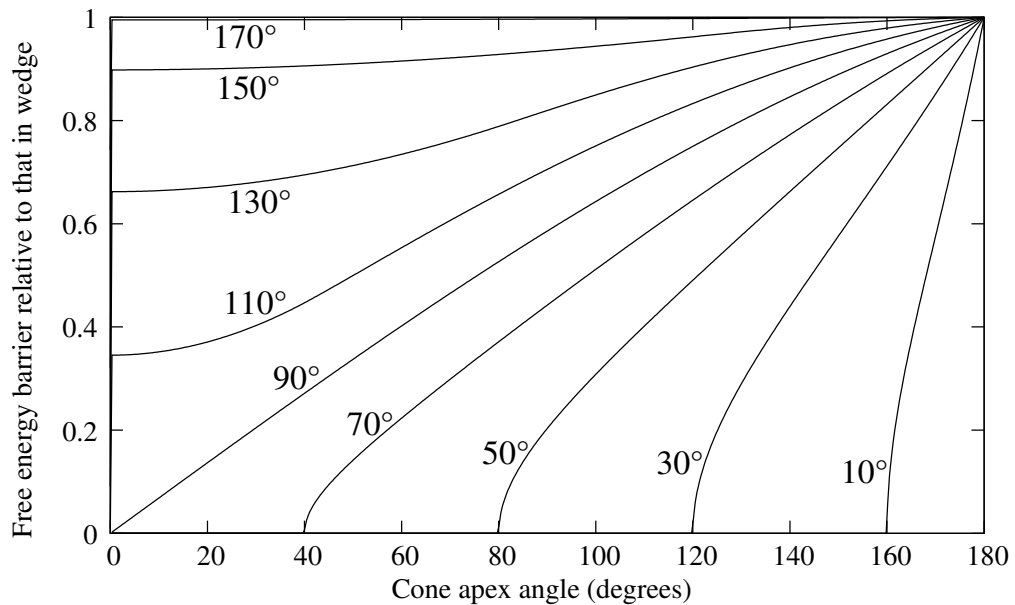


FIGURE 2.8: Graph showing the ratio of the results in Figures 2.7 and 2.6, i.e. the nucleation free energy barrier in a conical feature relative to that in a wedge. Each line represents a particular value of  $\theta$ .

factor as the probability of a single attempt succeeding. The dependence of  $B$  on various physical properties of the nucleating substance such as temperature, diffusion rate etc. is non-trivial, however clearly it must be approximately proportional to the number of nucleation sites in the system. Hence for a system nucleating homogeneously,  $B$  and therefore  $J$  must be proportional to the volume of the system. And if nucleation is occurring at an interface, then  $B$  must be proportional to the area of that interface. If nucleation occurs along a linear feature such as a scratch or a contact line between three phases, then  $B$  must be proportional to its length. Finally if nucleation occurs at one or more specific points, such as in pits or on contaminant particles, then  $B$  must be proportional to the number of these.

It is not then immediately clear that heterogeneous nucleation will greatly enhance nucleation rates. As we move from homogeneous nucleation in the bulk (three-dimensional) to flat heterogeneous nucleation (two-dimensional) to nucleation in a linear wedge (one-dimensional) to nucleation in the apex of a pit (zero-dimensional), not only are we reducing  $\Delta G^*$  but we are reducing  $B$ , as the lower-dimensional features offer a smaller number of sites. If we approximate  $B$  as  $bx^n$ , [3, 12] where  $b$  is a constant,  $n$  is the dimension of the nucleation feature and  $x$  is a characteristic length scale, then we get an expression for nucleation rate  $J_n$  in a feature of dimension  $n$  as

$$J_n = bx^n \exp\left(-\frac{\Delta G_n^*}{k_B T}\right) \quad (2.20)$$

where  $\Delta G_n^*$  is the free energy barrier to nucleation in an  $n$ -dimensional feature. Now we can see that the ratio of nucleation rates in any dimension compared to a lower dimension is, from Equation 2.20,

$$\frac{J_n}{J_{n-1}} = x \exp\left(-\frac{\Delta G_n^* - \Delta G_{n-1}^*}{k_B T}\right) \quad (2.21)$$

Thus if  $\Delta G_n^* - \Delta G_{n-1}^* \gg k_B T$  then a lower-dimensional feature offering a lower energy barrier can still dominate the nucleation rate despite a much lower number of sites. However if  $\Delta G_n^* - \Delta G_{n-1}^* \ll k_B T$  then the higher-dimensional site will always dominate. Thus topographically-aided nucleation is likely to be most important when energy barriers are very large compared to  $k_B T$ , i.e. when nucleation rates are low.

### 2.2.5 Contact angles of liquids and crystals

As shown in Section 2.2.3, the effect of surface geometry upon nucleation is highly dependent upon the contact angle of the nucleating phase with the substrate. This in itself is determined by the relative strengths of the surface energies between the three

phases, as per Equation 2.11. The value  $\gamma_{sl} - \gamma_{sv}$  is especially important: if this is negative, the compound has a contact angle of less than  $90^\circ$  and the compound can grow from a highly acute feature without a barrier. If it is positive, the contact angle is more than  $90^\circ$  and the new phase must first nucleate in order to form, regardless of geometry. Although solid “contact angles” are almost impossible to experimentally measure, I here make a qualitative argument about how these are likely to vary between systems.

Regarding a liquid nucleating from vapour, both the liquid-vapour and substrate-vapour interfaces are likely to have large surface energies: the vapour phase provides few molecules for those at the edge of the condensed phase to bond with. The liquid-substrate interface is likely to have a much lower interfacial energy as the molecules may form attractive bonds between the two phases. Therefore liquids tend to have contact angles considerably below  $90^\circ$  on flat surfaces, unless there are very particular unfavourable interactions between the liquid and the solid.[13, 14]

If we consider a solid phase nucleating from vapour, then its interfacial energy between itself and the substrate is likely to be higher than that of a liquid. The rigid structure of solids means that neither is likely to be able to effectively adjust its surface arrangement to bond efficiently with its neighbour, especially if one or the other or both is a crystalline phase. Efficient bonding between two solids may occur if there is a close lattice match between two crystals, but this is rare. I suggest that solids forming on foreign substrates may experience contact angles above or below  $90^\circ$ .

When a solid nucleates from solution, there is likely to be a much lower surface energy between the substrate and the solution than between the substrate and a vapour. For this reason, I suggest that crystals in this case are far more likely to have high contact angles than those nucleating from vapour, but low contact angles should still be possible, depending on the relative bond strengths of the solid and solution with the substrate.

Finally, for a solid nucleating from the melt, we must consider that the nucleus and the liquid are chemically identical, differing only in the arrangement and mobility of their molecules. Any foreign substrate is likely to have a lower surface energy with a liquid phase than a solid phase of the same compound, as the liquid can more easily adjust to the surface structure of the substrate, an effect observed experimentally in the phenomenon of surface melting of solids.[15, 16] Therefore, compounded by a low surface energy between two phases of the same compound, a solid nucleating from the melt is almost certainly going to have a very high contact angle on most substrates.

So in general, I propose that surface topography should be least important for crystals nucleating from the melt, more important for those nucleating from solution, more

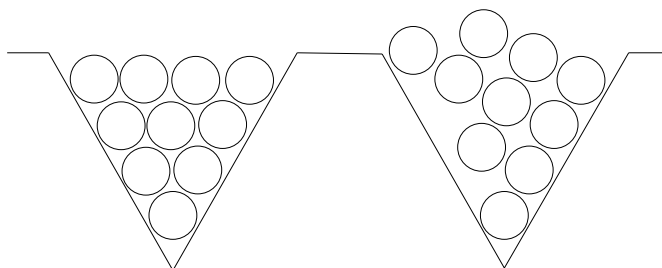


FIGURE 2.9: Illustration of two polymorphs of a two-dimensional crystal trying to form in two  $60^\circ$  triangular wedges.

important again for those nucleating from vapour, and most important of all for liquids nucleating from vapour.

### 2.2.6 Crystal anisotropy and nucleation site geometry

The free energy barrier calculations in Section 2.2.3 assumed an isotropic phase and therefore a spherical nucleus. A crystal is fundamentally anisotropic, and its equilibrium shape is non-spherical, often faceted. However, provided that the shape is not too extremely removed from spherical (e.g. a long needle), I suggest that the correction to the expressions derived is likely to be small. Assuming that the shape and orientation of the nucleus are known, exact expressions could easily be derived using the principles outlined in Appendix A.

There is however another effect of the anisotropy of crystals. The interfacial energy between a crystal and a substrate is dependent upon its orientation. On a flat surface, a crystal will tend to grow with a particular favourable crystal plane in contact with it to minimise surface energy. In a wedge or pit this may be frustrated: it may be geometrically impossible to align two or more favourable planes with the walls, and therefore it would be necessary to have one or more unfavourable planes in contact with the substrate. Therefore I suggest that surface features may offer slightly less reduction in nucleation free energy barriers for crystals than they do for amorphous materials.

This opens up a possibility. Consider Figure 2.9. It imagines two wedges, each having a  $60^\circ$  angle. A different polymorph is trying to form in each: in the left, a hexagonal lattice; in the right, a square lattice. Whilst the hexagonal lattice can align itself with both walls, for the square lattice it is impossible. A  $90^\circ$  wedge would have the opposite result. It is therefore possible for particular wedges to favour the nucleation of particular crystal polymorphs, as has been observed experimentally.[17–19]

### 2.2.7 Contact line nucleation

Where nucleation occurs from a liquid drop, there often exists a contact line where three phases meet: this is true for a drop sitting on a surface, or a small particle coming into contact with a suspended drop in the atmosphere. There has been some experimental evidence that this line is favourable for ice nucleation,[20–25] as well as theoretical support.[26, 27] If this is the case, surface topography along the contact line may still be an important factor. However, there is conflicting experimental evidence showing no preference for contact line nucleation.[28, 29]

### 2.2.8 Beyond the classical theory

Classical nucleation theory is far from being a perfect model for real nucleating systems. Whilst it succeeds in qualitatively describing nucleation phenomena well, experimental and simulational studies have shown that it often fails to predict nucleation rates by orders of magnitude.[30–34]

Its main failing is that it does not take into account the difference between bulk materials and those at the nanoscale. Both the surface energy and  $\Delta G_V$  of a nucleus containing only tens or hundreds of molecules is likely to be very different to that in the bulk, due to a highly curved interface from which no molecule is far removed. It also assumes that nucleation always proceeds via the most energetically favourable route, i.e. spherically, whereas simulations have shown that nucleation often proceeds via a more entropically favourable aspherical shape.[32, 35] Finally, it assumes a sharp interface between two phases, whereas at the length scale of nucleation the interface is likely to be diffuse.

Density functional theory, rather than calculating free energy barriers based on various assumptions and bulk values, attempts to derive the behaviour of a system from statistical treatment of intermolecular interactions.[36] Alongside Monte Carlo simulations, it has helped test and visualise nucleation theory.[37–40] However, unlike the classical theory, these non-analytical approaches are far from being able to predict behaviour in wide ranges of conditions and geometries. Therefore, in this thesis nucleation behaviour will be considered with respect to classical nucleation theory.

We have so far considered nucleation as occurring via a single step. However it is now widely accepted that nucleation often occurs in two or more steps via intermediate metastable phases.[41–45] These ideas are further explored in the next section. This is often described as “non-classical” nucleation, but it is broadly not in contradiction to the classical model.

## 2.3 Two-step nucleation

### 2.3.1 Ostwald's step rule

Ostwald suggested in 1897 that polymorphic materials may nucleate via a series of transitions, rather than in a single step.[46] He proposed that for a compound with several polymorphs of differing stability, it would be the least stable which crystallised first, which would then undergo a transition to the next most unstable, and so on, until the most stable polymorph was reached. This is a tendency in nature rather than an absolute rule, and explanations have been offered in terms of irreversible thermodynamics.[47]

In terms of classical nucleation theory, this means that the polymorph with the lowest  $\Delta G_V$  is unlikely to be that with the lowest free energy barrier to nucleation. This implies that less stable polymorphs are likely to have much lower interfacial energies. In a solution or in the melt, a phase will have a lower surface energy if its structure is closer to that of the liquid. For example, amorphous phases tend to have much lower surface energies in liquids than crystalline phases; as such, many crystals are thought to crystallise via highly metastable amorphous precursor phases.[41, 48, 49]

With regards to crystallisation in surface features, it has been established that phases having a smaller contact angle with the substrate receive a greater reduction in their nucleation free energy barrier. Therefore if less stable phases, particularly amorphous phases, are forming first, then it is the free energy barrier to form these in an acute feature with which we should be most concerned. As an amorphous phase is likely to have a smaller contact angle with any given substrate than a crystalline phase, as discussed in Section 2.2.5, this should increase the importance of surface topography in the nucleation of such compounds. In addition, it is possible that a favourable surface geometry may promote growth via precursor phases which do not feature in homogeneous nucleation.

### 2.3.2 Capillary condensation

Section 2.2.3 showed that a phase with a low contact angle may form in an acute feature without a nucleation barrier. This is explained by Equation 2.6: the radius of curvature is negative, and so a very small condensate does not experience an increased vapour pressure, rather the reverse.

As discussed in Section 2.2.5, liquids tend to have low contact angles on solid substrates. Therefore liquids often condense into acute features below saturation, a process known

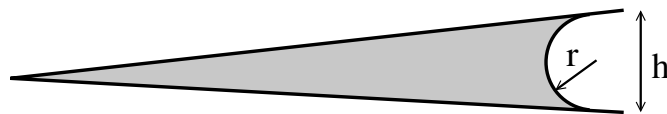


FIGURE 2.10: Illustration of a capillary condensate in an acute feature, showing the radius of curvature  $r$  and the condensate height  $h$ .

as capillary condensation. The liquid is not stable in the bulk, but will grow until the radius of curvature of its interface is such that it is in equilibrium with the vapour. At a saturation  $S$  in the limit of a  $0^\circ$  contact angle in an infinitely acute wedge, it will grow until it reaches a height  $h$  as shown in Figure 2.10 where

$$h = -\frac{2\gamma V_m}{RT \ln S} \quad (2.22)$$

in a wedge (cylindrical interface) or

$$h = -\frac{4\gamma V_m}{RT \ln S} \quad (2.23)$$

in a conical pit (spherical interface), from Equations 2.6 and 2.7.

The filling of wedges by a liquid has been extensively studied experimentally and theoretically.[50–55] A similar phenomenon may exist in some solutions with regards to the formation of an amorphous phase in acute features below the bulk solubility. This would rely on there being a sufficiently low contact angle between the amorphous phase and the substrate.

A crystalline phase may in theory continue to exist after melting/sublimating/dissolving as a small retained embryo in an acute feature. If not removed by sufficient heating/undersaturation, this may provide the seed for a new bulk phase when supercooled/supersaturated conditions are again obtained.[56, 57]

### 2.3.3 Liquid-mediated nucleation from vapour

Liquid capillary condensates may form even below the melting point of the compound. In this case the liquid will be supercooled. A solid condensate may also form in a similar manner, and having a lower vapour pressure would have a larger equilibrium size than a liquid in the same conditions. A supercooled liquid capillary may be in equilibrium with bulk solid.

As the liquid will almost certainly have a lower contact angle with the substrate than the solid phase, we can expect a liquid capillary to form first, as it will be most energetically favourable at the limit of zero volume. But as it grows, at some stage it must become

favourable to transform into the solid phase. We can estimate the minimum height  $h_{\min}$  at which solidification could occur: it must be at least twice the critical radius of a solid-in-liquid nucleus. However a critical nucleus is unstable with regards to the liquid; for the phase transition to reach a lower free energy than the liquid, it must grow to a radius of at least  $\frac{3}{2}r^*$ . [3] Therefore, using Equations 2.4 and 2.9 we find

$$h_{\min} = 3r^* = \frac{6\gamma_{sl}T_m}{\rho\Delta H_{fus}\Delta T} \quad (2.24)$$

where  $\gamma_{sl}$  is the solid-liquid surface energy.

The vapour pressure  $p_s$  of a solid can be related to that of a supercooled liquid  $p_l$  by this relation derived from the Clausius-Clapeyron equation: [1]

$$\ln \frac{p_l}{p_s} = \frac{\rho V_m \Delta H_{fus}}{R} \left( \frac{1}{T} - \frac{1}{T_m} \right) = \frac{\rho V_m \Delta H_{fus}}{R} \frac{\Delta T}{TT_m}. \quad (2.25)$$

This, alongside Equations 2.22 and 2.24, allows us to estimate the minimum saturation  $S$  with respect to a solid at which crystallisation from a liquid condensate in a wedge could occur as

$$\ln S = \left( 1 - \frac{1}{3} \frac{\gamma_{lv}}{\gamma_{sl}} \right) \frac{\rho V_m \Delta H_{fus}}{R} \frac{\Delta T}{TT_m} \quad (2.26)$$

where  $\gamma_{lv}$  is the surface energy between liquid and vapour, here disregarding temperature-dependent corrections to  $\gamma$  and  $\Delta H_{fus}$ . Thus nucleation via a supercooled liquid capillary condensate may potentially occur at very low  $S$ , indeed if  $\gamma_{lv} \geq 3\gamma_{sl}$  (which is not unreasonable) then we can expect crystallisation at  $S \leq 1$ , although if  $S < 1$  then the crystal will remain confined in the wedge and not grow into a bulk phase until  $S > 1$ .

## 2.4 Prior work

### 2.4.1 Nucleation on rough surfaces

A common approach for experiments on the effect of topography on crystal nucleation is to compare growth on otherwise-similar smooth and rough surfaces, coupled with some attempt to characterise the level and type of roughness. Such attempts are problematic, as most means of obtaining a rough surface lead to a varied and inhomogeneous distribution of surface features.

The effect of topography has been studied on the growth of diamond from vapour on silicon substrates. Higuchi et al. sonicated silicon substrates with various grades of diamond powder to pit the substrate and found the process to increase nucleation



density, with larger grades of powder having the greatest effect.[58] Ascarelli et al. confirmed this result and found a similar dependence on grit size with diamond-polished substrates.[59] Buijnsters et al. found even greater increases in nucleation densities by sonicating with mixtures of diamond powder and metal particles.[60]

Studies have also been made comparing nucleation on various polymeric films of differing topographies. Lin et al. found the nucleation density of gypsum grown from solution on various films to be higher on those with a rougher surface.[61] Diao et al. found a similar result looking at the induction time of aspirin nucleation, with crystals appearing faster on more porous films.[62] Di Profio et al. found a less conclusive relationship between contact angle, surface roughness and nucleation density.[63]

Sengupta Ghatak and Ghatak stretched, treated and relaxed elastomers to produce surfaces wrinkled on the nanometre scale.[64] These were found to be highly effective at nucleating several proteins.

Järn et al. used an atomic force microscope to quantify the roughness of various titania surfaces. They then found a positive correlation between this and the speed of calcium phosphate nucleation, but only on surfaces with a low water contact angle.[65] Keysar et al. reported higher nucleation density and stronger adhesion of calcite grown on rough than smooth steel.[66] Mu et al. used a fractal dimension to quantify the roughness of magnesium surfaces from atomic force micrographs, and found a positive correlation between this and water drop nucleation density.[67]

Conrad et al. reported ice nucleation at higher temperatures on barium fluoride surfaces pitted by partial dissolution compared to a flat surface, however the experimental arrangement leaves this conclusion in considerable doubt.[68] Asanithi found that films assembled from graphite flakes became less effective at nucleating hydroxyapatite if they were compressed, a process which reduced the surface roughness and porosity.[69]

## 2.4.2 Nucleation in pores

Much work has been done on studying nucleation in highly porous materials. Looking at vapour deposition of diamond films, Raiko et al. found enhanced nucleation on porous silicon compared to smooth.[70]

Chayen et al. demonstrated the efficacy of porous silicon as a protein nucleator.[71] They later found that porous glasses with wide pore size distributions are more effective nucleators than those with only a narrow range of pore sizes.[72] Shah et al. engineered porous glasses of varying pore diameters, and found that particular diameters nucleated particular proteins selectively.[73]

Ha et al. studied the nucleation of organic compounds in porous glass and polymers, and found some pore diameters to be effective at selectively nucleating certain polymorphs.[74] Diao et al. found a similar result with porous polymer microgels.[75] Cantaert et al. observed that confinement of nucleation within porous alumina greatly affected the morphology and orientation of calcium phosphate crystals.[76]

### 2.4.3 Nucleation in manufactured features

An approach to avoid the randomness and variability of most rough surfaces is to attempt to produce a well-defined topographical feature on a flat surface. However, producing features well-defined on the nanometre scale of nucleation is extremely difficult, and most milling procedures are accompanied by a risk of chemically modifying the surface.

Portavoce et al. used an ion beam to mill a regular array of pits into a silicon wafer. Upon growth of germanium from vapour, they found the crystals to grow from the pits and not on the flat surfaces.[77]

Diao et al. found that patterning a polymer with round pits hindered aspirin nucleation, whereas patterning with angular pits matching the angles between the crystal planes of aspirin promoted it.[78] López-Mejías et al. used a polymer surface patterned with angular pits to promote growth of a metastable polymorph of mefenamic acid, with the angles between walls proposed to direct the form of crystallisation.[19]

Some studies have reported behaviour contrary to that predicted by theory. Dennig et al. reported enhanced diamond nucleation on *convex* surface features of etched silicon.[79] Jiang et al. milled V-shaped grooves into titania surfaces and reported that calcium phosphate nucleated preferentially on the convex asperities.[80]

### 2.4.4 Nucleation in naturally-occurring features

There are a very few natural systems which provide nucleation sites offering a well-defined topography without the imprecision of milling. Georgieva et al. found human hair, with a surface rich in acute wedges, to be effective at nucleating several proteins.[81, 82]

Bonafede and Ward looked at nucleation of organic compounds from solution on crystalline surfaces. They reported the selective growth of usually unfavourable polymorphs along step edges, and attributed this to a match between the angle of the wedge and the crystal planes of the polymorph.[17, 18]

### 2.4.5 Two-step nucleation

The Surface Force Apparatus offers a unique experimental geometry whereby two cylindrical sheets of mica are held in contact at 90° to one another. This produces an annular wedge between the two, approximating a highly acute linear wedge running in a circle.

It has been used to test two-step nucleation of crystals from vapour via a supercooled liquid condensate.[83, 84] A reservoir of an organic crystal is left within the sealed apparatus, creating a saturated vapour. Any condensate can then be observed optically in the mica contact region, and its refractive index determined by multiple-beam interferometry. For some compounds with very low vapour pressures ((-)-menthol, pinacol) no condensate was observed. For others, the formation of a liquid capillary condensate was observed, possibly followed by freezing at lower temperatures (neopentanol, hexamethylcyclotrisiloxane). For other compounds capillary condensation was observed without freezing (cyclooctane, racemic menthol) or a crystal was seen to grow without a visible liquid condensate (norbornane, hexachloroethane).

Marcolli has reviewed literature on ice nucleation from vapour on aerosols and in porous media and concluded that “deposition mode” nucleation below about -38 °C is best explained by the filling of acute features with supercooled water which then freezes.[85] This has been supported by experiments by Welte et al. on ice nucleation on kaolinite.[86]

### 2.4.6 Simulations

Topographically-aided nucleation has also been studied by computer simulation. Page and Sear used a simple two-dimensional lattice gas model to observe nucleation in rectangular pits.[87] They observed nucleation at the concave pit corners, with pits narrow on the length-scale of nucleation enhancing nucleation rates. However they also noticed a second nucleation barrier for very narrow pits, as once the pit is filled to the top it cannot grow out into a bulk phase without another nucleation event if the pit mouth is narrower than the critical diameter. For this reason they concluded there is an optimum diameter of pore for nucleation of any particular compound. Hedges and Whitlam performed similar simulations in three dimensions and came to similar conclusions of there being an optimal pit size.[88] They also studied the effectiveness of differing shapes of rectangular pits and reached the conclusion that small square pits of the right dimensions were more effective nucleators than long rectangular grooves. Hedges and Whitlam later looked at nucleation in square pits in both two and three

dimensions and concluded that the optimal pit size in either case scales proportionally to the critical radius.[89]

Page and Sear also performed Monte Carlo simulations of a crystal forming in a planar wedge at several angles.[90] They observed a nucleation rate orders of magnitude higher than that on a flat surface, but not decreasing monotonically with wedge angle. They propose the nucleation rate peaks when the wedge angle matches that between two close-packed crystal planes.

Van Meel et al. performed Monte Carlo simulations of a supersaturated vapour and an inert wall with a pit.[91] It was observed that the presence of a pit greatly aided nucleation, and that nucleation occurred via a liquid condensate inside the pit. It was also noted that amorphous pit walls were preferential to crystalline ones, as crystalline walls led to epitaxial growth and considerable strain.

## Chapter 3

# Methods and materials

This chapter contains a description of the materials and the experimental methods used throughout the thesis. As many parts of the thesis are mostly self-contained, particularly Chapters 7 and 8, specific experimental procedures are explained in their relevant chapter, alongside descriptions of crystallisation cell designs. The procedures contained in this chapter are those of general relevance across the whole thesis.

### 3.1 Substrates

#### 3.1.1 Mica

Muscovite mica (obtained from Paramount Corp., New York) was an important substrate throughout the work, and throughout this thesis the term “mica” will be used as a shorthand for Muscovite. It is a naturally occurring mineral of composition  $\text{KAl}_2(\text{AlSi}_3\text{O}_{10})(\text{OH})_2$ . Structurally, it is made from rigid layers of oxygen, hydrogen, aluminium and silicon, bound together by inter-layer potassium ions. As the ionic bonding between the layers is relatively weak, the mineral is easy to cleave perfectly along its (001) plane. The face exposed by this consists of a hexagonal framework of oxygen ions, bound by ions of silicon and aluminium in a 3:1 ratio.

The (001) cleavage plane of mica may be atomically smooth over substantial areas, however the surface is usually punctuated by large and small steps between crystal planes.[92] Rarer, one finds the top layers lifted and folded away from the lower layers, leaving a narrow cavity in between, features produced by imperfect cleavage.[93]

When mica is cleaved, it is supposed that the potassium ions on the cleavage plane are divided evenly between the two new surfaces. There is some evidence that this

potassium does not remain long in this arrangement, and reacts with atmospheric gases to form potassium carbonate,[94–99] although the precise nature of this is not well understood. Leaving mica in contact with atmosphere, known as weathering, has a large impact on its surface chemistry, as does immersion in water, which removes potassium from the surface.

### 3.1.2 Other layered minerals

Biotite is a variant of mica offering similar cleavage on the (001) plane, of composition  $K(Mg,Fe)_3AlSi_3O_{10}(F,OH)_2$ . Similar to Muscovite it has strong layers weakly bound by potassium ions, and has similar surface topography after cleavage.

Lepidolite is another mica with cleavage on the (001) plane, of composition  $K(Li,Al)_3(Si,Al)_4O_{10}(F,OH)_2$ . Again potassium ions bind the layers, and cleavage produces similar features to Muscovite.

Vermiculite is a layered mineral of composition  $(Mg,Fe)_3((Al,Si)_4O_{10})(OH)_2 \cdot 4H_2O$ . Like the micas it cleaves along the (001) plane, with ions of magnesium and iron binding the layers.

Mineral samples were obtained from private sellers, and their nature was verified by comparison to verified mineral specimens, by visual inspection and Raman spectroscopy.

### 3.1.3 Glass

Microscope slides were used for glass substrates (“super premium” slides, Fisher Scientific). These were 0.8–1.0 mm thick. Glass slides were cleaned before use as a crystallisation substrate, as described in Section 3.1.5.

### 3.1.4 Silicon

Silicon samples were cut from wafers of boron-doped silicon, 425–550  $\mu\text{m}$  thick, from Compant Technology. Wafers were polished on one side to a reported root-mean-squared roughness of less than 18 Å. All substrates were cleaned before use, as described in Section 3.1.5.

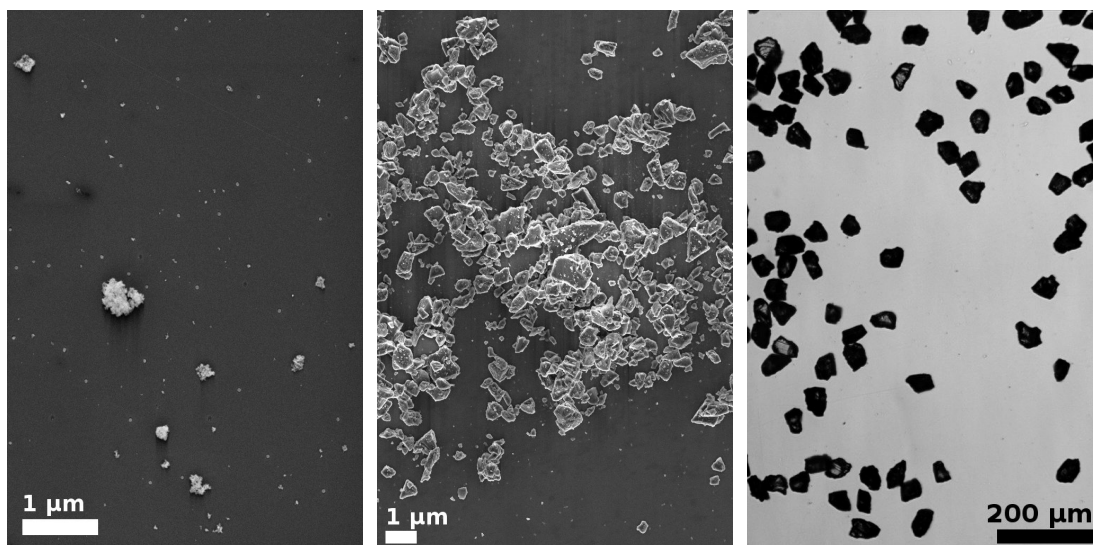


FIGURE 3.1: Electron micrographs of “ $< 10\text{ nm}$ ” (left) and “ $< 1\text{ μm}$ ” (centre) diamond powders, and an optical micrograph of “ $40\text{--}60\text{ μm}$ ” diamond powder (right).

### 3.1.5 Substrate cleaning

Glass and silicon substrates were cleaned by ultrasonication in a solution of about 1% “Decon 90” detergent for ten minutes, and then rinsed in deionised water. They were then ultrasonicated for ten minutes in each of the following: deionised water; acetone; deionised water. Finally they were rinsed with ethanol and dried in a nitrogen stream, before being stored in a clean sealed container until use. Substrates were cleaned in individual vials, positioned to ensure the crystallisation surface never came into contact with the vial walls.

Cleaved mineral surfaces were mostly not washed, as they were expected to be clean immediately after cleavage. Minerals were cleaved within a laminar flow cabinet to avoid contamination.

### 3.1.6 Diamond powder and scratching

#### Diamond powder

Three grades of diamond powder were used, known as “ $< 10\text{ nm}$ ” (Aldrich), “ $< 1\text{ μm}$ ” (Alfa Aesar) and “ $40\text{--}60\text{ μm}$ ” (Alfa Aesar). Figure 3.1 shows optical and electron micrographs of the three grades, in each case verifying the advertised size range. Significant clumping of grains was observed with the two smaller grades, but not with the largest grade.

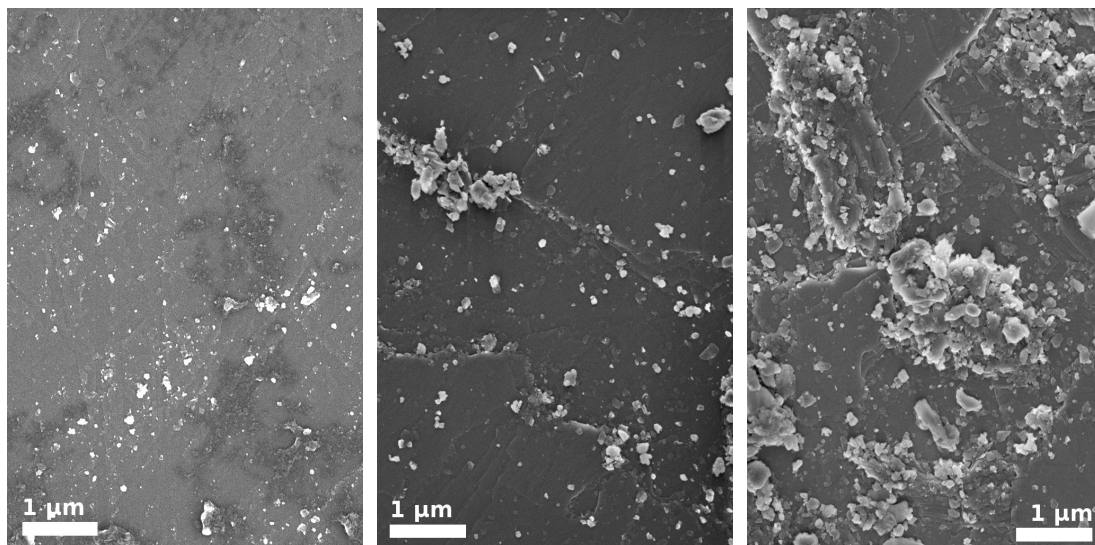


FIGURE 3.2: Electron micrographs of mica surfaces scratched with “<math>< 10\text{ nm}</math>” (left), “<math>< 1\ \mu\text{m}</math>” (centre) and “<math>40\text{--}60\ \mu\text{m}</math>” (right) diamond powders.

### Diamond scratching

To scratch surfaces, a small amount of the powder was placed on the finger of a nitrile glove. This was then rubbed gently back and forth across the surface for two minutes. To remove residue powder, glass and silicon substrates were rinsed in water before being cleaned as described in Section 3.1.5. Mica substrates were not sonicated for fear of damaging the more delicate structure of the mineral, instead they were rinsed thoroughly in water and ethanol to attempt to remove residue powder.

Figures 3.2–3.4 show electron micrographs of surfaces of mica, glass and silicon respectively scratched with each grade of powder. On glass and silicon, the powders cut long grooves into the material. On mica, the powder appears to strip the top layers of the material, leaving a rough surface strewn with mica debris.

## 3.2 Compounds

### 3.2.1 Compounds for crystallisation from vapour

Alongside water/ice, five organic compounds were used extensively, chosen for a high vapour pressure and an ability to crystallise at room temperature. They are: neopentanol (2,2-dimethyl-1-propanol, Aldrich, 99%), carbon tetrabromide (tetrabromomethane, Aldrich, 99%), camphor (1,7,7-trimethylbicyclo[2.2.1]heptan-2-one, (+), Aldrich, 98%), norbornane (Aldrich, 98%) and hexachloroethane (Alfa Aesar, 98%). The physical properties of each are summarised in Table 3.1.



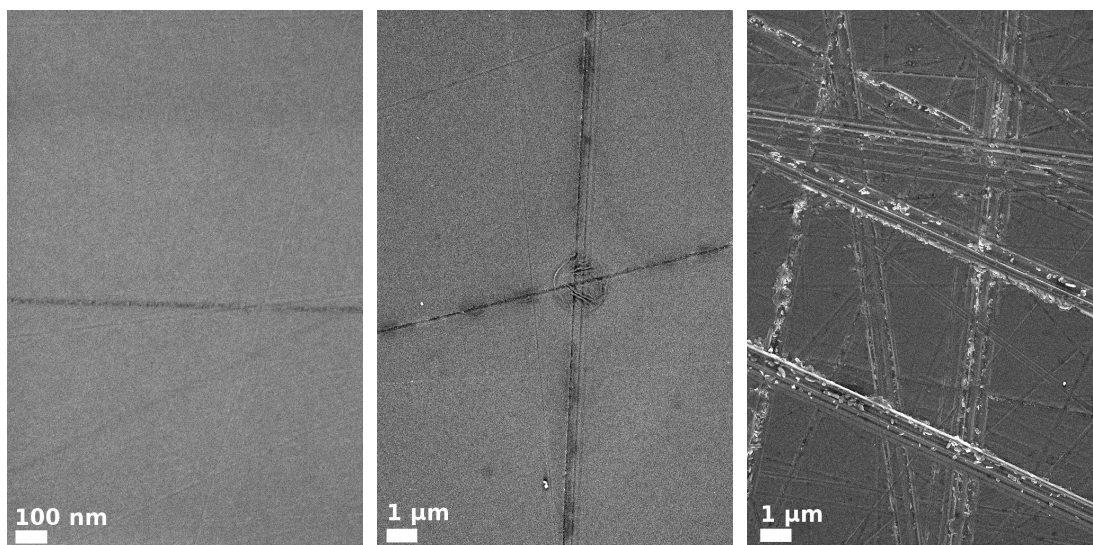


FIGURE 3.3: Electron micrographs of glass surfaces scratched with “< 10 nm” (left), “< 1 μm” (centre) and “40–60 μm” (right) diamond powders.

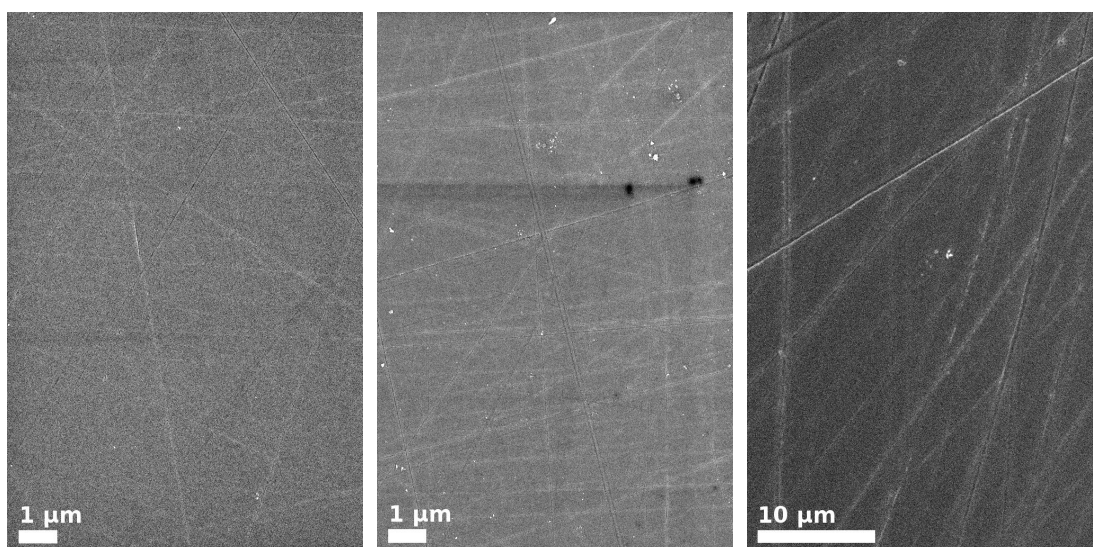


FIGURE 3.4: Electron micrographs of silicon surfaces scratched with “< 10 nm” (left), “< 1 μm” (centre) and “40–60 μm” (right) diamond powders.

Other compounds used include naphthalene (bicyclo[4.4.0]deca-1,3,5,7,9-pentene, Acros Organics, 99%), menthol ((1R,2S,5R)-2-isopropyl-5-methylcyclohexanol (-), Sigma-Aldrich, 99%), isomenthol ((1S,2R,5R)-2-isopropyl-5-methylcyclohexanol (+), Molekula), pinacol (2,3-dimethyl-2,3-butanediol, Acros Organics, 99%) and hexamethylcyclotrisiloxane (Acros Organics, 98%). Table 3.2 lists the composition and melting points of each.

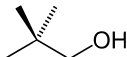
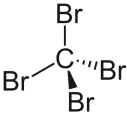
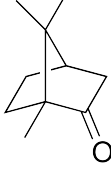
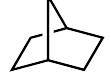
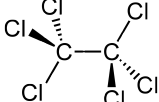
Compound	formula	structure	$T_m$	$\Delta H_{\text{sub}}$	$\Delta H_{\text{fus}}$	$p_0$
water	H <sub>2</sub> O		0	2800 [100]	330 [100]	27 [100]
neopentanol	C <sub>5</sub> H <sub>12</sub> O		53 [100]	590 [101]	51 [101]	11 [101]
carbon tetrabromide	CBr <sub>4</sub>		92 [100]	160 [102]	11 [100]	1.0 [101]
camphor	C <sub>10</sub> H <sub>16</sub> O		179 [100]	340 [103]	45 [101]	0.21 [101]
norbornane	C <sub>7</sub> H <sub>12</sub>		88 [100]	420 [104]	45 [104]	39 [104]
hexachloroethane	C <sub>2</sub> Cl <sub>6</sub>		187[100]	210 [105]	41 [100]	0.75 [101]

TABLE 3.1: Table showing the physical properties of the principal compounds used for crystallisation from vapour; here  $T_m$  is the melting point in °C,  $\Delta H_{\text{sub}}$  is the enthalpy of sublimation in kJ kg<sup>-1</sup>,  $\Delta H_{\text{fus}}$  is the enthalpy of fusion in kJ kg<sup>-1</sup> and  $p_0$  is the equilibrium vapour pressure in mm Hg at 300 K.

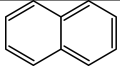
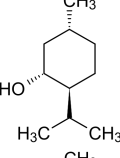
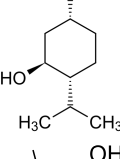
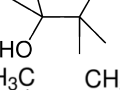
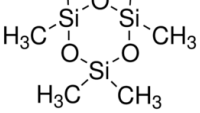
Compound	formula	structure	$T_m$
naphthalene	C <sub>10</sub> H <sub>8</sub>		80
menthol	C <sub>10</sub> H <sub>20</sub> O		43
isomenthol	C <sub>10</sub> H <sub>20</sub> O		83
pinacol	C <sub>6</sub> H <sub>14</sub> O <sub>2</sub>		43
hexamethylcyclotrisiloxane	C <sub>6</sub> H <sub>18</sub> O <sub>3</sub> Si <sub>3</sub>		65

TABLE 3.2: Table showing the composition and melting point (in °C) of additional compounds used for crystallisation from vapour.[100]

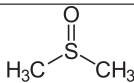
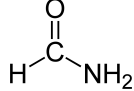
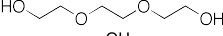
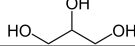
Compound	formula	structure	$T_m$	$\Delta H_{fus}$
dimethyl sulphoxide	$C_2H_6SO$		18	180
formamide	$CH_3NO$		2	190
triethylene glycol	$C_6H_{14}O_4$		-7	210 [101]
glycerol	$C_3H_8O_3$		18	200

TABLE 3.3: Table showing the composition, melting point (in °C) and enthalpy of fusion in  $\text{kJ kg}^{-1}$  of liquids used for freezing.[100]

### 3.2.2 Compounds for freezing

Most freezing experiments were performed using water, which was either deionised water obtained from a Milli-Q filtering unit or condensed from laboratory air. Other liquids used include dimethyl sulphoxide (Fisher, 99+%), formamide (methanamide, Fisher, 99.5+%), triethylene glycol (2-[2-(2-Hydroxyethoxy)ethoxy]ethanol, Fisher, 99%) and glycerol (propane-1,2,3-triol, Fisher, 99.5+%). Table 3.3 lists the liquids alongside their physical properties.

### 3.2.3 Compounds for crystallisation from solution

The primary compound used for studying crystallisation from solution was calcium carbonate, precipitated by mixing calcium chloride (Fisher, general purpose grade) and sodium carbonate (monohydrate, Acros Organics, 99.6%). Calcium fluoride was also used, precipitated by mixing calcium chloride and sodium fluoride (Fisher, 98+%).

## 3.3 Imaging techniques

### 3.3.1 Optical microscopy

Two microscopes were used for most of the thesis: a Vickers M41 Photoplan reflected/transmitted brightfield polarising microscope, and a Vickers M17 reflected/transmitted brightfield/darkfield microscope. Other images were taken on a Nikon Eclipse LV100 polarising microscope and on an Olympus BX41 microscope.

The two Vickers microscopes were equipped with objectives between  $2.5\times$  and  $63\times$  magnification. The M41 used a halogen light source passing through a hot mirror (Knight Optical) to remove infra-red wavelengths from the illumination. The M17 used

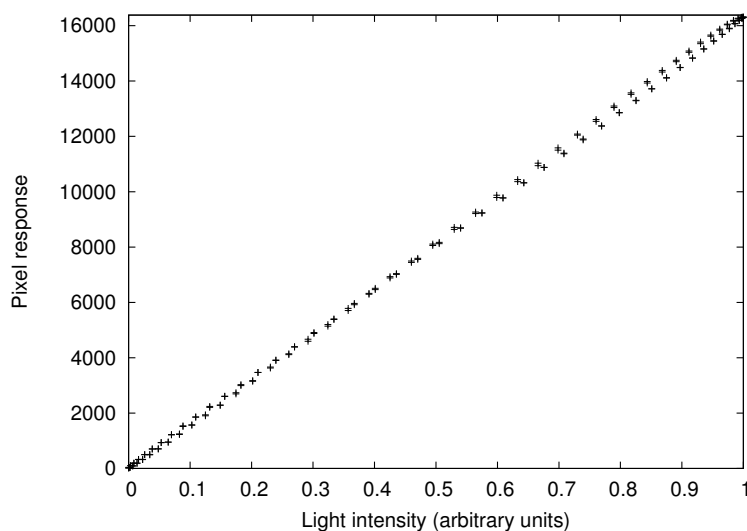


FIGURE 3.5: Graph of green pixel response of Canon camera to known relative light intensities.

halogen illumination for earlier work, but this was replaced with a green light-emitting diode radiating at a peak wavelength of 529 nm. An optical filter (Knight Optical) could be inserted to transmit a narrower 3 nm bandwidth around 532 nm.

All crystallisation cells were held in position under the microscope by clamping them firmly to the stage.

### Camera

Photographs were taken through both Vickers microscopes using a Canon EOS 550D digital single-lens reflex camera, having an 18-megapixel colour sensor with 14-bit colour depth. This was controlled remotely to enable time-lapse photography over long intervals. Image scale was calibrated by photographing a standard 1 mm scale graduated in 10  $\mu\text{m}$  divisions through each microscope/lens combination.

The light response of the green channel of the camera was calibrated by photographing light transmitted through two polarisers at a varying angular offset. Figure 3.5 plots the pixel response as a function of light intensity, showing excellent linearity.

### 3.3.2 Electron microscopy

Most electron micrographs in this thesis were taken on a LEO 1530 high resolution field emission gun scanning electron microscope. Others were taken on a JEOL Neoscope JCM-5000 benchtop scanning electron microscope.

Before imaging, all samples were sputtered with a 5 nm layer of platinum, and silver or carbon paint applied to the sample sides to electrically connect the surface to the base.

## 3.4 Temperature control and measurement

### 3.4.1 Thermocouples

K-type thermocouples were used to measure temperatures throughout this thesis. Measurements were taken using either an Omega CN7200 temperature controller or a Tenma dual-input digital thermometer, both of which reported temperatures to a 0.1 °C resolution. Thermocouples used to measure temperatures of surfaces were secured in place with a small amount of thermal paste to ensure good thermal contact.

When measuring small temperature differences between thermocouples, calibration was performed by sealing both thermocouples inside a hole in an aluminium block and leaving them to equilibrate; any temperature offset between the two probes could then be quantified. For measuring absolute temperatures, thermocouples were calibrated in a similar way with reference to a calibrated Fluke 1524 reference thermometer equipped with a PT100 resistance thermometer.

### 3.4.2 Temperature control

Temperature control was achieved by use of electric cartridge heaters embedded within cell bases. Voltage to these was moderated by an Omega CN7200 temperature controller, using proportional-integral-derivative control to maintain a given temperature. The controller could also ramp the temperature linearly with time. Temperature control was imperfect, and tended to oscillate by about 0.2 °C above and below the desired temperature.

### 3.4.3 Liquid nitrogen cooling stage

Low temperatures were achieved through use of liquid nitrogen cooling. Figure 3.6 shows the cooling stage. Liquid nitrogen flows through two copper pipes embedded within the stage. Between these are two electric cartridge heaters, connecting to the temperature controller: temperature is controlled by varying the amount of heat offsetting the constant nitrogen flow. Cells screw to the top of this, and the block is mounted on a polytetrafluoroethylene block, for insulation and for clamping onto the microscope

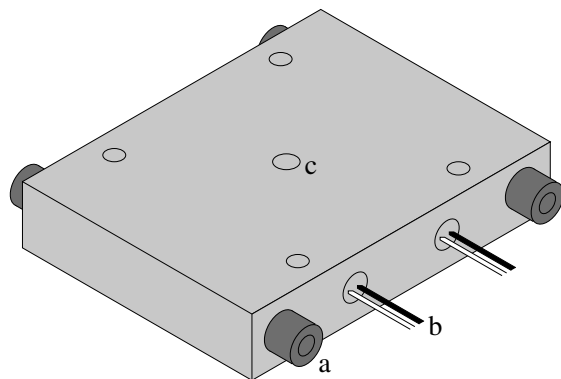


FIGURE 3.6: Illustration of liquid nitrogen cooling stage, showing: (a) liquid nitrogen flow channel; (b) electric cartridge heaters; (c) optical port.

stage. A narrow hole drilled vertically through the centre of the stage allows use of transmitted light. The stage was capable of maintaining any temperature between room temperature and  $-100\text{ }^{\circ}\text{C}$ .

## Chapter 4

# On crystal nucleation from vapour

### 4.1 Introduction

Crystallisation from vapour is an ideal system for studying topographical influences on nucleation. As mentioned in Section 2.2.5, a crystal in vapour may be expected to have a lower contact angle than in solution or in the melt, so topography is likely to have a larger effect. In addition, the issues of contaminants associated with nucleation from liquids are largely not present.

Crystallisation is induced by having a temperature difference between a reservoir at  $T_r$  and a substrate at  $T_s$ . This creates a saturation  $S$  relative to a crystal nucleating on the substrate such that [1]

$$\ln S = \frac{\rho V_m \Delta H_{\text{fus}}}{R} \left( \frac{1}{T_s} - \frac{1}{T_r} \right) = \frac{\rho V_m \Delta H_{\text{fus}}}{R} \frac{\Delta T}{T_s T_r} \quad (4.1)$$

where  $\Delta T = T_r - T_s$ .

For crystallisation at room temperature, a reservoir of the compound is heated inside a sealed cell. The substrate forms the top of the cell and is thermally insulated from the base, creating a temperature difference leading to crystallisation.

For crystallisation at lower temperatures, a stream of gas is partly saturated with the compound and run over a cold surface. If the surface is colder than the saturation temperature of the gas, crystals may form.

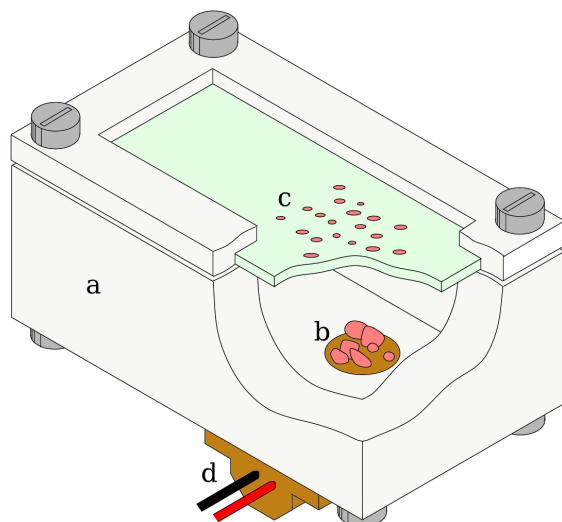


FIGURE 4.1: Cut-away illustration of crystallisation cell used in early experiments: (a) polytetrafluoroethylene walls; (b) copper plug loaded with crystals; (c) glass substrate with growing crystals; (d) resistor.

## 4.2 Prior work with neopentanol and carbon tetrabromide

### 4.2.1 Method

Early experiments with neopentanol and carbon tetrabromide were performed by J. Holbrough.[106] Figure 4.1 shows the experimental cell used. The walls are made from polytetrafluoroethylene for thermal insulation and to deter nucleation; at the top of the cell a standard 1'' × 3'' microscope slide forms the roof of the chamber, screwed down against a rubber o-ring to complete the seal. A mica substrate could optionally be placed under the glass slide. A crystal reservoir was placed on a copper plug in the base of the cell, which is in contact with a 1 k $\Omega$  resistor.

To initiate crystallisation, a voltage was applied to the resistor, causing the copper plug to heat up, warming the reservoir and supersaturating the vapour. Crystals were observed growing on the substrate under the microscope, and their nucleation density determined by sampling four random areas of the substrate. The induction time was also measured, this being the time elapsed between applying voltage to the resistor and the first observed nucleation.

The thermal response to applied voltages was calibrated by using thermocouples to measure the base and substrate temperatures. Different voltages were used to vary the growth rate, these are quantified by the saturation  $S$  attained at equilibrium as expressed in Equation 4.1.



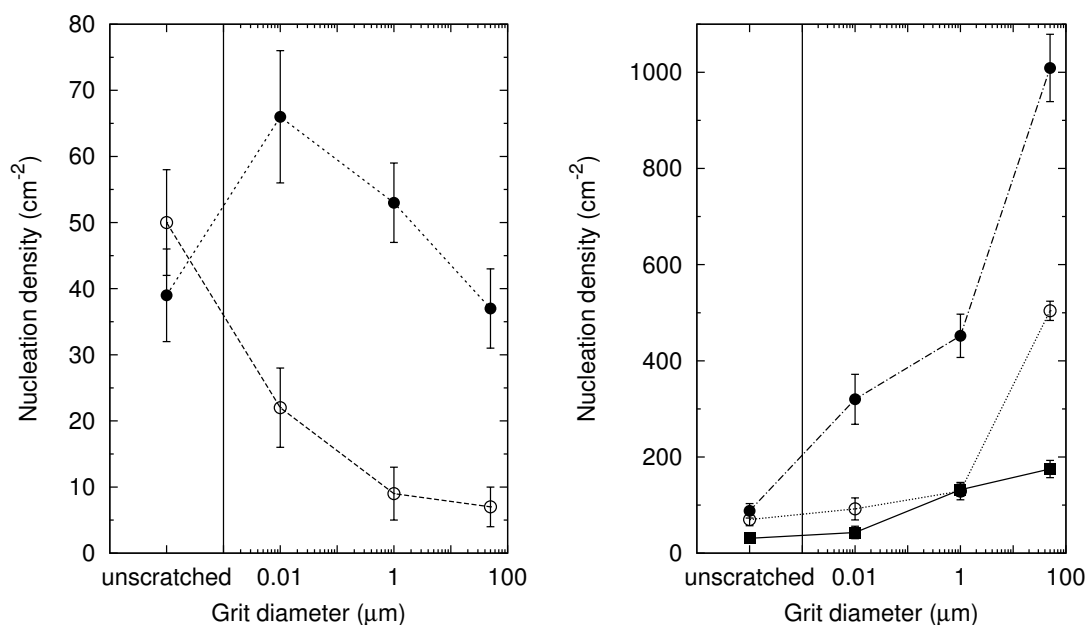


FIGURE 4.2: Graphs showing mean nucleation density of crystals grown on glass (left) and mica (right) scratched with various grades of diamond powder: (●) neopentanol at  $S = 1.47$ ; (○) neopentanol at  $S = 1.25$ ; (■) carbon tetrabromide at  $S = 1.57$ . Each point is the average of three experimental runs. Lines are to guide the eye only.

#### 4.2.2 Results

Smooth glass and mica substrates were compared to those scratched with three grades of diamond powder as described in Section 3.1.6. Figure 4.2 shows the nucleation density of neopentanol on glass and mica at two saturations, and of carbon tetrabromide on mica at a single saturation. There is little conclusive effect of scratching on glass substrates, however on mica there is a clear trend of increasing nucleation density with increasing grit size. This can be explained with reference to Figures 3.2 and 3.3: on scratched mica there is a great variety of topographical sites produced by scratching, more so at higher grit sizes; on scratched glass there are many neat grooves but no great variety of available geometries.

Figure 4.3 shows the accompanying induction times. Neopentanol shows no conclusive trend on either substrate, however carbon tetrabromide shows a clear reduction in induction time with increasing grit size on mica.

Using the same experimental procedure, I looked at the repeatability of induction times. Using neopentanol and 45 V across the resistor, I performed eight consecutive measurements on two substrates: one smooth mica, one scratched with “40–60 μm” diamond powder. Between each measurement, the cell was opened to allow crystals to evaporate and left to cool. Figure 4.4 shows the results. It is clear that the random

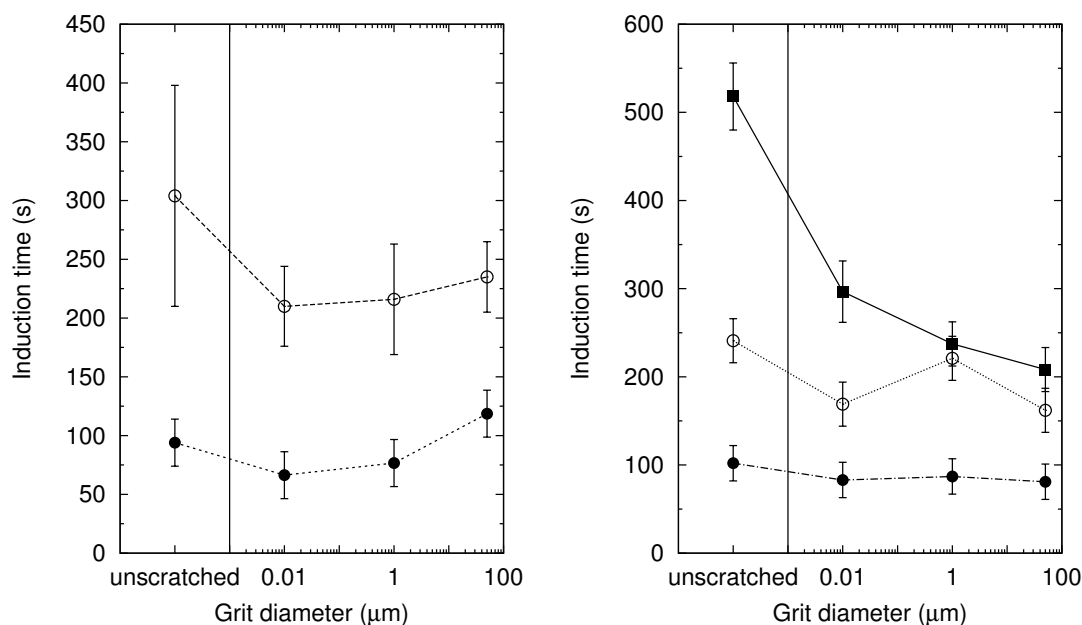


FIGURE 4.3: Graphs showing mean induction time of crystals grown on glass (left) and mica (right) scratched with various grades of diamond powder: (●) neopentanol at  $S = 1.47$ ; (○) neopentanol at  $S = 1.25$ ; (■) carbon tetrabromide at  $S = 1.57$ . Each point is the average of three experimental runs. Lines are to guide the eye only.

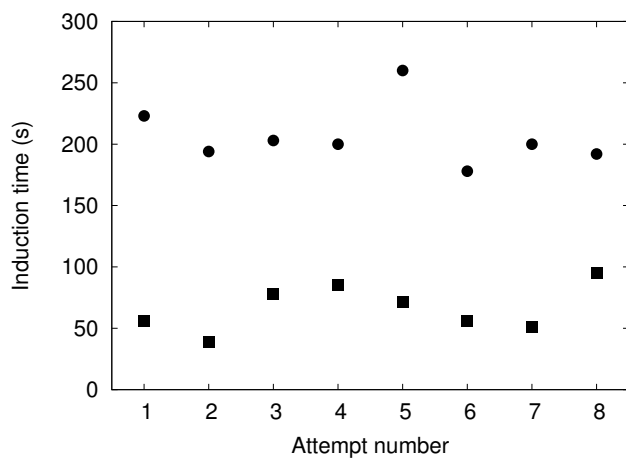


FIGURE 4.4: Graph showing the induction times of neopentanol crystallised repeatedly on smooth (●) and “40–60 μm” scratched (■) mica substrates. Error bars are invisible due to being smaller than the symbols.

variation in induction time is much less than the difference in induction times between the two surfaces.

## 4.3 Methods for room temperature nucleation

### 4.3.1 Cell design

The procedures used in the previous section had several problems. Firstly, the temperatures of the reservoir and substrate were not measured during runs. Also, the shape of the cell and high temperature ramp rate produced large diffusion gradients across the substrate, with the end of the slide above the reservoir nucleating far more crystals than that away from it. To address these and other minor issues, I designed a new cell for these experiments which was used for all subsequent room temperature work.

Figure 4.5 shows the cell. An aluminium base contains a circular trough holding a reservoir of the crystal, heated by two electric cartridge heaters and its temperature measured by a thermocouple inside a narrow hole, terminating just underneath the reservoir. The walls are made from polytetrafluoroethylene and contain two gas ports for flushing the cell with gas, during experiments these were each connected to a stopcock. A steel ring screws down over a 1" × 1" × 1 mm glass substrate into the base, sealing the substrate to the walls and the walls to the base via two o-ring seals. A thermocouple in contact with the top of the glass measures the substrate temperature. Mica substrates were secured underneath the glass, although in later high-magnification experiments (Chapter 6) a steel ring of similar dimensions substituted the glass to enable higher magnification objectives to be used and to increase contrast in reflected light. A perspex optical port in the base allows use of transmitted light.

Although the substrate thermocouple is in contact with the top of the substrate near the edge, rather than on the underside near the centre where crystallisation is observed, calibration measurements indicated that the temperature at the two positions is identical to within a 0.1 °C resolution at ramp rates up to 2 °C/minute. Similarly, the temperature of the aluminium base was not found to vary measurably between the thermocouple position and any point on the surface of the trough.

### 4.3.2 Procedure

A small amount, typically 100–300 mg, of the relevant crystal, finely divided, is placed evenly around the trough. The cell is then sealed with the relevant glass or mica substrate. Unless otherwise specified, these were mica substrates freshly cleaved in a laminar flow cabinet or glass substrates cleaned as in Section 3.1.5. The cell was sealed within a laminar flow cabinet to prevent surface contamination.

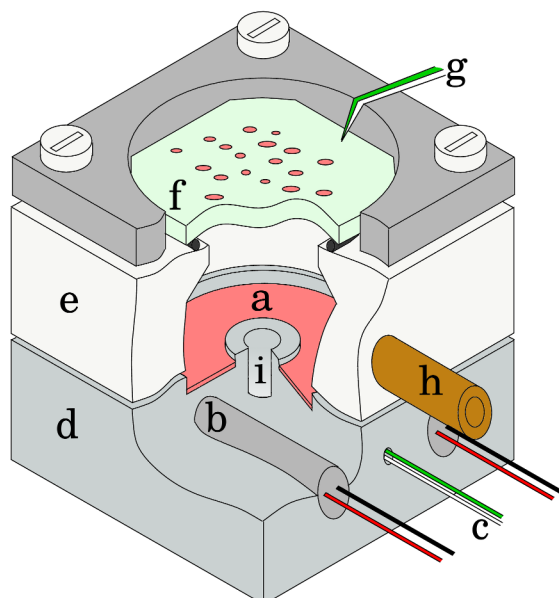


FIGURE 4.5: Cut-away illustration of crystallisation cell used for room temperature experiments from vapour: (a) crystal reservoir; (b) electric cartridge heaters; (c) thermocouple; (d) aluminium base; (e) polytetrafluoroethylene walls; (f) glass substrate with crystals growing; (g) thermocouple; (h) inlet/outlet; (i) perspex optical port.

The cell was secured under the microscope and flushed with nitrogen gas to remove water vapour from the system; this was necessary to prevent condensation or absorption of water from affecting results. The cell being flushed, the inlet and outlet stopcocks were closed to seal the system.

The temperature was ramped upwards linearly from room temperature, whilst time-stamped photographs were taken periodically, until crystals were observed. Precise temperature differences at nucleation were found by subsequent inspection of the series of images, identification of the images identified as before and after nucleation (these were not always consecutive photographs if the nucleation event was ambiguous) and reference to the temperature logs for this time period.

Where it was desired to perform multiple crystallisation runs on a single substrate, after one run was complete, the cell base was cooled to slightly below the substrate temperature using cold metal blocks from a freezer. The cell would again be flushed with nitrogen to quickly remove existing crystals from the substrate, this would typically be continued for at least twice the time needed to sublimate all visible crystals to ensure that even small embryos were removed. The temperature would then be ramped upwards as before.

Compound	1	2	3	Mean
carbon tetrabromide	2.3	2.3	2.2	$2.3 \pm 0.1$
camphor	2.8	2.9	2.95	$2.9 \pm 0.1$
norbornane	0.3	0.3	0.35	$0.3 \pm 0.1$
hexachloroethane	1.6	1.05	0.9	$1.2 \pm 0.3$

TABLE 4.1: Table showing the observed  $\Delta T$  in  $^{\circ}\text{C}$  at equilibrium between crystals on the substrate and in the reservoir for each of three experiments per compound, with mean.

### 4.3.3 Issues with saturation

It was noticed after performing most of the experiments in this thesis that crystals on the substrate were sometimes seen to sublime away at positive  $\Delta T$ , when the atmosphere should have been supersaturated. Investigations concluded that crystals of each compound on the substrate reached equilibrium with the reservoir at some particular  $\Delta T$  greater than zero.

Experiments to characterise this discrepancy were performed on a mica surface with a single small scratch made by a needle to induce nucleation. After flushing the cell with nitrogen gas the reservoir was heated at  $0.5^{\circ}\text{C}/\text{minute}$  until nucleation was observed, and then the heaters were disabled. The cell would then gradually cool, and  $\Delta T$  slowly approach zero. As it did so, the crystals growing from the scratch would at first grow, and then shrink away. The  $\Delta T$  at which the crystals were neither growing nor shrinking was taken as the equilibrium  $\Delta T$  for that system.

Three identical experiments like this were performed for each compound, each on a different substrate. Table 4.1 shows the results of this. It may be seen that there was little variability between experiments for carbon tetrabromide, camphor and norbornane, but significant deviation for hexachloroethane.

It is unclear whether or not these values were applicable to all experimental conditions, and so to avoid a potentially inappropriate correction, throughout the rest of the thesis results will whenever possible be given not in terms of saturation, but directly in terms of measured  $\Delta T$ . Whenever an estimate of saturation is required, the mean values found here will be subtracted from measured  $\Delta T$  to generate an effective  $\Delta T$  for the purposes of the calculation.

Tests were performed using camphor in an attempt to discover the cause of this discrepancy. The equilibrium  $\Delta T$  was not noticed to be dependent upon the length of time the cell was left in position before beginning the experiment, as might be expected if the effect were due to residual temperature gradients across the cell (the ambient temperature in the room containing the laminar flow cabinets, where the cell was sealed, was typically several degrees lower than that in the room containing the microscope).

No change in equilibrium  $\Delta T$  was seen when using distilled camphor instead of stock camphor, nor was there any reduction by using a significantly lower incident light intensity. Equilibrium  $\Delta T$  was seen to increase for very small quantities of compound placed in the reservoir (3.6 °C for 12 mg) but did not vary noticeably across the range of compound quantities used in other experiments. A poor air seal around the perspex optical port was identified and rectified, this allowed the equilibrium camphor  $\Delta T$  to drop as low as 1.7 °C, and for hexachloroethane it dropped to  $\lesssim$  0.2 °C.

I hypothesise that the discrepancy is due to an imperfectly airtight cell, potentially aggravated by unfavourable temperature gradients within the cell.

## 4.4 Methods for low temperature nucleation

### 4.4.1 Cell designs for the liquid nitrogen stage

Experiments at lower temperatures were performed by running gas with a high partial pressure of the desired compound over a cool substrate.

#### First flow cell

Figure 4.6 shows the first flow cell used for low-temperature crystallisation. The substrate is placed on an aluminium base, screwed onto the liquid nitrogen cooling stage described in Section 3.4.3. A thermocouple embedded in this base measures the temperature. The cell is sealed by an aluminium plate, screwed down over a flat rubber seal. A glass window in this plate allows optical observation. Gas flow is directed through a pipe penetrating the cooling stage and base, through channels in the underside of the top plate, over the substrate, then out through another pipe through the base and cold stage.

This cell design allows for movement of the stage under the microscope, and the cold narrow channels through which the gas must flow prior to reaching the substrate prevent warming of the surface by the gas. However the glass window does not allow an objective of more than 10 $\times$  magnification to be used. Also, as the glass window is cold and exposed to the atmosphere, it experiences considerable frosting which progressively obscures the view over the course of an experiment. This was partly remedied through use of a particular 10 $\times$  objective which when focused on the substrate very nearly came in contact with the glass surface, thus significantly slowing frost formation through physical obstruction of incoming vapour.

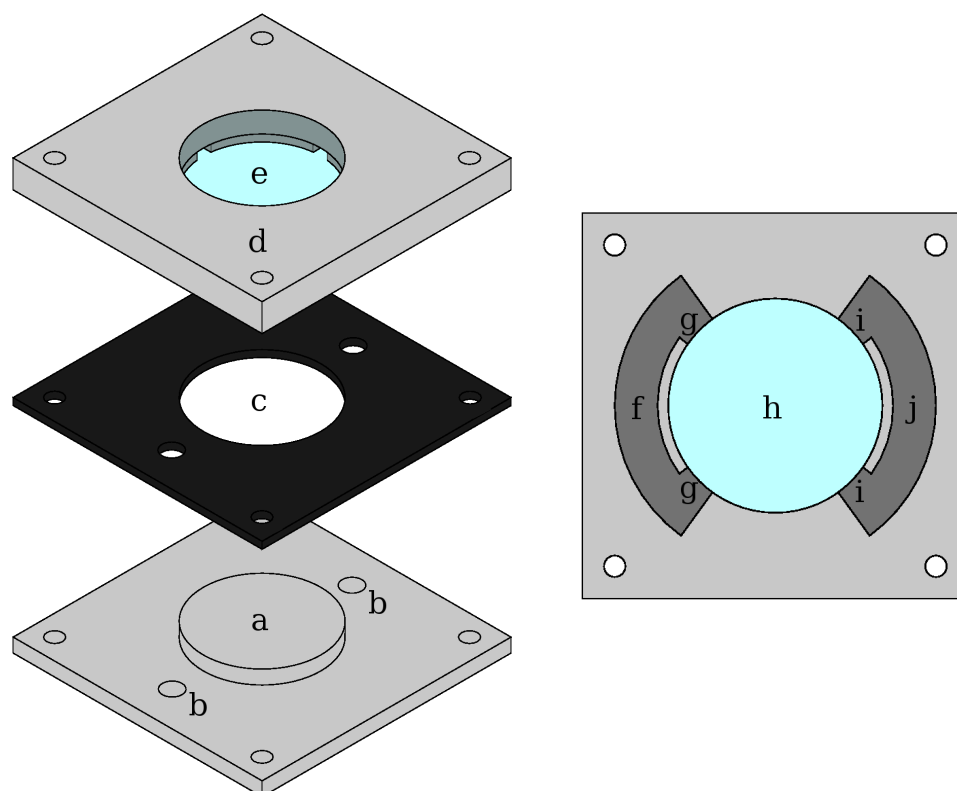


FIGURE 4.6: Diagrams showing the design of the first flow cell. Left: exploded view, showing (a) aluminium base; (b) gas inlet/outlet; (c) rubber seal; (d) aluminium top plate; (e) glass window. Right: underside of aluminium top plate showing gas channels in darker grey. Air enters from the inlet pipe (f), is channelled towards the main chamber (g), flows over the substrate (h), enters a channel at the opposite side (i) and leaves through the outlet pipe (j).

The cold gas input pipes had a tendency to promote crystallisation before the flow reached the substrate. This made it difficult to quantify the saturation of the flow, as the amount of material depleted in this way was unknown, and likely to be time and temperature dependent.

### Second flow cell

A second flow cell was designed to address the issues of the first, this is shown in Figure 4.7. It uses the same aluminium base as the first cell, but a different top piece, made from polytetrafluoroethylene, screws down over an o-ring seal. The cell fits directly over an objective lens, an o-ring seal allowing the lens to move up and down to focus; the cell fits either a 10×, 20× or 40× objective. The gas flow does not come through the base but through the sides, which should be warmer than the substrate.

This cell design allows for higher magnification imaging, and does not suffer from frosting in the optical path. However the cell cannot be moved to view different areas of

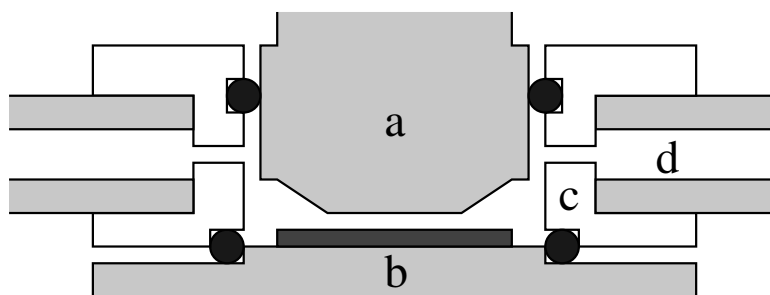


FIGURE 4.7: Diagram illustrating the second flow cell in cross-section: (a) microscope objective; (b) aluminium base with substrate; (c) polytetrafluoroethylene walls; (d) steel inlet/outlet pipe.

the substrate. Although there is no longer a problem with crystallisation too early along the flow path, here the flow of gas is much warmer and heats the substrate considerably above that measured by the thermocouple in the base. In the first design of the cell, gas flowed directly onto the substrate, and measurements indicated that at typical ice nucleation temperatures (-40 to -50 °C) there was a temperature discrepancy of up to 20 °C when using a 10× objective. A slight correction to the design greatly reduced this, leading to a measured discrepancy of 1.2 °C at -40 °C with a 10× objective at a flow rate of 400 mL/minute. Presented temperatures have been corrected accordingly, but should be considered approximate, as it is unknown to what extent the characterisation tests were perfectly representative of an actual experimental run, or to what extent using a higher magnification lens with a very low working distance affects the substrate warming.

#### 4.4.2 Peltier-cooled cell

A problem shared by all cells using the liquid nitrogen cooling stage is that the copper piping supplying the liquid nitrogen contracts with decreasing temperature, pulling the stage to one side. This is a particular problem with the second flow cell, as at high magnification the area of substrate in view may “drift” irreversibly out of view, making high-magnification observation of particular sites almost impossible.

To remedy this and address other issues a new cell was designed using a Peltier cooler rather than liquid nitrogen to achieve low temperatures. Figure 4.8 shows the cell. The substrate sits on an aluminium plate containing a PT100 resistance temperature detector. This is secured onto the top of a two-stage Peltier cooler, the bottom of which connects to a water circulator to remove heat. The polytetrafluoroethylene-walled cell, screwed to the base, seals around a 10× to 40× microscope objective in an identical way as the second flow cell, and gas flow passes through an inlet and outlet pipe at either end of the cell.



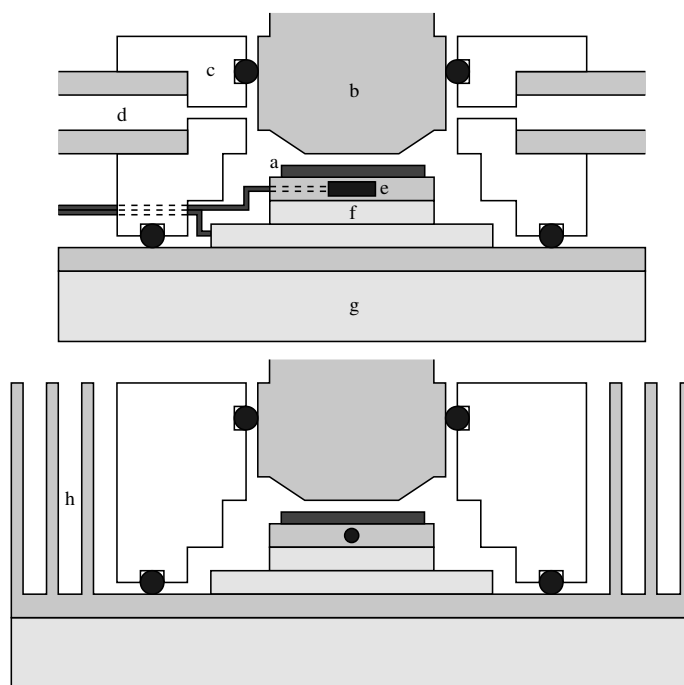


FIGURE 4.8: Diagram showing two orthogonal cross-sections of the Peltier-cooled cell: (a) substrate; (b) microscope objective; (c) polytetrafluoroethylene walls; (d) steel inlet/outlet pipe; (e) aluminium plate with embedded PT100 temperature detector; (f) two-stage Peltier component; (g) water circulation block; (h) heat sink.

Unfortunately, due to numerous delays in manufacture, this cell was not completed until an extremely late point in the project. For this reason, and as a suitable temperature control device had not yet been completed, no experiments in this thesis use this cell. However initial tests showed it to reach a minimum substrate temperature of  $-52\text{ }^{\circ}\text{C}$  with water flow at  $5\text{ }^{\circ}\text{C}$ , and to have excellent optical quality and no discernible drift, making this cell ideal for future research.

#### 4.4.3 Flow control and saturation

Gas flow of a low and controllable humidity was produced in a three step process. First, nitrogen from a cylinder was dried by passing it through a dehumidifier: a long narrow coil of polyvinyl chloride tubing wound tightly around the liquid nitrogen supply pipe, to freeze out most of the water vapour. Second, part of the gas is brought to 100% humidity by bubbling it finely through a tube of water. The temperature of the water was measured using a thermocouple attached to the outer surface, and to prevent small water droplets produced by bubble rupture from being carried in the gas stream, it was made to pass through a wad of cotton wool immediately after humidification. Finally, the humid gas is diluted to the required humidity by mixing with dry gas in a two-step mixing process. This is shown in Figure 4.9.

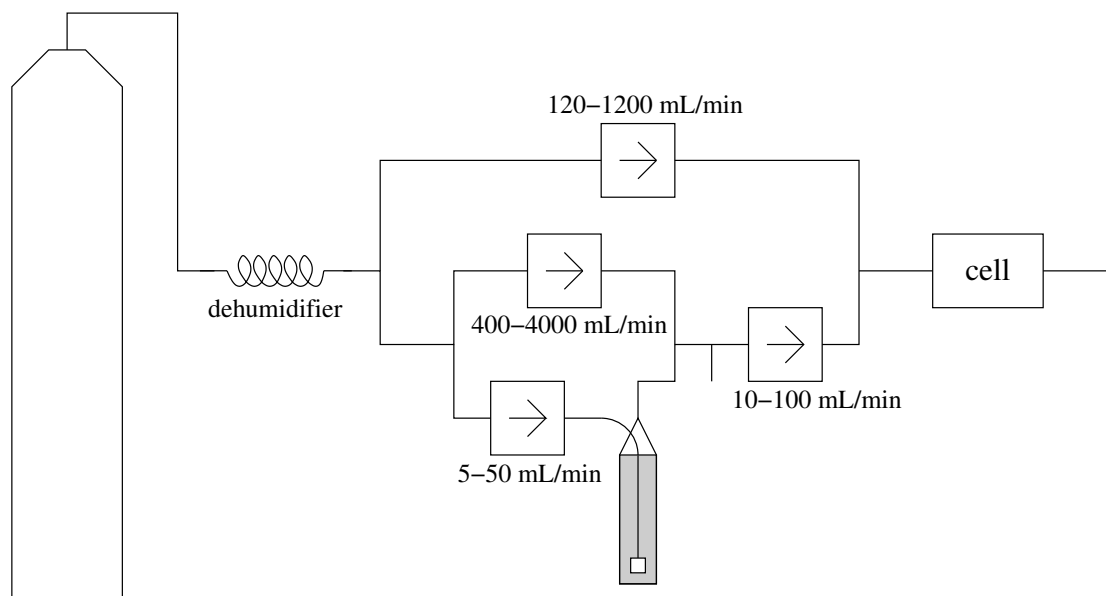


FIGURE 4.9: Diagram illustrating the humidity control system. Nitrogen flows from a cylinder (left) through a dehumidifier, then a stream is humidified by bubbling it through water, which is diluted with dry nitrogen in a two-step mixing process.

Gas mixing was controlled by means of four rotameters with flow control valves, accurate to within 2% of their maximum flow rate. After the first mixing step, excess gas was vented through a valve before the second step.

Flow control was also used for compounds which are solid at room temperature. In this case, the humidifier and first mixing step was removed and replaced by a tube filled with a powdered sample of the compound, sealed with gauze at either end.

Apart from the dehumidifier, all connecting piping was made from polytetrafluoroethylene, chosen for its low water absorption and low permeability, or from stainless steel.

Humidity measurement was attempted using a frost point hygrometer, which chills a surface until it reaches an equilibrium between ice growth and sublimation, positioned so that gas flowed through it after mixing but before the cell. However this had little practical application as the hygrometer proved unable to reduce its temperature below about  $-35\text{ }^{\circ}\text{C}$  on most occasions, despite being known in other settings to reach much lower temperatures. It was however useful for measuring the saturation temperature of vapour partially saturated with organic compounds, as these were considerably higher than those of ice.

#### 4.4.4 Procedures

Substrates were placed in the cell using thermal paste to achieve good thermal contact. Mica substrates were back-painted in black enamel (Revell #8) to improve optical

contrast in reflected light.

Holding the cell at room temperature, the gas flow was adjusted as required and held for 5–10 minutes (for organic compounds) or 20–30 minutes (for water) to achieve an equilibrium saturation. Then the cell temperature was ramped downwards linearly until crystallisation was observed.

## 4.5 General and miscellaneous observations

### 4.5.1 Crystallisation behaviour by compound

Figure 4.10 shows examples of large crystals of each of the six principal compounds. Their qualitative nucleation behaviour is as follows.

#### Neopentanol

Neopentanol at room temperature may form crystals with no visible liquid intermediary, or it may form large liquid drops which can grow, coalesce and eventually freeze. The critical factor in deciding which occurs appears to be the quantity of water present in the cell: neopentanol is highly hygroscopic, and having absorbed water will have a reduced melting point. Flushing the cell with nitrogen gas prior to experiments is an effective means to prevent neopentanol forming as a liquid, provided the reservoir itself has not become overly contaminated with water.

Having a high vapour pressure, neopentanol tended to form a small number of rapidly-growing crystals.

#### Carbon tetrabromide

Carbon tetrabromide was always seen to nucleate directly as a crystal, with no liquid intermediary observed. Experiments with this compound were eventually discontinued due to concerns over its tendency to decompose to form bromine when heated.

#### Camphor

Camphor was also exclusively seen to form directly as a crystal. Nucleation densities were particularly high, with crystals appearing across a wide area nearly simultaneously.

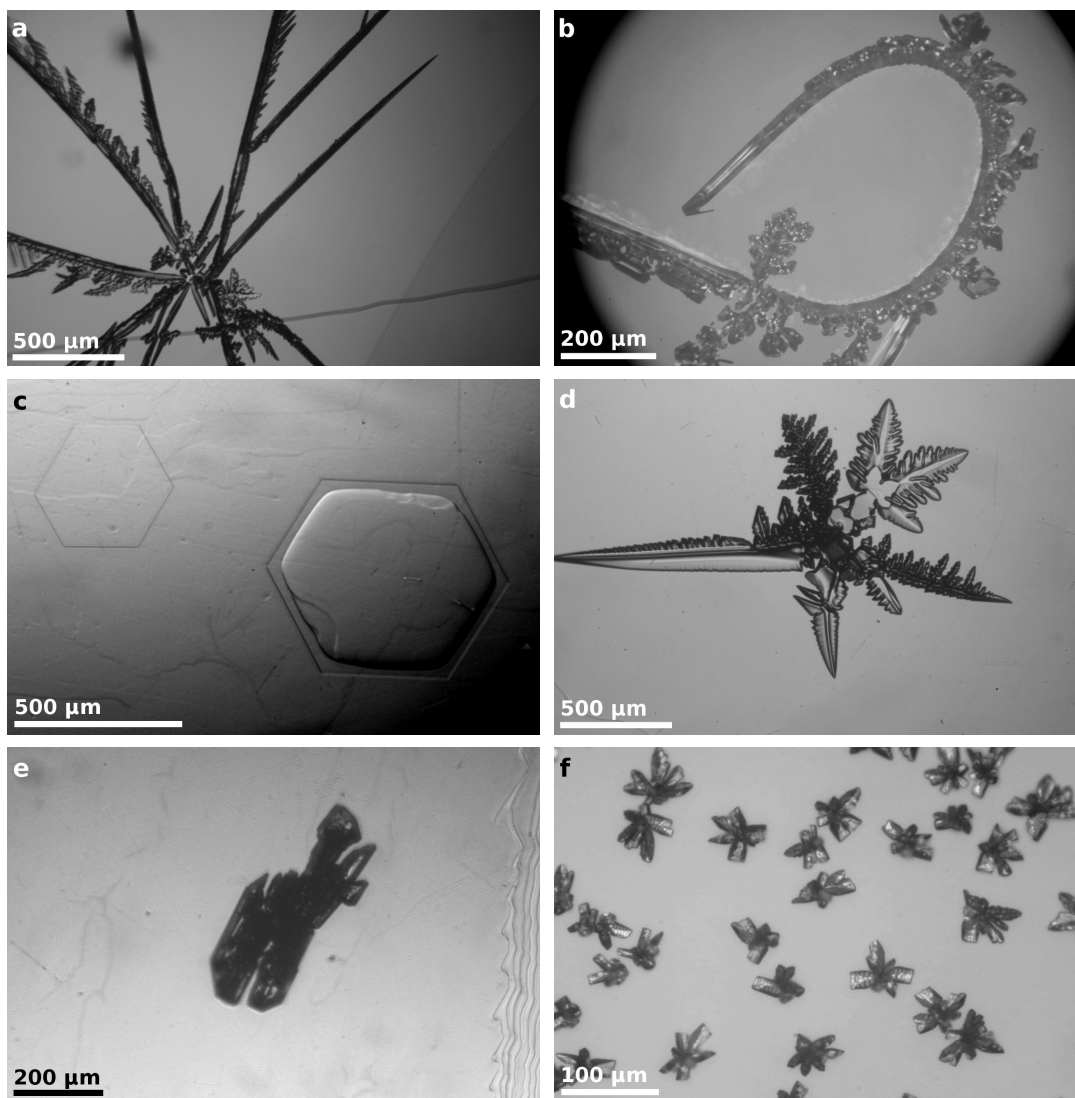


FIGURE 4.10: Optical micrographs showing crystals grown from vapour on mica surfaces: (a) neopentanol; (b) carbon tetrabromide; (c) camphor; (d) norbornane; (e) hexachloroethane; (f) ice.

### Norbornane

Like neopentanol, norbornane has a very high vapour pressure and tends to form a small number of fast-growing crystals. Unlike neopentanol, no condensation of liquid norbornane was ever observed. However, uniquely among the compounds studied, norbornane had a tendency to nucleate on the polytetrafluoroethylene walls of the crystallisation cell, sometimes to the complete exclusion of nucleation on the substrate.

### Hexachloroethane

Hexachloroethane was always seen to form directly as a crystal with no liquid intermediary observed. Like camphor, the crystals grew slowly, but still generally yielding low nucleation densities.

### Hexamethylcyclotrisiloxane

Hexamethylcyclotrisiloxane appears directly as a crystal, however it generally has a nucleation density so low that it is quite improbable to observe nucleation whilst observing any particular area of substrate under a microscope.

### Menthol, isomenthol, naphthalene, pinacol

These four compounds were all observed to exclusively form supercooled liquid drops rather than crystals at room temperature, perhaps surprising considering naphthalene and isomenthol's melting points of 80 and 83 °C respectively. Apparently direct crystal nucleation was observed in the cases of menthol and naphthalene by crystallising them significantly below room temperature.

### Ice

Water condenses as supercooled liquid drops above about -38 °C, which at the lower end of this temperature range may then subsequently freeze. Below this, ice crystals appear to form directly. Nucleation densities for ice nucleation were considerably higher than those for any other compound studied.

## 4.5.2 Nucleation density and repeatability

By nucleation density I mean the number of nucleation events per area of substrate. The previous section discusses the variation in nucleation density between compounds, all other things being equal, but this is necessarily highly qualitative as the nucleation density is dependent on many factors, such as number and distribution of nucleation sites, substrate material and temperature ramp rate. Specifically, higher temperature ramp rates lead to higher nucleation densities.

Nucleation tends to occur in a very short period of time relative to the length of the experiment, often with all crystals appearing within seconds of one another. This is

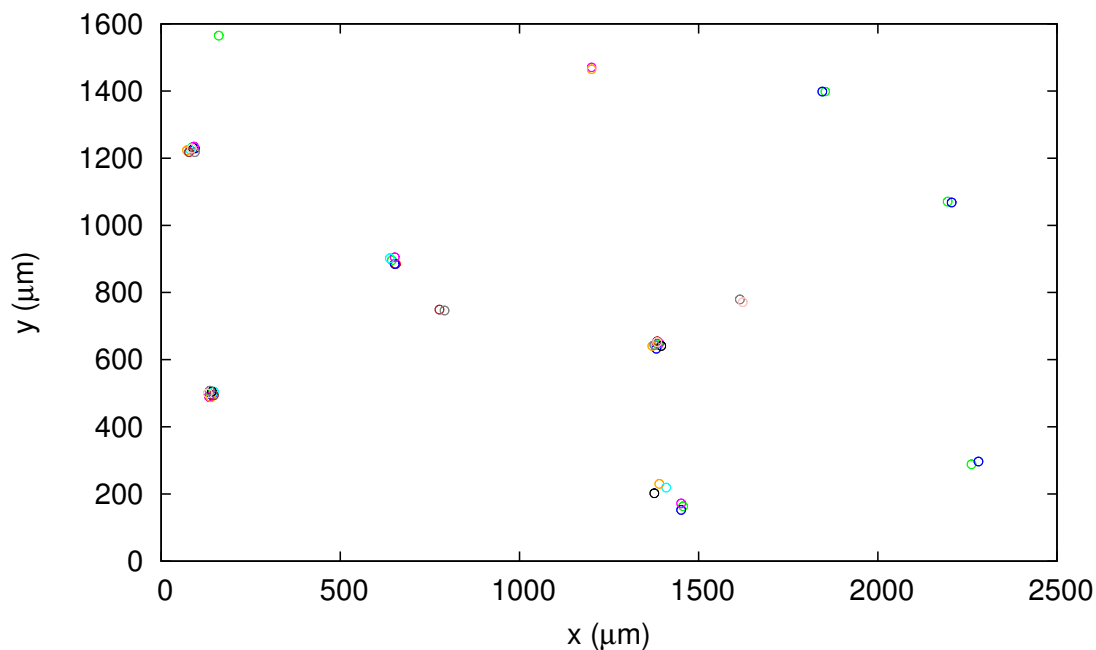


FIGURE 4.11: Graph illustrating the positions of observed nucleation of neopentanol on glass scratched with “ $< 1 \mu\text{m}$ ” diamond powder. Each circle represents a nucleation event, and the events of each run are a different colour. The size of the circles indicates the approximate error in site location.

attributed to the growth of the first crystals depleting the vapour, dropping the effective saturation and preventing any further nucleation on the surface.

These first nucleation sites are likely to be those with the lowest free energy barriers to nucleation. A question which presents itself is then: to what degree are the sites at which nucleation occurs repeatable between runs? Will crystals repeatedly grow from a small number of sites, or will they grow from different sites each time?

A test of this was performed using neopentanol on glass scratched with “ $< 1 \mu\text{m}$ ” diamond powder. Such a surface would be expected to have a great number of nucleation sites available. Ten consecutive runs were performed at a temperature ramp rate of  $16 \text{ }^\circ\text{C}/\text{minute}$  and the positions of nucleation on each run were noted. Figure 4.11 shows the results, with each circle showing the position of a nucleation event, and each colour representing a different run. Clearly, nucleation is dominated by a small number of sites, with two sites nucleating a crystal on every run and one site nucleating on nine out of ten, and only a single site not nucleating a crystal more than once.

This behaviour is apparent even on smooth surfaces. A mica surface, cleaved and sealed within the cell within a laminar flow cabinet, should be extremely smooth and

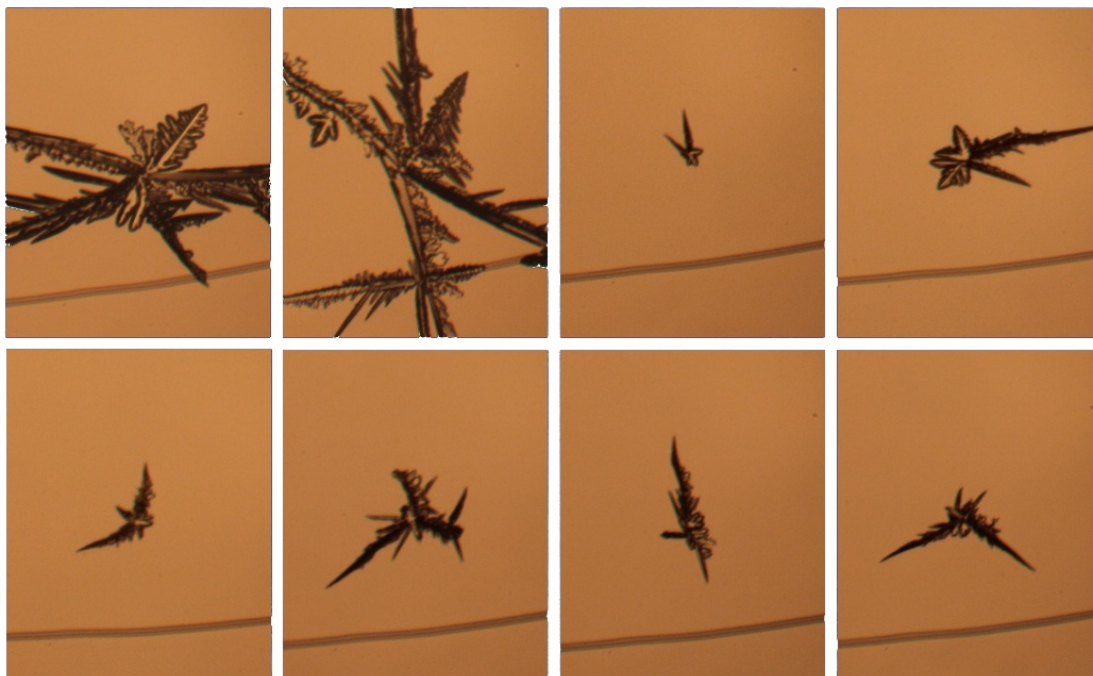


FIGURE 4.12: Optical micrographs from eight consecutive runs of neopentanol nucleation on untreated mica, showing nucleation repeatedly in the same site.

clean. When growing crystals upon such a surface, however, invariably a small number of sites are still seen to dominate. Figure 4.12 shows a series of optical micrographs of neopentanol crystals grown on smooth mica at a temperature ramp rate of  $2\text{ }^{\circ}\text{C}/\text{minute}$ . Each image is from one of eight consecutive runs, and each shows a neopentanol crystal growing from an identical location. Before the appearance of the crystal, there is no visible feature at this site, however there is obviously some contamination or topographical feature at this location which provides a considerably more favourable nucleation site than the flat mica or the nearby step edge.

Nucleation fairly evenly across a surface can be achieved, however it requires a smooth surface and a very high ramp rate. Figure 4.13 shows the positions of neopentanol nucleation on a smooth, apparently featureless sheet of mica at a ramp rate of  $30\text{ }^{\circ}\text{C}/\text{minute}$  across ten consecutive runs. Although some sites show a tendency to nucleate crystals across multiple runs, by and large there is a random scatter of sites.

So apart from in these extreme conditions, it makes little sense to consider the nucleating ability of a *surface*, as was done in e.g. Section 4.2, but rather we must consider the nucleating ability of particular *sites*. This line of thought is central to Chapter 5.

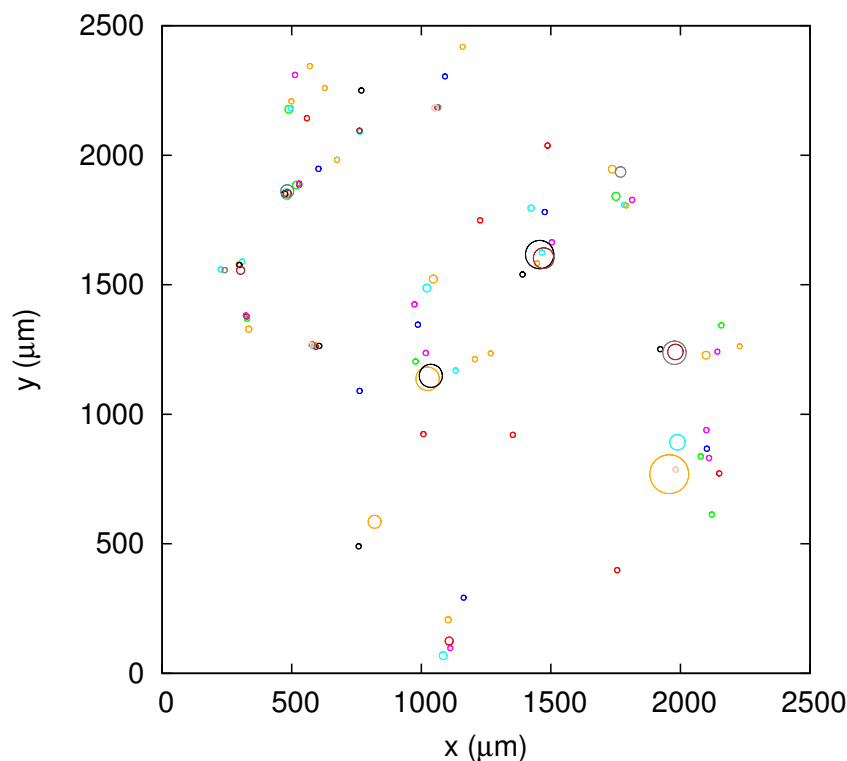


FIGURE 4.13: Graph illustrating the positions of observed nucleation of neopentanol on smooth mica at a ramp rate of  $30\text{ }^{\circ}\text{C}/\text{minute}$ . Each circle represents a nucleation event, and the events of each run are a different colour. The size of the circles indicates the approximate error in site location. Note that the corners of the graph area were not under observation and so the lack of sites here should not be considered significant.

## 4.6 Nucleation on rough surfaces

### 4.6.1 Scratches

A sharp steel point was used to make a small, roughly 1 mm long scratch on mica surfaces. Neopentanol and carbon tetrabromide were grown on such features, and compared to nucleation on a smooth mica surface. Figures 4.14 and 4.15 show the results for neopentanol and carbon tetrabromide respectively at  $2\text{ }^{\circ}\text{C}/\text{minute}$ . In each case, nucleation occurs at a significantly lower temperature difference than on the flat surface. Nucleation density within the scratch was very high, with in each case a large number of crystals nucleating apparently simultaneously.

Scratches were made on glass surfaces by scoring with a diamond-tipped pen, followed by washing before crystallisation. Figure 4.16 shows such a scratch, in which camphor crystals were grown. The red dots indicate positions of nucleation owing to a temperature ramp of  $2\text{ }^{\circ}\text{C}/\text{minute}$ , with many nucleating on the rough surface in the trough of the scratch and none elsewhere.



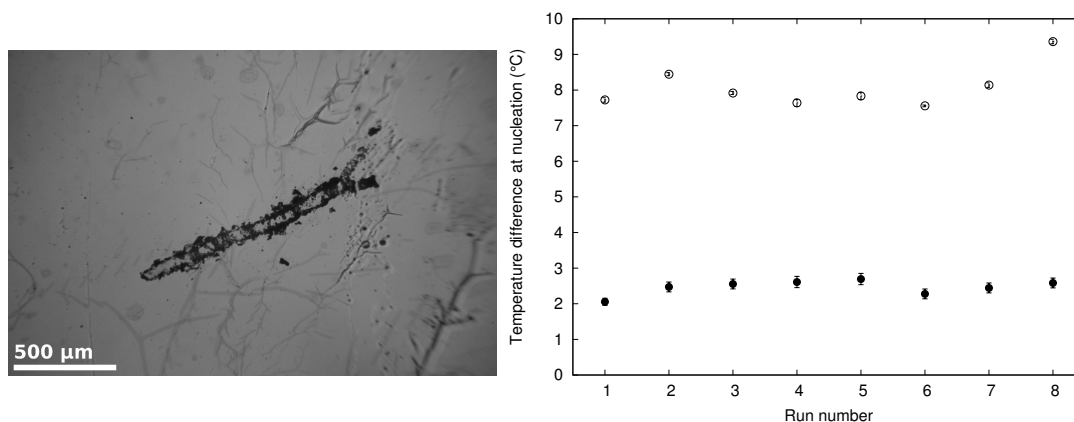


FIGURE 4.14: Left: optical micrograph of a rough scratch in mica. Right:  $\Delta T$  upon nucleation of neopentanol in the same scratch ( $\bullet$ ) and on smooth mica ( $\circ$ ) over eight consecutive runs on each.

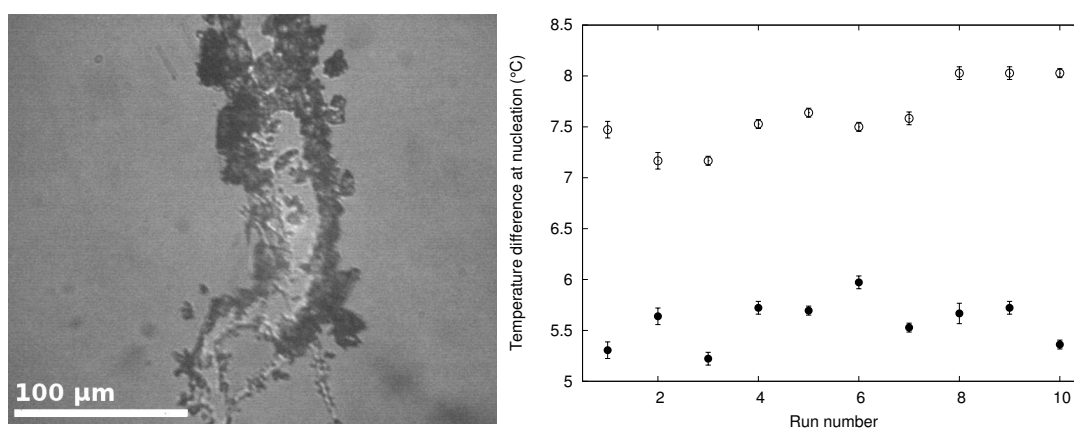


FIGURE 4.15: Left: optical micrograph of part of a rough scratch in mica. Right:  $\Delta T$  upon nucleation of carbon tetrabromide in the same scratch ( $\bullet$ ) and on smooth mica ( $\circ$ ) over ten consecutive runs on each.

A mica surface was scratched using only a few grains of “40–60  $\mu\text{m}$ ” diamond powder, to produce a largely flat surface with a few distinct scratches. Figure 4.17 shows the growth of neopentanol on this surface during a temperature ramp of 2  $^{\circ}\text{C}/\text{minute}$ . Tiny crystals are seen to grow everywhere from the scratches and grow and coalesce to form long linear crystals.

Similar behaviour is seen on a mica surface fully scratched with “40–60  $\mu\text{m}$ ” diamond powder. Figure 4.18 shows growth of neopentanol on such a surface during a temperature ramp of 2  $^{\circ}\text{C}/\text{minute}$ . Here there are many scratches, and electron microscopy of a similar surface (Figure 3.2) indicates that the whole mica surface is roughened, but nevertheless most of the nucleation occurs in just a couple of scratches, from which a large number of small crystals are seen to emerge, grow and coalesce.

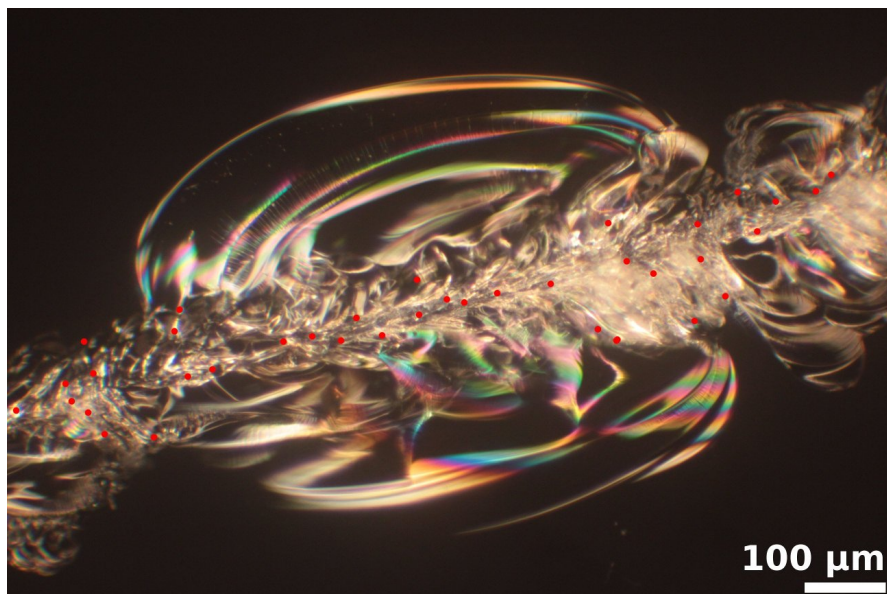


FIGURE 4.16: Optical micrograph of a rough scratch on glass, with red spots showing camphor nucleation sites.

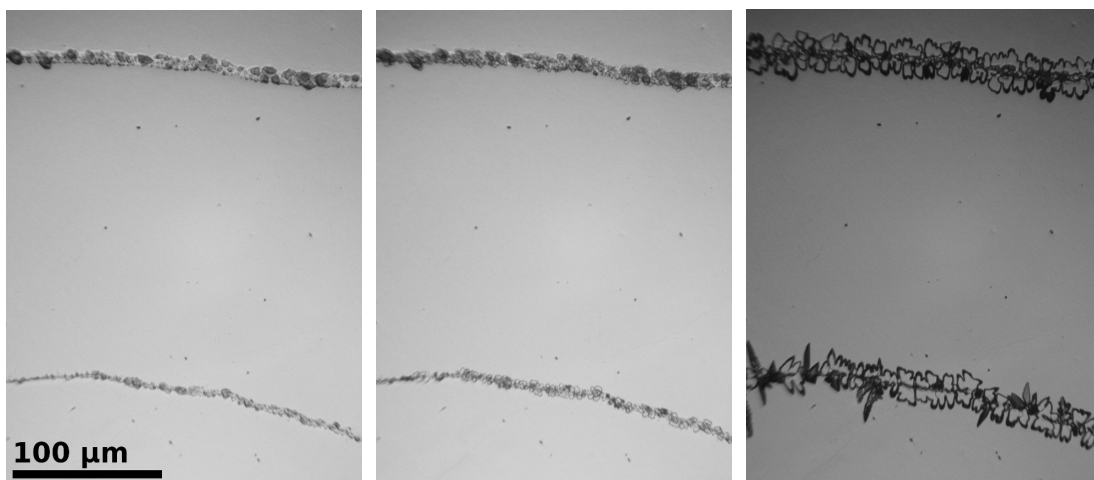


FIGURE 4.17: Time series of optical micrographs showing neopentanol growth in scratches made by diamond grains on mica.

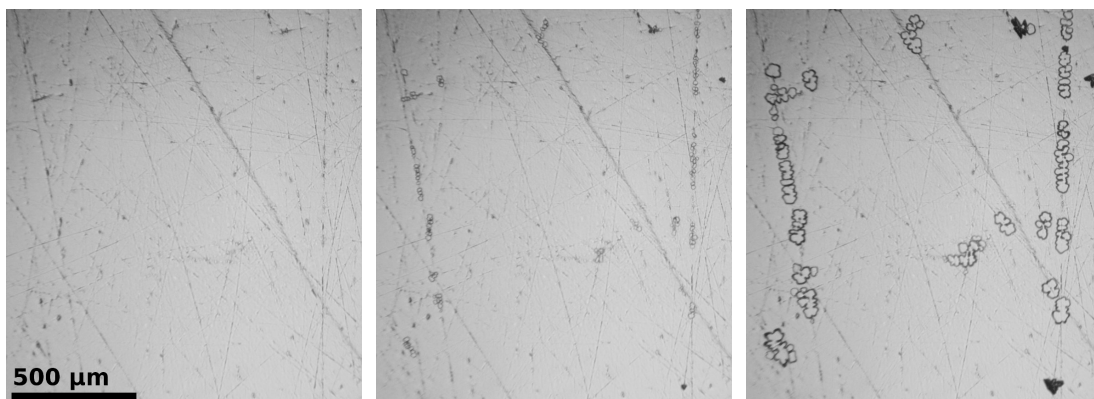


FIGURE 4.18: Time series of optical micrographs showing neopentanol growth in scratches on a mica surface scratched with “40–60  $\mu\text{m}$ ” diamond powder.

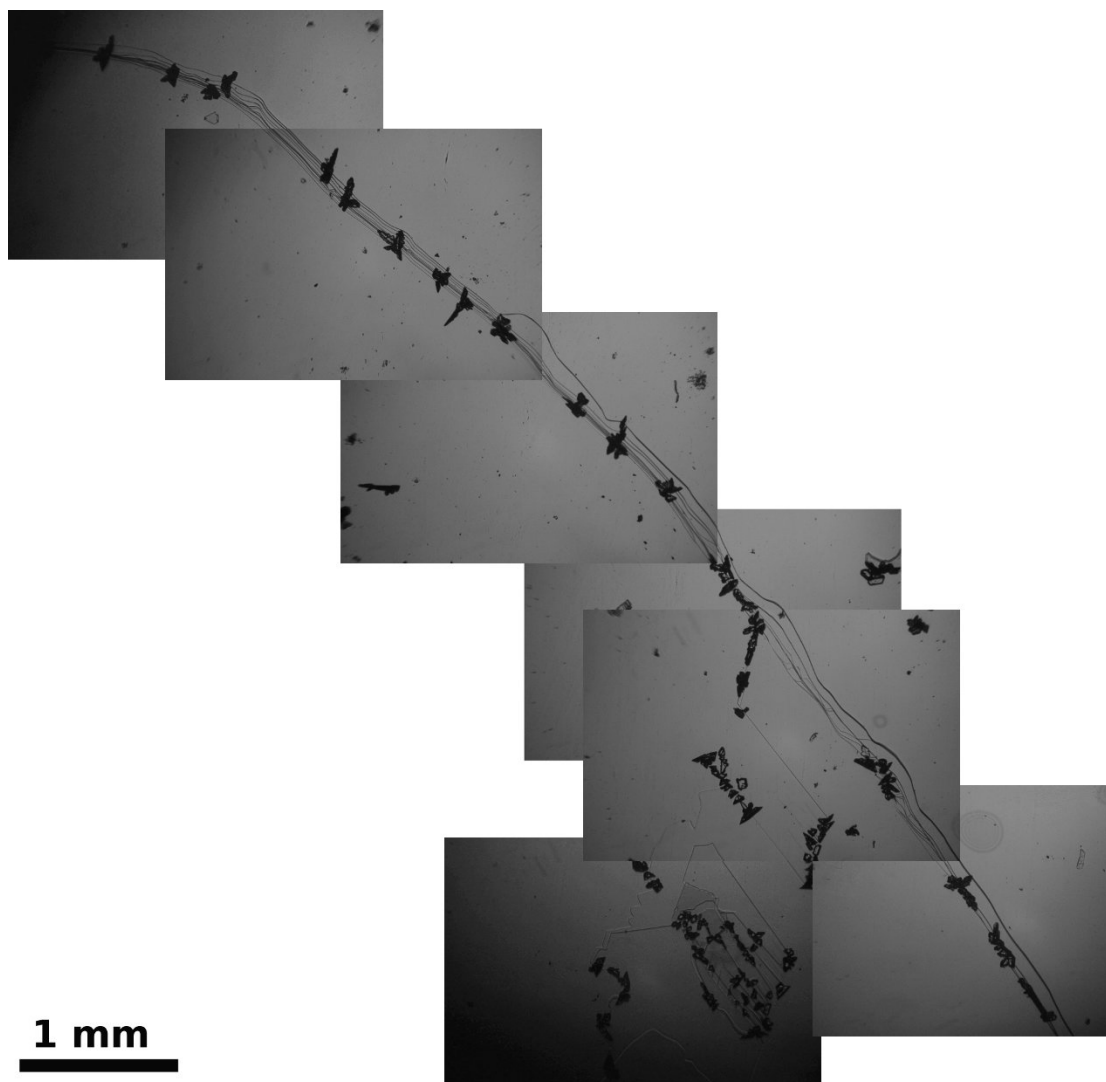


FIGURE 4.19: Montage of optical micrographs showing mica defects following growth of carbon tetrabromide.

#### 4.6.2 Mica defects

When growing crystals on cleaved and untreated mica surfaces, they were often seen to nucleate at steps or other surface defects. Figure 4.19 shows a series of defects across a mica surface with carbon tetrabromide crystals growing preferentially along the features, following a temperature ramp of  $2\text{ }^{\circ}\text{C}/\text{minute}$ . This behaviour has been observed with all of the compounds studied, and Figure 4.20 shows example optical micrographs of this for each.

Unlike coarse scratches, nucleation on mica defects does not usually appear to occur all along the feature simultaneously, rather a small number of distinct nucleation sites can be identified. These sites often dominate nucleation across multiple experimental runs, a fact which is explored in depth in Chapter 5.

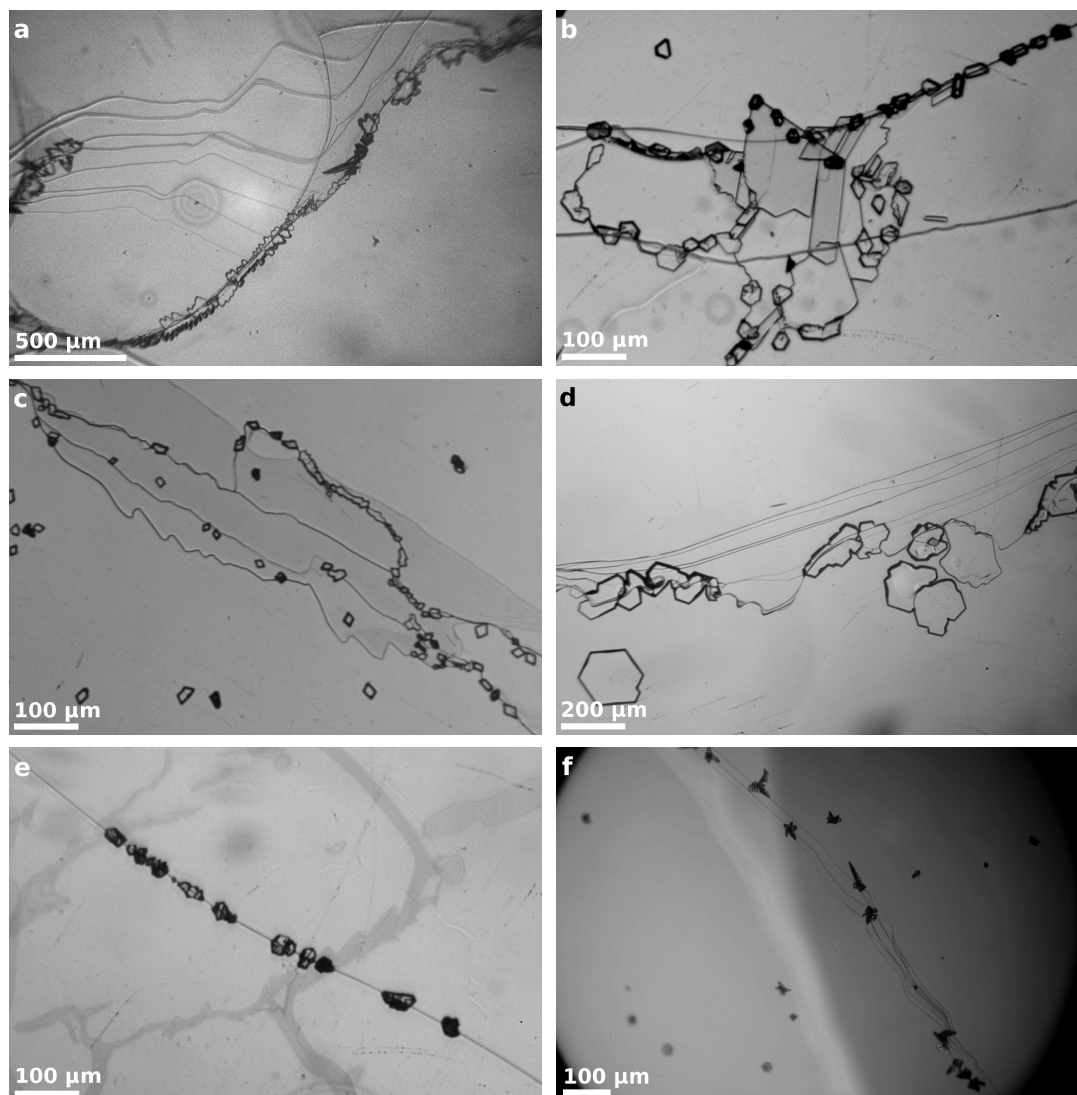


FIGURE 4.20: Optical micrographs showing crystals grown from vapour on mica defects: (a) neopentanol; (b) carbon tetrabromide; (c) camphor; (d) norbornane; (e) hexachloroethane; (f) ice. Image f taken by Hannah Pearce.

## 4.7 Nucleation on milled silicon

The coarse scratches studied in the previous section are easy to manufacture but have a poorly defined topography. In contrast, defects on mica and other minerals, central to the next two chapters, have a well-defined topography but are inherently random in their nature and distribution.

Manufacturing well-defined features is difficult, as they need to have a known topography down to the nanometre scale of nucleation. Here I explore two possibilities for creating long troughs in silicon wafers: ion milling and reactive-ion etching.

Substrates were prepared by Mark Rosamond, using  $1\text{ cm} \times 1\text{ cm}$  silicon wafers with an oxide layer of about 100 nm. On all substrates, trenches were produced by applying

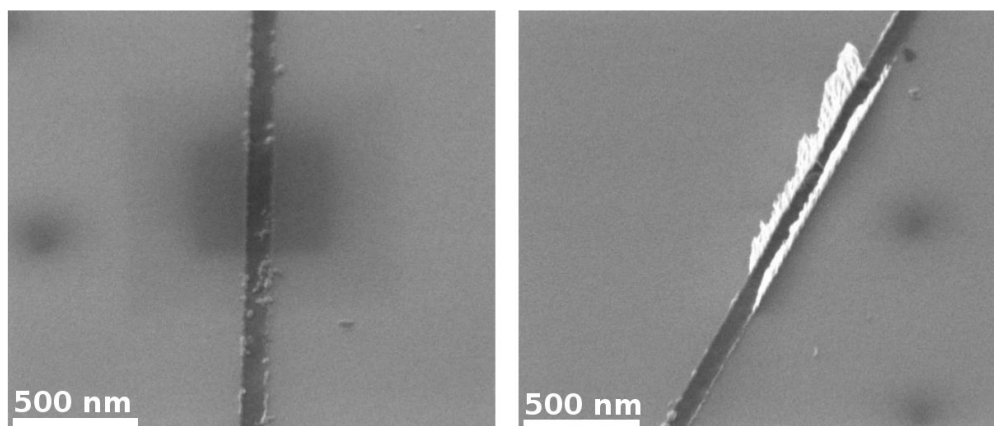


FIGURE 4.21: Two scanning electron micrographs showing ion-milled trenches in silicon. Micrographs taken by Mark Rosamond.

a layer of 420 nm ZEP resist, and removing this selectively in 70 nm wide lines spaced every 20  $\mu\text{m}$ .

### 4.7.1 Ion milling

#### Substrate manufacture and characterisation

Trenches were produced by exposing the surface to a beam of argon and oxygen ions. These were applied at an angle of  $35^\circ$  to normal, and the substrate rotated for ten minutes.

Following milling, the resist layer was removed by dipping in heated n-methyl-2-pyrrolidone twice with a dip in piranha solution in between.

Figure 4.21 shows scanning electron micrographs of the resulting trenches. They are shallow, having an estimated depth of less than 10 nm, with much material redeposited on the walls of the trenches.

The substrate was rinsed in water and ethanol immediately before use.

#### Early tests

Early tests of ice nucleation on ion-milled silicon predated any of the flow cells described earlier in the chapter. Hence a cell designed for studying the freezing of water drops, described in Section 7.4.1, was used as an improvised flow cell.



FIGURE 4.22: Optical micrograph showing ice grown on ion-milled silicon.

The substrate was cooled to  $-60\text{ }^{\circ}\text{C}$  with dry nitrogen passing through the cell. The flow was then suddenly switched off, allowing atmosphere to diffuse into the chamber, leading to rapid ice formation.

Figure 4.22 shows the result of the first such run, with ice nucleating along the troughs with a strong preference. Three subsequent runs were performed in similar conditions with identical results.

### With the first flow cell

After the manufacture of the first flow cell, it was used to study the nucleation of ice and camphor on the ion-milled substrate.

These experiments predate the humidity control system outlined above, so control was achieved by a cruder means. Nitrogen flow from a cylinder was directed along two paths and rejoined prior to entering the cell. One path flowed through the dehumidifier, the other through a valve. By opening or closing the valve, the gas stream could be made more or less moist.

Ice crystallisation was induced by allowing the temperature to drop to  $-70\text{ }^{\circ}\text{C}$ . Figure 4.23 shows the results for three conditions: in the first, the valve was closed (nucleation at  $-65.8\text{ }^{\circ}\text{C}$ ); in the second, the valve was open (nucleation at  $-66.8\text{ }^{\circ}\text{C}$ ); in the third, the valve was closed but was suddenly opened at the first sight of nucleation

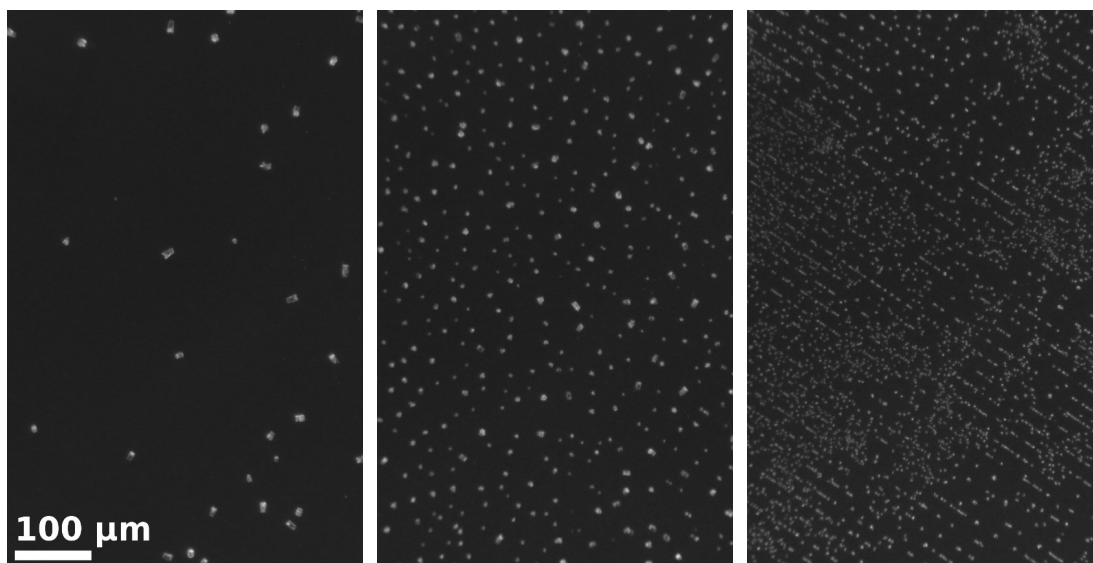


FIGURE 4.23: Optical micrographs of ice crystals grown on ion-milled silicon in differing flow conditions: (left) valve closed; (middle) valve open; (right) valve opened at onset of nucleation.

(nucleation at  $-67.0\text{ }^{\circ}\text{C}$ ). In the first two cases, crystals grew almost exclusively along the line of the trenches. In the last case, crystals grew in the trenches but to a lesser extent also across the whole surface.

Camphor flow saturation was achieved by passing a dry nitrogen stream through a tube of fine camphor crystals without any subsequent dilution with additional nitrogen. The substrate was cooled to a fixed temperature with a dry nitrogen stream passing through the cell, and then suddenly switched so that the flow through the camphor tube passed through the cell. Figure 4.24 shows the results for three different substrate temperatures. It can be seen that the majority of crystals appear to nucleate along the troughs, with a substantial minority nucleating elsewhere. At this magnification it is impossible to quantify how many nucleate in the troughs and how many on the flat surface.

#### With the second flow cell

The second flow cell was used to study ice nucleation on the surface at higher magnification. The flow control system described in Section 4.4.3 was used to provide gas with an expected frost point of  $-34\text{ }^{\circ}\text{C}$ , and then the temperature was ramped down at a very high ramp rate of about  $30\text{ }^{\circ}\text{C}/\text{minute}$ . Nucleation was seen at about  $-40\text{ }^{\circ}\text{C}$ . This was repeated six times, with the substrate held at  $-10\text{ }^{\circ}\text{C}$  for several minutes between runs to allow ice crystals to sublime away.

Figure 4.25 shows the results for each of the six runs. It can be seen that there is a strong preference for growth in the trenches, with only 8 out of 74 observed nucleation sites

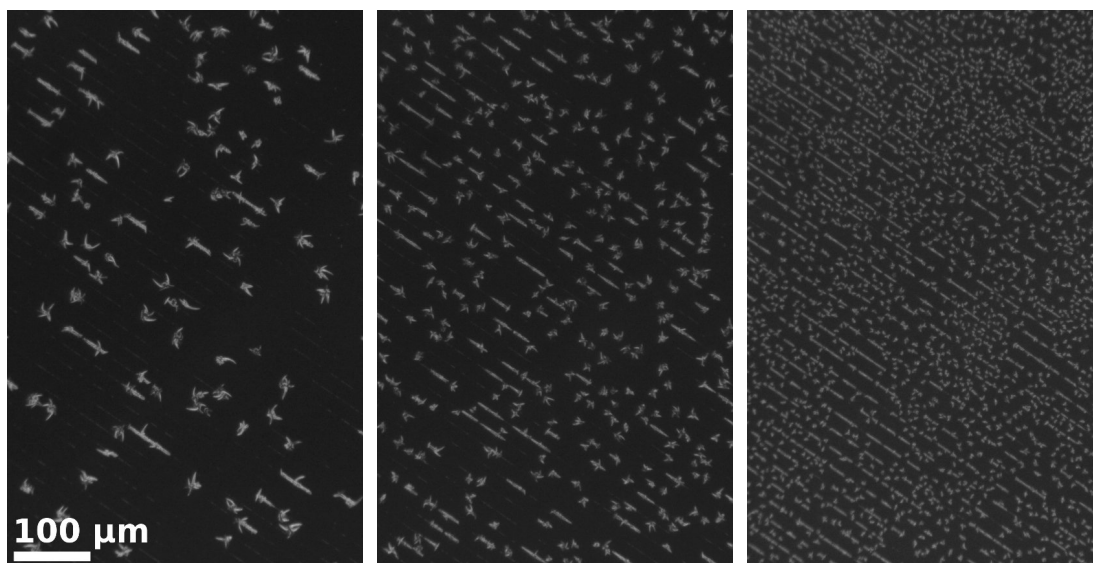


FIGURE 4.24: Optical micrographs of camphor crystals grown on ion-milled silicon at differing temperatures: (left)  $-15\text{ }^{\circ}\text{C}$ ; (middle)  $-20\text{ }^{\circ}\text{C}$ ; (right)  $-25\text{ }^{\circ}\text{C}$ .

being away from the grooves, which are only just visible in the images. There was also no significant correlation of nucleation positions between runs (see Figure 4.30).

## 4.7.2 Reactive-ion etching

### Substrate manufacture and characterisation

Trenches were produced by exposing the surface to a low pressure plasma of argon and reactive fluoroform ions. Two substrates were made this way: one etched for three minutes, and another etched for two minutes. Following milling, the resist layer was removed from the three minute substrate as with the ion milled substrate. For the two minute substrate, heated *n*-methyl-2-pyrrolidone only was used.

Figure 4.26 shows electron micrographs of trenches on each substrate where they open onto a wide etched area. On the three minute substrate, much material had not been cleared from the trenches, leaving an inconsistent pitted topography, and the flat surface had also become slightly pitted. The etched depth was 150 nm in large etched areas, and lower in the trenches.

On the two minute substrate, the flat surface is not pitted and the trenches have been more evenly cleared of material. The trench depth was measured to be 40–50 nm.



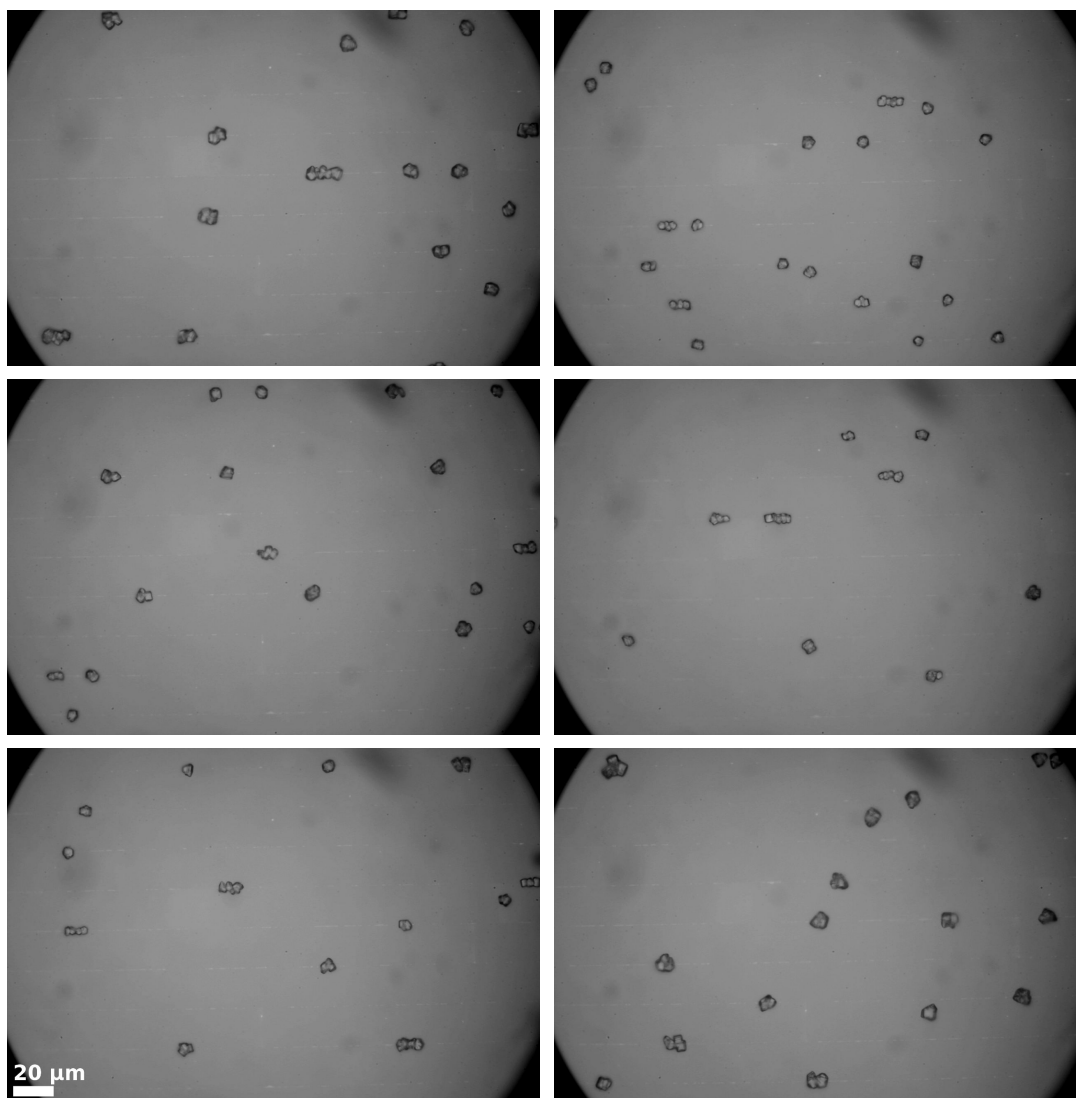


FIGURE 4.25: Optical micrographs showing ice crystals grown on the same region of ion-milled silicon on six consecutive runs.

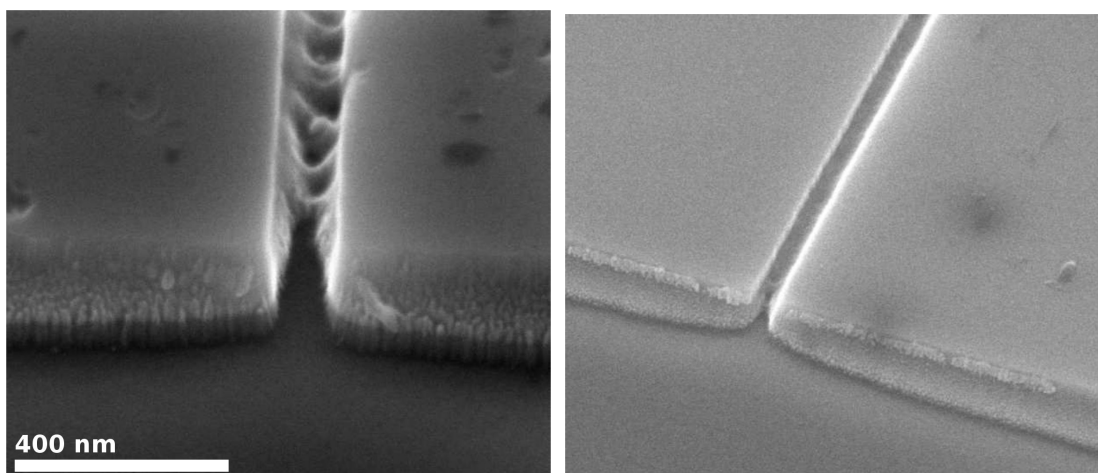


FIGURE 4.26: Scanning electron micrographs showing the ends of reactive-ion etched trenches in silicon, after: (left) three minutes; (right) two minutes. Micrographs taken by Mark Rosamond.

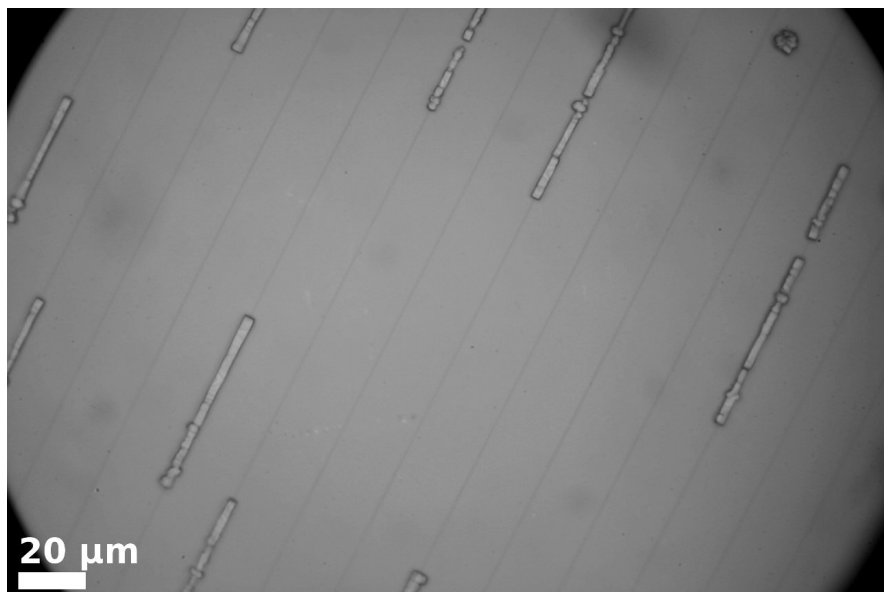


FIGURE 4.27: Optical micrograph showing linear ice crystals grown on three-minute reactive-ion etched silicon at  $-40\text{ }^{\circ}\text{C}$ .

### Three minute etched substrate

Ice was grown on the three-minute etched substrate using the same parameters as used for repeat runs on the ion-milled substrate. Nucleation was again observed at about  $-40\text{ }^{\circ}\text{C}$ , but leading to long linear crystals running along trenches, as shown in Figure 4.27. This is attributed to the formation of supercooled capillary condensates along the trenches prior to crystallisation.

Nucleation was observed at lower temperatures by passing supposedly dry gas through the cell and then ramping down the substrate temperature at  $30\text{ }^{\circ}\text{C}/\text{minute}$ . Nucleation was observed between  $-50$  and  $-55\text{ }^{\circ}\text{C}$ . Six consecutive runs were performed, with the substrate warmed to  $-10\text{ }^{\circ}\text{C}$  for several minutes between runs. Figure 4.28 shows the results. It can be seen that crystals grow from points along the trenches, with no off-trench nucleation seen out of 52 observed nucleation sites. Some sites nucleated crystals repeatedly between runs, see Figure 4.30, but most nucleation occurred at unique sites.

### Two minute etched substrate

Crystallisation on the two minute substrate was performed using the same method and parameters as used for repeat runs on the three-minute substrate, and again nucleation was seen between  $-50$  and  $-55\text{ }^{\circ}\text{C}$ . Figure 4.29 shows the results. Again, nucleation occurs at the trenches, with one off-trench nucleation site seen out of 15 observed sites. The only significant difference between this and the three-minute substrate was that

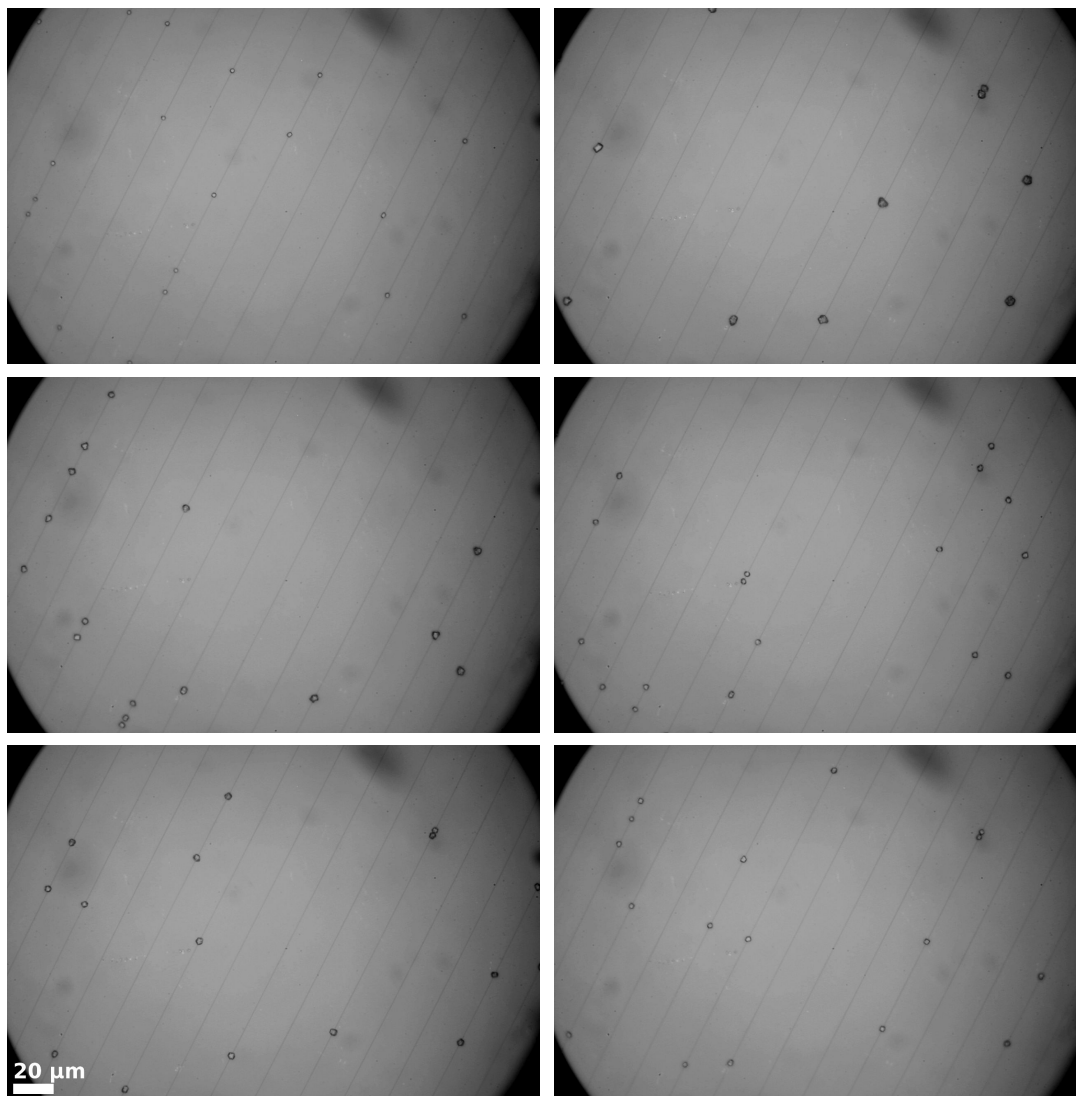


FIGURE 4.28: Optical micrographs showing ice crystals grown on the same region of reactive-ion etched silicon (three minutes' etch) on six consecutive runs.

here crystals nucleated in only a small number of sites, but in these repeatedly, see Figure 4.30.

### Site correlation

The correlation of nucleation site locations between runs was studied on all three substrates. For each site where a crystal was seen to nucleate at least once, the total number of runs on which that site nucleated a crystal was found by comparing images closely. Figure 4.30 shows the results for each substrate, with bars representing the number of sites at which crystals were seen to nucleate each possible number of times out of six. So if there was no correlation between runs, almost all sites would be seen to nucleate a crystal only once, whereas if crystals appeared in exactly the same sites on

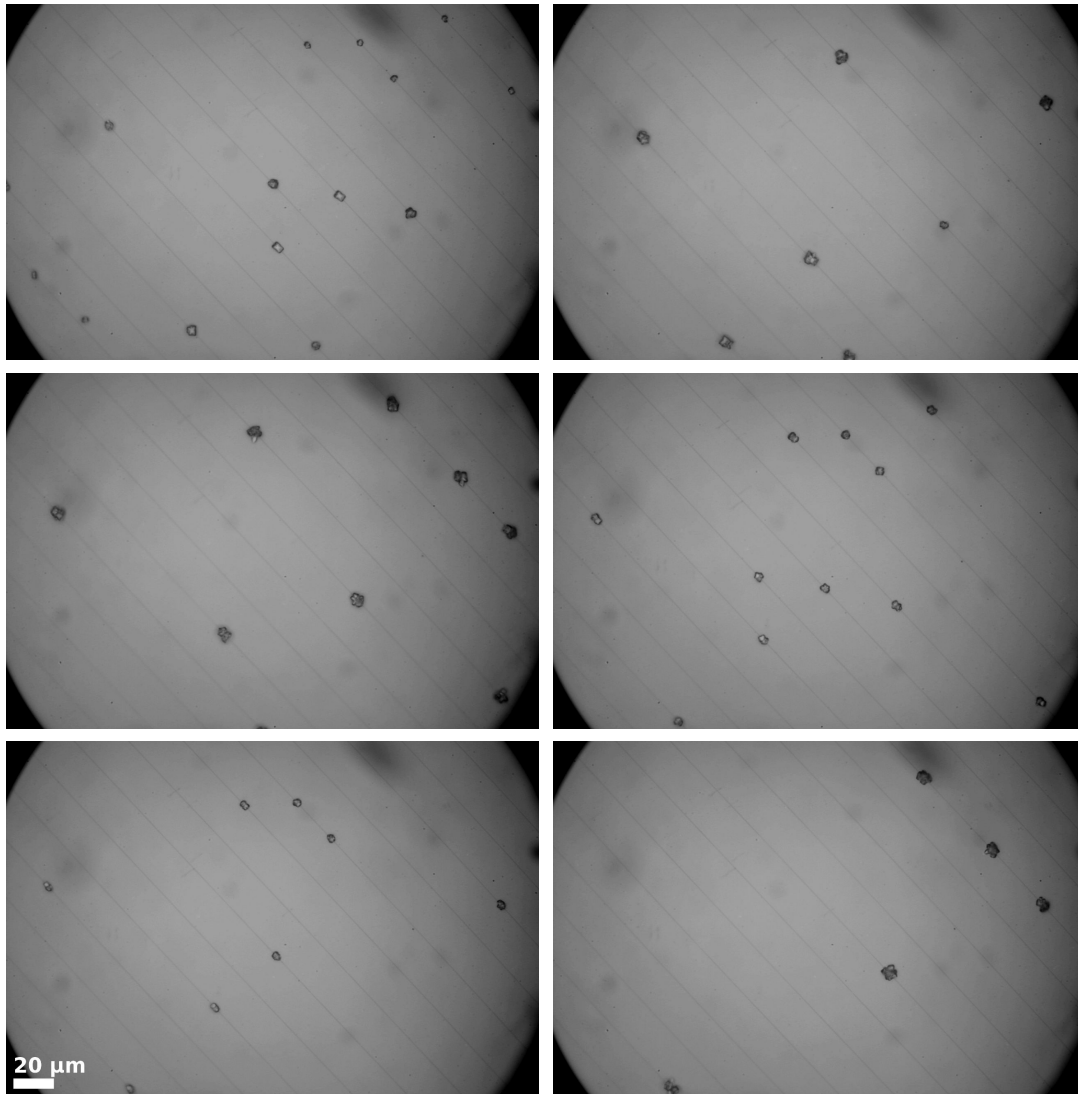


FIGURE 4.29: Optical micrographs showing ice crystals grown on the same region of reactive-ion etched silicon (two minutes' etch) on six consecutive runs.

each run, a smaller number of sites would be observed to all nucleate crystals six times. There was some image drift between runs, particularly for the two minute substrate, and only sites visible on all runs were considered.

It may be seen that for the ion-milled substrate, there is very little correlation between runs, perhaps no more than can be explained by coincidence. For the three-minute reactive-ion etched substrate, there is slightly more correlation, somewhat above coincidence, with some sites nucleating crystals on most runs. For the two-minute substrate there is significant correlation, with a small number of sites nucleating crystals repeatedly, although still some variability between runs.

Quantitatively, we can find the probability, given that a crystal grows from one site on a particular run, that a crystal will grow from the same site on the next run. This

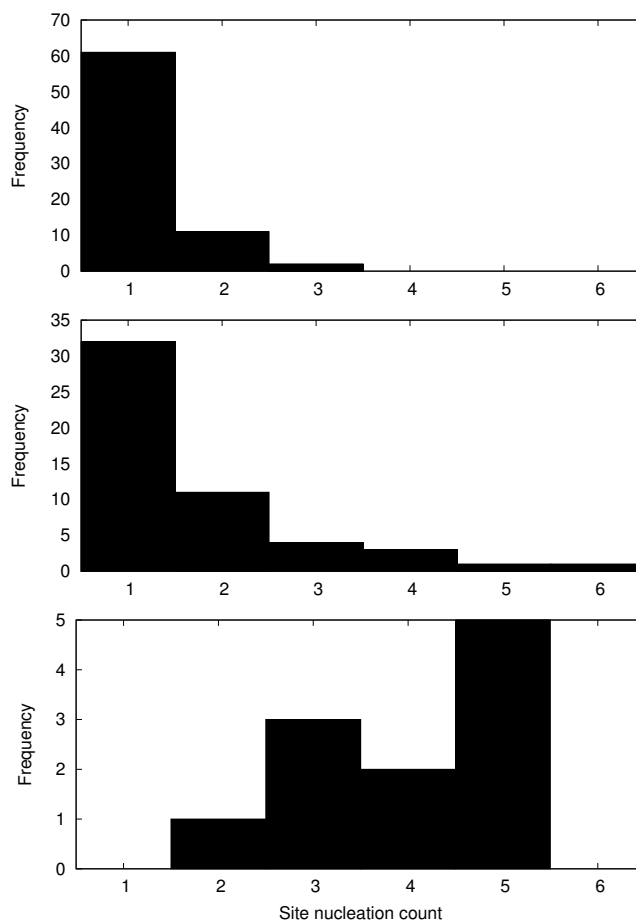


FIGURE 4.30: Graphs showing the number of sites seen to nucleate a crystal one to six times on: (top) ion-milled silicon; (middle) reactive-ion etched silicon, three minutes' etch; (bottom) reactive-ion etched silicon, two minutes' etch.

can be estimated by counting the number of times this does and does not occur in the experiments. It is found that this probability is  $0.05 \pm 0.03$  for the ion-milled substrate,  $0.37 \pm 0.06$  for the three-minute reactive-ion etched substrate and  $0.60 \pm 0.07$  for the two-minute reactive-ion etched substrate.

I hypothesise that preferential nucleation in the trenches of these substrates is not determined by the 100 nm trenches themselves, but by smaller-scale imperfections within the trenches. On the two-minute substrate the trenches are nearly perfect, so there are likely to be only a few such sites, which therefore nucleate crystals repeatedly due to limited competition. On the less perfect substrates, there would be many favourable sites, only a few of which can nucleate crystals on any one run, and so the site correlation is less evident.

For higher temperature nucleation on the three minute substrate, where ice formed as long linear crystals, it appears to be the 100 nm length-scale trenches themselves which are responsible for nucleation. This leads to the hypothesis that the length scale of

feature critical to nucleation is dependent on the supercooling: at smaller supercooling a larger feature is needed to condense a condensate large enough to freeze, whereas at larger supercooling much smaller features are likely to be preferable.

## **4.8 Summary**

I have studied the growth of various organic compounds and ice from vapour on various surfaces. Starting from existing findings that neopentanol crystals nucleated with greater density on rougher mica surfaces, I have shown that many different crystals grow preferentially on scratches and defects on several surfaces, to the extent that the behaviour appears to be universal. In fact, crystals have never been observed to nucleate randomly across any surface, except in the extreme case of featureless mica following a rapid quench into heavily supersaturated conditions. Rather, on any surface there are a small number of favourable sites which dominate nucleation.

Several attempts were made to mill submicron trenches into silicon wafers. These were found in all cases to provide favourable nucleation sites for ice crystals, although as the trenches became neater it was seen that a small number of sites dominated.

## Chapter 5

# On the identification of dominant nucleation sites on mica surfaces

### 5.1 Introduction

As discussed in the previous chapter, many compounds tend to nucleate on defects present on mica surfaces. As model sites for studying topographical features these have definite advantages: they are well-defined on the nanometre scale; there are a variety of possible geometries that could be produced; and they are surrounded by large areas of atomically flat surface.

One disadvantage is that they are random. Upon cleaving a piece of mica, one cannot predict what manner of defects it will contain, how many, or even if there will be any. Certain types are likely to be very common, others very rare. Another problem is that it is difficult, using only an optical microscope, to identify the nanometre-scale geometry of a surface feature from its appearance (with exceptions, as exploited heavily in Chapter 6).

When repeated crystallisation runs are performed on a mica surface rich in defects, it is apparent that particular sites dominate nucleation, with crystals growing from these places time and again. These must be the most favourable sites for nucleation, and clearly it is of considerable interest to determine the geometric nature of these sites.

The concept used for experiments in this chapter, then, is as follows. A series of crystallisation runs are performed on a single mica substrate, observing with an optical microscope. The most dominant nucleation sites are noted, and their positions identified. The substrate is finally transferred to an electron microscope, in which the dominant sites are located and imaged at high resolution.

## 5.2 Techniques

### 5.2.1 Crystal growth

Crystals were grown from vapour using the cell described in Section 4.3.1. Mica sheets were cleaved in a laminar flow cabinet and cut to a 1'' × 1'' dimension with scissors. These were then sealed inside the cell under a glass slide, still within the laminar flow cabinet to prevent contamination. Substrates were not left to weather or treated in any way.

The cell was flushed with nitrogen gas before any experimental runs were performed. Crystallisation was induced by ramping the reservoir temperature upwards at a steady rate of 2 °C/minute until crystals were observed.

Observations were made at low magnification (3× objective), however the area of mica in view at one time was no more than about 1.8 mm<sup>2</sup>. Hence, if I were to observe the first nucleation events within any given area, I could not guarantee that these were the first nucleation events on the whole substrate. It was clearly preferable to be observing the region where nucleation first occurs, as otherwise local nucleation may be retarded by the growth of crystals elsewhere depleting the vapour. Hence, before the first experimental run for each substrate, a pre-run was performed, which was identical to a normal run in every way except that instead of watching a small area, the view was continuously scanned across the whole surface. Wherever crystals were seen first in the pre-run became the area for study in the experimental runs. Although this did not guarantee that crystals would nucleate first in the observed area, it did ensure that the area was at least a relatively preferable region for nucleation.

The substrate was photographed once every five seconds. After crystals had been observed, the cell reservoir was cooled to slightly below room temperature (which was typically 21–22 °C) using cooled metal blocks and the cell was flushed with nitrogen to sublimate all crystals on the mica. Then the next run was begun. After all runs had been completed, the cell was opened in a laminar flow cabinet and the mica substrate sealed in an airtight tube until it was needed for the electron microscope.

### 5.2.2 Site identification

After the final run, a small scratch was placed on the mica surface near the region of interest with the tip of a fine pair of tweezers. This allowed the region to be located quickly and unambiguously in the electron microscope.



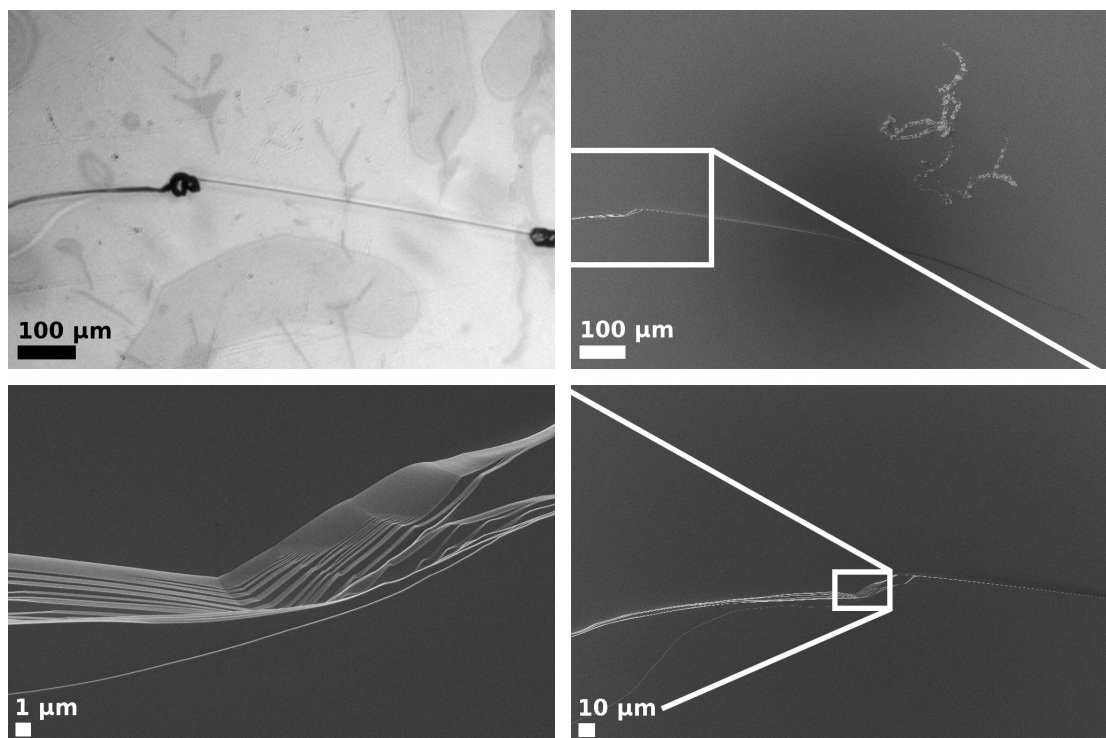


FIGURE 5.1: Demonstration of nucleation site location in an electron microscope: (top left) optical micrograph showing crystal of hexachloroethane nucleating on a defect; (top right) electron micrograph of same defect, located by scratch placed after experiments; (bottom right) higher-magnification view of nucleation region; (bottom left) high magnification view of nucleation region.

Individual sites were located with reference to the distinct shapes of defects. Figure 5.1 shows an example of locating a hexachloroethane nucleation site in the electron microscope. As with most sites, electron micrographs were taken at both low and high magnification to provide both fine detail and broader context of a site. Very high magnification images were generally not possible due to the inability to locate sites sufficiently precisely from low-magnification optical micrographs.

### 5.3 Early results

Early tests of the procedure were performed using neopentanol, carbon tetrabromide and camphor. The procedure was identical to that outlined above except that a pre-run was not used; rather, an area of defect was selected by eye, and nothing was known about nucleation outside this area.

Carbon tetrabromide nucleation was observed in two separate regions of one mica substrate. I shall describe this substrate in some detail as it exemplifies some of the general results found in this chapter.

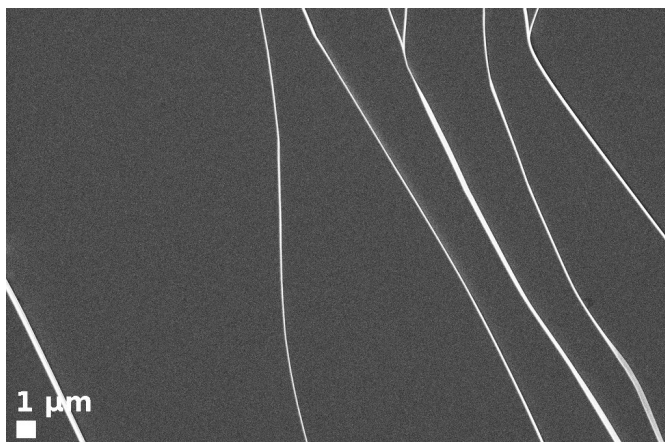


FIGURE 5.2: Electron micrograph showing a region of preferable nucleation of carbon tetrabromide on mica, although the precise site is unknown.

One region contained a great number of step edges, on which nucleation occurred, and no other visible features. There were preferable sites along these steps, but electron micrographs of these such as that in Figure 5.2 reveal no distinguishing features.

The other region also contained step edges, but it also contained places where the top layer of mica appeared to be breaking away from the layers below. No nucleation whatsoever was seen along the ordinary step edges, however it was seen to prefer sites where one mica sheet was lifting away from another; two such sites are shown in Figure 5.3a–c. Where nucleation did occur along the step edges, it was where several bunched together and appeared to overhang those below, as shown in Figure 5.3d.

On another mica substrate, carbon tetrabromide nucleation was observed in a single area. After this, neopentanol nucleation was observed in the same area under similar conditions. Neopentanol crystals appeared to grow from the entire length of the defect simultaneously. Carbon tetrabromide grew from a number of sites, but one site in particular was identified as dominant. Upon electron microscopy, it was found that the defect had a highly imperfect edge along its whole length, as though a thicker sheet had been violently torn. The dominant site, shown in Figure 5.4, was that where there seemed to be the largest concentration of torn material.

Figure 5.5 compares  $\Delta T$  at first nucleation of carbon tetrabromide on this latter substrate with that on the two regions of the first substrate. It can be seen that crystals appear to form most easily on the torn-looking site, slightly less easily on the sites with mica lifting off the surface and least easily of all on the ordinary step edges.

When repeatedly growing carbon tetrabromide crystals on a flat, defect-free mica surface, they were seen to nucleate in the same sites each time. Attempts were made to locate these sites in the electron microscope, using a nearby scratch to triangulate the

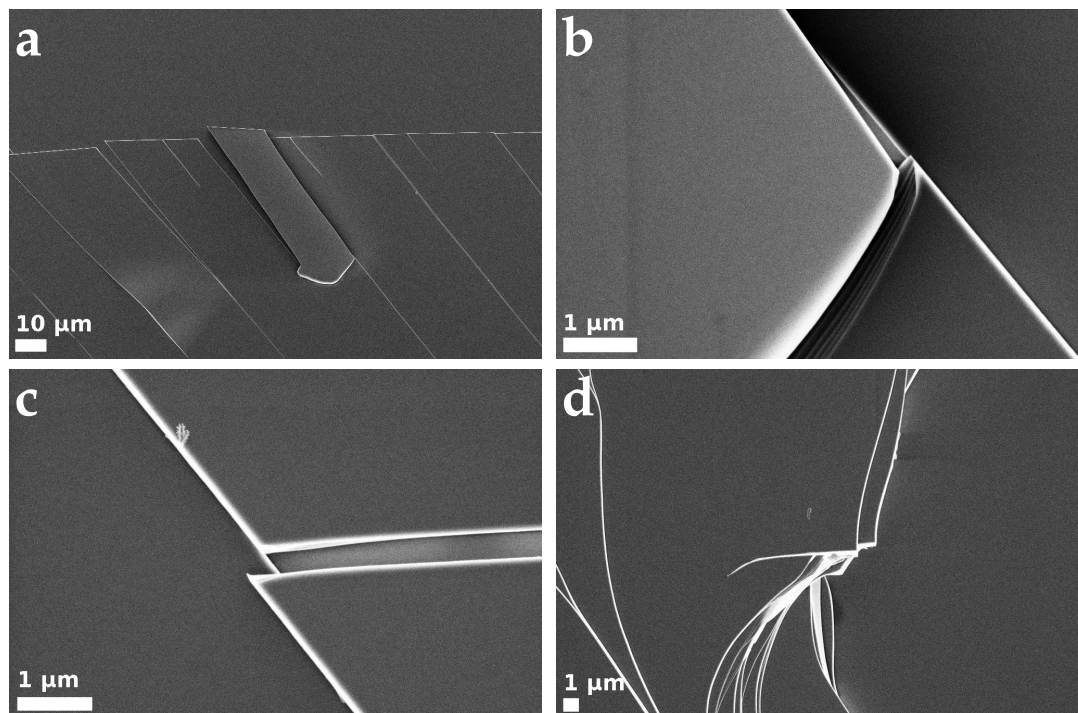


FIGURE 5.3: Electron micrographs showing carbon tetrabromide nucleation sites on mica: (a) mica delamination; (b) magnified view of nucleation site at corner of delaminating sheet in centre of (a); (c) corner of mica sheet lifting away from surface; (d) major defect of step edges featuring an apparent overhang.

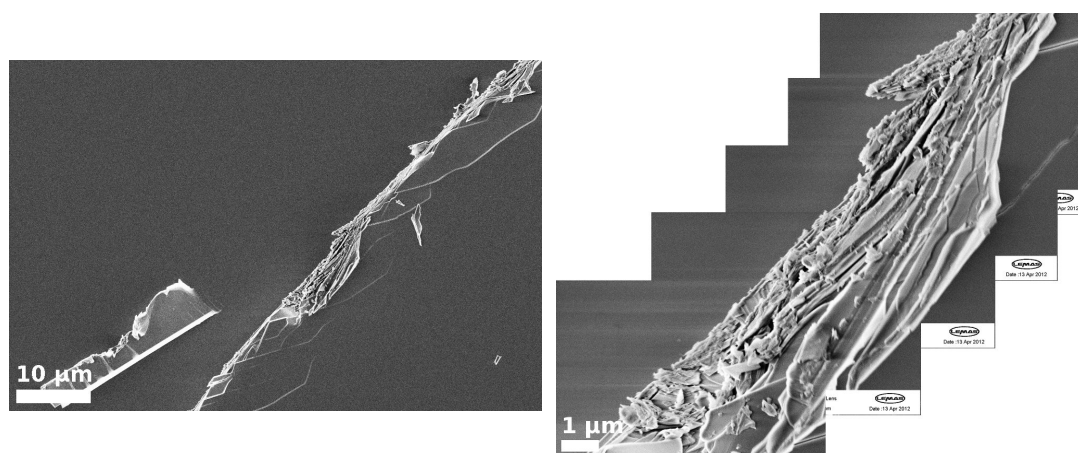


FIGURE 5.4: Electron micrographs showing a dominant nucleation site for carbon tetrabromide on mica, at high magnification (right) and in context (left).

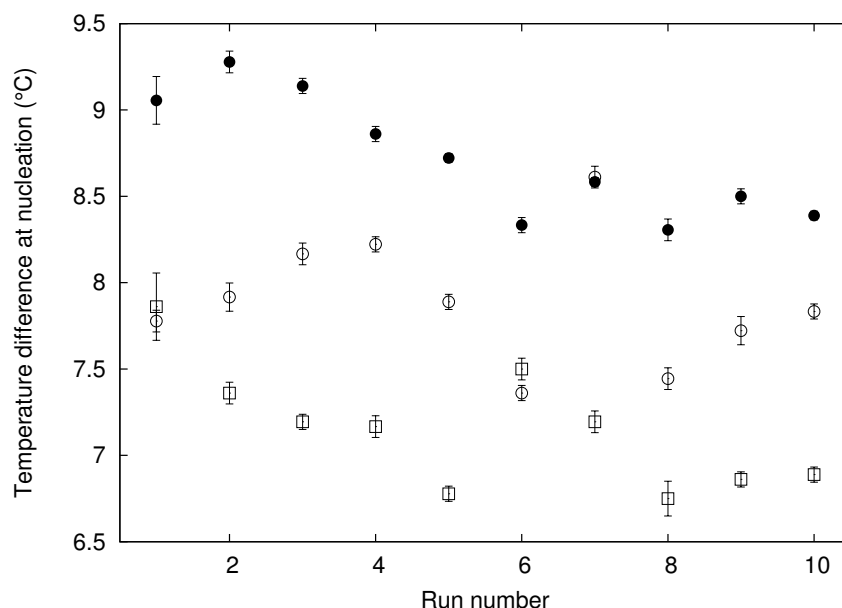


FIGURE 5.5: Graph showing  $\Delta T$  at first observed nucleation of carbon tetrabromide in three regions, as corresponding to Figures 5.2 (●), 5.3 (○) and 5.4 (□).

position. However, this proved insufficiently precise: there could well have been a feature responsible for this behaviour large enough to observe, however it was impossible to know where to zoom in to find it.

Experiments were performed with camphor on two substrates, however a different electron microscope was used from the previous substrates which did not possess sufficient resolution to obtain conclusive results. One substrate appeared to have simple step edges and nothing else, upon which the crystals grew. On the other substrate crystals grew from what was probably small flakes of mica peeling from the surface.

## 5.4 On mica defects

It is becoming clear that before we can attempt to interpret the results from a larger number of substrates we are going to need to characterise the various types of feature common on mica surfaces and consider their microscopic geometry.

### 5.4.1 Common topographic features of mica surfaces

#### Step edges

The simplest feature possible after a flat surface is a step edge. A diagram and example of this are shown in Figure 5.6. Geometrically, this is assumed to offer a sharp wedge

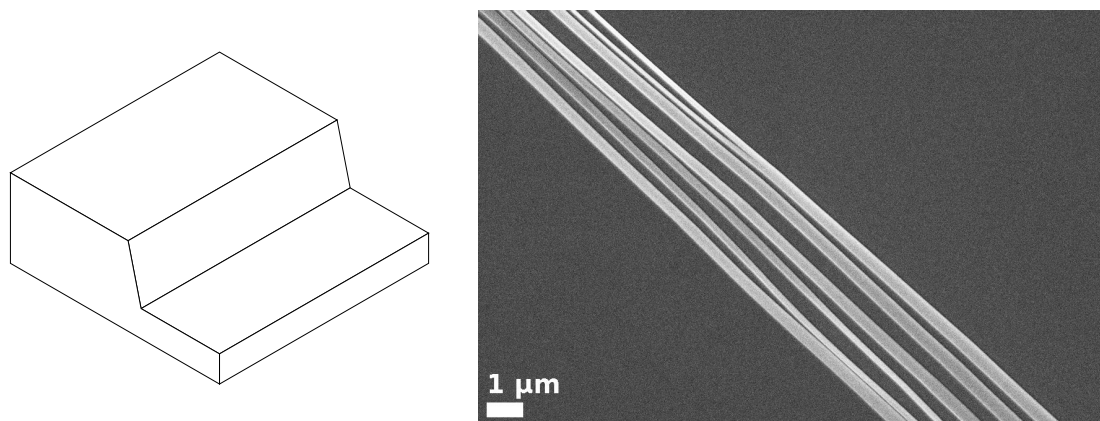


FIGURE 5.6: Diagram (left) and scanning electron micrograph (right) exemplifying a step edge geometry.

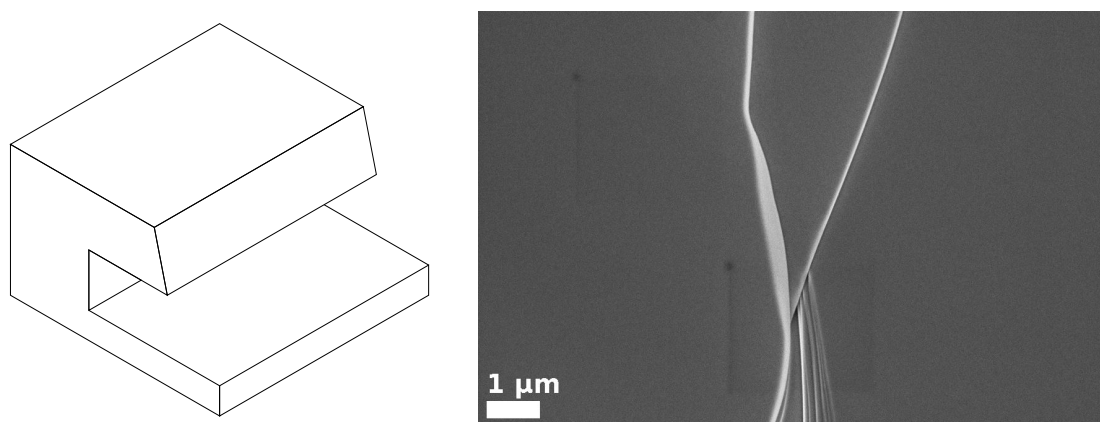


FIGURE 5.7: Diagram (left) and scanning electron micrograph (right) exemplifying a step overhang geometry.

geometry at its base; the angle of this cannot be estimated, but by the fact that the step face is generally observed in the electron microscope, it must often be greater than  $90^\circ$ . Step edges often occur running in closely-spaced parallel lines.

### Overhanging steps

Where one step overhangs another it leaves a narrow space underneath. These features are difficult to identify from the top-down perspective of electron micrographs, but can usually be found by observing where one step edge runs underneath another. Figure 5.7 shows an example.

### Hanging flakes

Where the top sheet of mica has partly detached from the surface, it leaves a hanging flake, as shown in Figure 5.8. The white areas in the electron micrograph indicate where

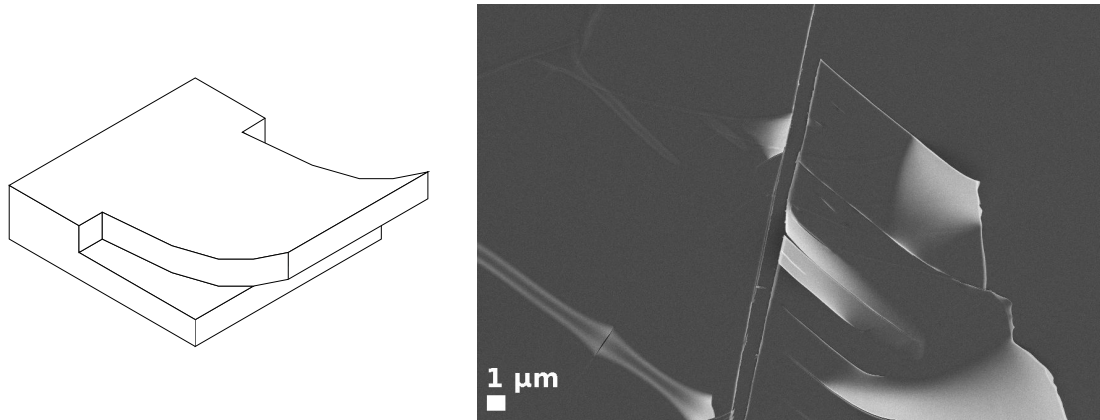


FIGURE 5.8: Diagram (left) and scanning electron micrograph (right) exemplifying a hanging flake geometry.

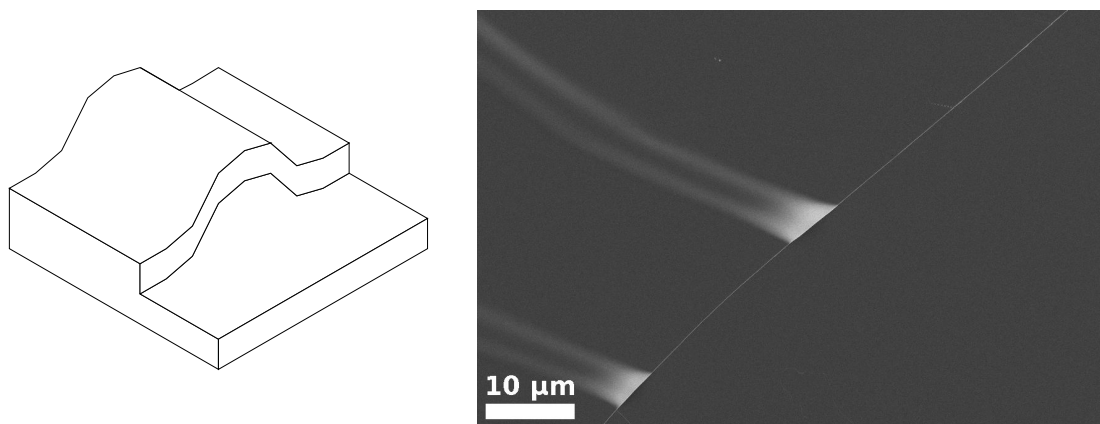


FIGURE 5.9: Diagram (left) and scanning electron micrograph (right) exemplifying a pocket geometry.

a thin sheet of mica is detached from the surface below it, leading to charging under the electron beam. Hanging flakes are assumed to provide a highly acute wedge geometry along their line of delamination from the surface.

### Pockets and tunnels

Although not encountered on the early substrates, the pocket geometry was found repeatedly in later experiments. Here, an air pocket under the mica surface intersects a step edge, as shown in Figure 5.9. These can occasionally intersect two step edges to form a two-ended tunnel feature. Geometrically these should provide similar nucleation sites to a hanging flake, except here there are two lines of delamination running down the sides of the feature.

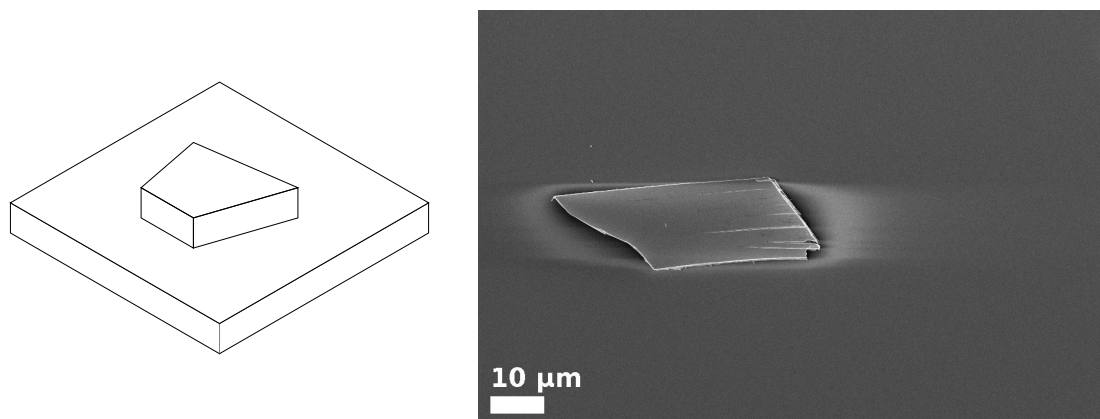


FIGURE 5.10: Diagram (left) and scanning electron micrograph (right) exemplifying a loose flake.

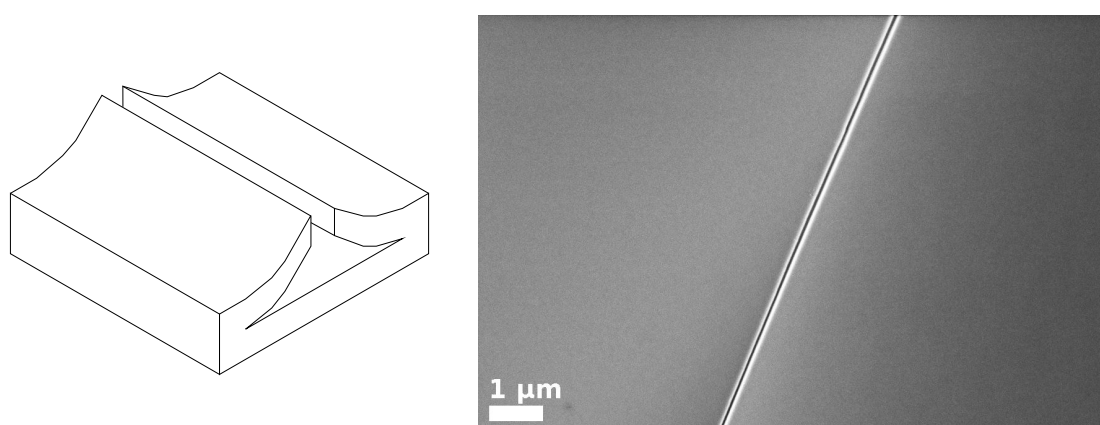


FIGURE 5.11: Diagram (left) and scanning electron micrograph (right) exemplifying a crack or split geometry.

### Loose flakes

Flakes of mica may become entirely detached during cleavage and sit loose on the surface, as shown in Figure 5.10. Mica flakes are likely to rest on their (001) cleavage plane, potentially sitting perfectly to form step edges around its perimeter. However if the flake is imperfect, there will be some highly acute geometry at the point or points of contact, the precise nature of which is hard to predict.

### Cracks and splits

The top layer of mica may rupture, leaving a crack or split in the surface, as shown in Figure 5.11. The diagram illustrates the surface layer peeling away at each side, leaving two lines of delamination offering acute wedge geometries. In reality, it is impossible to know what the geometry of these sites is, as we cannot probe beneath the surface.

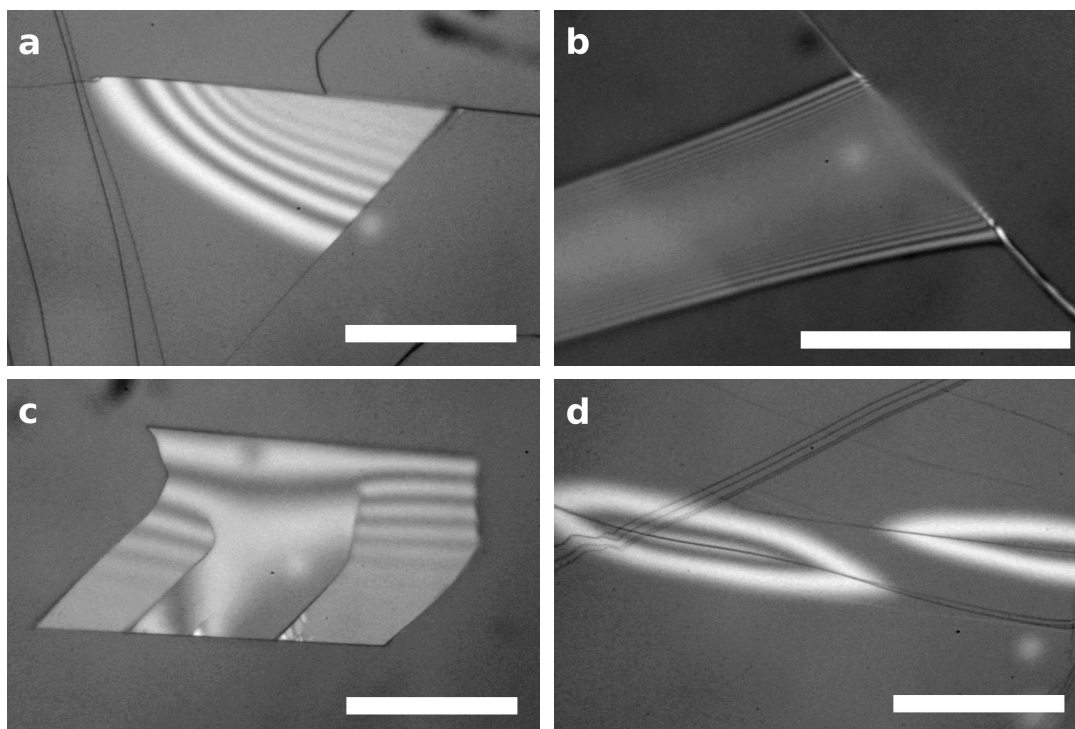


FIGURE 5.12: Optical micrographs showing interference fringes in 532 nm light arising from: (a) a hanging flake; (b) a pocket; (c) a loose flake; (d) a split. The white bar in each image represents 50  $\mu\text{m}$ .

There is, however, evidence from reflected light microscopy that at least some such splits delaminate in this way. Figure 5.12 shows micrographs of four types of feature hypothesised to provide an acute wedge geometry. Interference fringes are visible in all, diagnostic of a highly acute wedge. Particularly, note the presence of fringes around a surface split in image d. The estimated wedge angles in images a-d, calculated from the fringe spacing between the first two fringes, are  $(1.8 \pm 0.1)^\circ$ ,  $(6.3 \pm 0.3)^\circ$ ,  $(2.3 \pm 0.1)^\circ$  and  $(1.6 \pm 0.2)^\circ$  respectively. For the loose flake, the rightmost fringes are used, although where the point of contact is is not clear.

### 5.4.2 Ambiguity

When trying to divide sites into distinct categories, an issue arises: the decision is frequently ambiguous. This has three causes.

Firstly, there was the problem of there being not just one type of feature in an identified area but several. When this clash involves flat mica or step edges, the rarer feature is given priority. This is essential: flat mica is always present around features, and all pockets, hanging flakes and overhangs necessarily exist alongside a step edge.



When there were multiple feature types other than flat mica and step edges at a single site, the site was characterised by whichever feature type dominated the area. For example, the region shown in Figure 5.8 would be categorised by the hanging flakes, despite the presence of splits and pockets (typically however the nucleation site could be pinpointed to a slightly more precise area than that covered by this micrograph).

Secondly, there was the problem of being unable to see beneath the top layer of mica in an electron micrograph. For example, what appears to be a simple step edge could easily be an overhang. Occasionally such features could be identified by charging effects: if a step edge overhangs, then the platinum coating will not connect one surface to the other, which leads to slight charging above (the edge appears brighter) and undercharging below (the edge appears to have a dark shadow). This however is only clearly visible on quite large overhangs.

Finally there was much ambiguity between overhangs, hanging flakes and pockets, partly because the categorisations themselves are ambiguous. There were so many ambiguous sites between overhangs and hanging flakes that they were combined into a single category to avoid making too many arbitrary decisions. Although there were some ambiguities between flakes and pockets, these were left as separate categories as the large majority of sites were distinctly one or the other.

The categories used, then, were as follows:

**flat:** flat mica, including sites far from visible defects where no precise site could be identified;

**step:** step edges, where no site lower down this list was present;

**overhang/flake:** overhangs and hanging flakes;

**pocket:** pockets and tunnels;

**split:** cracks and splits;

**loose fragment:** loose fragments of mica or visible foreign contaminants;

**uncharacterisable:** any site where no meaningful characterisation could be made, usually due to an abundance of site geometries, or because the mica was badly damaged.

## 5.5 Results by compound

The nucleation of each compound was observed on six unique substrates, except for carbon tetrabromide which was observed on only three. These experiments were all performed in a consistent manner as described in Section 5.2, with twelve experimental runs per compound and a constant ramp rate of 2 °C/minute.

Throughout the rest of this chapter, substrates for each compound will be referred to by a geometric symbol such as ■ or ○. These correspond to the symbols used on graphs and in the published article,[107] for easy cross-reference. Note that the substrates were used only for a single compound, and so camphor substrate  $\Delta$  has no relation to norbornane substrate  $\Delta$ , etc. In addition there were two substrates,  $\diamond$  and  $\blacklozenge$ , which were used to study nucleation of all four compounds, so camphor substrate  $\diamond$  is identical to norbornane substrate  $\diamond$ , etc.

Substrates for each compound were chosen to give a mix between substrates with no or very few defects and those with a high density of defects. Site selection for electron microscopy was not completely systematic, but sites which nucleated crystals particularly frequently or earlier than other sites were given priority. Where there were six observed nucleation sites or less on a substrate, all were examined.

### 5.5.1 Carbon tetrabromide

The following summarises the three substrates studied:

**substrate □:** a wide variety of defects, including overhangs, torn edges and splitting, although no pockets or hanging flakes were seen. Six nucleation sites of fairly equal favourability were investigated, and were found to mostly correlate to overhang and split geometries, e.g. Figure 5.13;

**substrate ■:** this substrate offered step edges and no other visible defects. Two nucleation sites were identified: one on a step edge (see Figure 5.14), the other in an apparently featureless area of mica;

**substrate ○:** the mica of this substrate was locally highly split and lifting away from the surface, as shown in Figure 5.15. Nucleation sites were observed along splits and at the edge of lifted-off mica sheets.

Figure 5.16 shows  $\Delta T$  at first observed nucleation as a function of substrate temperature, for all three substrates as well as substrates  $\diamond$  and  $\blacklozenge$  discussed in the next section. There

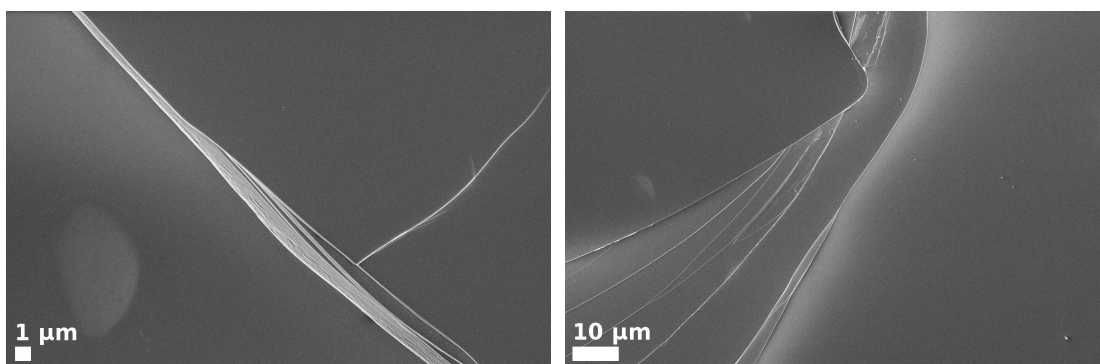


FIGURE 5.13: Two carbon tetrabromide nucleation sites on substrate □: (left) a split intersecting a series of step edges; (right) an overhanging step edge, centre-top of image.

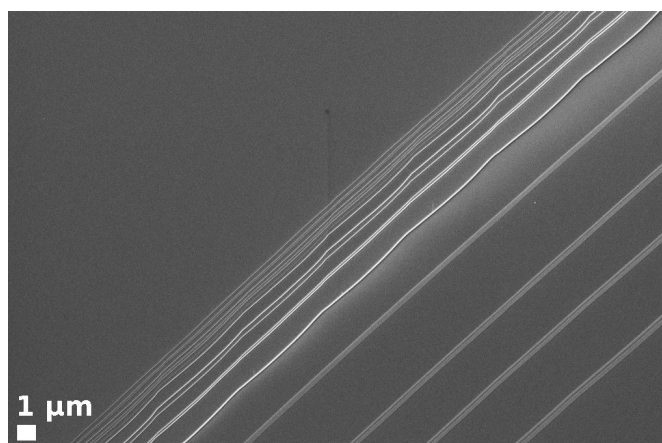


FIGURE 5.14: Electron micrograph showing step edges on substrate ■ preferable to carbon tetrabromide nucleation.

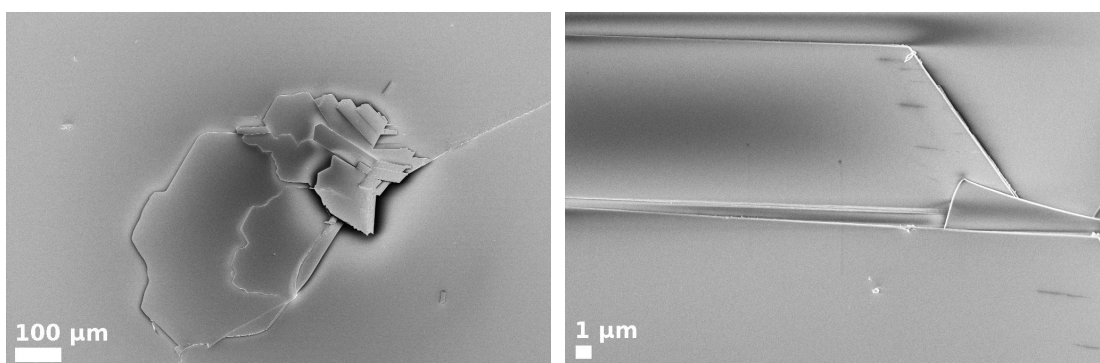


FIGURE 5.15: Electron micrographs overlooking carbon tetrabromide substrate ○ (left) and showing a typical nucleation site (right).

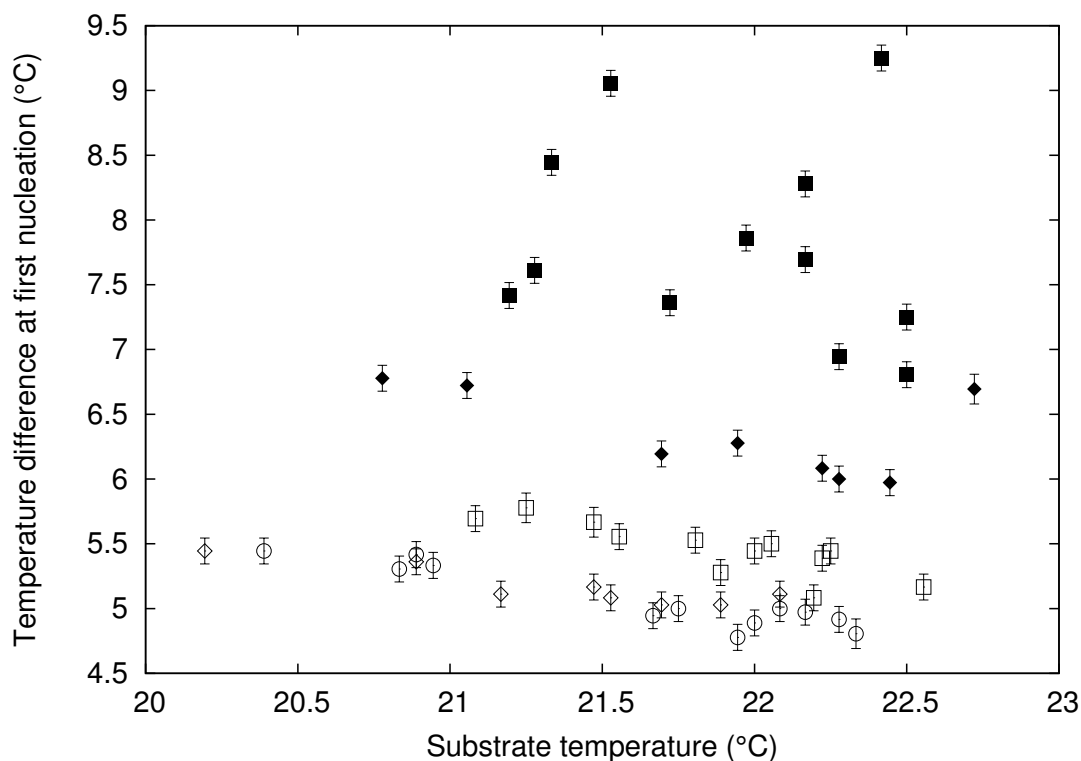


FIGURE 5.16: Graph showing temperature difference at the moment of first observed nucleation on each run of carbon tetrabromide growth.

are clear differences between the substrates, with substrate ■ needing the highest temperature difference to induce nucleation, followed by ◆, then □, and finally substrates ○ and ◇ needing the least temperature difference.

### 5.5.2 Camphor

The following summarises the six substrates studied:

**substrate □:** this substrate contained step edges, splits and several pocket geometries. Each of four nucleation sites investigated coincided with a pocket, two examples of which are shown in Figure 5.17, and each pocket appeared to be a nucleation site;

**substrate ■:** this substrate contained large numbers of step edges however they did not act as effective nucleation sites. One small area nucleated many small crystals apparently simultaneously, and was found to be rich in pocket and tunnel features; other nucleation sites on the substrate were found to correspond closely to pocket features. Figure 5.18 shows examples of both;

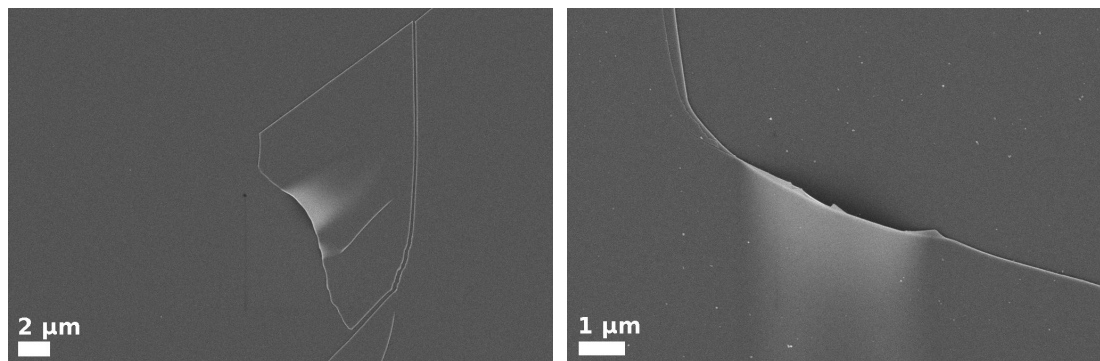


FIGURE 5.17: Electron micrographs showing pocket geometries at camphor nucleation sites on substrate □.

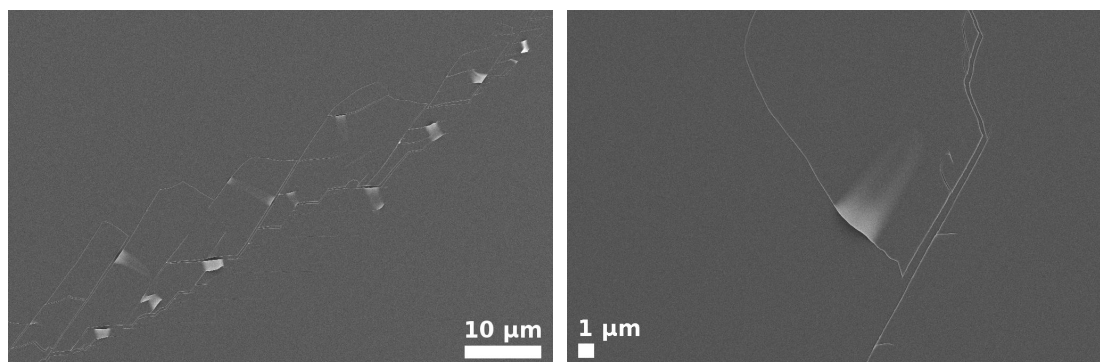


FIGURE 5.18: Electron micrographs showing camphor nucleation sites on substrate ■: (left) an area rich in pockets and tunnels; (right) a pocket geometry.

**substrate ○:** there was only a single linear defect on this substrate. Crystals were seen growing along it at highly reproducible positions. Electron microscopy revealed step edges with occasional pocket features, the positions of the pocket features corresponding exactly to positions of nucleation sites. This is illustrated in Figure 5.19;

**substrate ●:** despite a great number of step edges, nucleation on this substrate was dominated by a region where mica peeled from the surface, leaving many hanging flakes, caves and tunnels, as shown in Figure 5.20;

**substrate △:** this substrate had no visible defects. Nucleation was seen to occur preferentially in several positions, but subsequent electron microscopy could not find any surface features to account for this;

**substrate ▲:** here were many step edges and overhangs, plus a scatter of loose mica fragments. One site which consistently promoted the first observed nucleation was seen to be a loose fragment (see Figure 5.21), other effective sites were seen to correspond to overhangs and other loose mica flakes.

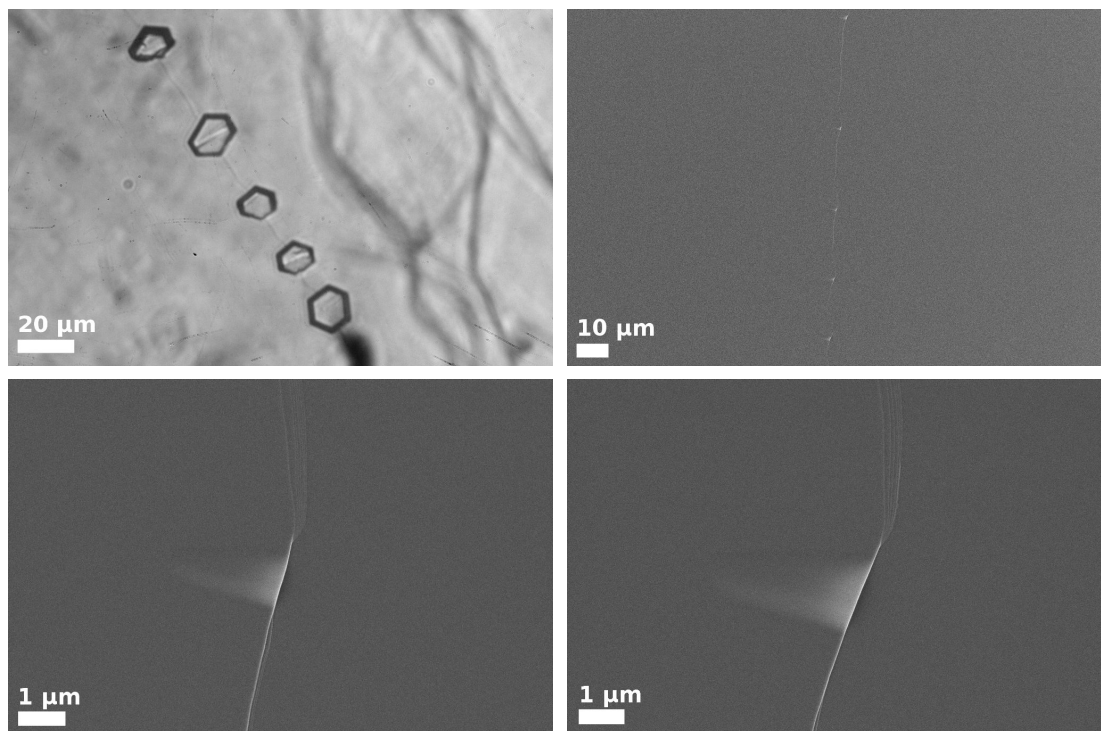


FIGURE 5.19: Nucleation sites on camphor substrate ○: (top left) optical micrograph showing crystals nucleating along a feature; (top right) electron micrograph showing the same feature, with five pocket features just visible; (bottom) electron micrographs of two of the pocket features.

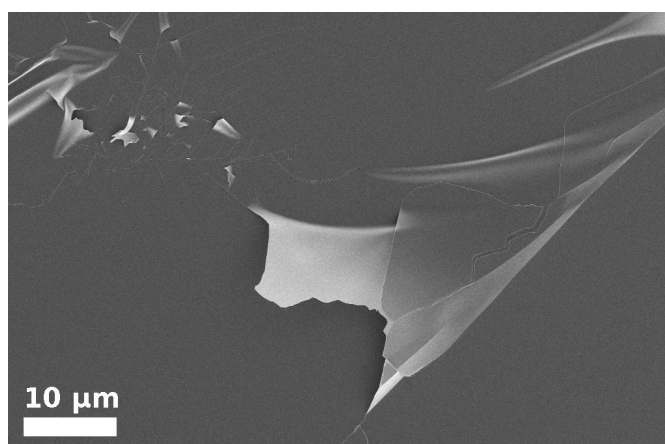


FIGURE 5.20: Electron micrograph showing flaking mica on substrate ● preferable to camphor nucleation.

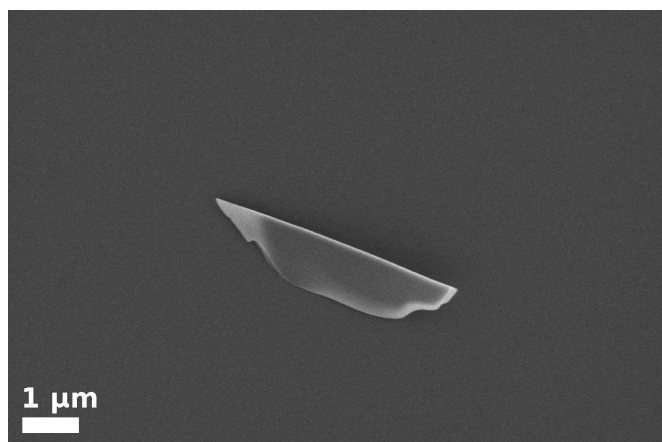


FIGURE 5.21: Electron micrograph showing loose mica flake on substrate  $\blacktriangle$  which dominated camphor nucleation.

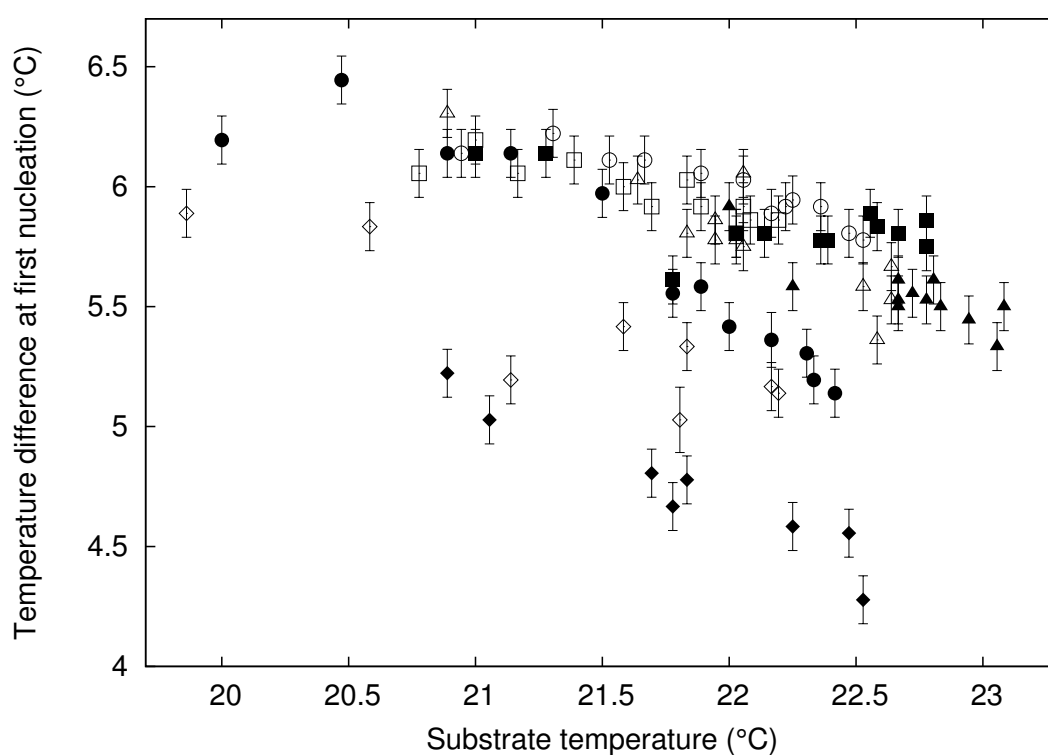


FIGURE 5.22: Graph showing temperature difference at the moment of first observed nucleation on each run of camphor growth.

Figure 5.22 shows  $\Delta T$  at first observed nucleation as a function of substrate temperature, for all six substrates as well as substrates  $\diamond$  and  $\blacklozenge$  discussed in the next section. For most substrates, the points lie nearly coincidental along a line, however substrates  $\diamond$  and particularly  $\blacklozenge$  required significantly less temperature difference to initiate nucleation. Substrate  $\bullet$  also appears to have required a slightly lower temperature difference.

### 5.5.3 Norbornane

Owing to norbornane's tendency to nucleate on the polytetrafluoroethylene walls of the cell, substantial temperature differences were sometimes required before growth was seen on the substrate, and occasionally no crystals were seen at all. On two substrates, no crystal growth was observed on several runs; on all other substrates, crystals were seen to grow on every run. To partly address the issue, between runs the substrate was cooled to several degrees below room temperature using a chilled metal block.

The following summarises the six substrates studied:

**substrate □:** there were no defects on this substrate, however there was a single loose fragment visible in the optical microscope, from which crystals invariably grew. The fragment appeared to have detached from the surface prior to electron microscopy, as it could not be found;

**substrate ■:** despite a wealth of large step edges, nucleation on this substrate was concentrated in a couple of regions where the mica was peeling from the surface, as shown in Figure 5.23. Finding the precise nucleation sites was difficult, as these regions were not clearly visible in the optical microscope;

**substrate ○:** this substrate offered a great number of defects, including steps, overhangs, splits and badly damaged regions of mica. Nucleation occurred on a variety of these, particularly on overhangs. Figure 5.24 shows an example of an overhang and a badly damaged region of mica which acted as effective nucleation sites;

**substrate ●:** this substrate had no visible surface defects. Nucleation occurred at a single site, at a point where a small particle or feature was just visible optically. Subsequent electron microscopy located several foreign contaminants on the surface, but none could be firmly identified as being in the correct site. Out of twelve runs, only six successfully nucleated a crystal;

**substrate △:** on this substrate were low step edges, splits and pocket features. Norbornane was seen to nucleate in a region where mica flakes were peeling from the surface, and elsewhere nucleation positions corresponded to positions of pocket features. Electron micrographs of both are shown in Figure 5.25;

**substrate ▲:** this substrate was flat and featureless. Norbornane was again seen nucleating at a particular site, this time with no visible feature in the optical microscope. No feature could subsequently be found in the electron microscope. Out of twelve runs, a crystal formed on the surface only three times.



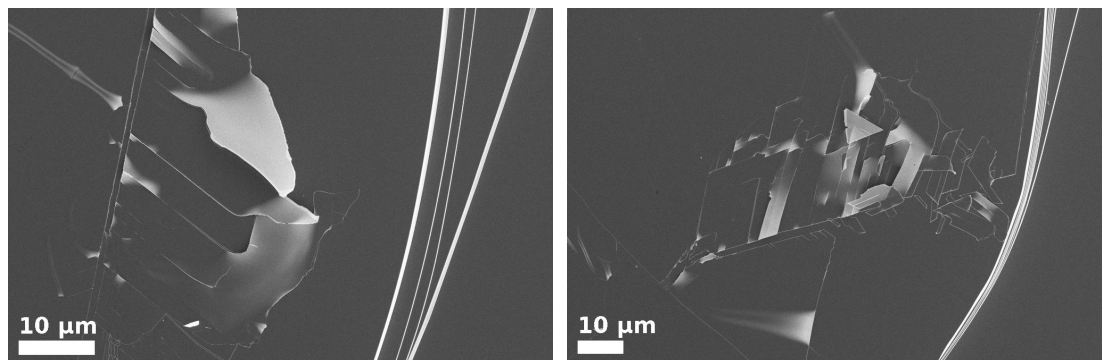


FIGURE 5.23: Electron micrographs showing regions of preferential norbornane nucleation on substrate ■.

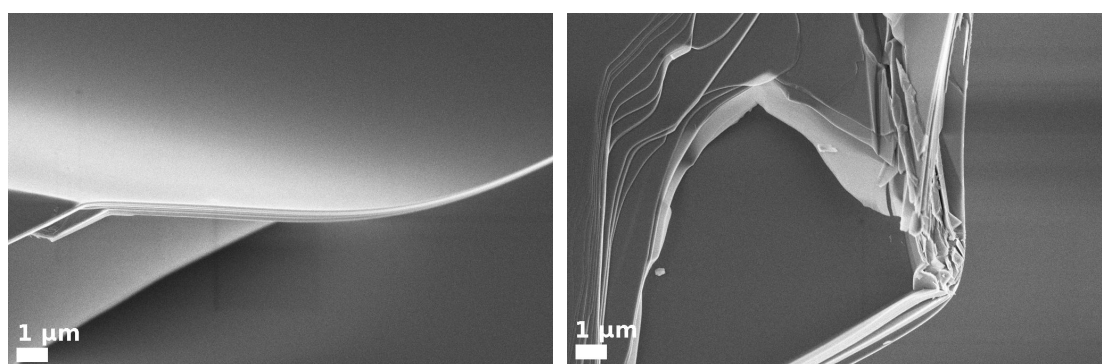


FIGURE 5.24: Electron micrographs showing norbornane nucleation sites on substrate ○: (left) step overhang; (right) badly damaged mica.

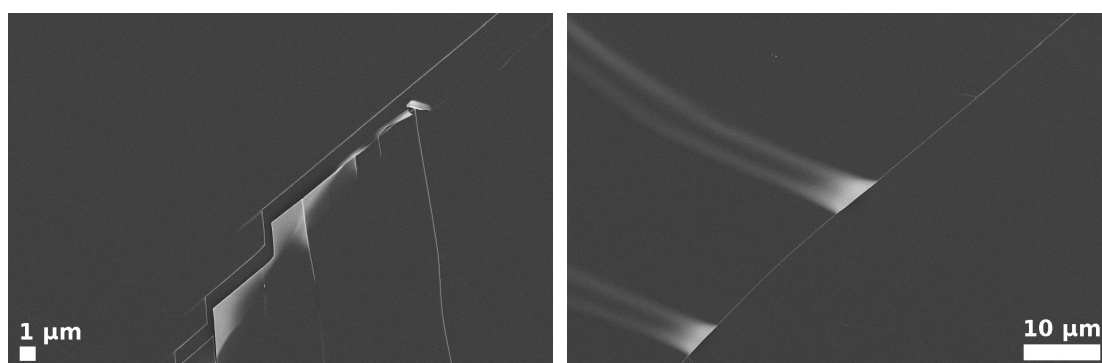


FIGURE 5.25: Electron micrographs showing norbornane nucleation sites on substrate △: (left) area with peeling mica; (right) pocket feature.

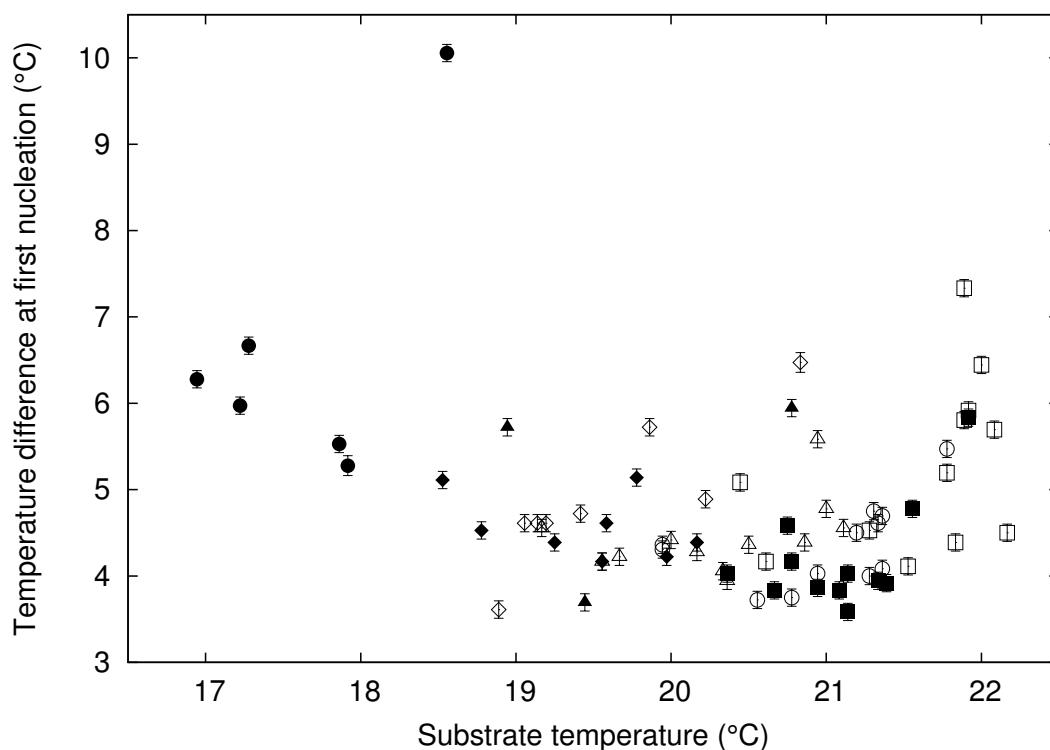


FIGURE 5.26: Graph showing temperature difference at the moment of first observed nucleation on each run of norbornane growth.

Figure 5.26 shows  $\Delta T$  at first observed nucleation as a function of substrate temperature, for all six substrates as well as substrates  $\diamond$  and  $\blacklozenge$  discussed in the next section. There are no obvious significant differences in the quantitative nucleating abilities of the surfaces, however those substrates with especially cool substrate temperatures, particularly substrate  $\bullet$ , have these because the substrate needed to be cooled further than others to enable nucleation to occur on the substrate at all.

#### 5.5.4 Hexachloroethane

The following summarises the six substrates studied:

**substrate  $\square$ :** this was a flat substrate, with a single nucleation site where there was a slight visible particle or feature on the surface. This was located in the electron microscope and identified as a loose fragment, probably a foreign contaminant;

**substrate  $\blacksquare$ :** there was a high density of features on this substrate, primarily steps with many overhangs. The overhangs provided favourable nucleation sites, but there was also some nucleation on the step edges. Figure 5.27 shows an example of each;

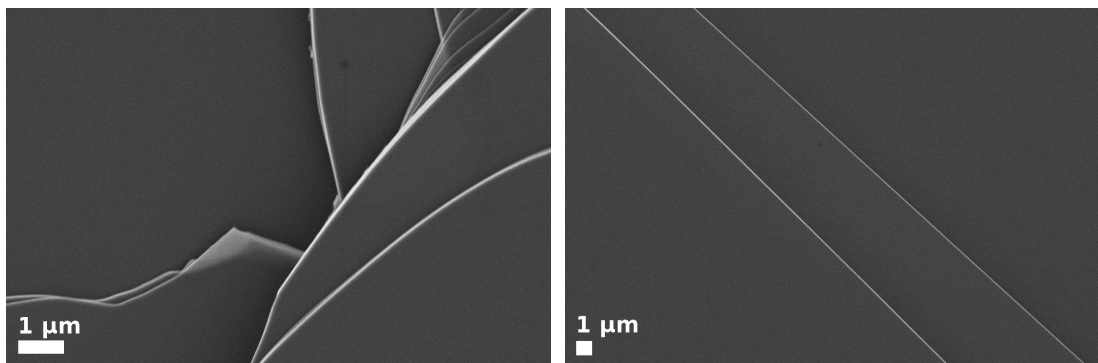


FIGURE 5.27: Electron micrographs showing hexachloroethane nucleation sites on substrate ■: (left) step overhang; (right) step edges.

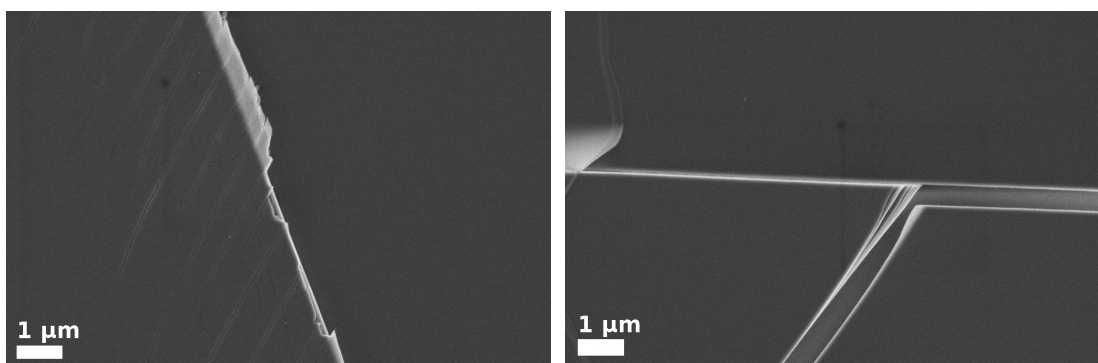


FIGURE 5.28: Electron micrographs showing hexachloroethane nucleation sites on substrate ○: (left) flaking and split step edge; (right) split in the mica surface.

**substrate ○:** alongside step edges, this substrate offered several points where the mica was flaking or split, e.g. Figure 5.28. These points were the most effective nucleation sites;

**substrate ●:** mostly, this substrate contained only step edges, with a single site where there appeared to be an overhang, shown in Figure 5.29. Nucleation occurred at this site, and also at several points along the step edges, although finding these precise spots along a uniform step edge in the electron microscope was not possible;

**substrate Δ:** this substrate had a rich variety of small-scale topographical features and very few simple features. As a result, most nucleation sites identified, such as those in Figure 5.30, could not be categorised;

**substrate ▲:** Nucleation occurred primarily on an apparently foreign contaminant, although occasionally it instead occurred on a badly broken region of mica on a nearby step edge. These are both shown in Figure 5.31.

Figure 5.32 shows  $\Delta T$  at first observed nucleation as a function of substrate temperature, for all six substrates as well as substrates ◇ and ◆ discussed in the next section. There

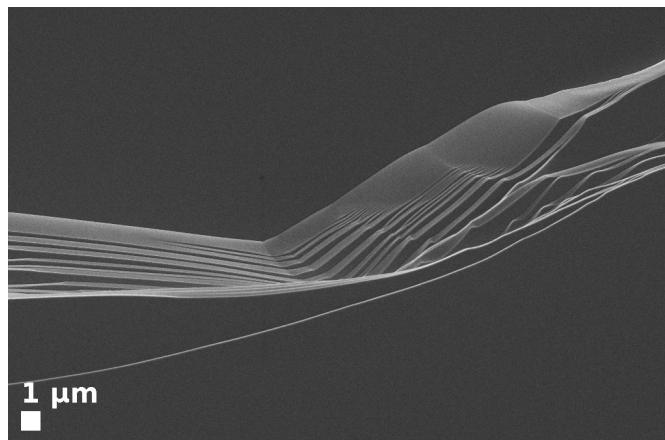


FIGURE 5.29: Electron micrograph showing overhanging steps on substrate ● preferable to hexachloroethane nucleation.

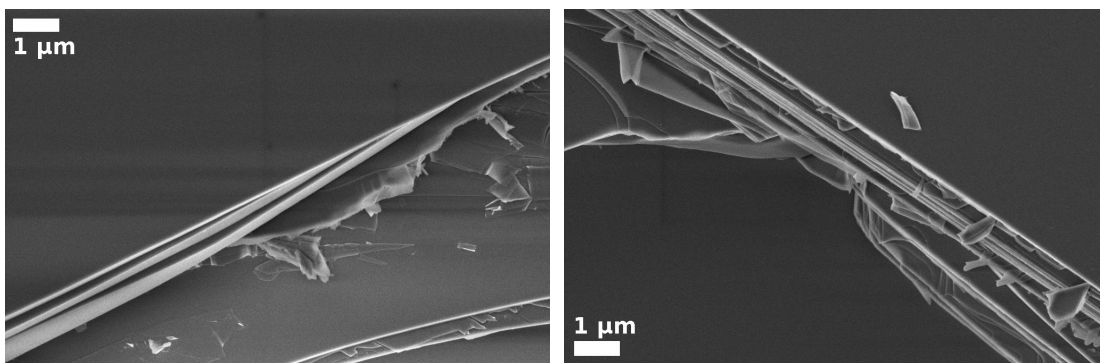


FIGURE 5.30: Electron micrographs showing uncategoryable hexachloroethane nucleation sites on substrate  $\Delta$ .

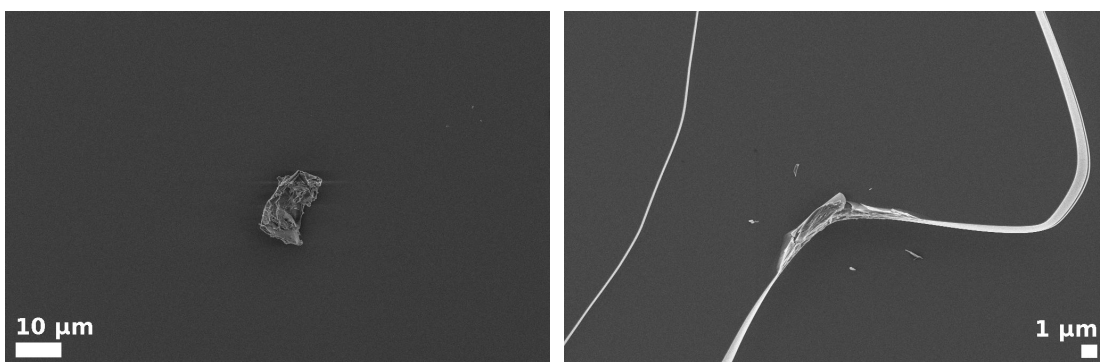


FIGURE 5.31: Electron micrographs showing hexachloroethane nucleation sites on substrate  $\blacktriangle$ : (left) foreign contaminant; (right) damaged mica on step edge.



For each compound on each substrate, five sites were selected which were found to be the most dominant: those which were most commonly host to the first or joint-first observed nucleation. There was some coincidence between sites for different compounds, with the results that fourteen sites were thus selected from each substrate for electron microscopy. Those on substrate  $\diamond$  were designated a–n, and those on substrate  $\blacklozenge$  were designated A–N.

Figures 5.33 and 5.34 show electron micrographs of each of the sites a–n and A–N respectively, alongside categorisations of each site. It may be noted that each substrate offers a wide variety of defect types.

Substrate  $\diamond$  has many pocket geometries, which were frequently popular nucleation sites, there was also one region with mica flaking away from the surface (site e). The other sites (a, b, c, f, m) all had some evidence to suggest small-scale pocket geometries; none of them were at all certain, however, and hence none were categorised as such, but the coincidence of nucleation sites with such features is suggestive.

Substrate  $\blacklozenge$ , in contrast, features only a single identified pocket geometry (site J), although site B was another ambiguous case. There were several splits on the substrate, and points of flaking/overhanging mica. Also present were points where nucleation appeared to nucleate on plain step edges (sites A, N) or away from any visible features (site L).

To compare the level of site coincidence between compounds, and thus find how dependent the preferable nucleation site geometry is on the compound, nucleation of each compound was observed at each of the sites a–n and A–N. A count was made of how many times, out of the eight runs, a crystal was seen to nucleate at that site. The results of this are presented in Figure 5.35.

It is immediately evident that there is significant coincidence of sites between the different compounds. Although all twenty-eight sites were selected on the basis of being effective at nucleating one compound, all were nucleation sites for two or more compounds, twenty-two were nucleation sites for three or more and fifteen were nucleation sites for all four.

This leads to a conclusion that, by and large, the different compounds studied have preferences for the same nucleation site geometries. However, there are differences in the distribution of sites: most likely, there must be to some extent a compound-dependence on what makes an effective nucleation site, even if the general guidelines remain the same.

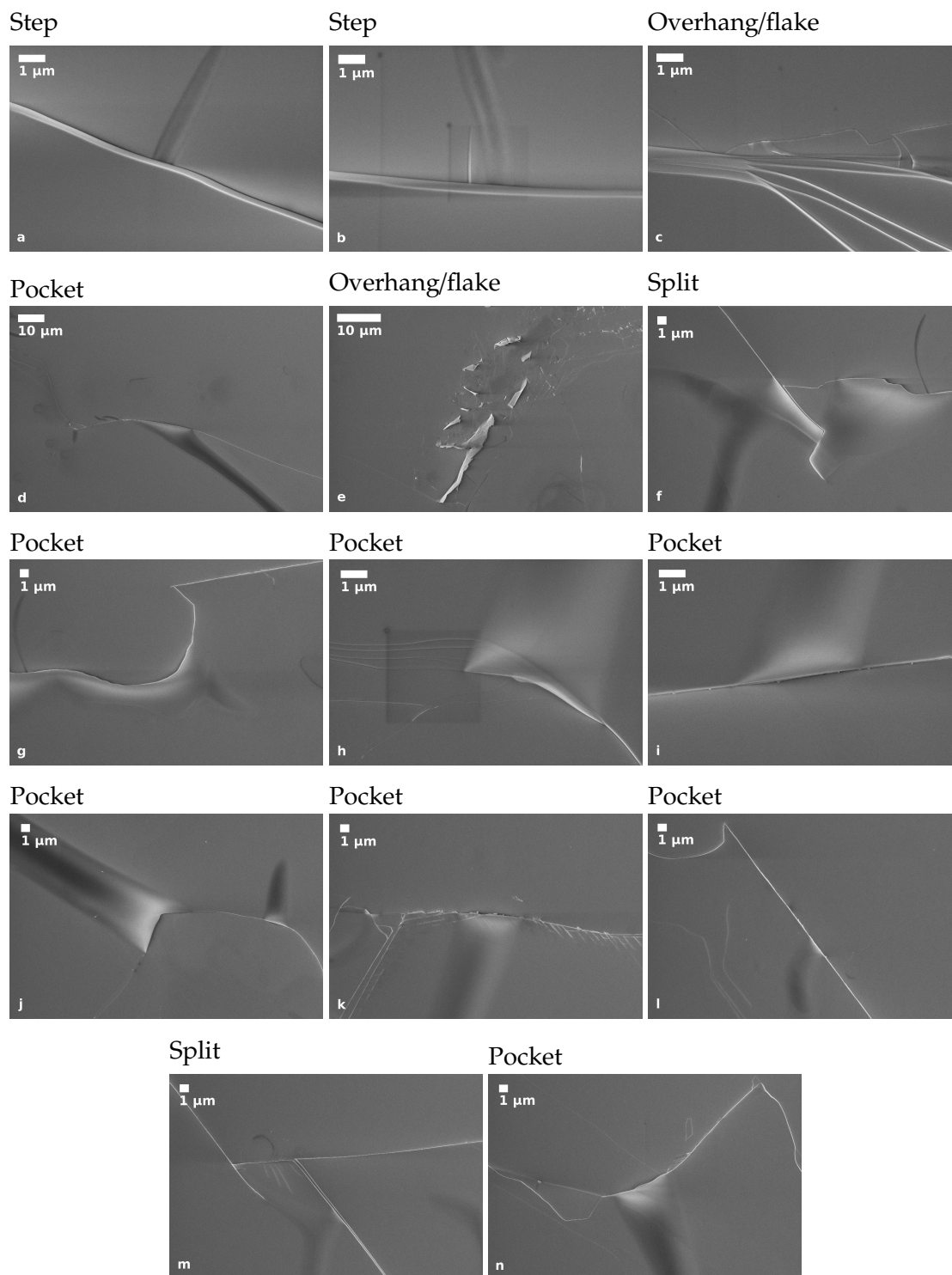


FIGURE 5.33: Scanning electron micrographs of sites a–n on substrate  $\diamond$ , with site type designations.

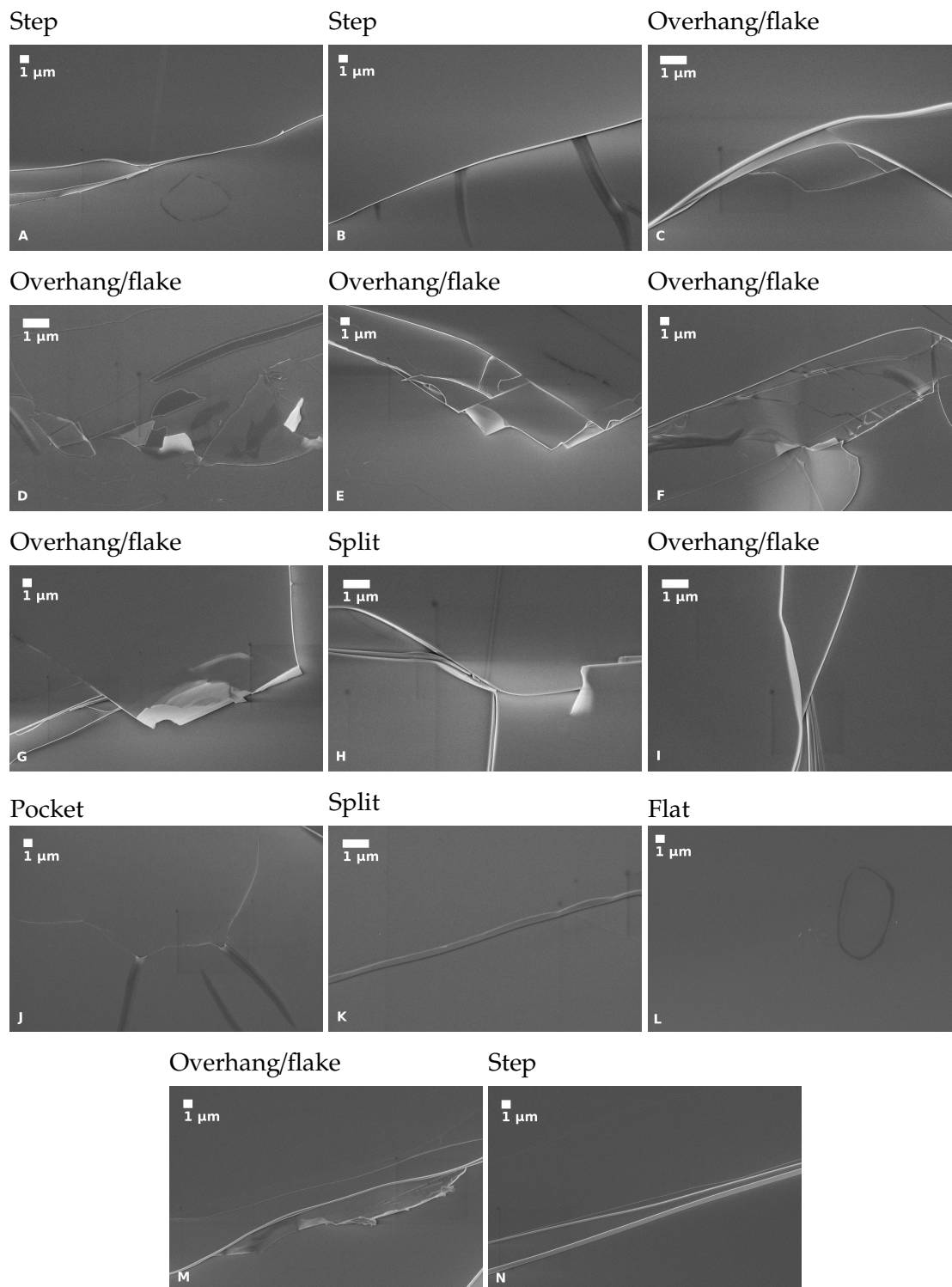


FIGURE 5.34: Scanning electron micrographs of sites A–N on substrate  $\blacklozenge$ , with site type designations.



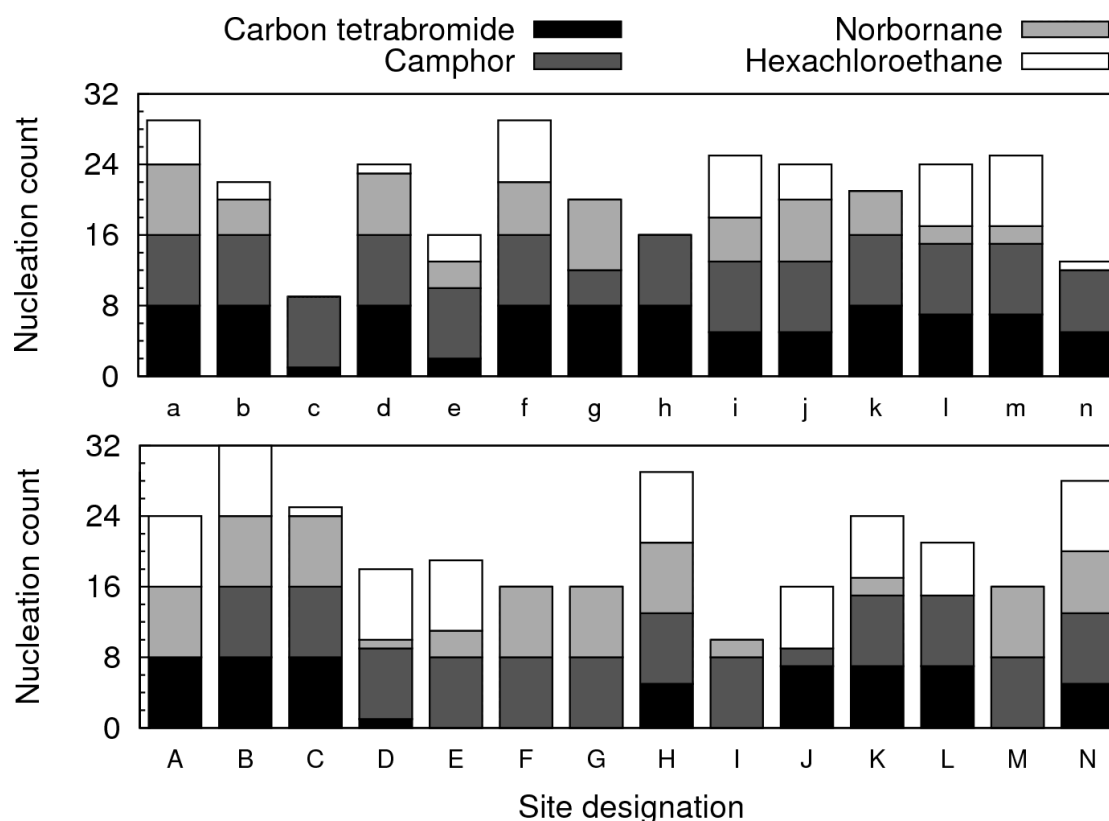


FIGURE 5.35: Graph showing the nucleation count of each compound at sites a–n on substrate  $\diamond$ , and at sites A–N on substrate  $\blacklozenge$ , out of eight experimental runs per compound per substrate.

## 5.7 Aggregated results and conclusions

Each nucleation site observed was assigned to one of the seven categories described in Section 5.4. Table 5.1 shows the results of this listed by substrate. Figure 5.36 shows the total count for each site type and compound. Note that sites on the common substrates  $\diamond$  and  $\blacklozenge$  are counted once for each compound seen to nucleate there. This graph should not be taken as being directly representative of the relative effectiveness of each site type. The distribution is strongly dependent upon the particular substrates chosen, on the means of selecting sites for study, on the number of sites studied on different types of substrate and on ambiguous site categorisations, all of which are somewhat arbitrary. It does however demonstrate one important point: there are very few nucleation sites on the flat mica, more on step edges, but most nucleation occurs on the other feature types, particularly overhangs, hanging flakes and pockets. This is precisely the reverse of the trend one would expect if nucleation was not influenced by site geometry: based only upon the occurrence frequency of the different site types across typical surfaces, one would expect most nucleation on the flat surface, much less on step edges, and much less again on all other feature types combined.

compound	substrate	flat	step	O/F	pocket	split	LF	U
carbon tetrabromide	□	0	1	2	0	1	1	1
	■	1	1	0	0	0	0	0
	○	0	0	3	0	3	0	0
	◇	0	2	2	8	2	0	0
	◆	1	3	2	1	2	0	0
camphor	□	0	0	0	4	0	0	0
	■	0	1	1	2	0	0	1
	○	0	0	0	5	0	0	0
	●	0	2	1	0	0	0	1
	△	3	0	0	0	0	0	0
	▲	0	0	2	0	0	3	0
	◇	0	2	2	8	2	0	0
	◆	1	2	7	1	2	0	0
norbornane	□	1	0	0	0	0	0	0
	■	0	0	5	1	0	0	0
	○	0	1	3	0	0	0	2
	●	1	0	0	0	0	0	0
	△	1	0	1	2	0	0	0
	▲	1	0	0	0	0	0	0
	◇	0	2	1	6	2	0	0
	◆	0	3	7	0	2	0	0
hexachloroethane	□	0	0	0	0	0	1	0
	■	0	3	3	0	0	0	0
	○	1	0	2	0	2	0	0
	●	0	4	1	0	0	0	0
	△	0	0	2	0	0	0	4
	▲	0	0	0	0	0	1	2
	◇	0	2	1	5	2	0	0
	◆	1	3	3	1	2	0	0

TABLE 5.1: Table showing the number of each site category found on each substrate by compound. O/F: overhang/flake; LF: loose fragment; U: uncharacterisable. For substrates ◇ and ◆, for each compound all sites were counted which were seen to nucleate that compound.

It may be stated safely, therefore, that nucleation on step edges is considerably preferable to nucleation on flat surfaces, and that nucleation in flake and pocket geometries, and others, is considerably preferable to nucleation on step edges. Consider also that most substrates where nucleation was observed on the flat surface offered no available defects, and that most where nucleation occurred on step edges offered no other available defect geometries.

Quantitatively, looking at Figures 5.16, 5.22, 5.26 and 5.32, results are more ambiguous. We might expect that sites offering only step and flat geometries would require higher temperature differences before nucleation occurs. Looking at Table 5.1, we find seven substrates with no defects other than step edges: carbon tetrabromide ■, camphor △, norbornane □, ● and ▲ and hexachloroethane □. We count hexachloroethane □ here

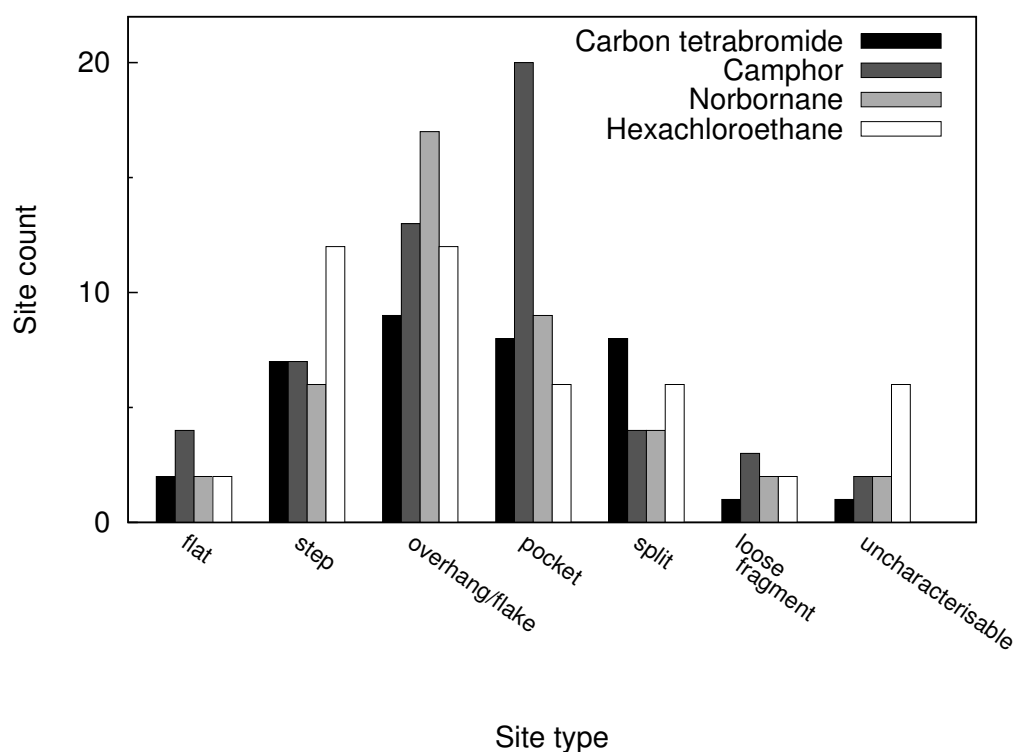


FIGURE 5.36: Graph showing the number of nucleation sites observed of each category for each compound.

despite observing nucleation on an apparently foreign contaminant; given the near impossibility of keeping surfaces perfectly clean, all surfaces must be assumed to feature some level of contamination, which sites may only become important for nucleation in the absence of favourable topographical features.

Carbon tetrabromide substrate ■ requires a significantly higher temperature difference for nucleation compared to other carbon tetrabromide substrates. Camphor △ is not significantly quantitatively different from most other camphor substrates, however it is not one of the three substrates with lower observed  $\Delta T$ . Norbornane substrate □ features an above-average  $\Delta T$ , whilst norbornane ● and ▲ were the two substrates on which no nucleation was observed on many runs. Finally, hexachloroethane substrate □ was one of only two hexachloroethane substrates to have a significantly increased  $\Delta T$ . Across all compounds, only one substrate has a  $\Delta T$  significantly higher than these seven: hexachloroethane ▲, where  $\Delta T$  was so high as to be almost certainly anomalous, either due to an improperly sealed cell or favourable nucleation sites just out of the field of view depleting the vapour.

So several feature types have been identified as being favourable to nucleation: hanging flakes and step overhangs, pockets and tunnels, splits and loose flakes. I propose that these sites share one feature in common: a highly acute geometry. Any defect featuring

a line of delamination must have a highly acute wedge geometry along this line: this includes hanging flakes, pockets and tunnels. Step overhangs are likely to offer an acute cavity underneath them, a deep yet narrow slit pore, although it is difficult to make assumptions about the exact geometry. With splits also it is hard to make assumptions about the geometry, but as Figure 5.12d shows, at least some of them feature lines of delamination. Mica flakes resting on a surface do not feature lines of delamination, but the contact point between the two surfaces may form a similarly acute wedge geometry. The mechanics of nucleation in highly acute wedges is investigated in more detail in Chapter 6.

## 5.8 Extension to ice

Similar experiments were performed to find favourable nucleation sites for ice nucleation on mica surfaces. Experiments here were performed by Hannah Pearce under my supervision. Electron micrographs were taken by both Hannah and myself.

### 5.8.1 Procedure

Experiments were performed using the second flow cell described in Section 4.4.1 and a 10× objective lens. Using the humidity control system described in Section 4.4.3, flow levels were adjusted to give an expected frost point of  $(-40 \pm 1) ^\circ\text{C}$ . This was maintained throughout the experiments.

The substrate was held at room temperature for half an hour to allow the flow humidity to reach an equilibrium. The temperature was then rapidly lowered to  $-30 ^\circ\text{C}$  and then ramped downwards at  $2.7 ^\circ\text{C}/\text{minute}$  until nucleation was observed. This was observed at recorded temperatures between  $-46.2 ^\circ\text{C}$  and  $-37.4 ^\circ\text{C}$ , however due to simultaneous concerns with both the heating of the substrate by the gas flow and intake of additional water vapour due to a leak, these numbers should not be taken as precisely representative of the saturations involved.

Seven substrates were studied, however only a single run was performed for each. Site selection and electron microscopy was performed in a similar way to that described for organic compounds. No pre-runs were performed. Unlike for the runs with organic compounds, reflected light microscopy was used, which allowed for the unambiguous identification of large overhangs and flakes through optical interference.

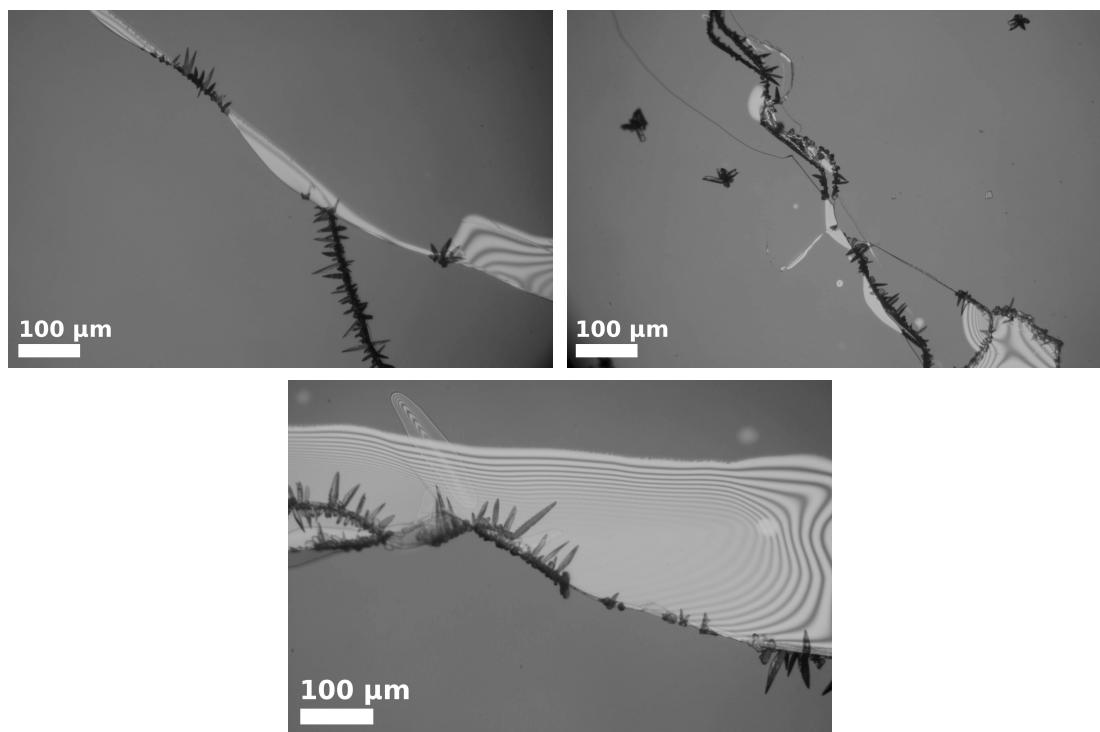


FIGURE 5.37: Optical micrographs of ice nucleation on substrates three (top left), four (top right) and six (bottom).

### 5.8.2 Results

Substrates were numbered from one to seven. On substrates three, four and six there were many defects with considerable lifting of parts of the mica away from the surface, invisible in the electron microscope but made clear by interference fringes in reflected light. Nucleation temperature was not recorded for substrate three, however nucleation was observed at  $-37.4\text{ }^{\circ}\text{C}$  and  $-38.9\text{ }^{\circ}\text{C}$  on substrates four and six respectively. All three of these substrates displayed the same behaviour: crystal growth from all along defect edges simultaneously, as shown in Figure 5.37. This is believed to be due to condensation of water along the features which then freezes: note the relatively high nucleation temperatures.

On other substrates, nucleation was seen at lower temperatures and occurring at discrete points. Substrate one featured many step edges and one region where there appeared to be a slight overhang, shown in Figure 5.38 and confirmed by reflected light microscopy. Nucleation was observed on step edges however the first nucleation at  $-46.2\text{ }^{\circ}\text{C}$  was seen at the overhang sites.

Substrate two featured many defects and many nucleation sites, including one which appeared to be a loose mica flake. Some regions, looking unremarkable in the electron microscope, nucleated many crystals; reflected light microscopy revealed the presence

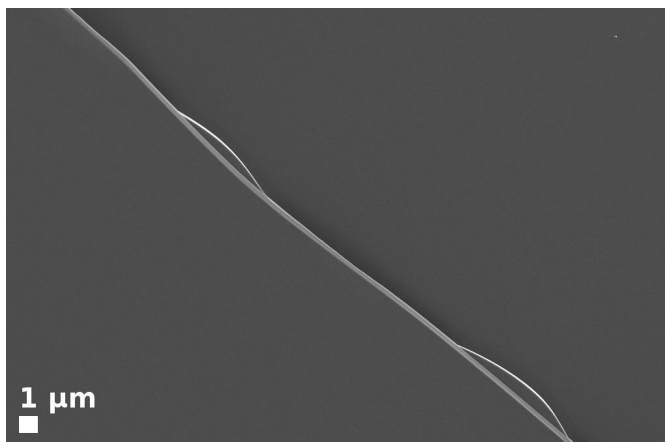


FIGURE 5.38: Electron micrograph of a nucleation site on substrate one, showing small overhanging mica edges.

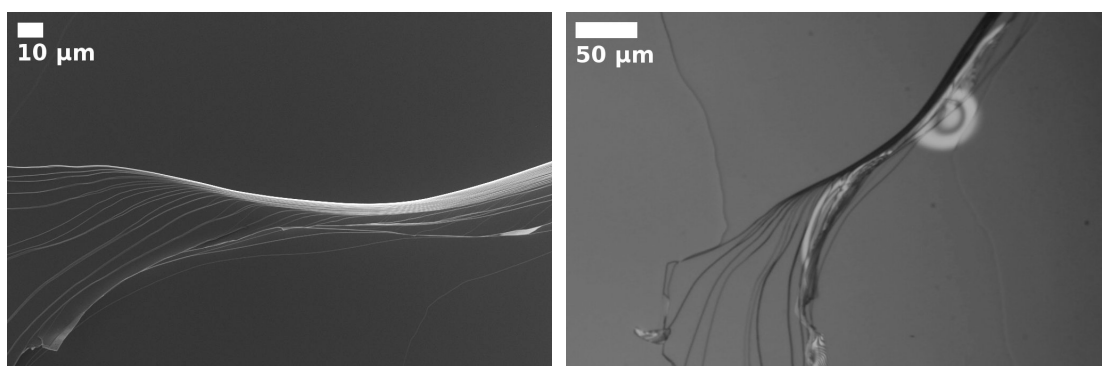


FIGURE 5.39: A region of substrate two favourable to ice nucleation: (left) electron micrograph, several crystals nucleated along the bottom edge of this feature; (right) optical micrograph, revealing mica lifting away from surface in this region.

of mica lifting away from the surface in these areas, as shown in Figure 5.39. Nucleation was observed at  $-39.5\text{ }^{\circ}\text{C}$ .

Substrate five featured a single defect with lengths of considerable overhang, as seen in reflected light microscopy. Nevertheless, the only ice nucleation at  $-41.9\text{ }^{\circ}\text{C}$  was at a point *without* visible overhang, as shown in Figure 5.40.

Substrate seven was the only one to feature pocket geometries. Figure 5.41 shows the substrate before and after ice crystal nucleation at  $-39.3\text{ }^{\circ}\text{C}$ . Several pockets can be observed, the identity of which as pocket geometries was later supported by electron microscopy. Crystal growth occurs in several small pockets, and in a large pocket, at which crystals grow from the two corners.

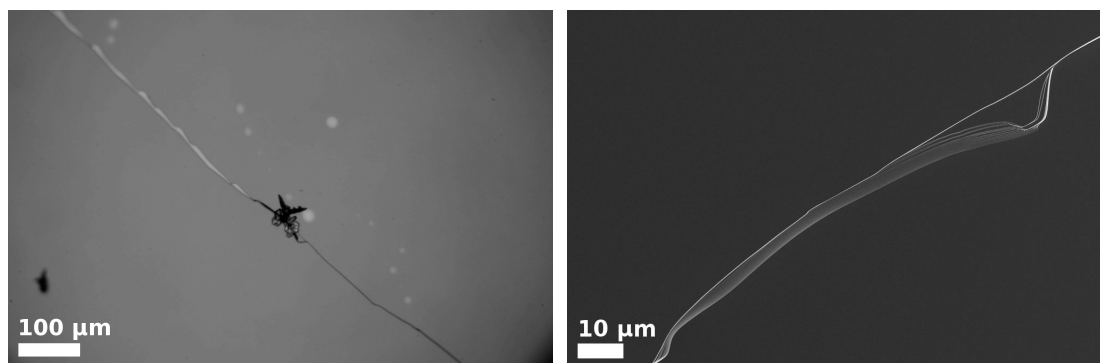


FIGURE 5.40: (Left) nucleation of ice on mica defect on substrate five, with considerable overhang visible along defect upwards and leftward of the crystal; (right) electron micrograph of nucleation site.

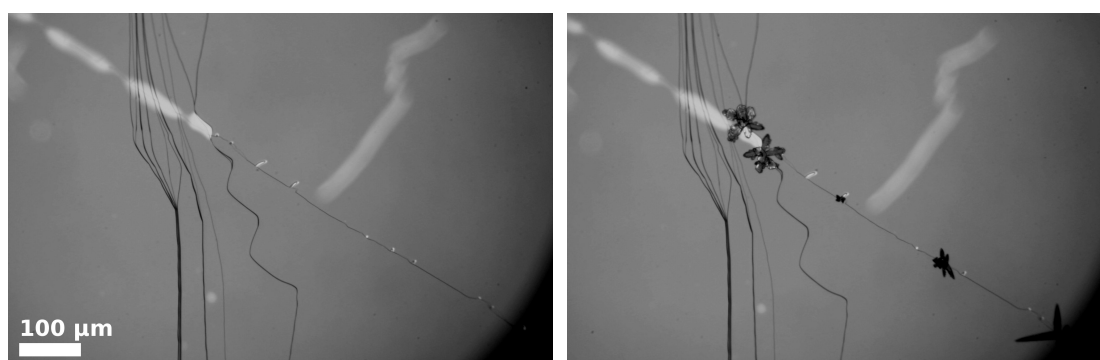


FIGURE 5.41: Optical micrographs showing substrate seven, before (left) and after (right) ice nucleation. Several pockets may be seen as bright spots along a step edge, a large pocket is present where this step edge joins the other defects.

## 5.9 Summary

Carbon tetrabromide, camphor, norbornane, hexachloroethane and ice have been grown on varied mica surfaces to identify favourable nucleation sites. In all cases crystals were not seen to nucleate randomly along defects but rather particular sites dominated nucleation across multiple runs. Electron microscopy of these favourable sites revealed that step edges, common on most substrates, were rarely effective nucleation sites, whilst sites seen to be highly effective at promoting nucleation were those offering a highly acute wedge, where two mica sheets delaminated. This tendency appears to be universal across the diverse compounds studied.





## Chapter 6

# On the nucleation of crystals from vapour in acute wedges

### 6.1 Introduction

In Chapter 5 it was demonstrated that compounds nucleating from vapour on mica surfaces prefer sites featuring acute wedge geometries. However the explanation for this remains uncertain. On one hand, we could suppose the direct nucleation of a crystal phase within a narrow wedge, which we would expect from classical nucleation theory to provide a reduced free energy barrier, as shown in Section 2.2.3. On the other hand, we could suppose the formation of a supercooled liquid capillary condensate, which could then freeze to form the crystal phase, as suggested in Section 2.3.3.

Table 6.1 shows the results of free energy barrier calculations for each of the four compounds used in the last chapter, calculated using the equations presented in Chapter 2 and the values from Table 3.1. No values for surface energies were available, so rough estimations of  $30 \text{ mJ/m}^2$  and  $10 \text{ mJ/m}^2$  were used for crystal-vapour and crystal-melt interfaces respectively. The saturations used are those typical at nucleation in the previous chapter, corrected according to the equilibrium temperature differences found in Section 4.3.3.

So, the formation of a crystal nucleus within a liquid condensate is considerably preferable to that directly from the vapour. Realistically, this means that if liquid condensates are present in the system, and they are large enough to be able to freeze, we should expect nucleation to occur via freezing of these condensates rather than directly from vapour.

compound	S	from vapour		from liquid	
		$r^*$	$\Delta G^*$	$r^*$	$\Delta G^*$
carbon tetrabromide	1.3	9.0	2500	2.7	75
camphor	1.2	21	13000	1.3	17
norbornane	1.3	10	3300	2.8	81
hexachloroethane	1.3	11	3400	0.65	4.3

TABLE 6.1: Estimated critical radius ( $r^*$ ) in nanometres and homogeneous nucleation free energy barrier ( $\Delta G^*$ ) in units of  $k_B T$  of a solid nucleus forming from a liquid and from a vapour of each compound at 22 °C, alongside the saturation (S) used in the calculations for each compound.

Note that in the cases of hexachloroethane and arguably camphor nucleating from the melt, the critical radii are far too small for classical nucleation theory to be a relevant description. Rather, these numbers should be taken as demonstrating that for these compounds, there is essentially no nucleation barrier to the freezing of a liquid.

To complicate things further, we must also consider the possibility of solid condensate: a solid phase formed in a wedge slightly below saturation; stable but unable to grow out of the wedge until a supersaturated vapour is achieved. This could arise by the freezing of a capillary condensate below saturation, or potentially by direct crystal nucleation. With this in mind, we now have four potential pathways for nucleation in a wedge:

1. direct nucleation of a crystal in supersaturated conditions, leading to immediate growth into a bulk phase;
2. formation of a supercooled liquid condensate, which freezes in supersaturated conditions and grows immediately into a bulk crystal;
3. formation of a supercooled liquid condensate, which freezes in undersaturated conditions, forming a solid condensate which grows larger than the liquid condensate but is still confined in the wedge, and does not grow out until supersaturated conditions are achieved;
4. direct formation of a solid condensate in undersaturated conditions, which remains confined in the wedge until supersaturated conditions are achieved.

Thermodynamically, in undersaturated conditions we could expect either a solid or liquid phase to nucleate in the apex of an infinitely acute wedge provided the contact angle is below 90°, which is also the criterion for the phase being stably confined in the wedge. Which will be preferable? When the condensate first forms, i.e. at the limit of zero size, the most stable phase will be that with the lowest surface energy with the wedge walls, which is likely to always be the liquid phase. Therefore we expect a supercooled liquid to form first, and the solid phase to become thermodynamically

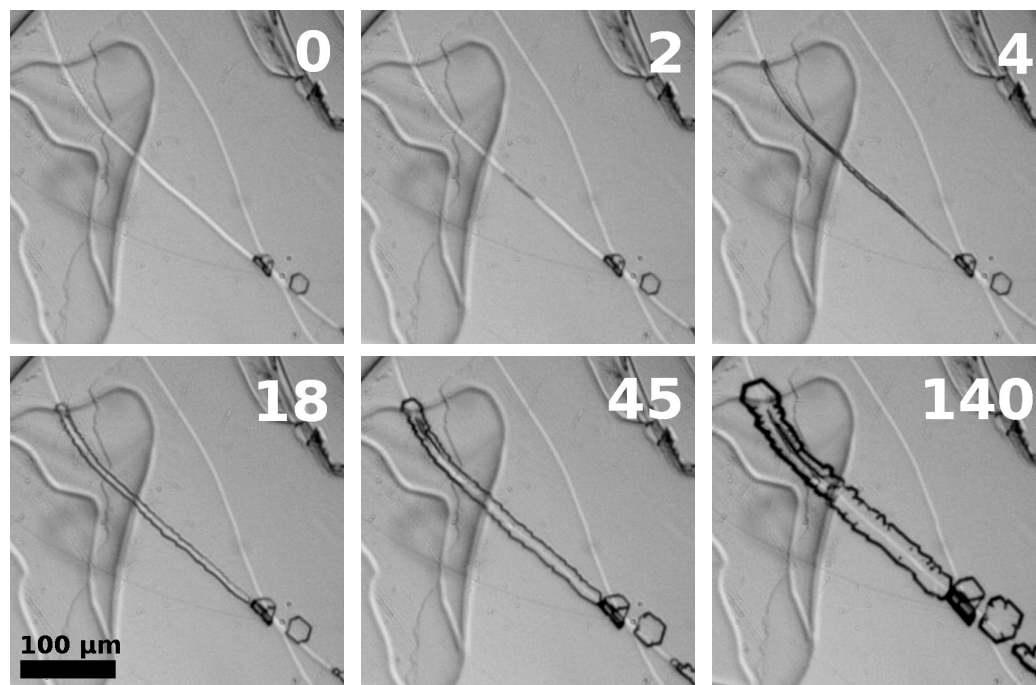


FIGURE 6.1: Time series of optical micrographs showing growth of camphor along a linear feature. The number in the top right of each image is the number of seconds since the first image.

preferable only after the condensate has passed a critical size. For camphor and hexachloroethane, this critical size is likely to be so small that there is little meaning in describing it as a solid or a liquid.

There was some suggestion from the experiments in Chapter 5 that crystals were forming via a confined condensate. Consider Figure 6.1. It shows a camphor crystal growing along a linear defect, and it is seen not to grow from a single point but from all along the feature nearly simultaneously. Similar growth was observed with carbon tetrabromide, neopentanol and ice. To explain such a phenomenon in terms of direct nucleation in supersaturated conditions, one would have to hypothesise a growth rate from the nucleation point along the feature orders of magnitude faster than that out from the feature. It seems more likely that the crystal has grown from a previously confined condensate formed along the feature.

However to make any stronger statements about the presence of confined condensates prior to bulk phases, let alone comment on their nature, it was necessary to look closer at the nucleation of crystals in acute wedges. The rest of this chapter details a series of experiments looking at high magnification at nucleation in large pocket features on mica. Thanks to optical interference phenomena, wedges may be precisely characterised, and even small condensates may be observed, and their growth quantitatively recorded.

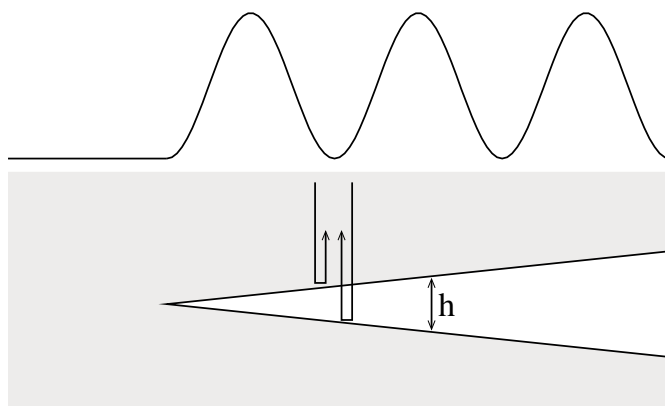


FIGURE 6.2: Illustration of an acute wedge, showing a beam of light reflecting from each surface. The curve above is the intensity profile produced.

## 6.2 Wedges, interference and condensates

An acute wedge is distinctly recognisable in reflected light microscopy by the presence of interference fringes. Figure 6.2 shows a schematic of a wedge in a sheet of mica. The light reflected back is the superposition of two waves: one reflected from the top surface, and one reflected from the bottom surface. The beam reflecting from the bottom surface is out of phase with the other one by  $\pi$  (from the reflection) plus twice the optical length of the extra distance ( $\frac{4\pi h}{\lambda}$ , where  $h$  is the height of the wedge and  $\lambda$  is the wavelength of light in the wedge-filling material). The two beams are therefore in phase when  $h$  is equal to  $\frac{\lambda}{4}$ ,  $\frac{3\lambda}{4}$ ,  $\frac{5\lambda}{4}$  and so on, leading to bright fringes.

The intensity of light  $I$  reflected from a wedge at height  $h$  can be expressed as

$$I \propto \sin^2 \frac{2\pi h}{\lambda}. \quad (6.1)$$

This can be used to calculate the height profile of a wedge from a set of fringes. Figure 6.3 shows an example of a typical large pocket feature and a magnification of interference fringes near the corner. Figure 6.4 shows a wedge profile derived from these fringes, using an intensity profile found as described in Section 6.5.

If the wedge is filled with a condensate, there will be two effects on the fringes. Firstly they will be closer spaced, as  $\lambda$  will be lowered due to the increased refractive index. But also, their intensity will be significantly lower, due to a much closer match between the refractive indices of the mica and wedge-filling material leading to reduced reflection from either surface.

If the wedge is partly filled with a condensate, as shown in Figure 6.5, the fringes will appear as for a filled wedge up to the condensate edge, then there will be a transition

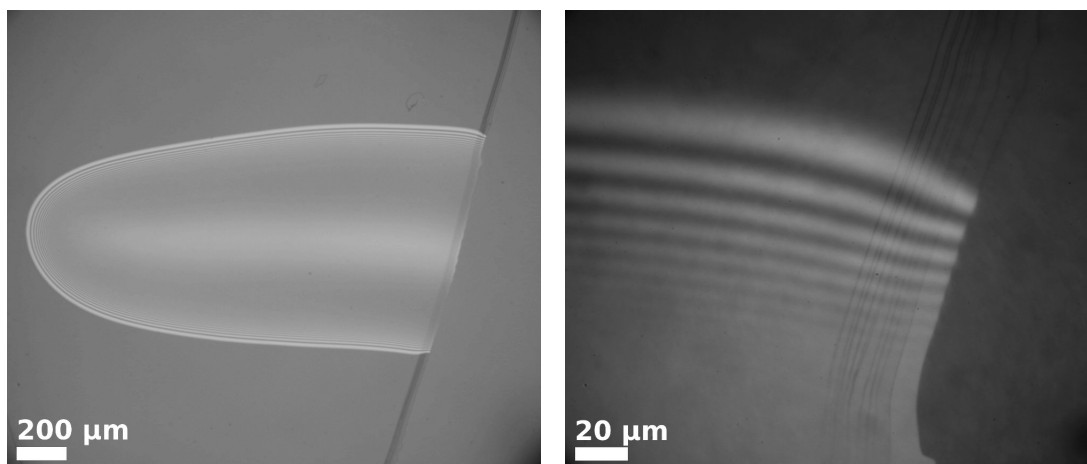


FIGURE 6.3: Optical micrographs showing (left) a large pocket feature, and (right) a high-magnification view of interference fringes at the edge of the feature, imaged in 529 nm green light.

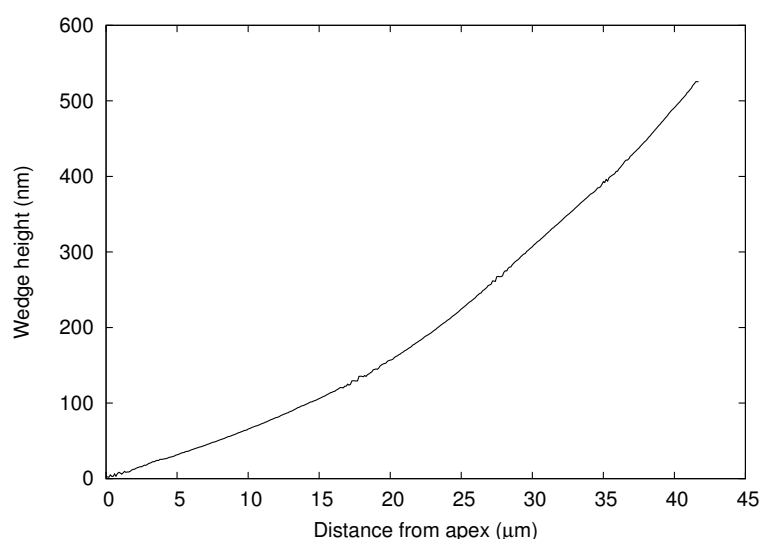


FIGURE 6.4: Graph showing calculated profile of mica wedge shown in Figure 6.3. Note that the exact position of the apex is uncertain.

to the pattern of fringes associated with an empty wedge. The intensity curve in Figure 6.5 assumes zero reflection from the condensate; this is not strictly accurate, however usually reflection from condensates was seen to be so much weaker than reflection from an empty wedge that the former contribution was negligible.

By comparing fringes for a particular wedge with fringes for the same wedge when it was known to be empty, small condensates can be detected. Often these are visible as a sharp cut-off on the last optical fringe, as shown in Figure 6.6. Smaller condensates, invisible in photographs, may still be detected by close comparison of intensity curves, which allowed condensates of heights down to about 20 nm to be accurately sized, and condensates of heights down to about 10 nm were often detectable. Section 6.5

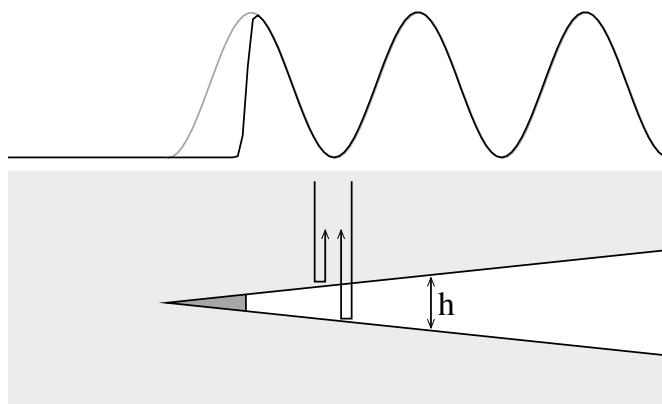


FIGURE 6.5: Illustration of an acute wedge with a small condensate, showing a beam of light reflecting from each surface. The curve above is the intensity profile produced, with the grey curve showing the curve for an empty wedge for comparison.

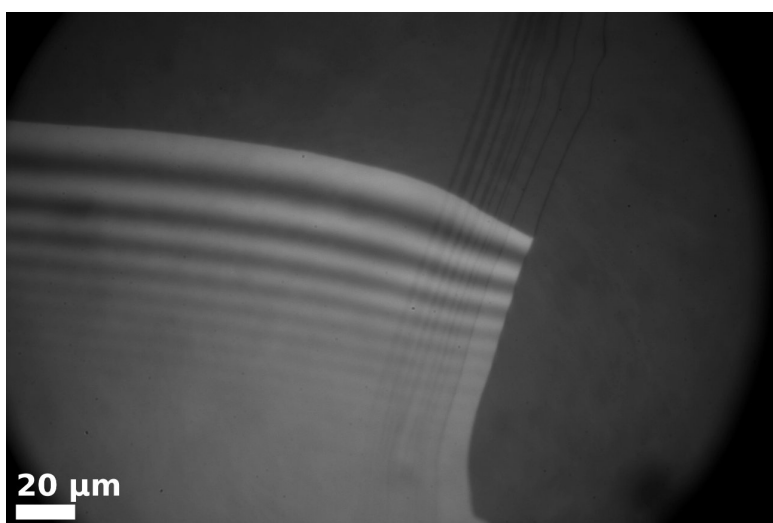


FIGURE 6.6: Optical micrograph of a mica wedge containing a condensate of norbornane. Numerical analysis of the type described in Section 6.5 found the condensate to be of height  $(95 \pm 1)$  nm.

discusses the procedures involved in more detail.

For many early tests, narrow-bandwidth 532 nm light was used. This allowed optical fringes to remain coherent up to quite large wedge heights. However, it also meant that interference effects between more highly separated pairs of surfaces such as the wedge and the top mica surface needed to be taken into account: the net effect of this was a potential offset  $\phi$  in the phase of interference, such that Equation 6.1 becomes

$$I \propto \sin^2 \left( \frac{2\pi h}{\lambda} + \phi \right). \quad (6.2)$$

This was impossible to predict and difficult to adjust for, and so larger bandwidth light with 529 nm peak emittance was used for all further tests. Equation 6.1 was found to give a good fit to intensity curves for all wedges viewed in 529 nm light. Figure 6.7



FIGURE 6.7: Optical micrograph of a mica pocket opening viewed in narrow bandwidth 532 nm light. The first fringe is dark, in direct contradiction to Equation 6.1.

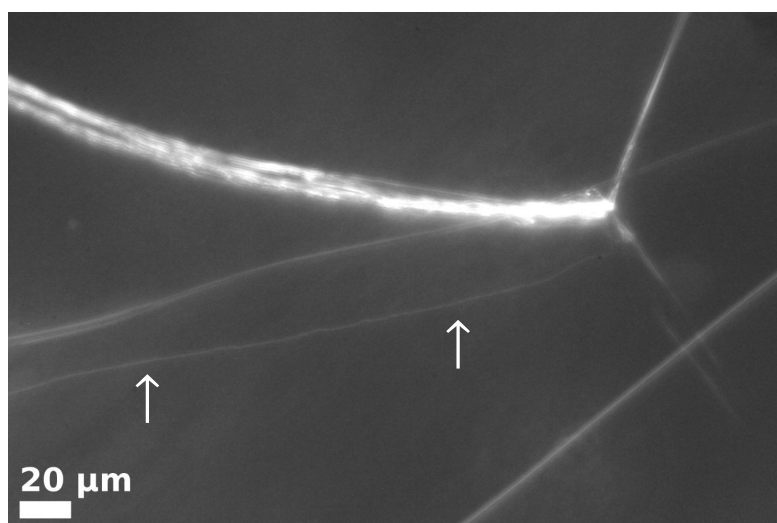


FIGURE 6.8: Darkfield optical micrograph of a wedge geometry prior to bulk growth of neopentanol. The line indicated by arrows is the edge of a small condensate along the wedge apex, and was not visible at the start of the experiment.

shows an example of a pocket viewed in 532 nm light with an exceptionally large phase offset.

Condensate interfaces were directly visible in darkfield illumination, as shown in Figure 6.8. However, this was found to be less effective at detecting very small condensates, and as interference fringes are not visible in darkfield there was no way to estimate their size.

## 6.3 General results

Large pocket features were located on freshly cleaved mica surfaces by eye and sealed within the sublimation cell described in Section 4.3.1. Features were chosen with a clear and simple geometry, well separated from other surface features.

After flushing the cell with nitrogen gas the temperature of the base was ramped upwards until bulk crystallisation was observed. Photographs were taken periodically using reflected light.

Many compounds were seen to grow from the pocket features. Across all compounds, crystals grew in a distinctive pattern from the two corners of the pocket, the points where the wedge apex intersects the edge of the feature. Six examples of this for different compounds are shown in Figure 6.9.

In all cases where growth in this manner was observed, it was also noted that there is visible but more limited crystal growth along the whole line of the wedge. This is consistent with growth from a condensate spanning the whole length of the wedge: in supersaturated conditions it grows outwards from all points at once, but only slowly, as diffusion into the pocket features is likely to be highly limited. At the very edges of the pocket, however, there is no barrier to diffusion and large crystals quickly grow from the two ends of the condensate.

### 6.3.1 General observations by compound

Two substrates with mica pockets were chosen for the study of neopentanol, camphor and hexachloroethane in wedges. For each wedge, three experimental runs were performed with each compound, the cell being cleaned between compounds. The cell base temperature was ramped upwards at a rate of 0.5 °C/minute, and observations made at one corner of the feature.

The first was seen to nucleate all three compounds on all three runs, each time with crystals growing from the intersection of the pocket edge and the wedge apex. The second pocket was seen to nucleate hexachloroethane on all three runs in the same manner. Camphor nucleated twice in the usual manner however on the first run nucleation occurred on the neighbouring step edge and not in the pocket. Neopentanol did not nucleate at all in this pocket.

The results of nucleation in the first pocket illustrate some of the distinctive features of the growth of each of the three compounds in wedges. Figure 6.10 shows the



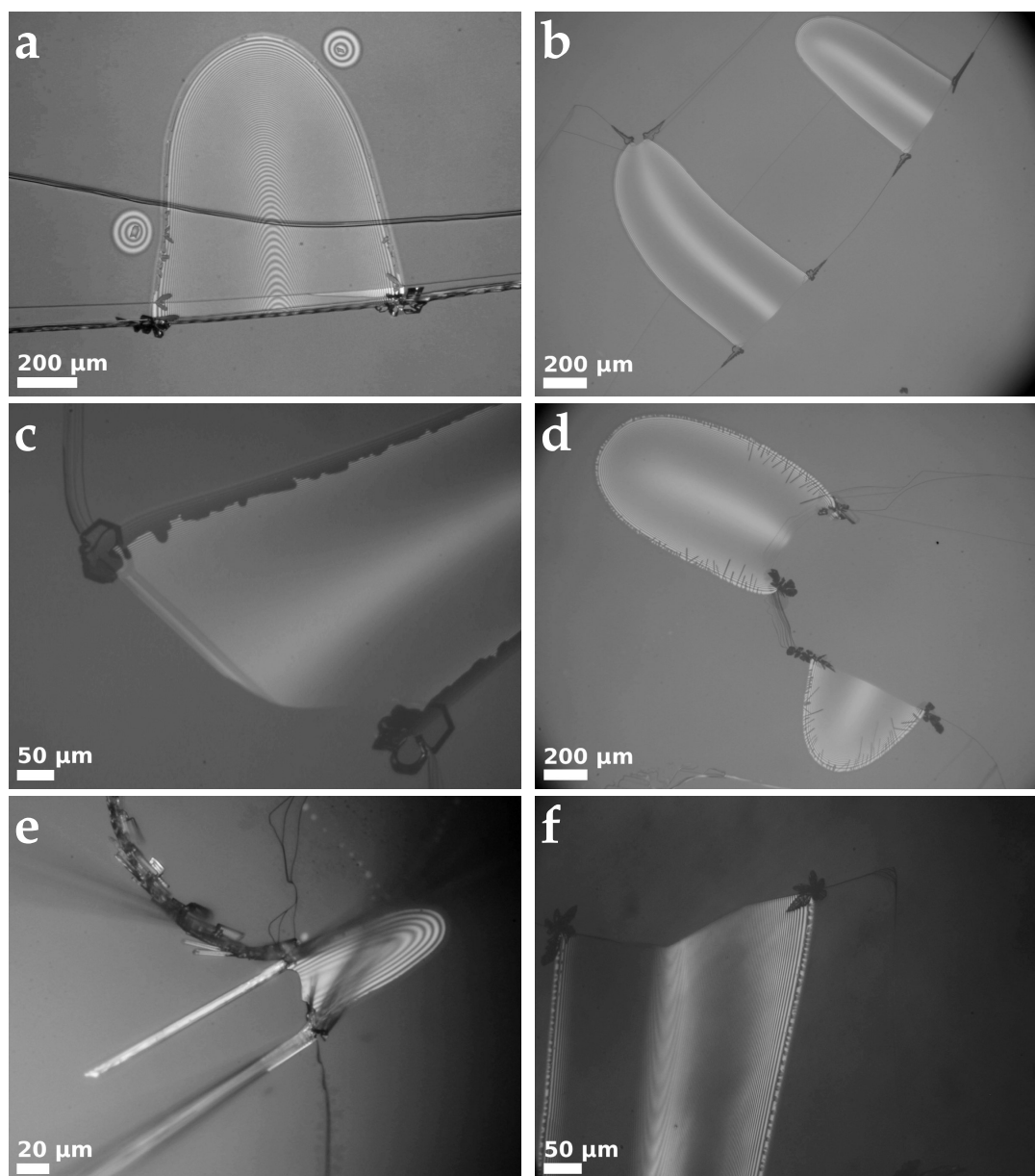


FIGURE 6.9: Optical micrographs showing crystals grown from vapour in mica pockets: (a) carbon tetrabromide; (b) camphor; (c) norbornane; (d) hexachloroethane; (e) naphthalene; (f) ice.

nucleation of hexachloroethane. Crystallisation is first observed at the pocket corner, with a low uniform condensate becoming visible roughly simultaneously. After bulk crystallisation has begun, this condensate grows as a series of needles.

For camphor growth, as shown in Figure 6.11, a condensate is visible prior to bulk crystal growth. This initially appears as a smooth line, but as it grows it takes on a slightly faceted appearance. After bulk crystal growth the condensate becomes much larger and the faceting much more distinct. Note that the pocket in Figure 6.11 is the same as that in Figure 6.10, but the pocket has translated slightly along the step edge.

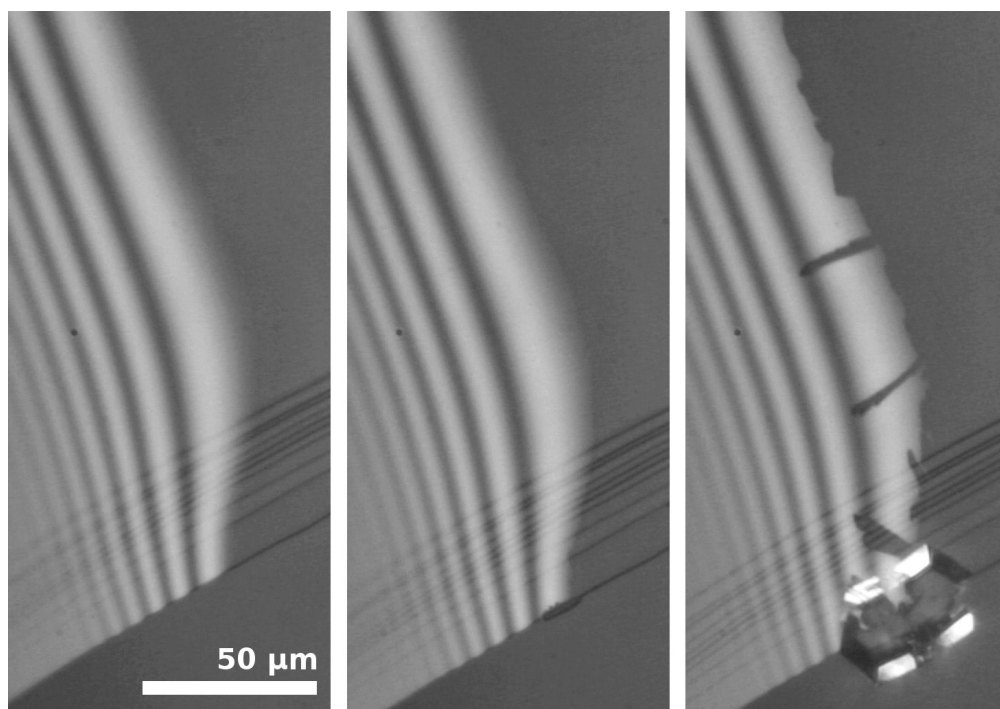


FIGURE 6.10: Time sequence of optical micrographs showing hexachloroethane nucleation in the corner of a mica pocket during a temperature ramp of  $0.5\text{ }^{\circ}\text{C}/\text{minute}$ .

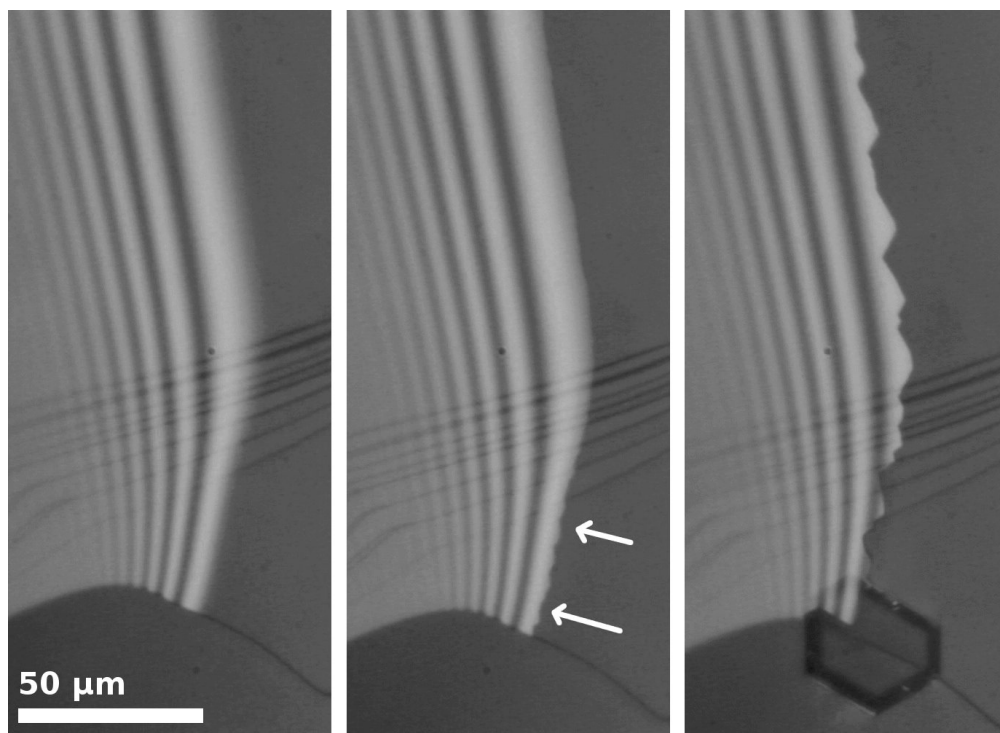


FIGURE 6.11: Time sequence of optical micrographs showing camphor nucleation in the corner of a mica pocket during a temperature ramp of  $0.5\text{ }^{\circ}\text{C}/\text{minute}$ . The arrows indicate evidence of a slightly faceted condensate prior to growth of the bulk crystal.

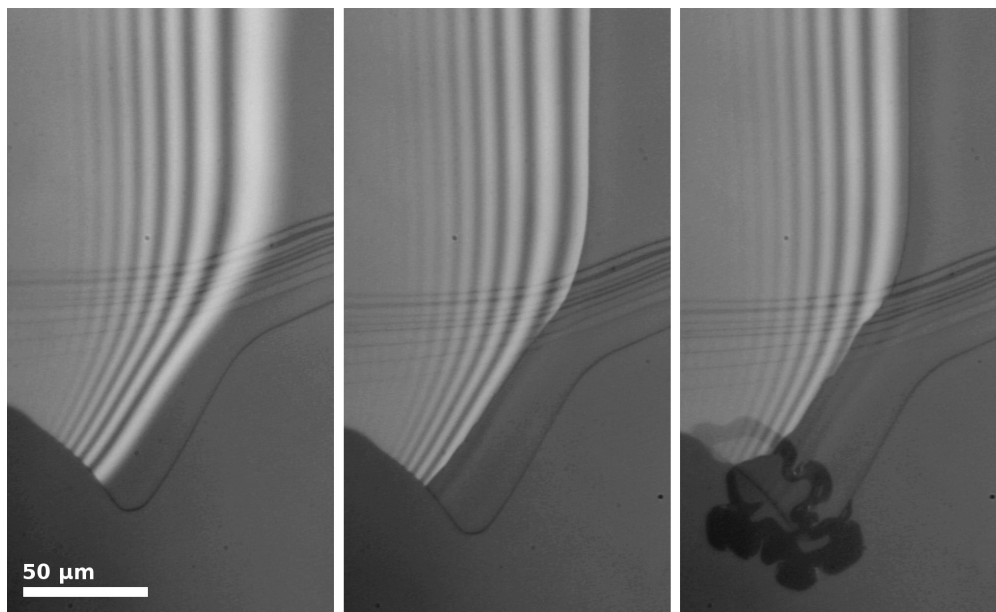


FIGURE 6.12: Time sequence of optical micrographs showing neopentanol nucleation in the corner of a mica pocket during a temperature ramp of 0.5 °C/minute.

Figure 6.12 shows neopentanol nucleation in the same pocket. Here it can be seen that a large condensate forms prior to bulk crystallisation. Initially the interface is a smooth line running parallel to the fringes, however it soon becomes much thicker nearer the pocket edge than further in, and starts to take on a slightly non-smooth interface prior to the emergence of a bulk crystal.

These results are generally typical for growth of these compounds observed in other pockets. Neopentanol was sometimes seen to form much larger condensates before the emergence of a bulk crystal, and sometimes much smaller, but generally large enough to obscure the first interference fringe. Hexachloroethane was usually seen to grow needles along apex lines, without any visible condensate prior to emergence of the bulk crystal. Needle growth was always seen to begin approximately simultaneously with emergence. Hexachloroethane has rarely been observed to grow with a small condensate visible prior to emergence, and no needle growth. Figure 6.13 shows examples.

Large norbornane condensates were seen prior to bulk growth, often obscuring one or more fringes completely, as shown in Figure 6.14. As with camphor and neopentanol, the condensate is seen to grow first with a smooth interface parallel to the fringes, and then to grow thicker nearer the pocket edge and simultaneously to begin to take on a non-smooth interface.

Carbon tetrabromide was only observed growing from a wedge at high magnification once: crystals grew from wedge corners as with other compounds. No condensate was

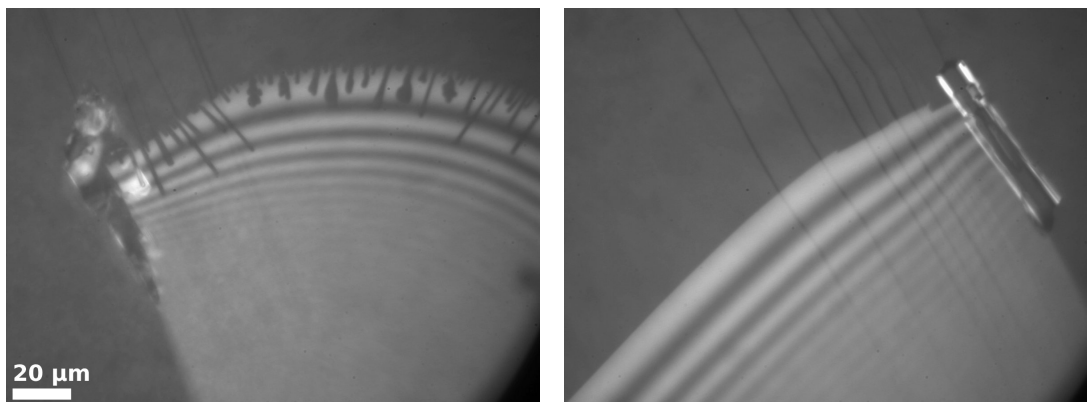


FIGURE 6.13: Optical micrographs showing hexachloroethane grown in two mica pockets, each in similar conditions at a ramp rate of  $0.5\text{ }^{\circ}\text{C}/\text{minute}$ .

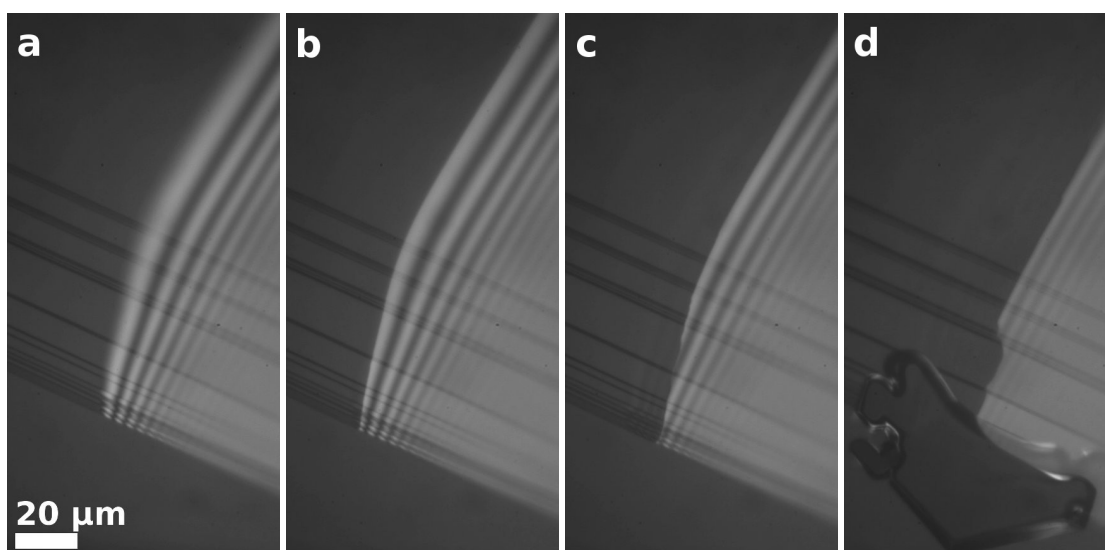


FIGURE 6.14: Time sequence of optical micrographs showing norbornane nucleation in the corner of a mica pocket during a temperature ramp of  $0.5\text{ }^{\circ}\text{C}/\text{minute}$ .

visible prior to bulk growth, but one was seen to grow rapidly along the line of the wedge appearing simultaneously with the bulk crystal at the edge.

Naphthalene has been seen growing from a mica pocket at temperatures below  $0\text{ }^{\circ}\text{C}$ , in the distinctive formation of crystals radiating from the two corners with visible growth along the line of the wedge. However this was seen only after the crystals had formed, and several attempts to observe the growth process met with no success. With both hexamethylcyclotrisiloxane at room temperature and menthol below  $0\text{ }^{\circ}\text{C}$ , crystal growth was seen to originate elsewhere on the substrate than from the observed mica wedge, although as only one attempt was made with each this may not be significant.

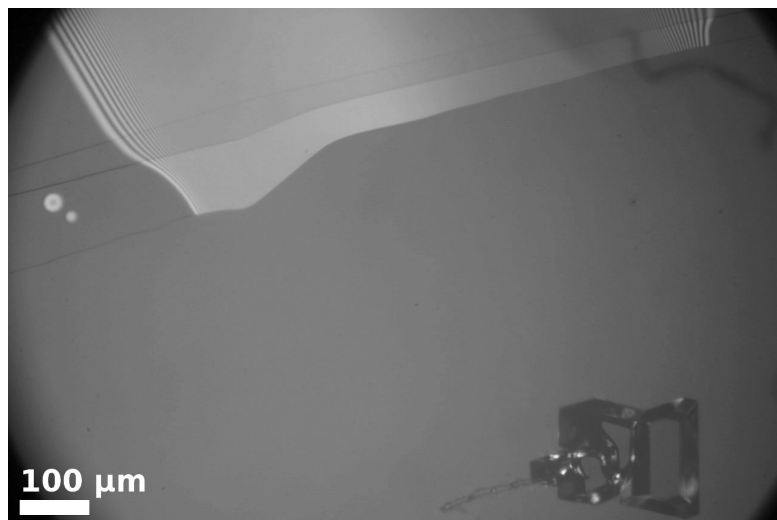


FIGURE 6.15: Optical micrograph showing norbornane crystal growing from a scratch in preference to a mica pocket.

### 6.3.2 Miscellaneous results

With regards to the orientation of crystals, it was noticed that there was no correlation between the orientation of a crystal growing from one edge of a pocket and that growing at the other. In other words, the system of two crystals and its connecting condensate is not a single crystal. No correlation was seen in the orientation of crystals growing from a single pocket corner across multiple runs, indicating that the orientation is not directed by the geometry.

Three substrates were prepared featuring a large pocket geometry, outside the mouth of which had been placed a small scratch made with the tip of a needle. One substrate was used for the crystallisation of each of camphor, norbornane and hexachloroethane, with three consecutive runs performed for each compound at a ramp rate of  $0.2\text{ }^{\circ}\text{C}/\text{minute}$ . With camphor and hexachloroethane, crystals were seen to grow from the scratch simultaneously with the emergence of crystals from the pocket corners. With norbornane, on every run crystals grew from the scratch to the complete exclusion of crystallisation from the pocket, as shown in Figure 6.15. Indeed, no condensate was observed in the wedge at all.

An experiment was performed to find if the observed temperature difference at crystal emergence was required, or if it was merely an artifact of time-consuming wedge-filling kinetics. Using norbornane and camphor, a run was performed with a ramp of  $0.2\text{ }^{\circ}\text{C}/\text{minute}$  until crystals were observed. After cooling and flushing the cell, another run was performed where the temperature difference was ramped up to a value considerably below that required for the first run and held there indefinitely. Norbornane, which produced crystals at a difference of  $1.6\text{ }^{\circ}\text{C}$  on its first run, was held

at 0.6 °C. Camphor, which produced crystals at a difference of 3.4 °C on its first run, was held at 1.2 °C. After two hours, both had developed visible condensates but neither had grown bulk crystals. Further increase of  $\Delta T$  led to emergence of bulk crystals. A test similar to those described in Section 4.3.3 was performed to find the equilibrium  $\Delta T$  for these crystals: that for norbornane was found to be  $0.7 \pm 0.1$  °C, and that for camphor  $2.3 \pm 0.1$  °C.

## 6.4 Repeatability

It was desired to know if the process of crystal growth from pockets is a stochastic process, as might be expected if it were limited by nucleation, or if it is not, as might be expected if it were limited by e.g. the growth rate of a condensate. I.e., does the process proceed immediately and predictably in a given supersaturation or does it take some random length of time determined by the overcoming of some nucleation barrier? To study this, repeated runs were performed at mica pockets. For each run,  $\Delta T$  was noted at the time of first emergence of a bulk crystal from the pocket edge. Whether or not the  $\Delta T$  was consistent between runs should provide information on whether or not the process is nucleation-limited.

In addition, it was desired to know the extent to which particular pocket geometries influenced the process. To this end, repeat runs were performed at multiple pockets for each compound, and compared to see whether or not there was a consistent  $\Delta T$  at bulk emergence between different pockets.

Three pockets were used for each compound, not counting any substrates where no nucleation was observed in the pocket, and six runs were performed for each. Between each run the cell base was cooled and the cell flushed as in Chapter 5. A ramp rate of 0.2 °C/minute was used.

### 6.4.1 Camphor

Three camphor pockets were studied and crystals were seen to form on each run from each pocket. Figure 6.16 shows the temperature difference at bulk emergence for each run. It can be seen that there is no significant variation between runs, or between pockets. The temperature differences are close to the value of  $2.9 \pm 0.1$  °C found in Section 4.3.3 for the temperature difference at saturation. This is suggestive of kinetically limited growth.

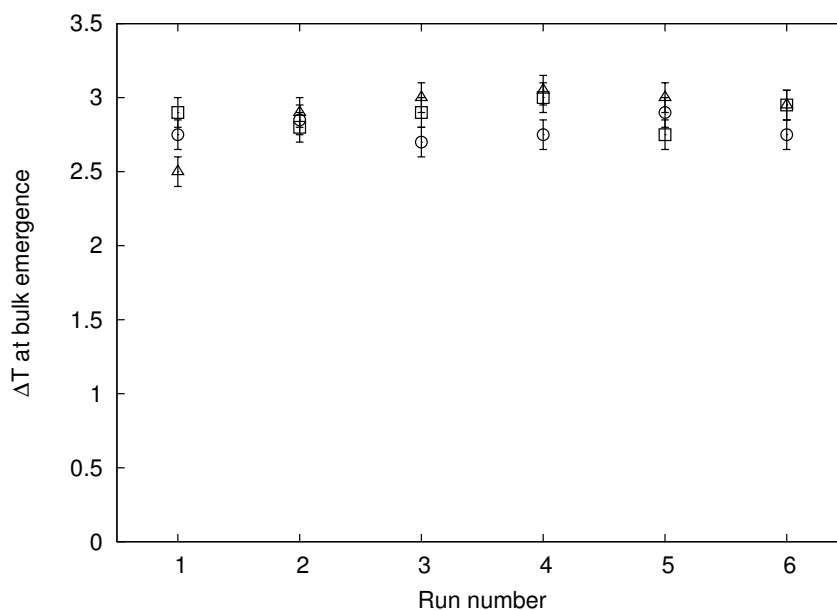


FIGURE 6.16: Graph showing  $\Delta T$  at observed bulk emergence of camphor crystals from three mica pockets ( $\square$ ,  $\circ$  and  $\triangle$ ) for six repeated runs.

#### 6.4.2 Hexachloroethane

Figure 6.17 shows similarly measured temperature differences for hexachloroethane. Crystals were seen to grow from the pocket corners on each run for all three pockets, however another pocket was studied which did not nucleate crystals (probably due to the presence of a nearby pocket which did). Although there is no significant variation between runs for each pocket, there is a large variation between pockets. In all cases the temperature difference is above the value of  $1.2 \pm 0.3$  °C found in Section 4.3.3.

#### 6.4.3 Norbornane

Eight pockets were observed before three were seen to nucleate norbornane. The temperature differences are shown in Figure 6.18. It may be seen that a considerably higher temperature difference was required on the first run than on subsequent runs, and that there was no significant variation between pockets or between runs after the first. Temperature differences are considerably higher than the value of  $0.3 \pm 0.1$  °C found in Section 4.3.3.

It is hypothesised that the increased temperature difference at emergence on the first run results from temperature gradients within the cell. The cell is sealed within a laminar flow cabinet in a cool room, and then transferred to a warmer room for the experiment. The thin mica substrate is likely to adjust to the new temperature much quicker than the thick cell walls, so if the cell has not equilibrated then the walls may be somewhat cooler

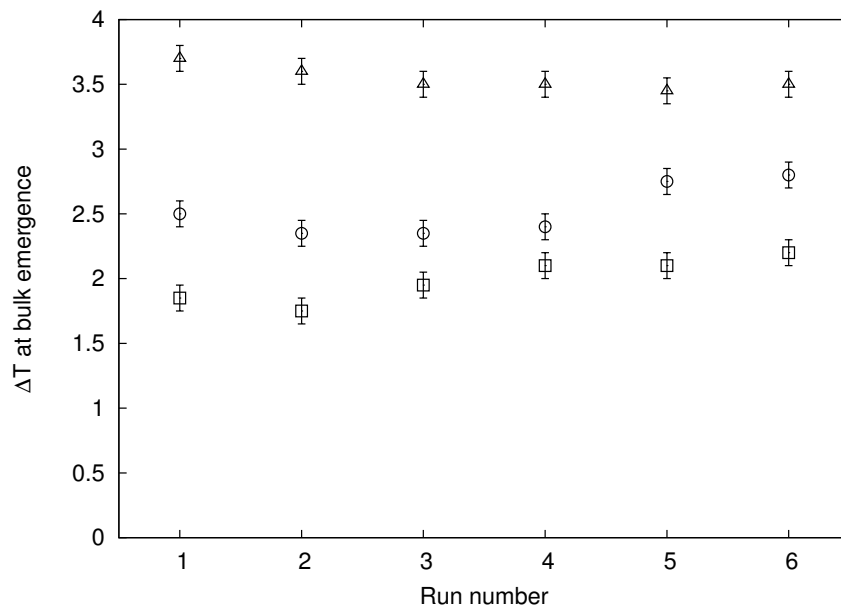


FIGURE 6.17: Graph showing  $\Delta T$  at observed bulk emergence of hexachloroethane crystals from three mica pockets ( $\square$ ,  $\circ$  and  $\triangle$ ) for six repeated runs.

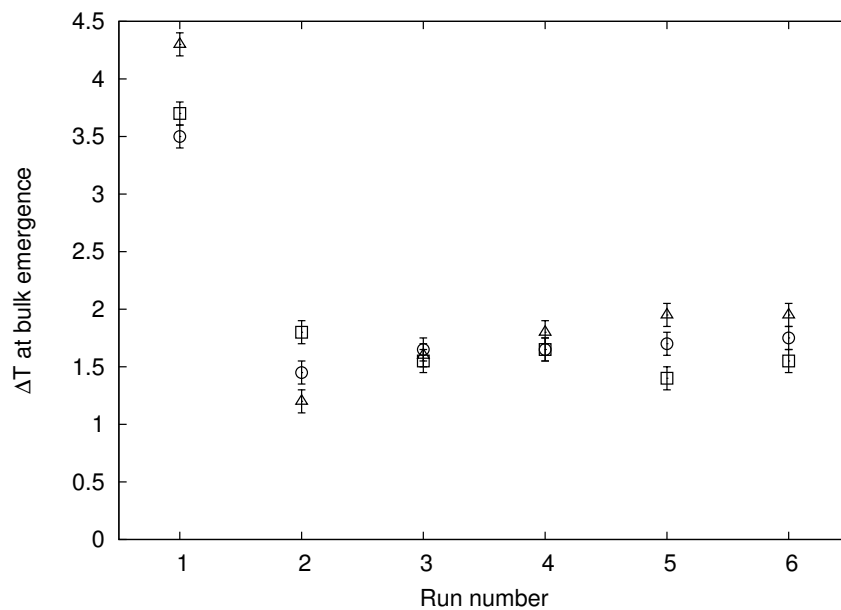


FIGURE 6.18: Graph showing  $\Delta T$  at observed bulk emergence of norbornane crystals from three mica pockets ( $\square$ ,  $\circ$  and  $\triangle$ ) for six repeated runs.



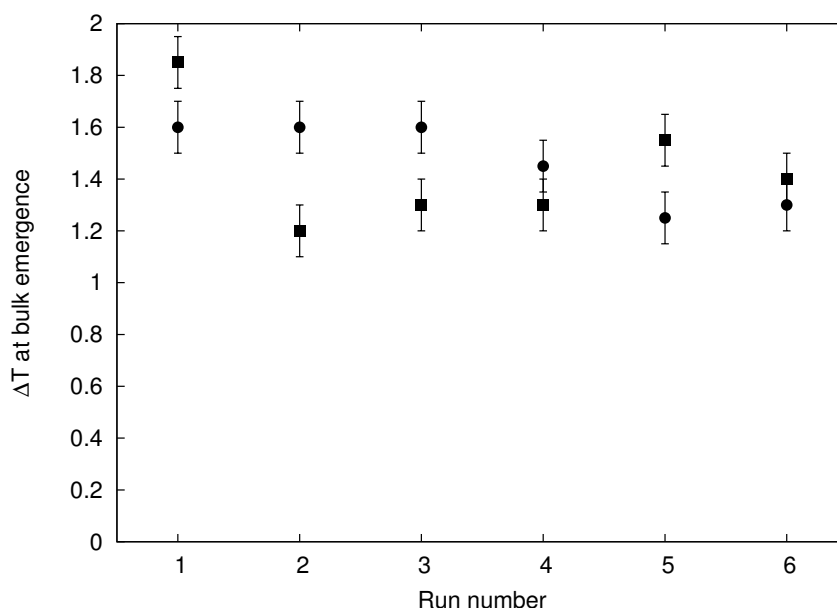


FIGURE 6.19: Graph showing  $\Delta T$  at observed bulk emergence of norbornane crystals from two mica pockets (■, ●) for six repeated runs following equilibration.

than the substrate. As norbornane, unlike the other compounds, tends to nucleate on polytetrafluoroethylene, it is likely to preferentially nucleate on the cooler walls and deplete the vapour over the substrate. After the first experimental run, the cell is likely to be much closer to equilibrium. This may also explain the high occurrence of pockets which did not appear to promote norbornane nucleation.

To test this hypothesis, the experiment was repeated on two further pockets, each of which was left to equilibrate in the warmer room for an hour prior to the first run. Crystals were seen to form from both pockets on each run, and the results are shown in Figure 6.19. It may be seen that the discrepancy between the first and subsequent runs has largely disappeared.

#### 6.4.4 Pocket geometries

Table 6.2 characterises the geometry of each pocket used in this section. The length is the length of the line of delamination curving from one corner of the pocket to the other. The width is the linear distance between the two pocket corners. The angle is an estimation of the wedge angle calculated from the distance between the first two interference fringes.

compound	substrate	length (mm)	width (mm)	angle (°)
camphor	□	1.0	0.36	1.6
	○	3.0	0.24	1.7
	△	2.3	0.33	1.7
hexachloroethane	□	5.9	0.41	1.6
	○	0.55	0.24	1.4
	△	2.5	0.64	1.2
norbornane	□	4.4	0.93	0.93
	○	2.8	0.50	2.3
	△	4.2	1.1	0.83
	■	5.3	0.40	1.1
	●	8.2	0.64	1.0

TABLE 6.2: Table categorising the mica pockets used for repeat crystallisation runs of each compound.

## 6.5 Condensate size analysis

It was desired to quantitatively study the growth of condensates prior to bulk crystal formation, i.e. to plot the condensate height as a function of  $\Delta T$ .

High resolution, high bit depth images were taken of fringes at the edges of pockets using a 40× objective. These images contained significant amounts of random noise, so to obtain smooth curves it was required to average a large number of pixels.

A path was chosen running perpendicular across the fringes, and this path divided into a large number of rectangular regions, each one long parallel to the fringes (typically a few hundred pixels) but short perpendicular to them (typically two pixels or 100 nm, below the optical resolution limit), as shown in Figure 6.20. Each rectangular region provided a single data point on the curve, with the intensity found from the mean green value of the many hundreds of pixels, and the error from the error on this mean, i.e. the standard deviation divided by the square root of the number of pixels.

Images of flat, featureless mica are not themselves featureless. There is a slightly inhomogeneous brightness distribution (brighter near the centre of the image), and various artifacts from imperfectly clean optics and illumination. To prevent these features from introducing artifacts into intensity curves, a “background” image was taken of featureless mica, close to the fringes being studied and at the same focus and exposure. The pixel values of this background image were subtracted from those of each of the images with fringes before generating intensity curves.

Across the course of an experiment, the positions of features tend to drift slightly within the images. In order to generate comparable intensity curves across a series of images, it was therefore necessary to align the images. All experiments were chosen to have

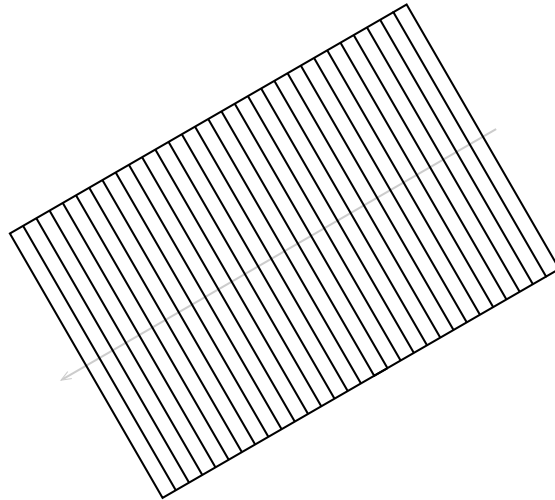


FIGURE 6.20: Illustration of rectangular regions (black) along a path (grey) into which pixels were binned.

in view some definite locatable point on the mica surface, usually the intersection of an interference fringe with a step edge. For every image, the co-ordinates of this point were identified and a path for the intensity curve chosen relative to this point.

This alignment was not perfect, and it was found necessary to slightly translate curves to correspond. One curve, typically the first in the sequence prior to condensate formation, was chosen as a reference curve, and each other curve was translated horizontally to obtain best correspondence with this. Vertical fitting was also performed, both translation and linear scaling, to allow for inconsistent exposure and focus between photographs. This was purely to allow for easier comparison of curves and should not have affected condensate height results in any way. No horizontal scaling was performed. Three-variable alignment was performed to minimise the discrepancy between each pair of curves in two regions: the flat region beyond the last interference fringe, and the peak of the last fringe not obscured by the condensate. Figure 6.21 shows an example pair of intensity curves and the effects of background correction and alignment.

A wedge height profile, such as that in Figure 6.4, was generated from the reference curve. This was done by comparing the intensity at every point to those at the neighbouring peaks and troughs. For example, consider a point of intensity  $I$  between the apex at  $P_0$  (having intensity  $I_0$ ) and the first peak at  $P_1$  (having intensity  $I_1$ ), as shown in Figure 6.22. If there is no condensate in the wedge, then the height  $h$  at that point is given by

$$h = \frac{\lambda}{2\pi} \sin^{-1} \sqrt{\frac{I - I_0}{I_1 - I_0}} \quad (6.3)$$

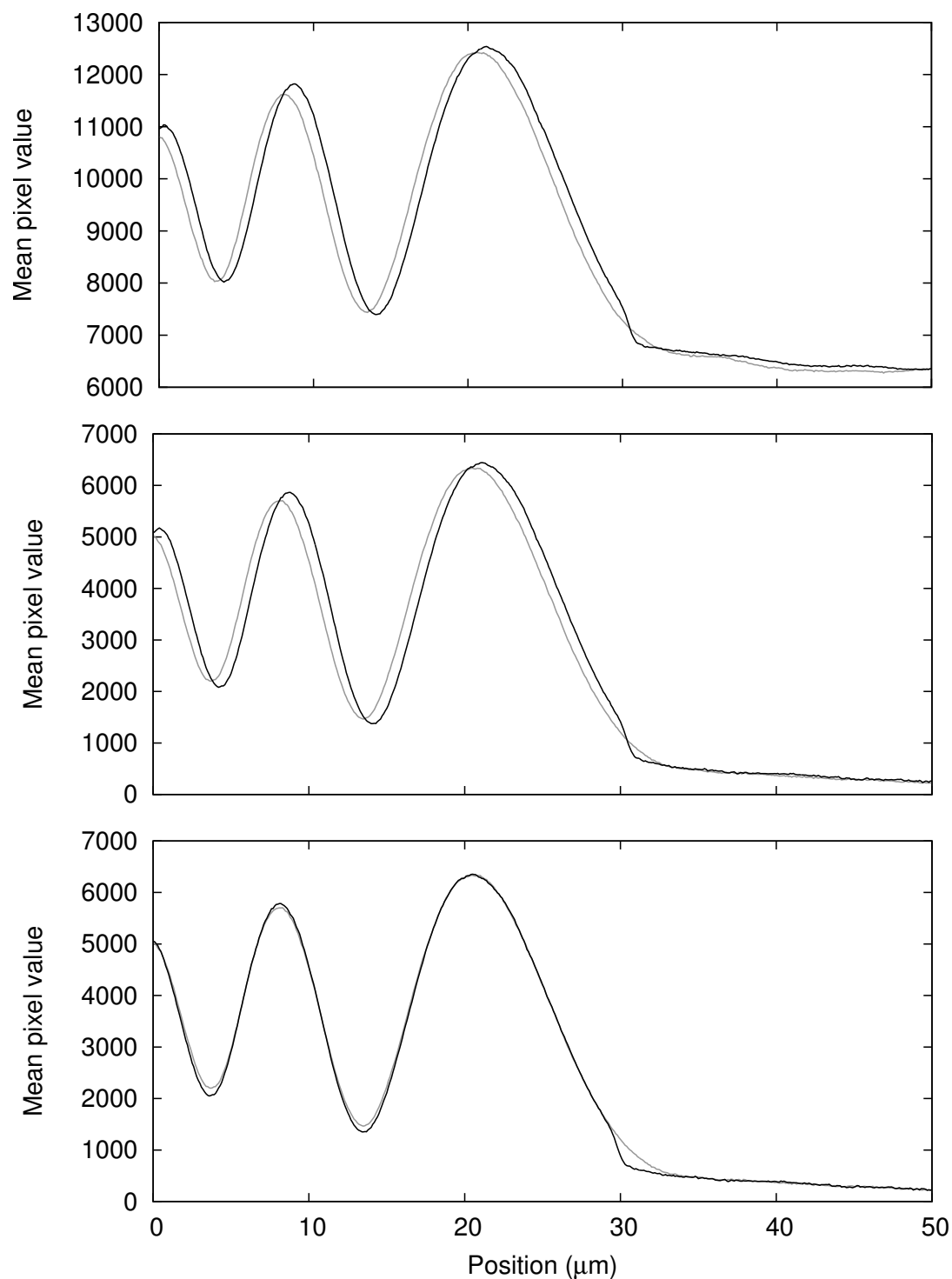


FIGURE 6.21: Graphs showing two intensity curves: a reference curve before condensate growth (grey) and a curve after the growth of a camphor condensate (black): (top) without background correction; (middle) with background correction; (bottom) with background correction and aligned.

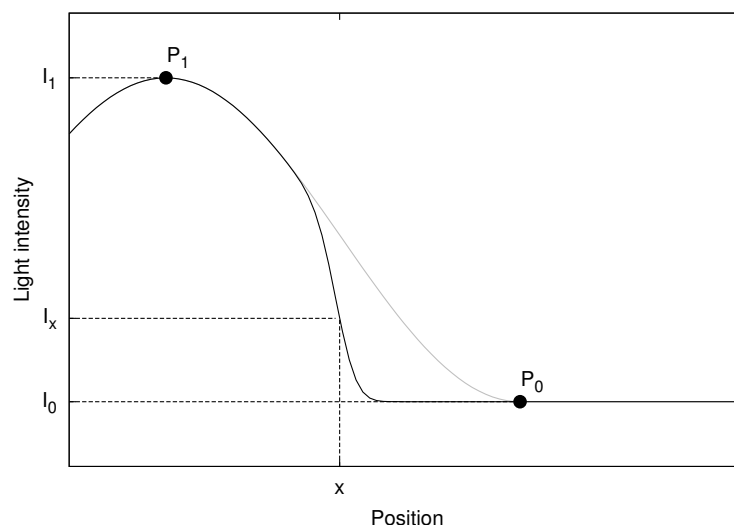


FIGURE 6.22: Graph showing a hypothetical intensity curve for a wedge with a condensate (black curve) and the same wedge without (grey curve). Points  $P_0$  and  $P_1$  show the positions of the apex and first peak respectively, at light intensities  $I_0$  and  $I_1$ . Position  $x$  is chosen such that its intensity  $I$  is half-way between the grey curve and the baseline.

from consideration of Equation 6.1. For points on other parts of the curve, heights are given by some number of half wavelengths plus or minus the expression in Equation 6.3, with  $I_0$  and  $I_1$  replaced by the intensities of an appropriate adjacent peak and trough.

Peak and trough positions are found precisely by local curve fitting of parabolic functions to the data. The apex  $P_0$  is more ambiguous, and was located by fitting a parabolic function of the form  $ax^2 + bx + c$  to the fringeward side of the apex, and a linear function  $bx + c$  on the other side.

The transition from the line of the reference curve to the baseline (the line which would be followed if the wedge were completely filled) was not immediate, but due to the limited resolution was seen as a gradual transition. The point of transition  $x$  was measured as the point at which the intensity  $I_x$  is half-way between the reference curve and the baseline, as shown on Figure 6.22. The wedge height profile was then used to find the wedge height at  $x$ .

Errors were from two distinct sources. One is from an imprecision in accurately determining  $x$ ; an error range was specified manually for each curve. This was a particularly large error when the condensate height was about an integer number of half-wavelengths, including for very small condensates, as there is little to no difference between the reference curve and the baseline at these points. The other error arose from errors in the condensate height profile, themselves a combination of errors from the measured light intensities and imprecision in the location of peak positions. These errors were larger close to an integer number of quarter wavelengths.

## 6.6 Condensate growth of organic compounds

To characterise the condensate growth process, quantitative analysis was performed on condensates of camphor, hexachloroethane and norbornane. For each compound, three substrates were selected with large, well-defined pocket features, and crystallisation was induced by applying a temperature ramp of 0.5 °C/minute to the cell base. Observations were made of one pocket corner using a 40× objective, and condensate heights found from each image by the methods described in Section 6.5. These substrates were labelled A–C for each compound. In addition, a similar experiment was performed on one or two additional substrates per compound at the slower ramp rate of 0.1 °C/minute, these were labelled D and E. Note that during experiments the substrate temperature typically warmed by about 0.05 °C/minute, meaning that base temperature ramp rates of 0.5 °C/minute and 0.1 °C/minute corresponded to ramp rates of  $\Delta T$  of about 0.45 °C/minute and 0.05 °C/minute respectively.

Condensate heights were found in regions 50–150  $\mu\text{m}$  from the pocket edge, with the locations chosen to lie along nearly parallel fringes without any step edges or other features.

### 6.6.1 Camphor

Figure 6.23 shows results for camphor condensates on substrates A and B. Results for substrate C are not shown, as nucleation on this feature occurred first elsewhere along the step edge than at the pocket corners, and although a clear faceted condensate formed, it did not lead to the formation of a bulk crystal, presumably due to competition with the earlier crystals. The curves for substrates A and B are mostly in agreement, with bulk crystal emergence after a height of about 55 and 65 nm respectively, and with substrate A showing a slightly more linear growth pattern. No discontinuity can be seen in the growth rate on either curve.

Figure 6.24 shows the results for substrate D. The trend is generally the same as at the higher ramp rate, but with emergence at a lower  $\Delta T$  and a higher condensate height of 130 nm.

### 6.6.2 Hexachloroethane

With hexachloroethane at 0.5 °C/minute, substrates B and C formed bulk crystals at the pocket corners prior to any detectable condensate growth, at high temperature differences of 4.5 and 6.0 °C respectively. This was immediately followed by the growth

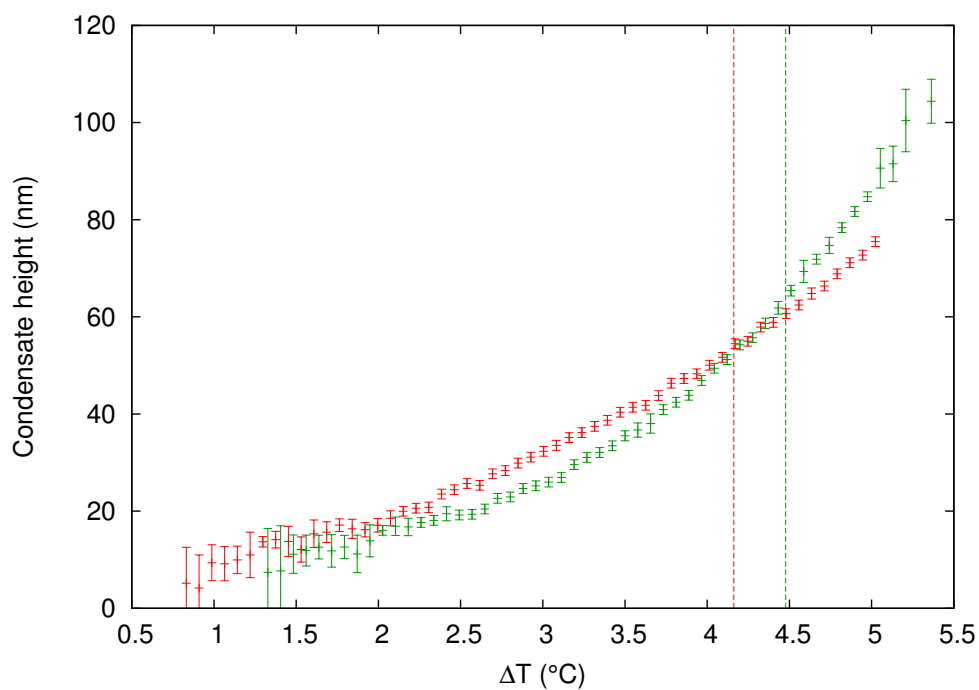


FIGURE 6.23: Graph showing the measured condensate height of camphor on substrates A (red) and B (green) against  $\Delta T$ , due to a base temperature ramp of  $0.5\text{ }^{\circ}\text{C}/\text{minute}$ . The vertical dashed lines indicate the moment at which a bulk crystal began growing from the pocket corner. These condensates appeared smooth until about  $3.0\text{ }^{\circ}\text{C}$  (A) and  $3.5\text{ }^{\circ}\text{C}$  (B), after which they became increasingly irregular and faceted.

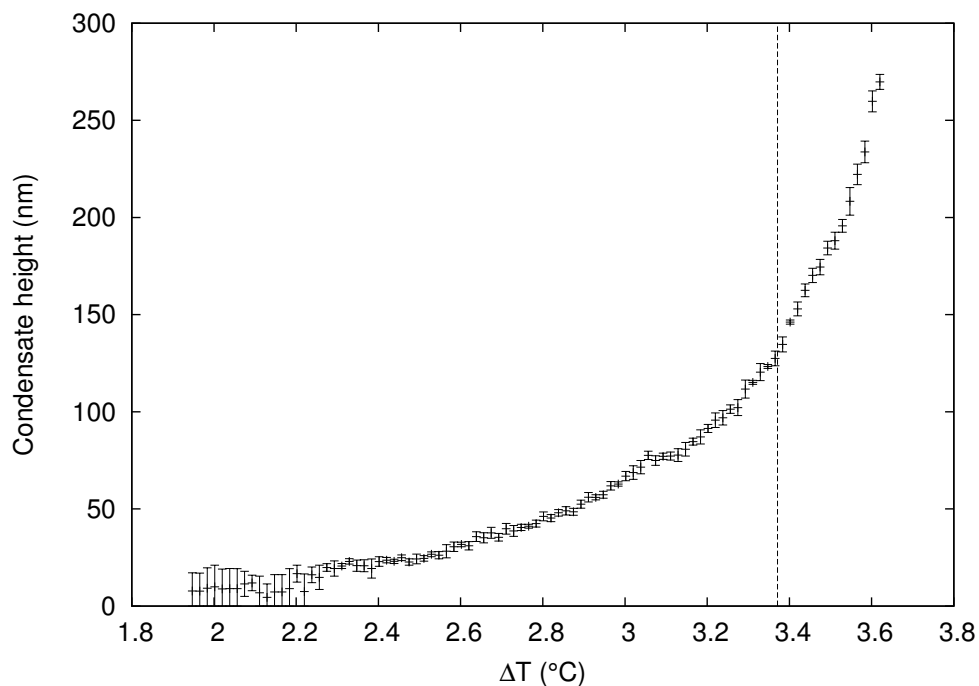


FIGURE 6.24: Graph showing the measured condensate height of camphor on substrate D against  $\Delta T$ , due to a base temperature ramp of  $0.1\text{ }^{\circ}\text{C}/\text{minute}$ . The vertical dashed line indicates the moment at which a bulk crystal began growing from the pocket corner. This condensate appeared smooth until about  $3.2\text{ }^{\circ}\text{C}$ , after which it grew thicker and slightly faceted towards the pocket edge.

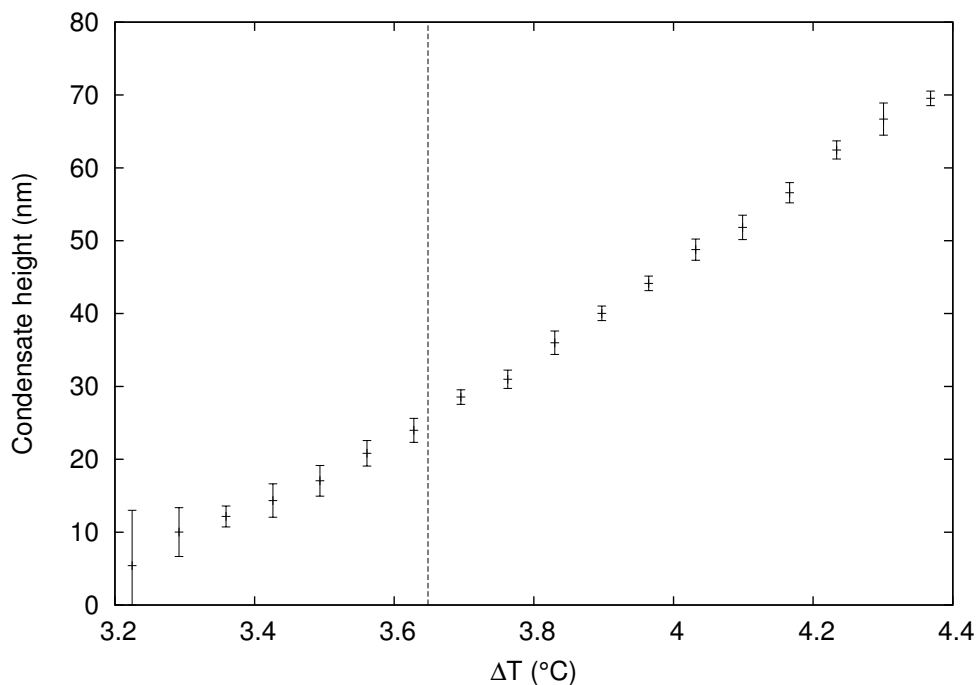


FIGURE 6.25: Graph showing the measured condensate height of hexachloroethane on substrate A against  $\Delta T$ , due to a base temperature ramp of  $0.5\text{ }^{\circ}\text{C}/\text{minute}$ . The vertical dashed line indicates the moment at which a bulk crystal began growing from the pocket corner. This condensate appeared smooth until bulk crystal emergence, after which it became kinked.

of needle-like crystals from all along the wedge apex. On substrate A, there was a slight detectable condensate prior to bulk emergence at a lower temperature difference of  $2.6\text{ }^{\circ}\text{C}$ , with no subsequent needle growth. Figure 6.25 plots condensate growth on substrate A. It may be seen that growth is linear, with no obvious discontinuity in the growth rate, and that the condensate reaches a height of about 25 nm before a bulk crystal emerges.

At a lower ramp rate, substrate D behaved qualitatively similar to substrate A, with a condensate prior to bulk emergence and an absence of needling. The condensate height is plotted in Figure 6.26. Here the condensate grows much larger, to about 125 nm, before bulk crystal emergence.

### 6.6.3 Norbornane

Norbornane growth was performed without leaving the cell to equilibrate with the lab temperature. Figure 6.27 shows the growth of condensates on substrates A, B and C after a base temperature ramp of  $0.5\text{ }^{\circ}\text{C}/\text{minute}$ . The curves are all in approximate agreement, and condensates grow to a fairly consistent 300–400 nm before the emergence of a bulk crystal. Of particular note is that there is a definite sharp transition in the condensate



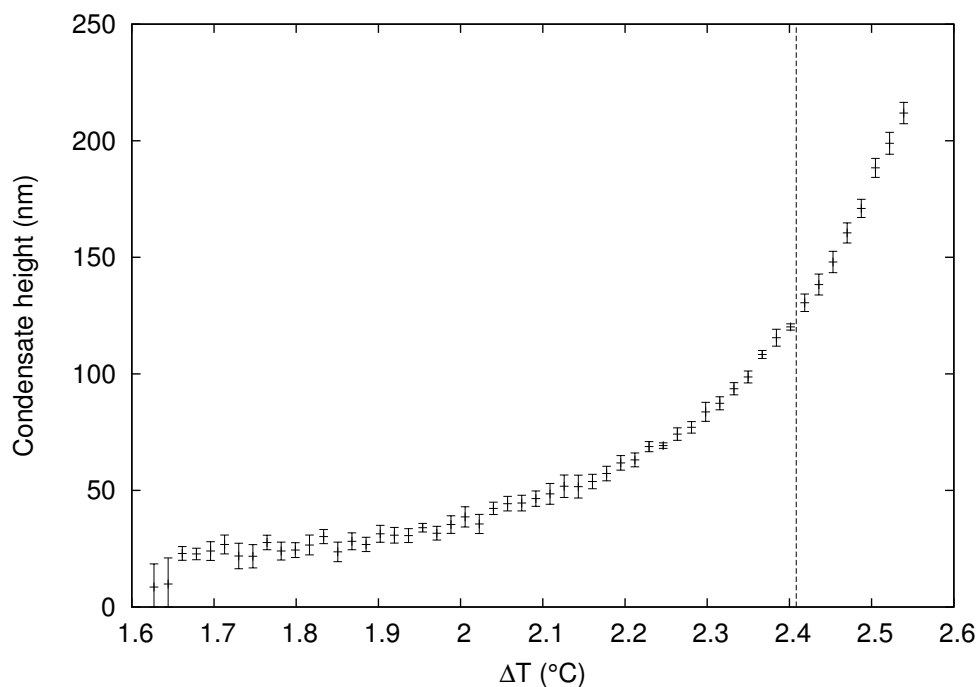


FIGURE 6.26: Graph showing the measured condensate height of hexachloroethane on substrate D against  $\Delta T$ , due to a base temperature ramp of  $0.1\text{ }^{\circ}\text{C}/\text{minute}$ . The vertical dashed line indicates the moment at which a bulk crystal began growing from the pocket corner. The apparent sudden appearance of a condensate to the left of the graph is due to a poor focus prior to this time. This condensate appeared smooth until about  $2.2\text{ }^{\circ}\text{C}$ , after which it became irregular and jagged.

growth rate, at a condensate height of 120–180 nm, shortly before crystal emergence. This transition also seems to at least approximately relate to the transition from a smooth to a slightly jagged condensate interface, although this may simply be a consequence of the increased growth rate.

Figure 6.28 plots the heights of condensates on substrate D and E after a base temperature ramp of  $0.1\text{ }^{\circ}\text{C}/\text{minute}$ . These curves do not closely agree, but they both show a sudden growth rate increase at 100–150 nm, and bulk emergence at about 600 nm. The uneven later growth rate on substrate E is an artifact of facets growing transversely across the region of interest.

#### 6.6.4 Solid or liquid condensates?

It is impossible to say whether the small condensates first observed in experiments are solid or liquid. However in the case of camphor, condensates are certainly crystalline prior to emergence from confinement, evidenced by the existence of clear facets. Figure 6.29 shows an example.

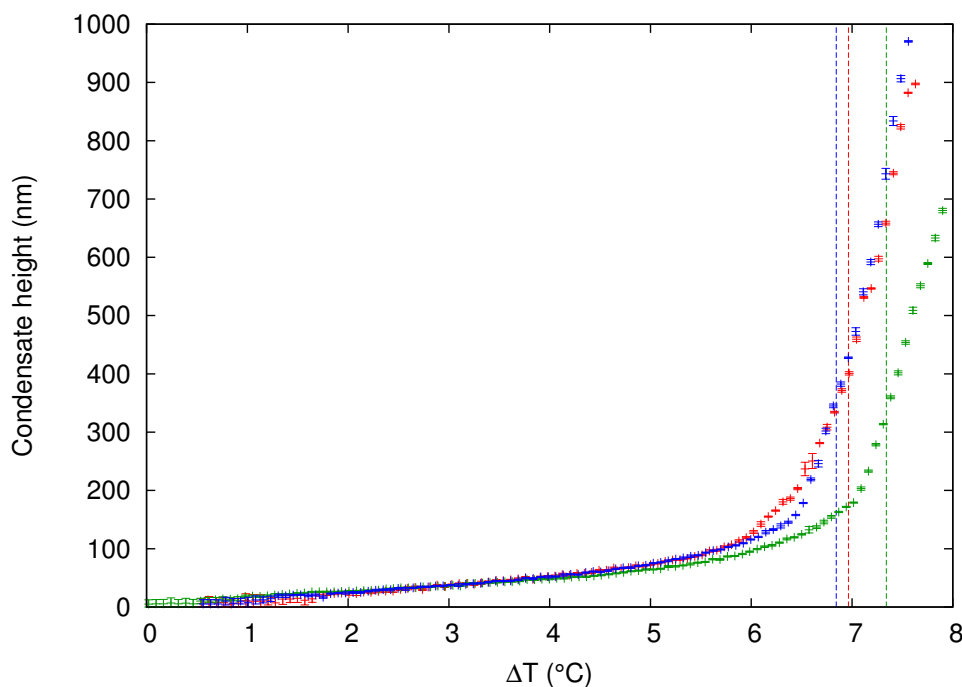


FIGURE 6.27: Graph showing the measured condensate height of norbornane on substrates A (red), B (green) and C (blue) against  $\Delta T$ , due to a base temperature ramp of  $0.5\text{ }^{\circ}\text{C}/\text{minute}$ . The vertical dashed lines indicate the moment at which a bulk crystal began growing from the pocket corner. These condensates appeared smooth until about  $6.2\text{ }^{\circ}\text{C}$  (A),  $7.2\text{ }^{\circ}\text{C}$  (B) and  $6.6\text{ }^{\circ}\text{C}$  (C), after which they developed a jagged appearance and grew thicker towards the edge of the pocket.

For norbornane, the interface takes on a jagged or kinked shape which does not clearly correspond to crystal facets. However, it must be noted that due to surface tension, the equilibrium shape for a liquid condensate in a wedge is a smooth interface at a constant separation. Although the system is not in equilibrium, and high effective viscosity in the narrow confines of the wedge may make non-smooth interfaces possible, jagged and kinked interfaces of norbornane exhibit such extreme changes in radius of curvature over very narrow length scales that it is almost impossible to entertain the notion of a liquid existing in such a configuration. Figure 6.30 shows an example, with the arrow pointing to a point where the interface appears to turn a sharp corner. This geometry requires the horizontal interface radius of curvature to change from infinity to at most  $600\text{ nm}$  within a distance of a couple of microns. Assuming a surface energy of  $30\text{ mJ}/\text{m}^2$  and using the Young-Laplace equation,[108] this relates to a pressure change of at least  $0.5$  atmospheres within the condensate over this distance, a number far too high to be supported by any liquid between surfaces  $150\text{ nm}$  apart.

Hexachloroethane condensates were generally too small to comment on whether they were solid or liquid prior to bulk emergence. However on hexachloroethane substrate D, the only run to show a visible large condensate, the jagged appearance appears to

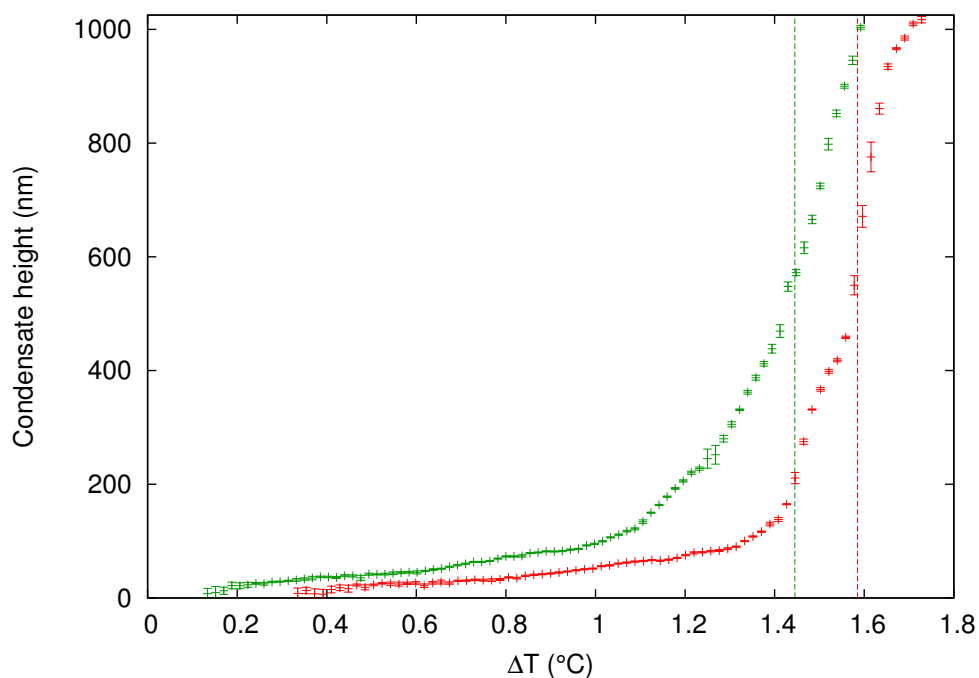


FIGURE 6.28: Graph showing the measured condensate height of norbornane on substrates D (red) and E (green) against  $\Delta T$ , due to a base temperature ramp of  $0.1\text{ }^{\circ}\text{C}/\text{minute}$ . The vertical dashed lines indicate the moment at which a bulk crystal began growing from the pocket corner. These condensates appeared smooth until about  $1.45\text{ }^{\circ}\text{C}$  (D) and  $1.1\text{ }^{\circ}\text{C}$  (E). After this temperature difference, D suddenly took on several sharp kinks in its interface and became thicker near the pocket edge. E became irregular and jagged and became hugely thicker near the pocket edge before bulk emergence.

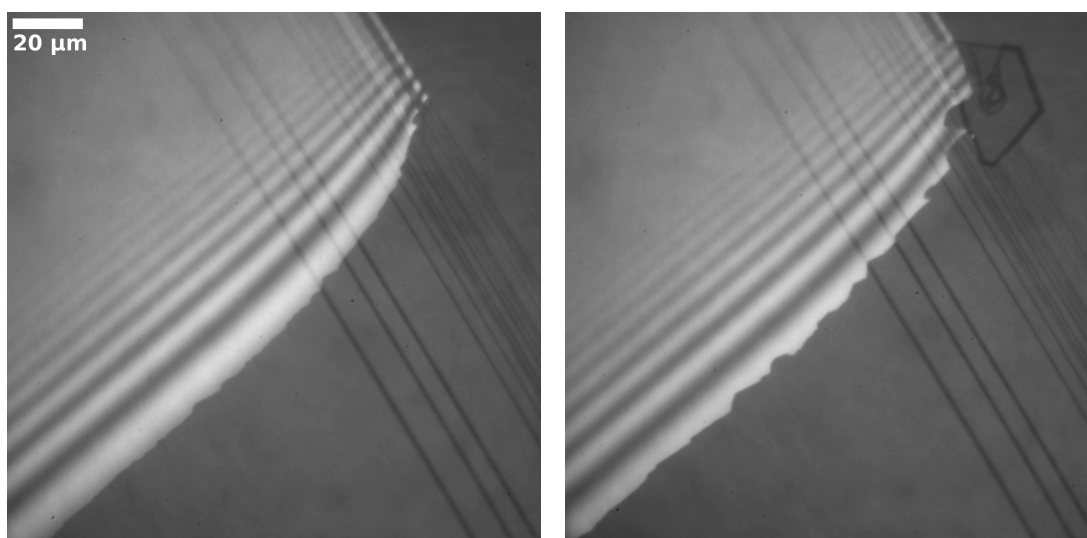


FIGURE 6.29: Optical micrographs showing a condensate of camphor (substrate B) before and after bulk emergence. Crystal facets are clearly visible in the wedge after bulk emergence, but development of these can already be seen prior to the appearance of a bulk crystal.

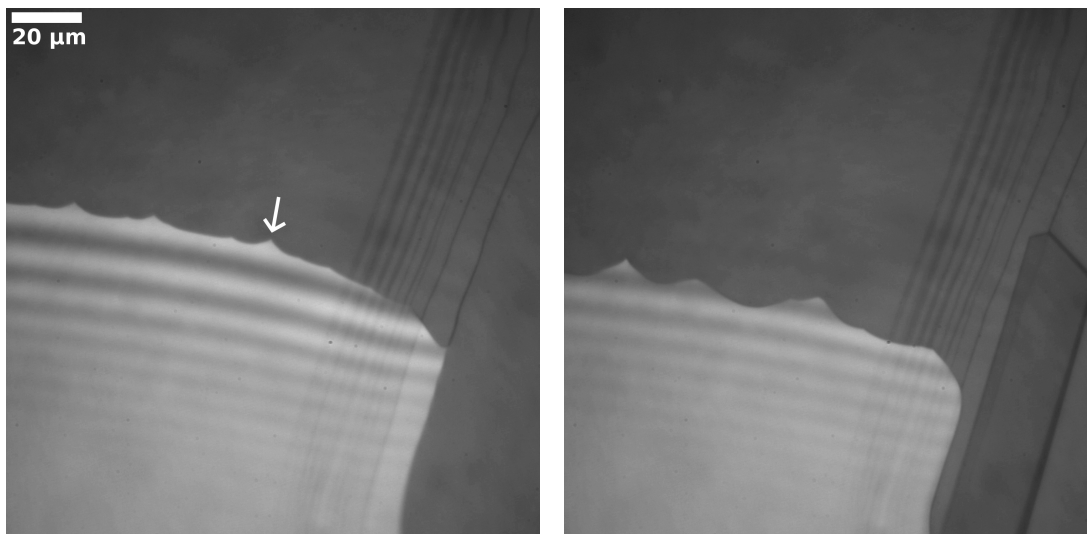


FIGURE 6.30: Optical micrographs showing a condensate of norbornane (substrate E) before and after bulk emergence. The arrow indicates a point on the jagged interface where there is a large discontinuity in radius of curvature over a very small distance.

preclude the possibility of a liquid by a similar argument to that for norbornane above.

### 6.6.5 Discussion

We must now consider the mechanism which best fits the following observations:

- there exists a condensate along the line of an acute wedge prior to the emergence of a bulk crystal;
- this condensate is visible at temperature differences below the saturation values found in Section 4.3.3 (indeed visible norbornane condensates will form if the cell is left for an hour with no temperature difference);
- this condensate is often not visible for hexachloroethane at higher ramp rates;
- for all compounds the condensate initially appears uniform with a smooth interface, but at higher saturations often becomes jagged, kinked or faceted, and significantly larger nearer to the pocket edge;
- for norbornane there appears to exist a sharp discontinuity in growth rate shortly before the emergence of a bulk crystal;
- bulk crystals emerge at a temperature difference consistently higher than the equilibrium values found in Section 4.3.3;
- at faster ramp rates, bulk crystals emerge at a higher saturation, and condensates grow larger before bulk crystal emergence.

compound	surface separation (nm)							
	12.5	25	50	100	200	400	800	1600
camphor	4.2	2.1	1.1	0.53	0.26	0.13	0.066	0.033
norbornane	3.9	1.9	0.98	0.49	0.24	0.12	0.061	0.031
hexachloroethane	3.3	1.6	0.82	0.41	0.21	0.10	0.051	0.026

TABLE 6.3: Estimated temperature differences (in °C) required for growth from between two surfaces of varying separation without a nucleation barrier. A substrate temperature of 22 °C is assumed, and a surface energy of 30 mJ/m<sup>2</sup> for each compound.

Firstly, it is clear that there is a solid phase confined in the wedges prior to the emergence of a bulk crystal. It also seems clear that the vapour is supersaturated before these crystals appear: not only from comparison of temperature differences to those in Section 4.3.3, but from the simple fact that when they do emerge, they typically grow with immediate rapidity. So if the vapour is at saturation before this point, and there is a solid phase present in the wedge, why does outward growth from the pocket edge not occur immediately? It is worth remembering that the condensate is small in one dimension, so a crystal would have to briefly form a concave curved surface in order to escape the confines of the wedge. The condition for being able to emerge without a nucleation barrier is equivalent to that of having a critical radius of at most half the surface separation, taking into account a cylindrical interface. Temperature differences corresponding to this condition for each compound and various surface separations are shown in Table 6.3.

These values are highly approximate, mostly due to the estimation of the surface energies, but they give a rough comparison to actual separations and temperature differences observed, which are shown in Table 6.4. Note that the condensate heights shown here are those at the very edge of the pocket just before the growth of a bulk crystal, and should be assumed to have a  $\pm 10\%$  uncertainty. It may be seen that the temperature differences, even after correction for observed positive temperature differences at saturation, are larger than those required for a crystal to emerge. This seems to imply that the saturation at the pocket edge is somewhat lower than is expected, perhaps because the close proximity of a growing condensate depletes the local vapour.

We must consider two reasons for a condensate staying confined within a wedge: thermodynamic and kinetic confinement. A thermodynamically confined phase is one which is in equilibrium with the local vapour, and grows as the partial pressure increases. A kinetically confined phase is below its equilibrium size, and its growth is limited by diffusion of material into the narrow geometry of the wedge. A thermodynamically confined condensate might be expected to be close to the equilibrium condensate shape, i.e. having an even height all around. A kinetically limited condensate would be likely to grow fastest, and hence thickest, nearer to the pocket edge

compound	substrate	condensate height (nm)	$\Delta T$ ( $^{\circ}\text{C}$ )	$\Delta T$ corrected ( $^{\circ}\text{C}$ )
camphor	A	130	4.2	1.3
	B	130	4.5	1.6
	D	210	3.4	0.5
hexachloroethane	A	40	3.6	2.4
	B	$\lesssim 20$	4.5	3.3
	C	$\lesssim 20$	6.0	4.8
	D	340	2.4	1.2
norbornane	A	1000	7.0	6.7
	B	480	7.3	7.0
	C	630	6.8	6.5
	D	850	1.6	1.3
	E	2100	1.4	1.1

TABLE 6.4: Table listing, for each substrate, the condensate height at the pocket's edge and the temperature difference at the time of bulk emergence of a crystal. The last column has been corrected by the equilibrium values found in Section 4.3.3.

(where there is the smallest diffusion barrier), and there would be nothing to prevent it from taking on an irregular faceted shape.

It therefore seems plausible that the widely observed transition from a smooth even condensate to a faceted or jagged condensate much thicker nearer the pocket edge is a result of the transition from a thermodynamically to a kinetically limited condensate. This transition is inevitable, because as the partial pressure of gas reaches the bulk vapour pressure, the equilibrium condensate height rises rapidly to infinity.

The orientation of crystal condensates is likely important. For example, norbornane grew in a hexagonal morphology on substrates D and E. On substrate D, facets were oriented parallel to the wedge apex (not parallel to the step edge), whereas on substrate E, facets were oriented parallel to the step edge (not parallel to the wedge apex). This is likely to greatly affect the condensate growth rate, appearance, and the ease with which a crystal may emerge into the bulk phase.

It is possible that the sharp discontinuity in the growth rate of norbornane condensates may relate to the freezing of the liquid phase. The solid phase has a lower vapour pressure, and so a jump in growth rate would be expected. In addition, no faceting was seen prior to the transition, but it often appears shortly afterwards. Norbornane has a much lower melting point than the other compounds ( $88\text{ }^{\circ}\text{C}$ ), and so the prospect of a supercooled liquid phase large enough to be visible is not unimaginable. However norbornane in mica wedges has been studied in the Surface Force Apparatus and no detectable liquid condensate was ever seen;<sup>[84]</sup> it is not clear why it would behave differently in this system. It is possible that the sharp jump in growth rate simply relates to the transition from a thermodynamically limited to a kinetically limited condensate.

For hexachloroethane growth, the typical pattern is that of no visible condensate followed by rapid needling growth all along the wedge at a high temperature difference, simultaneous with the growth of a bulk crystal. This is strongly suggestive of there being a condensate along the line of the wedge, too small to be visible, which cannot grow outwards until it overcomes some nucleation barrier. The other mode of hexachloroethane growth, the typical sequence of a smooth condensate becoming non-smooth and thicker at the edge and then emerging as a bulk crystal, could then be the consequence of early condensate nucleation, prior to bulk saturation being achieved. However the melting point of hexachloroethane is 187 °C, and its nucleation barrier from the melt was estimated in Table 6.1 to be vanishingly small, so it does not seem reasonable that there could be a liquid condensate, even at an invisibly small size. If hexachloroethane must pass a nucleation barrier to grow from a small condensate, the reason for this remains unknown.

In the Surface Force Apparatus, both norbornane and hexachloroethane were seen to immediately form a solid condensate with no detectable liquid intermediary.[84] In saturated conditions at room temperature, norbornane was seen to grow to a condensate height of about 200 nm, and hexachloroethane to 20 nm. That condensates were seen to grow much thicker than this in mica pockets before the emergence of a bulk crystal seems to confirm that the vapour was indeed supersaturated prior to this point.

## 6.7 Ice

Observations of ice growing in mica pockets were made using the first flow cell. Attempts were made with the second flow cell to obtain a high quality high magnification series of images of a pocket corner during growth, to enable a similar condensate size analysis as performed in the previous section, but enormous image drift associated with using the liquid nitrogen cooling stage made this practically impossible. The Peltier cooling cell, designed to eliminate image drift in these experiments, was not completed in time to allow it to be used.

Ice was grown on three substrates featuring pocket geometries, in each case by applying a constant humidity gas and lowering the temperature until crystals were observed. The first substrate, with a single large pocket, was used to nucleate ice on two separate runs, with the substrate warmed to 5 °C between runs for several minutes to remove any residual condensate. On both runs crystals were seen growing from the two corners of the pocket, with observed nucleation at  $(-42.3 \pm 0.1)$  °C on the first run (at 2 °C/minute) and at  $(-45.3 \pm 0.1)$  °C on the second run (at 0.5 °C/minute).

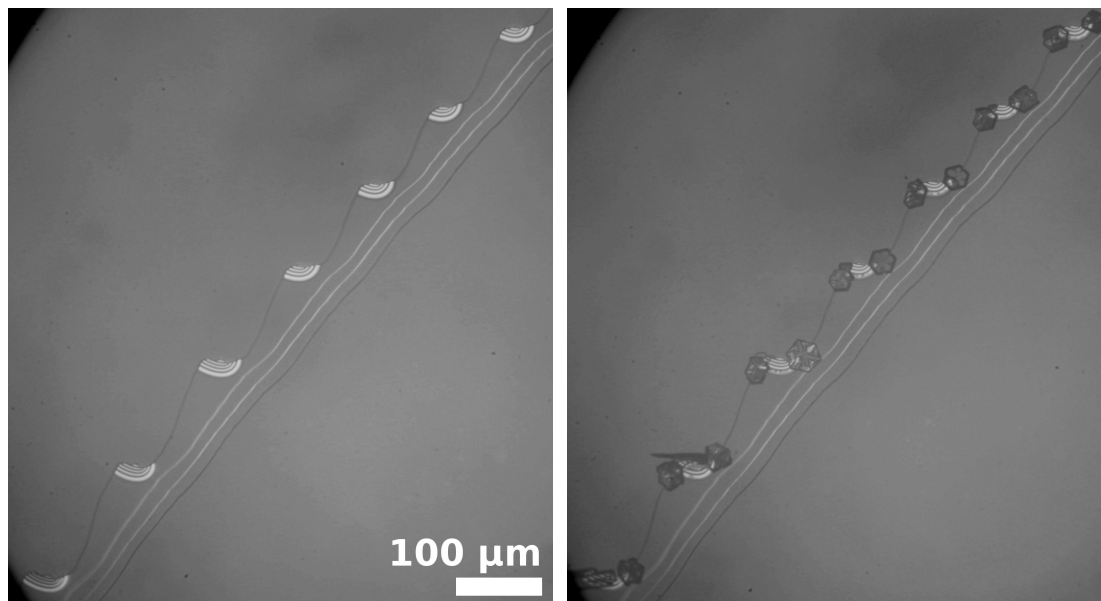


FIGURE 6.31: Optical micrographs showing a series of mica pockets before and after the growth of ice crystals.

The second substrate featured a regular series of similar small pockets along a step edge. Two runs at 1 °C/minute were performed, with the substrate temperature raised to 15 °C between runs to remove any residual condensate. On each run, crystals were seen growing from both corners of every pocket feature, appearing at -43.3 °C and -44.0 °C on the first and second run respectively. Figure 6.31 shows the pocket features before and after the first run. On both of these first two substrates there was no visible condensate prior to the emergence of a bulk crystal, although on both there was evidence of slight crystal growth all along the line of the wedge subsequent to the appearance of crystals at the pocket corners.

The third substrate again features a single large pocket feature and six crystallisation runs were performed, all at 1 °C/minute with substrates held for five minutes at 25 °C between runs, but with a slightly different (but not precisely quantified) humidity on each run. On five of the runs crystals were seen to appear between -40.0 and -38.2 °C, growing from the two corners of the pocket as previously. On one run, however, a large number of small liquid drops appeared across the surface at -37.0 °C. This was quickly followed by ice formation all along the length of the step edge and wedge apex, after which the liquid drops evaporated. Figure 6.32 shows a sequence of micrographs from this run, and Figure 6.33 one from a run forming crystals at -38.3 °C. It seems likely that on the higher nucleation temperature run a liquid condensate formed along not just the wedge apex but also the step edge, which then froze.

An attempt was made using this substrate to observe a condensate prior to the emergence of a bulk crystal. Although the relatively low magnification images were far from



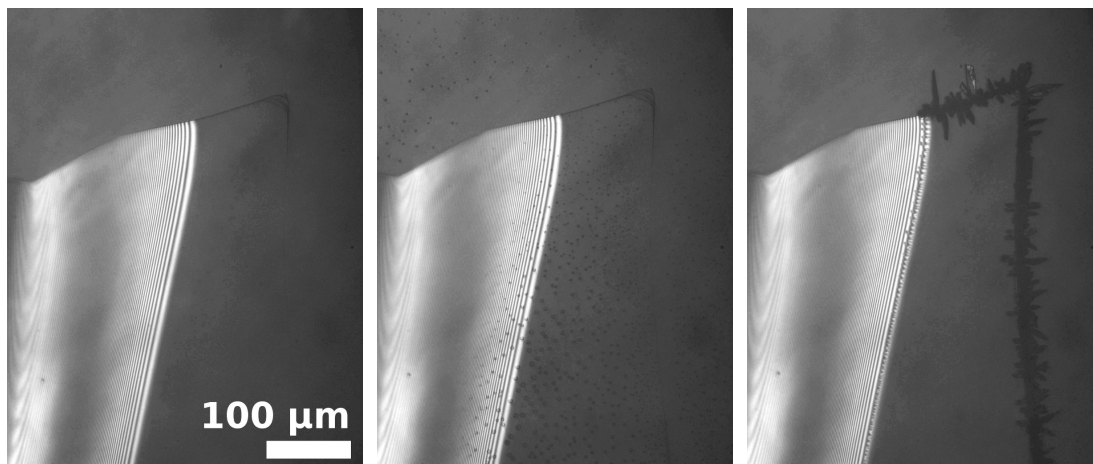


FIGURE 6.32: Time sequence of optical micrographs showing the growth of ice crystals from a liquid condensate around a mica pocket. The middle image shows liquid drops first observed at  $-37.0\text{ }^{\circ}\text{C}$

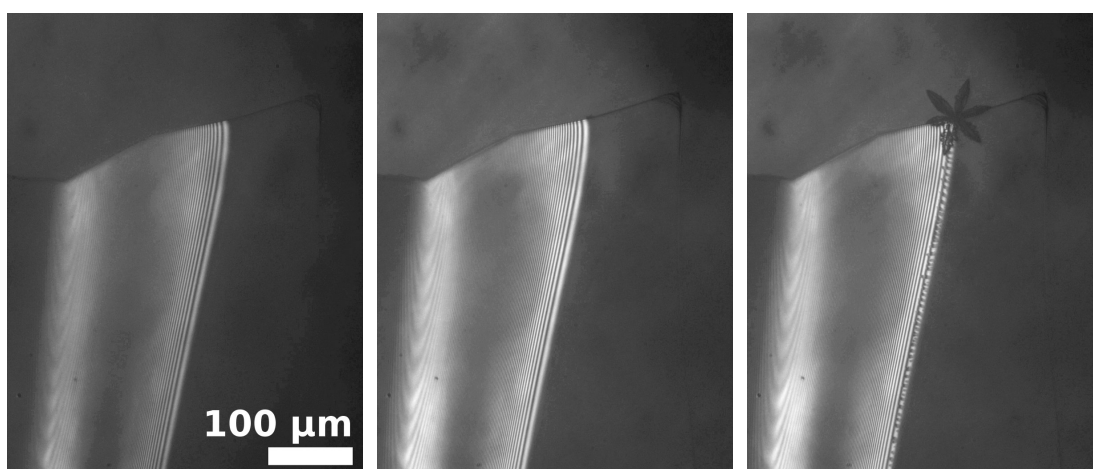


FIGURE 6.33: Time sequence of optical micrographs showing the growth of ice crystals from the corner of a mica pocket. The middle image shows the first observed nucleation at  $-38.3\text{ }^{\circ}\text{C}$

ideal, the pocket featured exceptionally straight and parallel fringes, and so a broad  $120\text{ }\mu\text{m}$ -wide path could be analysed, using  $200\text{ nm}$  (1 pixel) steps.

Looking at a run without observed liquid droplet nucleation, and chosen for having the highest quality sequence of images (that shown in Figure 6.33), no condensate was observed prior to the emergence of a bulk crystal. A pair of intensity curves are shown in Figure 6.34, generated from images well before and at the point of bulk emergence. The curves are of a lower quality than those seen in the previous section, however a condensate of about  $20\text{ nm}$  height would likely be unambiguously visible. Therefore if there was a condensate prior to nucleation, it must certainly have been of height no more than about  $15\text{ nm}$ .

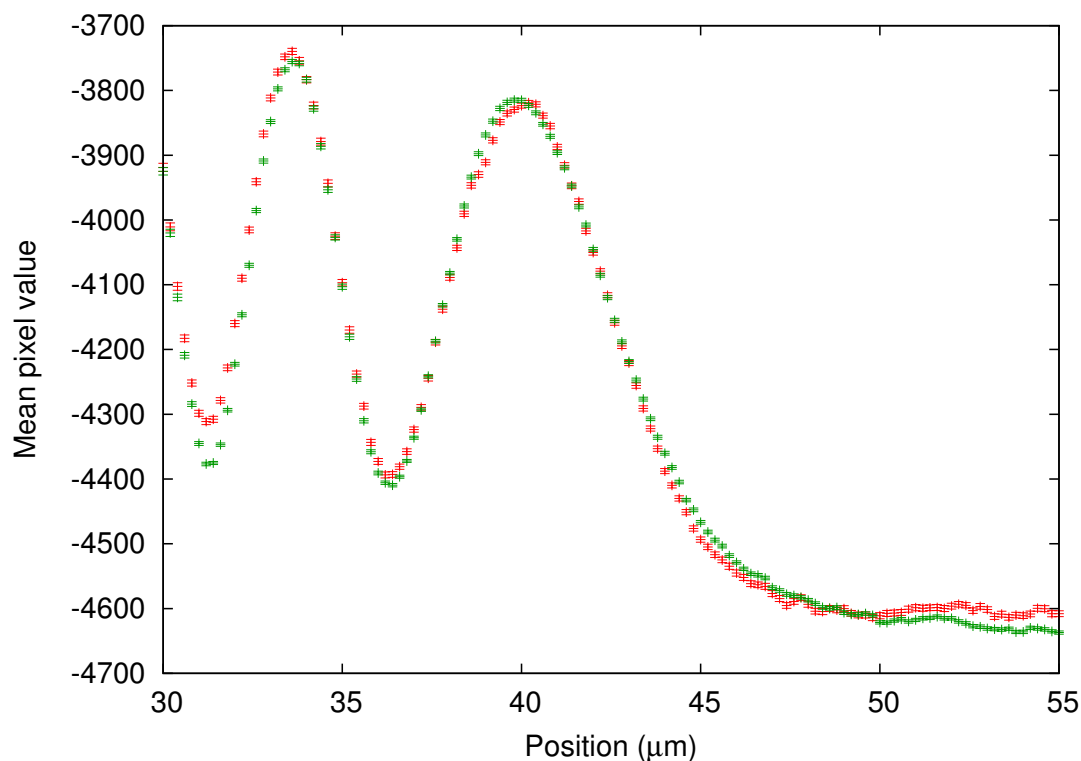


FIGURE 6.34: Graph comparing aligned intensity curves across a mica wedge apex at: (red)  $-37.0\text{ }^{\circ}\text{C}$ , well before observed nucleation, as seen on the left of Figure 6.33; (green)  $-38.3\text{ }^{\circ}\text{C}$ , at the moment of first observed bulk ice growth, as seen in the centre of Figure 6.33. The negative pixel values are an artifact of background correction without a suitable background image.

## 6.8 Summary

Various organic crystals and ice were observed growing from vapour in “pocket” geometries, features having a long acute wedge geometry and shown to be effective nucleation sites in the previous chapter. A distinctive growth pattern was observed across many systems, with two bulk crystals growing from the two “corners” of the feature, where the wedge angle opened onto a step edge, and more limited growth along the full line of the wedge. This is highly diagnostic of growth from a confined condensate along the wedge, with bulk crystals growing at the two edges due to less limited diffusion.

Closer observation confirmed the existence of condensates prior to bulk crystal growth for camphor, norbornane and hexachloroethane. No condensates could be observed for ice, but this may just be because the condensates were too small. Condensates were seen to be solid prior to the emergence of a bulk crystal, evidenced by facets in the case of camphor, and suggested by a sharply kinked interface for other compounds, despite supersaturated conditions. This suggests that the limiting barrier to bulk crystal growth

in these systems may be the transition from a confined phase to a bulk phase, to pass which the crystal must temporarily form an unfavourably curved interface.



## Chapter 7

# On ice nucleation from water

### 7.1 Introduction

In previous chapters we have considered the nucleation of crystals from supersaturated vapour, whether directly or via an intermediate liquid phase. Here we consider nucleation from a supercooled liquid. This is a qualitatively different process in several ways. Firstly, there are no obvious intermediary phases which may aid in nucleation: there is no analogue of capillary condensation here. Secondly, as discussed in Section 2.2.5, crystals are likely to have high contact angles in the melt on most foreign substrates. This may make the effect of heterogeneous nucleation on a majority of materials slight or non-existent. There do however exist materials known to promote ice nucleation, such as silver iodide,[109] kaolinite [110] and feldspar,[111] usually attributed to a close lattice match or other specific effects.

Another important difference to nucleation from vapour is that liquids usually contain a high concentration of contaminant particles. The freezing of bulk water is typically dominated by these contaminants: sufficiently pure water is highly unlikely to freeze homogeneously above about  $-30\text{ }^{\circ}\text{C}$  even in large volumes.[112, 113]

In order to study nucleation, we must have a system without contaminants. This is extremely difficult: even the most carefully distilled and filtered water still contains impurities, and it only requires one contaminant effective at nucleating ice to compromise the whole. Therefore I use a technique pioneered by Vonnegut: the study of a large number of very small volumes.[114] By splitting a volume of reasonably pure liquid into many small enough drops, it may be assumed that a majority of them will be free from contamination, and those which are not are easily identified as they will freeze at an elevated temperature compared to the rest. This method has been used in

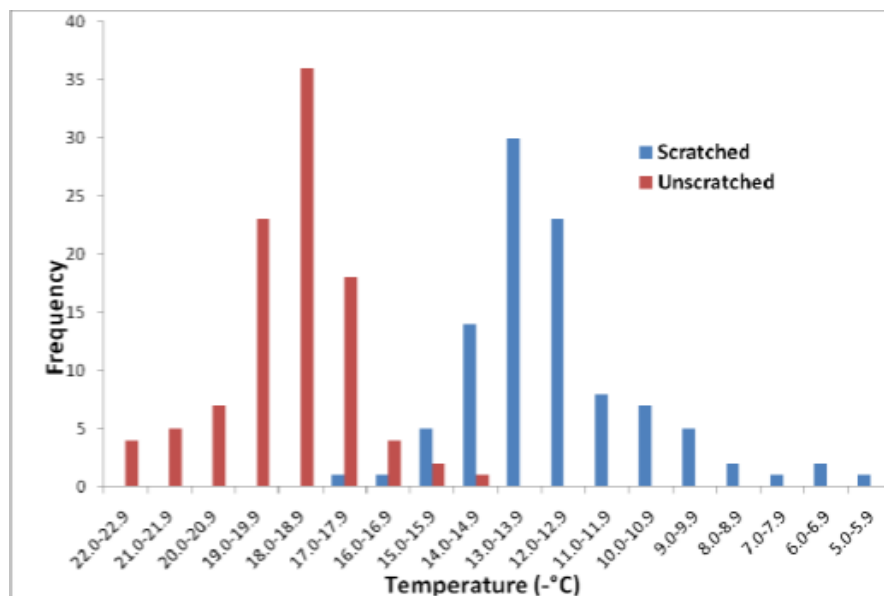


FIGURE 7.1: Graph of freezing temperatures of 0.5  $\mu\text{L}$  water droplets on smooth and scratched silicon wafers, reproduced from unpublished report by Shiri Stern.

a great number of nucleation studies,[112, 115–118] and provides an effective system provided that freezing in one droplet is isolated and does not affect that in others. With ice, complete freezing of a small droplet occurs in a small fraction of a second, and so one can be sure that a single freezing event was the consequence of a single nucleation event.

## 7.2 Nucleation from microlitre volumes

### 7.2.1 Prior work

Prior to this work, a series of unpublished experiments performed by Shiri Stern had appeared to demonstrate a difference in freezing temperature between water drops on smooth and roughened silicon surfaces. Silicon wafers were roughened by scratching with diamond powder and then cleaned, and several microlitre drops of water pipetted onto the surface. These were taken slowly down in temperature using a Peltier stage, and the temperature at each freezing event was recorded. After performing this experiment with a large number of drops on both smooth and scratched substrates, it was observed that drops on the scratched surfaces generally froze at a higher temperature than those on smooth surfaces, as shown in Figure 7.1. I endeavoured to repeat and verify this result.

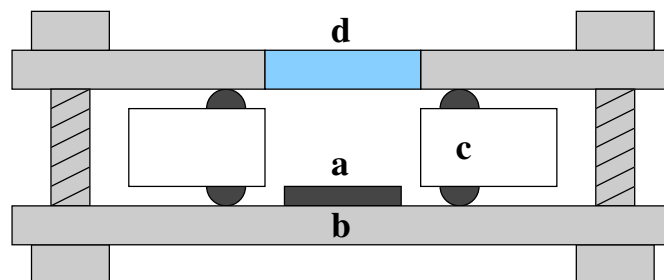


FIGURE 7.2: Diagram showing cell used for microlitre drop freezing experiments. The sample (a) sits between two steel plates (b) screwed tightly around a polytetrafluoroethylene wall (c) sealed with two o-rings. Observations were made through a glass window (d) set into the top plate.

### 7.2.2 Experimental procedure

Silicon wafers were cut to  $1\text{ cm}^2$ . After any scratching had been performed (see below) they were cleaned by means of ten minutes sonication in each of deionised water, ethanol, deionised water and dilute hydrochloric acid, and then rinsed in deionised water and dried with nitrogen gas. Between six and eight  $0.5\ \mu\text{L}$  droplets were applied to the surface with a pipettor. The wafer was then quickly sealed inside the cell shown in Figure 7.2: this consisted of two steel plates separated by a polytetrafluoroethylene wall, screwing shut and sealing via rubber o-rings, and having a glass window in the top plate. A narrow hole through the cell wall permitted the insertion of a thermocouple, which was placed to be in contact with the silicon surface without making contact with any drop.

The cell was placed on a Peltier cooling stage and the temperature allowed to drop; although the device did not allow for a controlled temperature ramp, the rate was typically  $6\text{--}8\text{ }^\circ\text{C}$  per minute. Freezing events were observed by eye, and the temperature at which each drop froze recorded. Some drops did not freeze by the minimum attainable temperature of  $-24\text{ }^\circ\text{C}$ . After this temperature had been reached, the substrate was warmed up to  $2\text{ }^\circ\text{C}$  to melt all ice, and the cooling was repeated once more.

Early scratching attempts used diamond powder or a diamond pen. These methods both made long furrows across the surface, albeit on very different scales. It was quickly found that drops lying along a single scratch would freeze simultaneously due to the rapid spread of a freezing event along such a feature. Therefore an array of disconnected scratches,  $1\text{ mm}$  long, made with a diamond pen, was used, and drops were placed over the scratches. This enabled substrates with different drops on both smooth and scratched sites to be used.

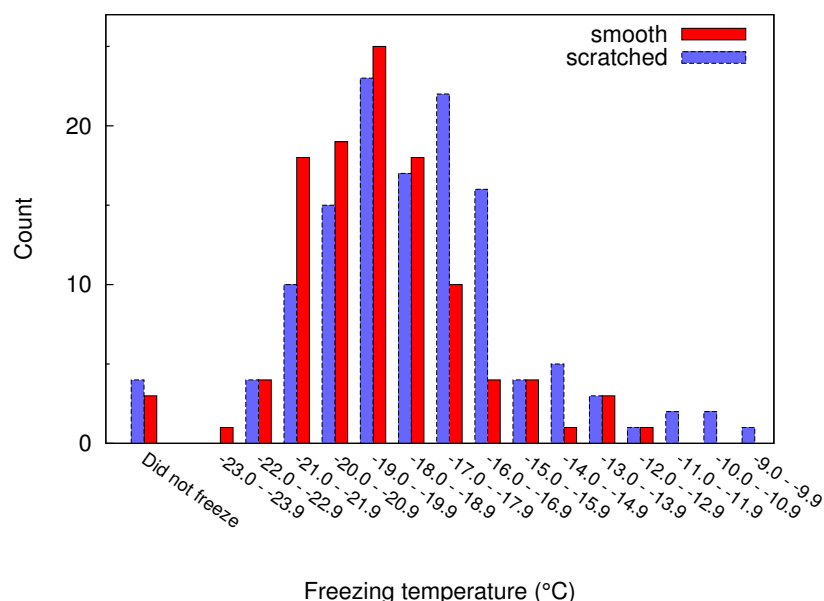


FIGURE 7.3: Graph of freezing temperatures of  $0.5 \mu\text{L}$  water droplets on smooth and scratched silicon wafers, following a similar method to that used to obtain Figure 7.1.

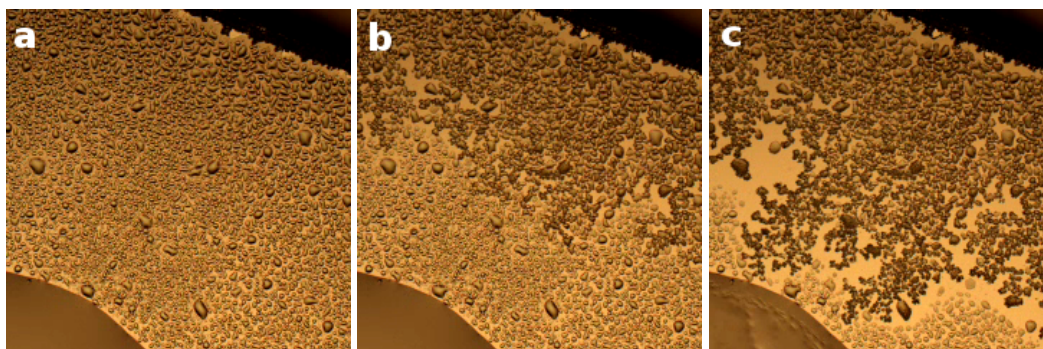


FIGURE 7.4: Time sequence of optical micrographs showing the spread of a freezing event across a smooth silicon wafer as the substrate temperature is lowered within a sealed chamber. At the top-right and bottom-left are visible the edges of two  $0.5 \mu\text{L}$  water drops. (a) small droplets condense between large drops; (b) one drop freezes and frost begins to spread from droplet to droplet; (c) the freezing event reaches the second large drop and freezes it.

### 7.2.3 Results and conclusions

Figure 7.3 shows the observed freezing temperatures for both scratched and smooth sites, compiling results for two freezing cycles per drop. No significant difference is observed between the two populations.

The use of an optical microscope to observe the progress of the experiment revealed an explanation for the discrepancies between the results in Figures 7.1 and 7.3. Many small water drops were seen to have condensed from the air inside the cell on the substrate between the large drops (Figure 7.4a). Upon one drop freezing, these froze sequentially,



each small drop freezing, growing slightly towards its liquid neighbours and freezing them upon contact (Figure 7.4b). By this means a single freezing event is transmitted across the surface, and eventually reaches the neighbouring large drop (Figure 7.4c). As such, it seems likely that the results observed are largely dominated not by nucleation but by the rate of spread of a freezing event across the surface, from a single nucleation event which may or may not have occurred in one of the large drops.

Hence the discrepancy between the two sets of results: in my own work, the surface between drops was smooth in both cases, whereas in the original experiments, on the scratched samples the surface between the drops was also scratched. This could have greatly increased the rate of spread of a freezing event.

## 7.3 The creation of picolitre droplet arrays

### 7.3.1 Introduction

The use of microlitre drops on a homogeneous surface, as described in Section 7.2, had two critical issues: freezing events could spread from one drop to another via surface frosting; and the volumes were much too large to expect nucleation not to be impurity-dominated. Both of these issues could be resolved by use of an array of picolitre droplets, templated by a pattern of hydrophobicity on the surface.

The concept is to coat a surface with a highly hydrophobic monolayer; this can then be selectively removed in a regular pattern using ultra-violet light, leaving comparatively hydrophilic patches at which droplets can sit. As the areas between sites remain hydrophobic, there should be little to no condensation between droplets, and hence no surface frosting. Such patterns can also be produced on a very small scale, making them ideal for the production of picolitre liquid droplet arrays.

### 7.3.2 The formation of hydrophobic surfaces

#### Silanes and thiols

Silanes and thiols represent the two main groups used to create hydrophobic monolayers on a surface. Both have the same basic form: a long hydrocarbon backbone, terminating with a head group at one end (the silane (-Si[H,Cl]<sub>3</sub>) or thiol (-SH) group) and a functional group at the other. These will tend to form an ordered monolayer if the head groups can bond strongly to the surface, leaving the functional groups exposed

at the outside. If the functional groups are hydrophobic, then a strongly hydrophobic surface is produced.

Monolayers of both molecule types may be oxidised by exposure to 254 nm ultraviolet light, after which they can be removed by immersion in a solvent. Initial attempts to construct a droplet array used a monolayer of 1H,1H,2H,2H-perfluorodecanethiol deposited from solution onto gold-coated mica. This could be selectively removed with ultraviolet light, and then the exposed area coated with hydrophilic mercaptohexadecanoic acid from solution. This method had been used previously to study nucleation from solution in droplet arrays,[119] and produced high quality arrays, however it was not suitable for these experiments as I required the plain substrate to be present at the base of each droplet to study heterogeneous nucleation. Therefore silane molecules were adopted, as these can bond directly to hydroxyl groups present on numerous substrates.

### Silanation

Substrates of glass and silicon were cleaned as in Section 3.1.5. To increase the concentration of hydroxyl groups on the surface, all substrates were plasma treated for two minutes in an air plasma. Mica samples were then rinsed in deionised water and dried in nitrogen gas, following a suggestion in the literature.[120]

Substrates were silanated in batches, being suspended face-down near the top of the chamber shown in Figure 7.5. Three drops of liquid silane were placed in a well at the base and the chamber was sealed and flushed with argon gas. The base was taken up to a predetermined temperature to produce a high partial pressure of gaseous silane, and held at that temperature for a variable duration before being allowed to cool. After removal, substrates were rinsed and left to soak in acetone to remove any excess silane.

### Octadecyltrichlorosilane

Early attempts used 1H,1H,2H,2H-perfluorodecyldimethylchlorosilane. Optimisation of silanation parameters had already been performed for this compound with the chamber available, and I adopted the recommended exposure of 150 °C for one hour. However silicon substrates treated in this way were found to be inhomogeneous, and it was decided to move to a trichlorosilane, in which it was thought that the extra chlorines would help to provide extra sites to bind the molecules together, producing a more consistent monolayer. Hence octadecyltrichlorosilane was adopted for all surface functionalisation.

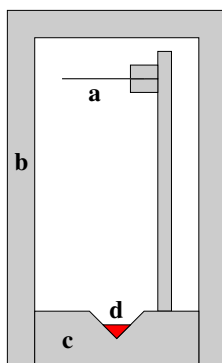


FIGURE 7.5: Diagram showing chamber used for silanation of surfaces. Substrates (a) are held face-down near at the top of a sealed steel cylinder (b). The cylinder base (c) is heated to a fixed temperature, partially vapourising a small pool of liquid silane held in a small well (d).

Spot diameter ( $\mu\text{m}$ )	Spot separation ( $\mu\text{m}$ )
50	100
30	60
20	40
10	25

TABLE 7.1: Table detailing dimensions of patterns used for surface patterning. The spot separation is the centre-centre distance between nearest neighbouring spots.

This has the formula  $\text{C}_{18}\text{H}_{37}\text{SiCl}_3$ ; it is a long hydrocarbon chain with a trichlorosilane group at one end. Early experiments used an exposure of  $100^\circ\text{C}$  for one hour, but this was found to sometimes deposit large persistent globs of polymerised silane, and so a slightly lower exposure of  $95^\circ\text{C}$  for forty minutes was soon adopted.

### 7.3.3 Ultra-violet patterning

#### Procedure

Surface patterning was achieved by use of a micropatterned quartz mask. This comprised a number of patterns, each a square array of circular spots of differing scales. The patterns used are detailed in Table 7.1. Henceforth these patterns shall be referred to by their spot diameter.

The quartz mask was placed with the relevant pattern directly over a deep ultra-violet lamp. The substrate was placed face-down on top of the pattern, with a small weight on top to ensure close contact. The lamp was switched on for a set amount of time and then the substrate removed, and soaked in acetone to remove detached silane from the surface. Exposure times of 45 minutes were used throughout most of the experiments. However this was found to be an overexposure, as became important when attempting

to produce well-defined spots of smaller size. Thus for the latter experiments (Section 7.6) a shorter exposure of only 15 minutes was used.

## Results

50  $\mu\text{m}$  droplet arrays formed on patterned silicon surfaces were seen to be of a high quality, with minimal inter-drop condensation. It was often seen that drop shapes were slightly elliptical, with the ellipse of every drop aligned in a common direction. Investigation determined that this related to the alignment of the substrate relative to the linear lamp filament during patterning. It was a symptom of overexposure, and was much less evident in latter experiments after the exposure time had been reduced.

If the edges of the remaining silane monolayer were perfectly sharp, it would be expected that a growing drop would reach the interface, and then expand further by increasing its contact angle without spreading its footprint, until it reached the contact angle of the silanated surface when it would spread further. Observation showed that drops continued to expand outwards slightly as they increased their contact angles, indicating that the boundary of the monolayer is diffuse.

## Contact angle measurement

The contact angle of water was used to test the efficacy of ultra-violet light to remove the hydrophobic monolayer. The contact angle was compared between substrates which had been cleaned only; those which had been then silanated without patterning; and those which had then subsequently had their entire surface exposed to ultra-violet light and been soaked in acetone. If the treatment was effective, the contact angle on the latter substrates would have matched those on the cleaned-only substrates, as the two should be essentially similar. Figure 7.6 shows the results, and it can be seen that the contact angles after ultra-violet treatment drop back almost to those before silanation, indicating that at least most of the silane has been removed.

### 7.3.4 Drop formation

#### Formation by condensation

It was possible to form droplet arrays on patterned substrates by drawing them out of a water surface. A liquid film clinging to the surface would quickly collapse into discrete drops on the hydrophilic patches. However this method did not tend to

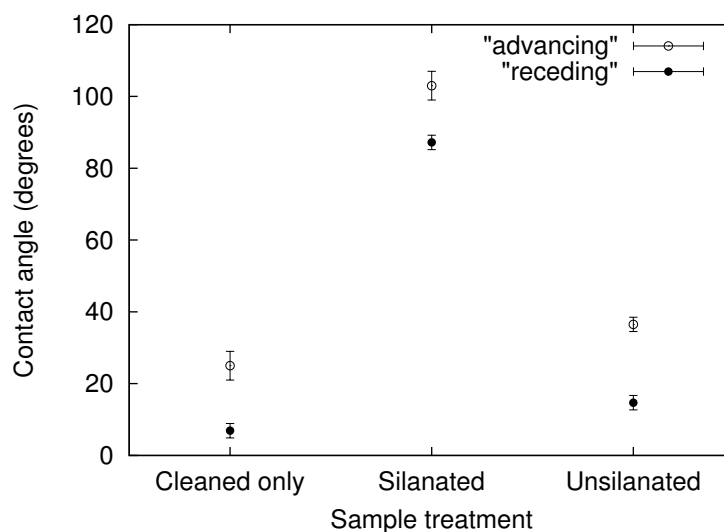


FIGURE 7.6: Graph to show advancing and receding contact angles of water on three silicon surfaces. Obtained by measuring the angle at drops' edges from photographs of growing/shrinking drops. Cleaned only: the surface was cleaned in the usual way without silanation. Silanated: the sample was cleaned and silanated without ultra-violet patterning. Unsilanated: the sample, after silanation, was exposed all over to ultra-violet light and soaked in acetone to remove the entire monolayer.

produce consistent drop sizes across the surface, and the purity of the liquid was limited by that of the bulk water. Therefore arrays were produced by condensation from the atmosphere. The sample was placed on a cooling stage and the temperature lowered until water began to condense, typically at temperatures between  $-3$  and  $7$  °C, depending on the surface and ambient humidity. Drops formed over a few minutes, with the condensation stopped after drops had grown to a size judged sufficient by eye.

### Inter-drop condensation

Silicon samples silanated with 1H,1H,2H,2H-Perfluorodecyldimethylchlorosilane exhibited large amounts of smaller droplets condensing in-between the larger ones. Figure 7.7a shows a typical result, with significant inter-drop condensation even before the main drops are well formed. Freezing events were seen to spread from drop to drop on such substrates.

Using octadecyltrichlorosilane silanation, the problem of inter-drop condensation was almost removed, as can be seen in Figure 7.7b. On glass, the quality was almost as good, with marginally higher occurrence of unwanted drop formation, as seen in Figure 7.8a. Mica surfaces silanated much less homogeneously, and the array quality was comparatively poor, with much condensation in-between sites, as seen in Figure 7.8b.

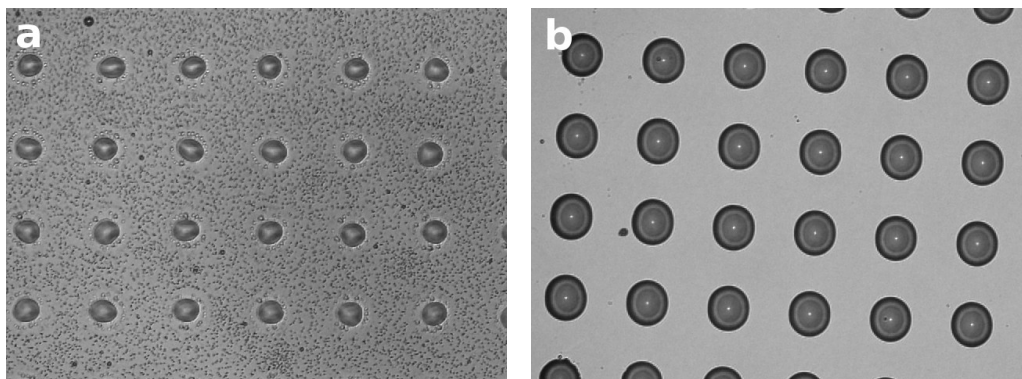


FIGURE 7.7: Optical micrographs of 50  $\mu\text{m}$  water droplet arrays on silicon formed by condensation: (a) using 1H,1H,2H,2H-Perfluorodecyldimethylchlorosilane monolayer; (b) using octadecyltrichlorosilane monolayer.

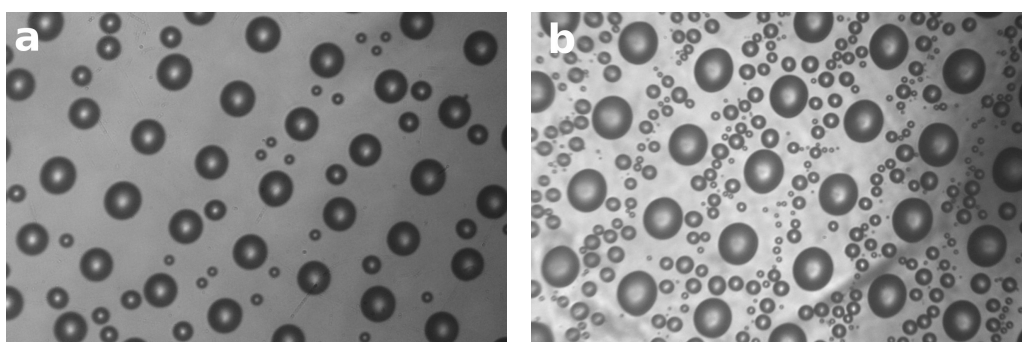


FIGURE 7.8: Optical micrographs of 50  $\mu\text{m}$  water droplet arrays formed by condensation on octadecyltrichlorosilane-patterned surfaces of flat (a) glass and (b) mica.

### A problem of vapour pressures

Solving the problem of inter-drop condensation did not solve the problem of isolating freezing events. After one drop freezes, it depletes the local humidity, due to the lower vapour pressure of ice than supercooled water. The result can be seen in Figure 7.9. A single drop in the centre of the image has frozen, and grown at the expense of nearby liquid drops, which evaporate in the reduced humidity. Several neighbouring drops have frozen via contact before they could evaporate fully.

#### 7.3.5 Oil immersion

In order to isolate nucleation events in neighbouring drops, it was necessary to immerse the array in oil. Early experiments used paraffin oil, but this was found unsuitable as components of the mixture began to freeze below  $-20\text{ }^{\circ}\text{C}$ , making the oil opaque. A silicone oil was found which did not begin to freeze until below  $-40\text{ }^{\circ}\text{C}$ . This oil was allowed to run over a surface after condensation, which it could do without disrupting the droplet array.

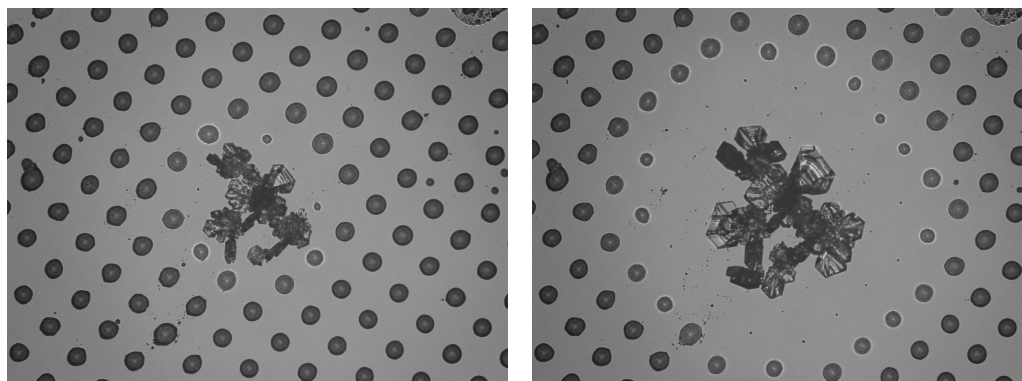


FIGURE 7.9: Optical micrographs of a freezing event in a  $50\ \mu\text{m}$  water droplet array on silicon. The image to the right was taken several minutes after that to the left.

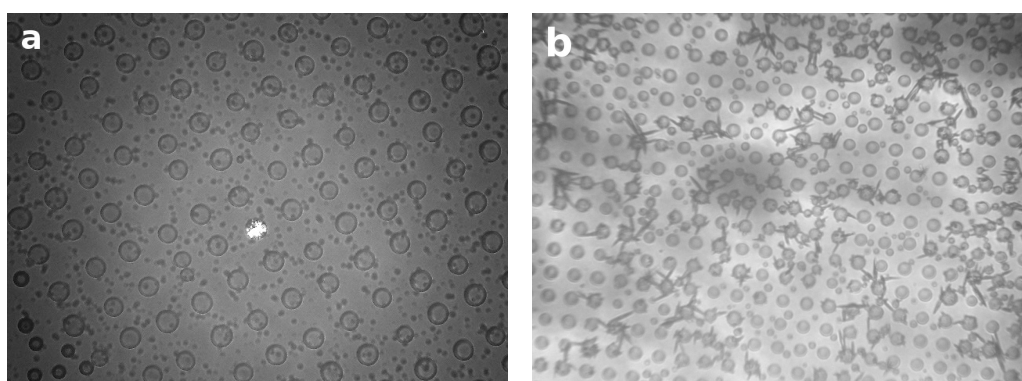


FIGURE 7.10: Optical micrographs showing freezing events in water droplet arrays immersed in silicone oil: (a) a freezing event is isolated in a  $50\ \mu\text{m}$  array on silicon, the frozen drop seen clearly between crossed polarisers; (b) after an hour, frozen drops in a  $20\ \mu\text{m}$  array on glass have grown long fingers extending between drops.

This was seen to successfully isolate freezing events, as can be seen in Figure 7.10a, in which a droplet has frozen without affecting those nearby. The isolation is not perfect, as water is not completely insoluble in the oil. If left on the timescale of an hour, fingers of ice can begin to grow from frozen drops and eventually these can trigger freezing in nearby drops. This is shown in Figure 7.10b, in which fingers of ice can be seen protruding from  $20\ \mu\text{m}$  drops. For most of the experiments performed this was not a concern, and it only became an important consideration when leaving small arrays for long periods, as was done in the latter experiments described in Section 7.6.

Due to the slight solubility, droplets left under the oil in a dry environment would eventually dissolve and evaporate through the oil. Oil was left standing over deionised water overnight before experiments to saturate it with water, to stop immediate dissolution upon application, which would otherwise significantly shrink smaller drop sizes.

## 7.4 Equipment and procedure

### 7.4.1 The cell

Low temperatures were achieved using the liquid nitrogen cooling stage described in Section 3.4.3. A specially-designed cell was used which provided a sealed chamber between sample and objective, preventing frost formation anywhere in the optical path. Figure 7.11 shows the cell. It fits a 5x microscope objective, which is free to move vertically within an o-ring seal. Four screws secure the perspex walls, the aluminium base and the aluminium cooling stage together, with an o-ring sealing the former together, and thermal paste between the latter two.

The perspex optical port shown in Figure 7.11 allows use of transmitted light with transparent samples, through a corresponding hole through the cooling stage. For early experiments with silicon (those described in Section 7.5.2), this was not present, and the base of the cell was smooth aluminium. The optical port was added for use with glass and mica samples, for which reflected light microscopy gave inadequate contrast. An early version of the port involved a hole in the cell base with a glass window further down, but it was found that oil from the sample formed a meniscus in the hole, lensing the light and greatly reducing the field of view. The perspex was used to prevent this occurrence.

Temperature differences between the thermocouple and the substrate centre were calibrated by cooling the cell whilst unsealed to allow entry of a second thermocouple to contact the area of interest directly. For silicon substrates prior to the drilling of an optical port, there was no measurable temperature difference within the 0.1 °C resolution of the probe. After the insertion of the optical port, there was a measured difference of 0.5, 0.7 and 0.5 °C for silicon, glass and mica respectively at -35 °C. Temperatures given subsequently are adjusted by these figures. It should be noted that due to uncertainty in both the calibration and the accuracy of the thermocouple, all absolute temperature should be considered to have an error of 0.3 °C. There is a slightly smaller error of 0.2 °C for relative differences between runs on substrates of the same material, estimated from the variation in freezing temperatures between runs on similar substrates.

The two inlet/outlet pipes were connected to closeable valves, to enable the cell to be flushed with nitrogen gas and then sealed.



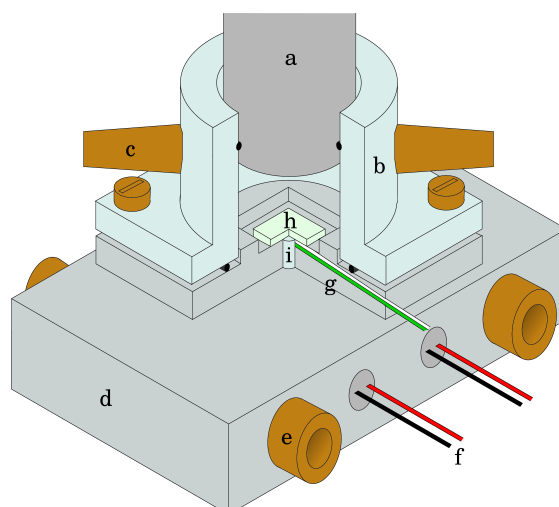


FIGURE 7.11: Diagram showing cut-away view of cell in place on cooling stage: (a) microscope objective; (b) perspex walls; (c) inlet/outlet pipes; (d) aluminium base; (e) liquid nitrogen flow pipes; (f) electric heaters; (g) thermocouple, terminating in a narrow trough beneath the sample, embedded in glue; (h) substrate; (i) perspex optical port.

## 7.4.2 Substrate preparation

Substrates were cut to a size of approximately  $1 \text{ cm}^2$ , and roughened (or not) as appropriate. For all three substrate materials diamond powder scratching was used with varying grit sizes as described in Section 3.1.6. Two other roughening techniques were used for specific substrates: silicon roughening via diamond powder sonication and mica roughening via chemical etching (see below). After roughening, samples were cleaned, plasma treated and silanated as in Section 7.3.2. They were then left under acetone for several hours before being patterned with ultra-violet light as in Section 7.3.3. All substrates were then left under acetone for at least twelve hours before use. Between cleaning and experiment, substrates were handled within a laminar flow cabinet to prevent contamination. They were exposed to unfiltered atmosphere only briefly upon insertion into and removal from the silanation apparatus, and again when condensing droplet arrays.

### Roughening via sonication

Following a method shown to enhance growth of diamond films on silicon surfaces,[60] samples were prepared by sonication in a suspension of diamond powder. This has the effect of producing a surface rich in pits, rather than the long scratches produced by scratching. Samples were placed face-up in a glass vial alongside about 20 mg of “40–60  $\mu\text{m}$ ” diamond powder in 3 mL of deionised water. These were sonicated for 50 minutes before being cleaned and processed in the same way as other substrates. A

smooth control for these substrates was produced by similar sonication in deionised water without diamond powder. Optical microscopy of roughened samples showed it to be roughened on an optically resolvable length scale, although the distribution of roughness across the surface was far from even.

### **Roughening via chemical etching**

Chemically etched mica substrates were produced by Alexander Kulak. Freshly cleaved mica surfaces were submerged in 25 mL of 10 M sodium hydroxide, this was placed in an autoclave and heated to 120 °C for several hours and then washed. The result, revealed by atomic force microscopy, was a very high density of step edges on the surface.

### **7.4.3 Preparing the array**

Substrates were removed from acetone and dried immediately before being placed into the cell. Early experiments with silicon used thermal paste between the sample and the aluminium base; after the optical port was added and there was a need for transparency, a single drop of silicone oil was used instead.

Without the perspex walls in place, the cell temperature was dropped until water was seen to start condensing on the surface. The temperature was then held several degrees below this threshold temperature until the drops were judged to be well-formed. The criteria for this were that they should have grown laterally to the expected size and that the contact angle should have increased considerably beyond that on the plain surface. It was not possible to measure drop contact angles, but those with relatively high angles can be distinguished optically by a strong dark band around the drops' perimeter in small-aperture illumination. This measure is subjective, but it was attempted to standardise drop contact angles between substrates as far as possible by matching the appearance of the drops by eye. Figures 7.12a and 7.12b show still-forming and well-formed droplets.

When drops were judged to have fully formed, the array was immersed in oil by the application of two drops of silicone oil from a pipette, placed to the edges of the substrate and allowed to run inwards. The cell was then sealed as quickly as possible, and flushed for a minute with nitrogen gas. Figure 7.12c shows droplets immersed in oil.

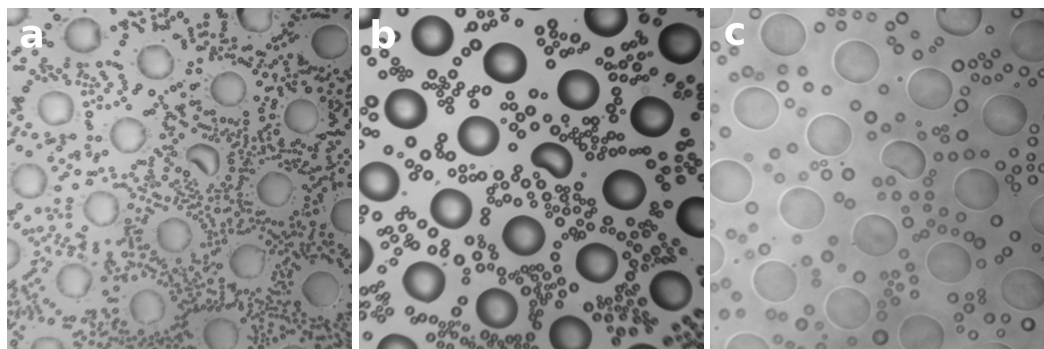


FIGURE 7.12: Time-sequence of optical micrographs showing the preparation of a droplet array by condensation. Droplets are  $50\ \mu\text{m}$  in diameter; the substrate is smooth glass: (a) water drops have condensed but not yet fully formed; (b) droplets have fully condensed onto surface; (c) array has been immersed in silicone oil.

#### 7.4.4 Freezing and melting

With the chamber sealed, the temperature was allowed to drop linearly. From an initial temperature of  $15\ ^\circ\text{C}$ , a rapid ramp was performed to reach  $-15\ ^\circ\text{C}$  in three minutes (no freezing events were ever observed until significantly below this temperature). A slow cool of  $1$  or  $3\ ^\circ\text{C}/\text{minute}$  was then performed until all drops had been seen to freeze. A few minutes after this point the temperature was raised rapidly up to  $15\ ^\circ\text{C}$ , where it was held for a minute, a precaution to avoid retained ice embryos between runs. The cycle was then repeated again to observe a second freezing event in each drop.

Micrographs were taken every  $10\ \text{s}$  when cooling at  $1\ ^\circ\text{C}$ , and every  $5\ \text{s}$  when cooling at  $3\ ^\circ\text{C}$ ; these were timestamped, and could be later related to the temperature in the cell, which was recorded twice per second throughout the experiments. When using silicon as a substrate, crossed polarisers were used to observe the array and freezing events were easily visible as frozen drops appear much brighter than liquid ones, as seen in Figure 7.13a. When using transmitted light for glass and mica substrates, freezing events were found to be clearer without the use of polarisers, and events could be identified by the sudden appearance of structure within the drop, usually coupled with a sudden apparent darkening of the perimeter of the drop. This can be seen in Figure 7.13b.

#### 7.4.5 Analysis

Each sequence of photographs was analysed to find, for each drop, the first image in which it appears frozen. This could then be related to temperature to obtain a distribution of freezing events with temperature. Some drops, if they were grossly missized or misshaped or contained visible contamination, were omitted from the data

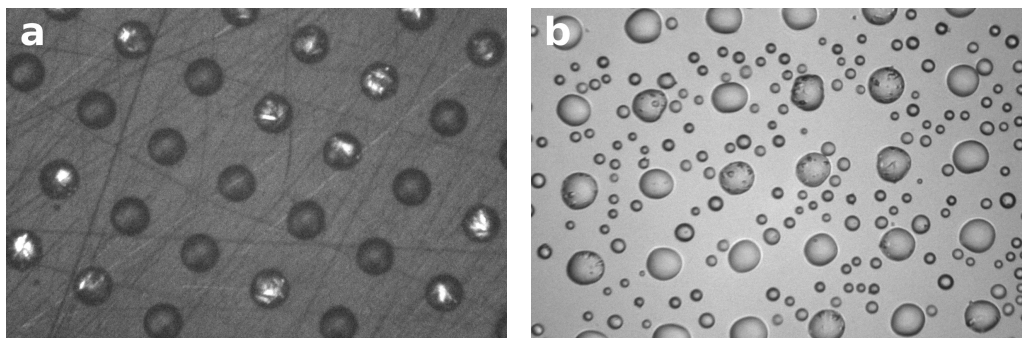


FIGURE 7.13: Sections from optical micrographs showing  $50\ \mu\text{m}$  water droplet arrays at a time at which around 50% of drops have frozen: (a) drops on “ $40\text{--}60\ \mu\text{m}$ ” scratched silicon viewed through crossed polarisers, with frozen drops appearing brighter and taking on structure; (b) drops on smooth glass viewed without polarisers, with frozen drops taking on structure.

set prior to analysis. Some drops which were only just visible at the edge of the view were omitted if it was felt that a freezing event might not be unambiguously identifiable. For all drops not omitted, the first image after freezing could be identified with certainty. Even if the visible change in the drop was very subtle, it could easily be observed by moving backwards and forwards through the sequence of images until a change was found. For  $50\ \mu\text{m}$  arrays, there were typically about 100 droplets in each image.

The analysis was performed for both first and second freezes, with care taken to keep a record of which drop froze at which temperature. This revealed information about the stochasticity of the results, i.e., did the drops which froze early on the first run also freeze early on the second?

## 7.5 Results

### 7.5.1 Coincidence thresholds

In order to quantitatively compare freezing temperature distributions, the Kolmogorov-Smirnov test is used to determine whether or not discrepancies between two distributions can be explained by stochastic variations. The greatest difference between the two normalised cumulative distributions is found, and if the two distributions are results of the same probability distribution, then the difference should be no greater than about [121]

$$\sqrt{\frac{n_1 + n_2}{n_1 n_2}} \quad (7.1)$$

where  $n_1$  and  $n_2$  are the population sizes of the two distributions. Henceforth, two distributions with a maximum difference less than this shall be described as being *within coincidence*.

Most pairs of results were seen to be considerably outside coincidence. However in most cases results could be brought within coincidence by the application of a small temperature displacement to one set, usually of a magnitude comparable to the measurement error in relative temperatures between runs (estimated to be 0.2 °C). Therefore results are given in terms of the size of the temperature shift needed to bring results within coincidence of each other (a positive shift meaning the rougher surface exhibited higher freezing temperatures than the smooth one), with this being judged to be evidence of enhanced nucleation only if considerably above the 0.2 °C error.

## 7.5.2 Silicon

### First results at 3 °C/minute

The first results to be obtained were from a comparison between smooth and “< 1 μm” diamond scratched silicon. These are plotted in Figure 7.14 with freezing temperatures on the smooth surface at the top and on the scratched surface at the bottom. On both substrates the large majority of drops freeze between -34 and -36 °C, with a minority freezing at higher temperatures.

For flat silicon, only three drops froze at a significantly elevated temperature. On the second freeze, these same three drops all froze again above -29 °C, with no other drops freezing above -34 °C. This strongly indicates that these three drops are likely to be contaminated. For the scratched silicon, 14 out of 96 drops froze above -34 °C on the first freeze, 20 on the second. Figure 7.15 shows the first and second freezing temperatures of drops on the scratched surface, revealing little correlation. This suggests that the elevation in freezing temperature on this surface may be a stochastic effect, rather than the result of a few drops with favourable nucleation sites, however a temperature shift of 0.34 °C brings the two distributions within coincidence, so it is difficult to be sure that the difference is significant.

### Further results at 1 °C/minute

Using a slower ramp rate, freezing was compared on smooth silicon and on surfaces scratched with all three grades of diamond powder. Figure 7.16 shows the results. On flat silicon, no drops froze above -34 °C on either run. With the “< 10 nm” diamond

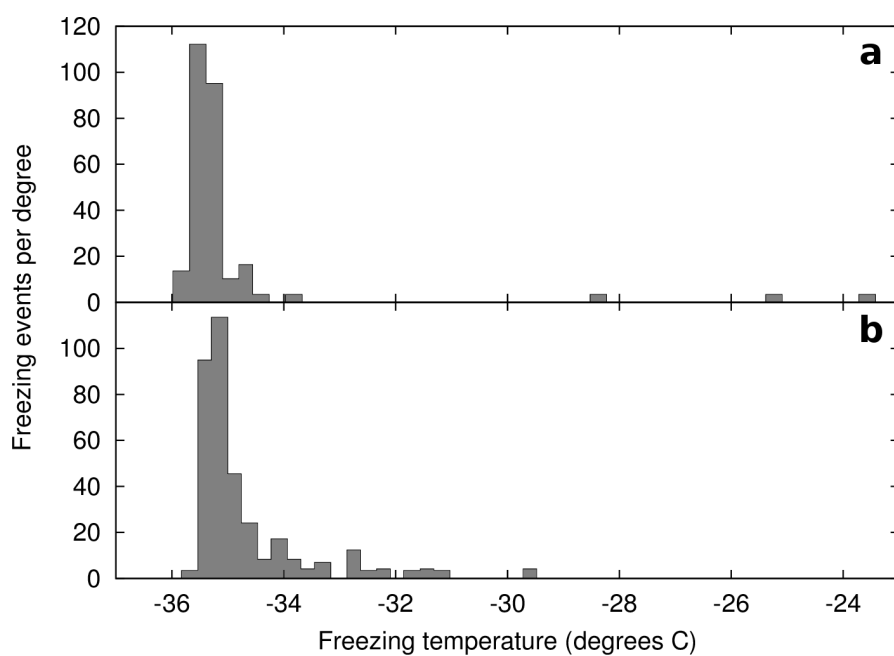


FIGURE 7.14: Histograms showing freezing temperatures on the first freeze of  $50\ \mu\text{m}$  water drops at a temperature ramp of  $3\ \text{°C/minute}$  on (a) smooth silicon and (b) silicon scratched with “ $< 1\ \mu\text{m}$ ” diamond powder.

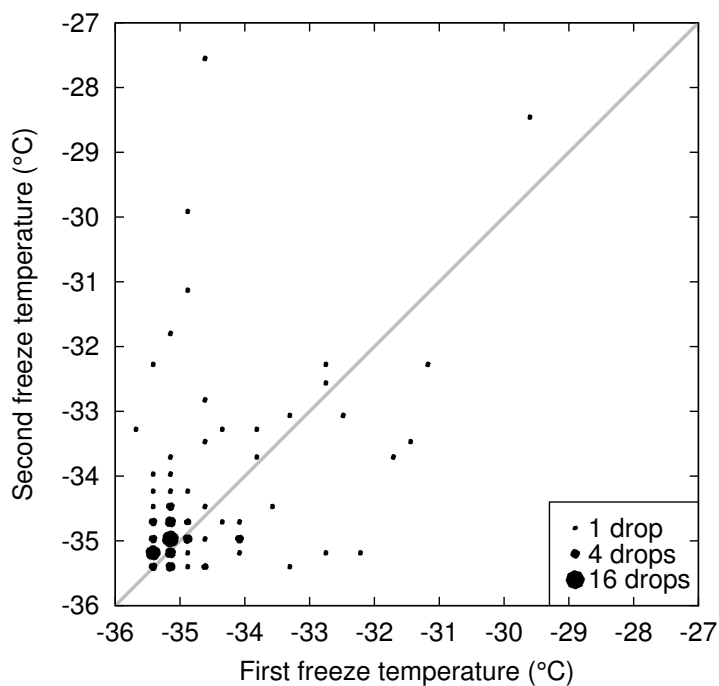


FIGURE 7.15: Correlation plot of freezing temperatures on first and second run on “ $< 1\ \mu\text{m}$ ” diamond scratched silicon, at a temperature ramp of  $3\ \text{°C/minute}$ . The area of each point indicates the number of drops it represents, and the grey line shows the line of equal temperatures. Pearson correlation coefficient: 0.447

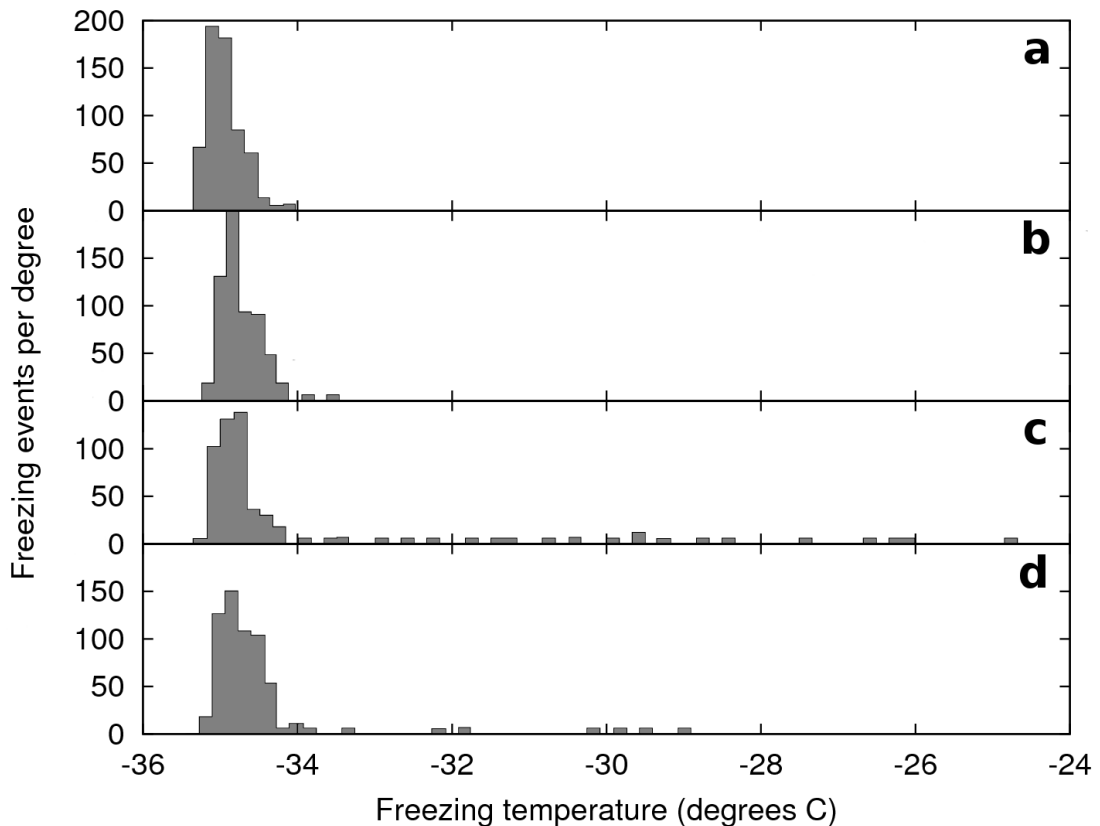


FIGURE 7.16: Histograms showing freezing temperatures on the first freeze of  $50\ \mu\text{m}$  water drops at a temperature ramp of  $1\ ^\circ\text{C}/\text{minute}$  on (a) smooth silicon; (b) silicon scratched with “ $< 10\ \text{nm}$ ” diamond powder; (c) silicon scratched with “ $< 1\ \mu\text{m}$ ” diamond powder; (d) silicon scratched with “ $40\text{--}60\ \mu\text{m}$ ” diamond powder.

scratched surface, only two drops froze slightly before  $-34\ ^\circ\text{C}$  on both runs (not the same drops). On the “ $< 1\ \mu\text{m}$ ” diamond scratched surface, 22 out of 101 drops froze before  $-34\ ^\circ\text{C}$  on the first run, and 19 on the second run. Finally on the “ $40\text{--}60\ \mu\text{m}$ ” diamond scratched surface, 8 out of 105 drops froze before  $-34\ ^\circ\text{C}$ , and 7 on the second run.

For substrates scratched with “ $< 10\ \text{nm}$ ” and “ $40\text{--}60\ \mu\text{m}$ ” diamond powder, results can be brought within coincidence of the smooth results with temperature shifts of  $0.13$  and  $0.18\ ^\circ\text{C}$  respectively: within error. For “ $< 1\ \mu\text{m}$ ”-scratched silicon, no such coincidence can be achieved, minimum discrepancy being at 1.4 times coincidence at a temperature shift of  $0.31\ ^\circ\text{C}$ .

Of the eight drops freezing before  $-34\ ^\circ\text{C}$  on the first run on the “ $40\text{--}60\ \mu\text{m}$ ” diamond scratched surface, four of them are amongst the seven freezing early on the second run, indicating strong correlation. For the “ $< 1\ \mu\text{m}$ ” diamond scratched surface, correlation between the first and second freezing temperatures is shown in Figure 7.17. It can be clearly seen that there is a strong positive correlation, indicating that the elevated freezing temperatures are due to heterogeneity in the droplet population rather than

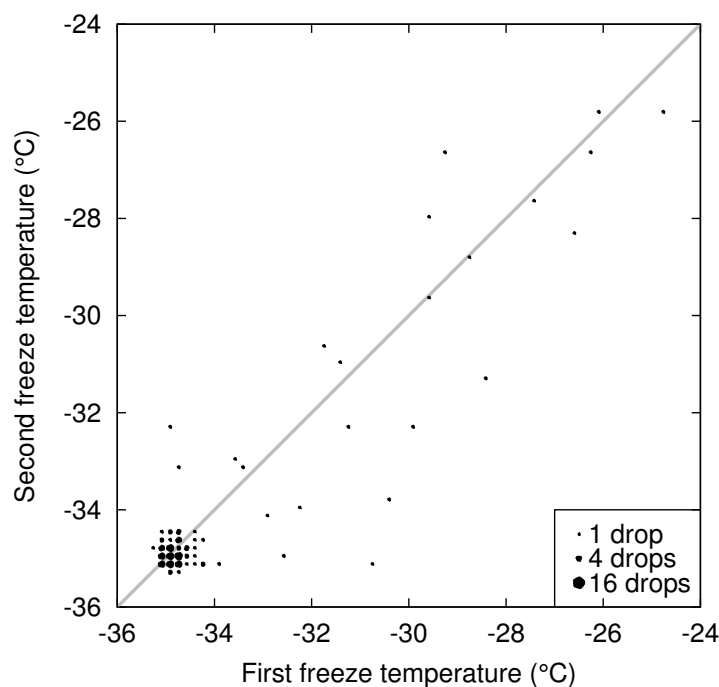


FIGURE 7.17: Correlation plot of freezing temperatures on first and second run on “ $< 1 \mu\text{m}$ ” diamond scratched silicon, at a temperature ramp of  $1 \text{ }^\circ\text{C}/\text{minute}$ . The area of each point indicates the number of drops it represents, and the grey line shows the line of equal temperatures. Pearson correlation coefficient: 0.918

a stochastic effect across the population. Considering that there is a high density of scratches under each droplet, this allows two possible conclusions: either a sizable minority of the drop population is contaminated, for example with residual diamond powder, or there is a real effect from the scratches but it is limited to a small number of favourable sites which do not occur under every drop. From the observation that about 20% of drops froze at elevated temperatures, this could be explained by an effective nucleation site density of one per  $10,000 \mu\text{m}^2$ , i.e. 100 sites per  $\text{mm}^2$ . This is of a similar order to observed nucleation densities of crystals from vapour on scratched and etched surfaces, although the wide range and incompatible procedures of such results make any meaningful comparison impossible.

### Diamond-pitted silicon

Drop freezing temperatures were compared on silicon pitted with “ $40\text{--}60 \mu\text{m}$ ” diamond powder as described in Section 7.4.2 and on a smooth control. Figure 7.18 shows the results. Only two out of 104 drops freezing above  $-34 \text{ }^\circ\text{C}$  on the smooth surface (three on the second run) and only one out of 95 drops freezing above  $-34 \text{ }^\circ\text{C}$  on the pitted surface on both runs; the two results are within coincidence after a temperature shift of  $-0.14 \text{ }^\circ\text{C}$ .



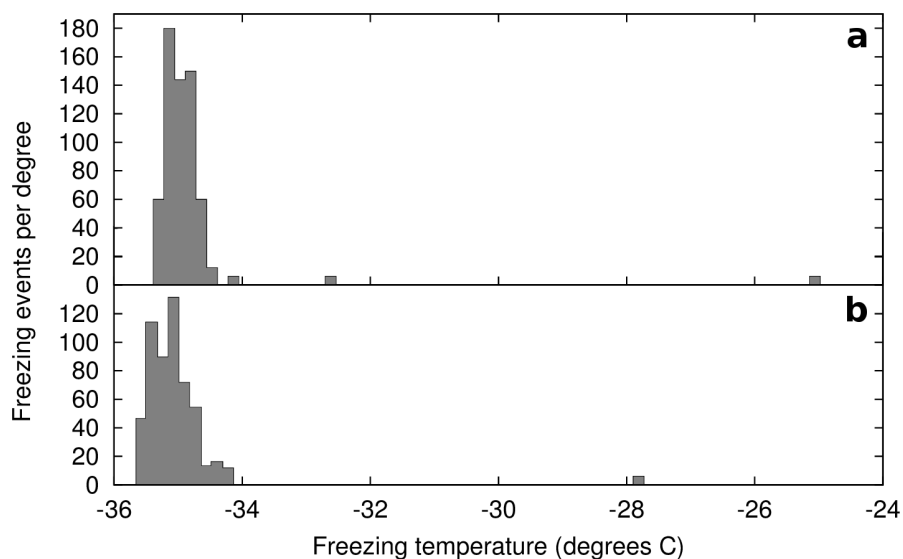


FIGURE 7.18: Histograms showing freezing temperatures on the first freeze of  $50\ \mu\text{m}$  water drops at a temperature ramp of  $1\ ^\circ\text{C}/\text{minute}$  on (a) smooth silicon and (b) silicon pitted with " $40\text{--}60\ \mu\text{m}$ " diamond powder.

### 7.5.3 Glass

The effect on ice nucleation of roughening a glass surface was studied by comparison of the freezing temperatures of water drops on a smooth surface and on one scratched with " $< 1\ \mu\text{m}$ " diamond powder. The results are shown in Figure 7.19. There is no significant difference between the smooth and scratched surfaces (results are within coincidence with no temperature shift), and out of 104 drops on each, four drops froze before  $-34\ ^\circ\text{C}$  on both on each run.

### 7.5.4 Mica

#### Chemically etched mica

Freezing of water was studied on a mica substrate which had been chemically etched to produce a high density of step edges, as described in Section 7.4.2. Figure 7.20 shows the results for both a smooth control and the etched mica. One drop froze above  $-34\ ^\circ\text{C}$  on the smooth sample and five drops out of 103 froze above  $-34\ ^\circ\text{C}$  on the etched sample on each run. A high temperature shift of  $0.49\ ^\circ\text{C}$  is required to bring results within coincidence: over twice the estimated uncertainty in temperature between runs.

The difference seems potentially significant, however is not quite large enough for this to be certain. If etched mica does promote nucleation, it is impossible to say whether this is due to the topography or because the surface chemistry has been changed by the etching process.

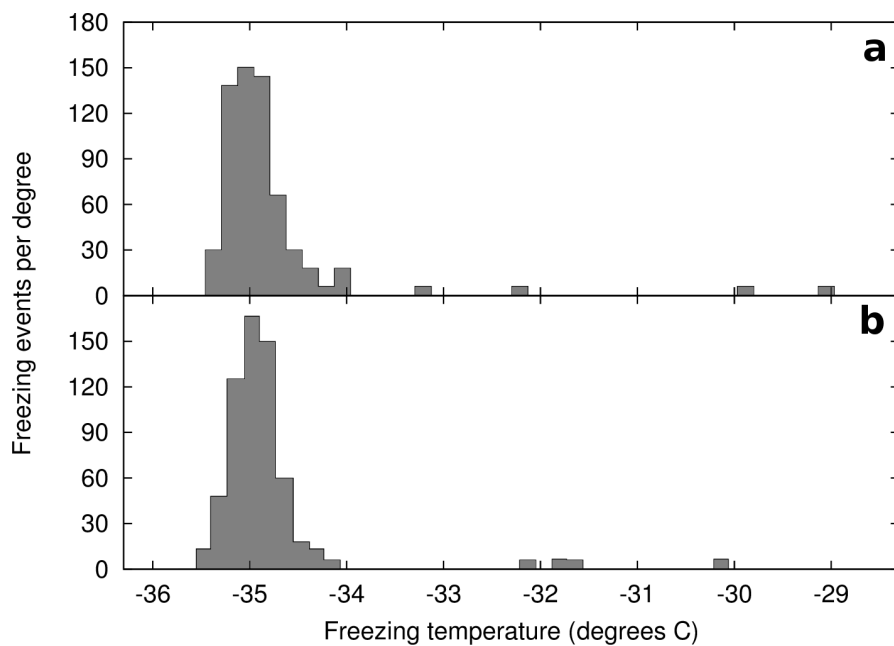


FIGURE 7.19: Histograms showing freezing temperatures on the first freeze of  $50\ \mu\text{m}$  water drops at a temperature ramp of  $1\ ^\circ\text{C}/\text{minute}$  on (a) smooth glass and (b) glass scratched with " $< 1\ \mu\text{m}$ " diamond powder.

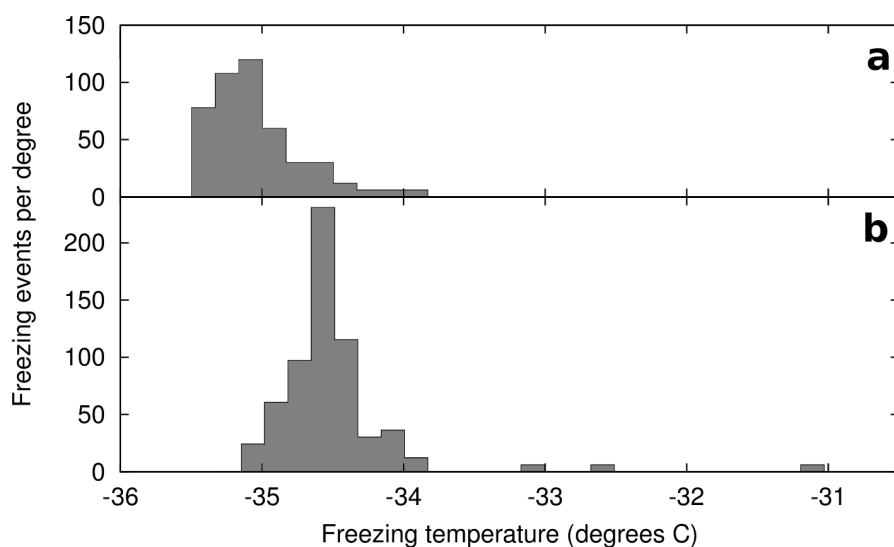


FIGURE 7.20: Histograms showing freezing temperatures on the first freeze of  $50\ \mu\text{m}$  water drops at a temperature ramp of  $1\ ^\circ\text{C}/\text{minute}$  on (a) smooth mica and (b) chemically etched mica.

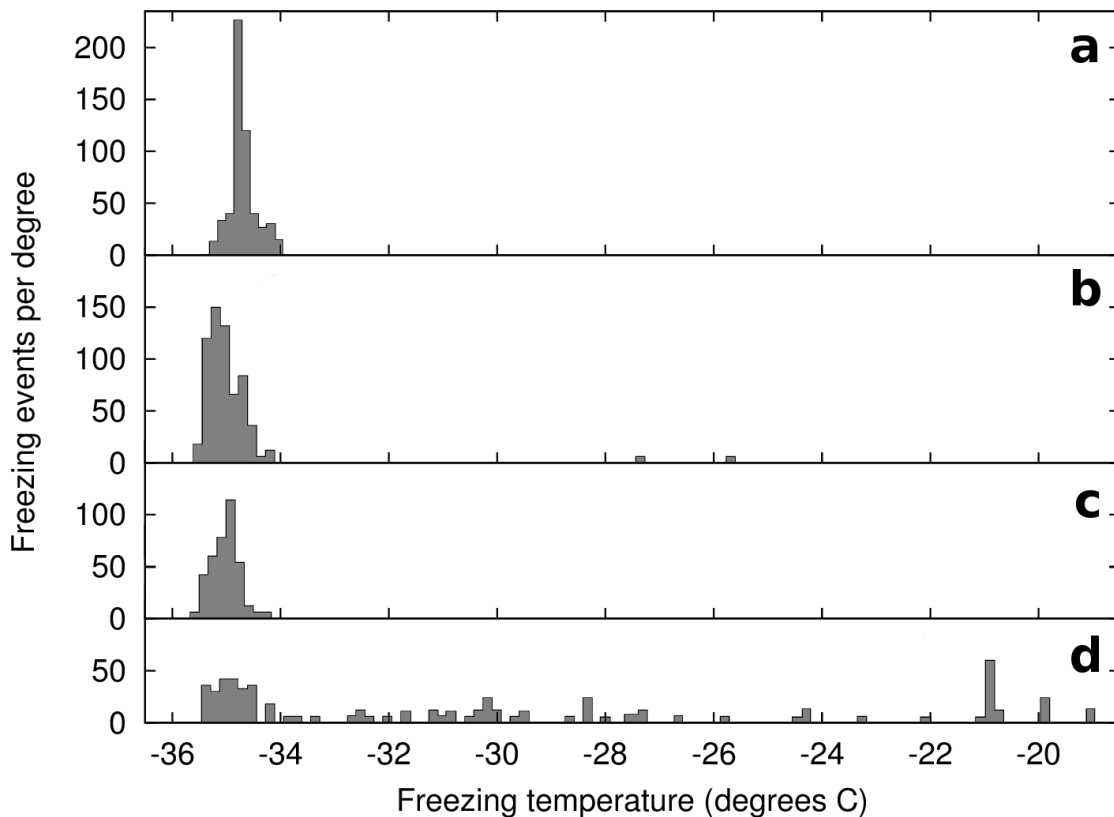


FIGURE 7.21: Histograms showing freezing temperatures on the first freeze of  $50\ \mu\text{m}$  water drops at a temperature ramp of  $1\ ^\circ\text{C}/\text{minute}$  on (a) smooth mica; (b) mica scratched with “ $< 10\ \text{nm}$ ” diamond powder; (c) mica scratched with “ $< 1\ \mu\text{m}$ ” diamond powder; (d) mica scratched with “ $40\text{--}60\ \mu\text{m}$ ” diamond powder.

### Scratched mica

Freezing points of water drops were studied on mica scratched with various grades of diamond powder. The results are shown in Figure 7.21. On both the smooth surface and that scratched with “ $< 1\ \mu\text{m}$ ” diamond powder, no drops froze above  $-34\ ^\circ\text{C}$ . On the surface scratched with “ $< 10\ \text{nm}$ ” diamond powder, on the first run two out of 106 drops froze above  $-34\ ^\circ\text{C}$ , five on the second run. The surface scratched with “ $40\text{--}60\ \mu\text{m}$ ” powder shows considerably higher occurrence of early nucleation, with 63 out of 103 drops freezing before  $-34\ ^\circ\text{C}$ . However on a second run, only nine drops froze above  $-34\ ^\circ\text{C}$ . Figure 7.22 shows freezing temperatures of all drops compared between the two runs on this substrate.

Results for “ $< 10\ \text{nm}$ ” and “ $< 1\ \mu\text{m}$ ”-scratched mica can be brought within coincidence with smooth mica by applying temperature shifts of  $-0.31$  and  $-0.23\ ^\circ\text{C}$  respectively. “ $40\text{--}60\ \mu\text{m}$ ”-scratched mica cannot be brought within coincidence, with a minimum discrepancy of 3.7 times coincidence across all possible temperature shifts.

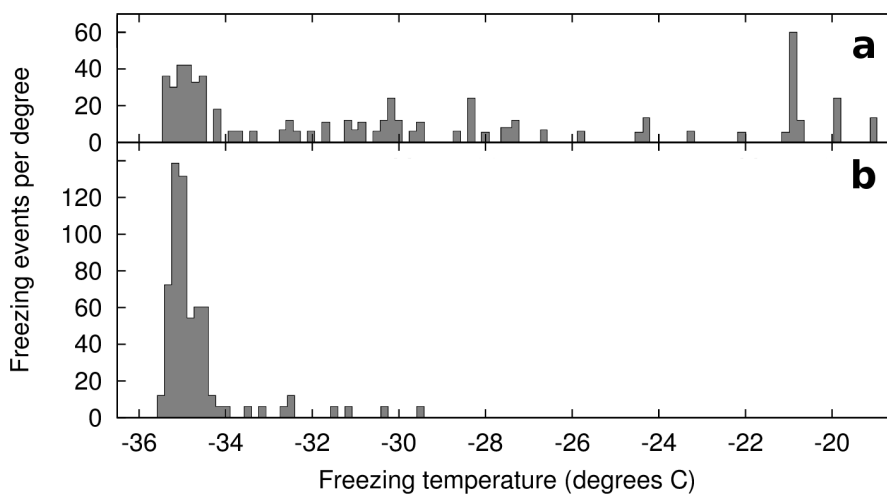


FIGURE 7.22: Histograms showing freezing temperatures on (a) the first and (b) the second freeze of  $50\ \mu\text{m}$  water drops at a temperature ramp of  $1\ ^\circ\text{C}/\text{minute}$  on mica scratched with “ $40\text{--}60\ \mu\text{m}$ ” diamond powder.

It was noticed that freezing events on the first run on this last substrate seemed to occur preferentially in drops adjacent to those already frozen. Only one drop was observed to freeze before the four adjacent to it. Disqualifying those drops at the edge of the view (i.e. those where not all four neighbouring drops could be seen) there were 52 drops on the surface. If nucleation was random, each drop would have a 20% chance of freezing before all four of its neighbours. This gives an expectation for the number of observed isolated freezing events of 10.4, and a probability of observing one event or less of 0.013%. Therefore it may be said with confidence that freezing events on this substrate were not isolated.

## 7.6 Heterogeneous or homogeneous nucleation?

### 7.6.1 The problem and the solution

The above results suggests that in most cases surface roughening does not significantly affect the freezing temperatures of  $50\ \mu\text{m}$  water drops on silicon, glass or mica, with a few potential exceptions. This however leaves us with two possible conclusions:

- ice nucleation on these substrates is heterogeneous, but roughening is not significantly enhancing nucleation;
- ice nucleation occurs homogeneously in these systems, or potentially at the oil-water interface, either of which would be unaffected by roughening of the substrate.

It is impossible to tell, from the results presented thus far, which of these explanations is correct. The observed freezing temperatures are comparable to those in the literature for homogeneous nucleation: Murray et al. report peak freezing of 10–40  $\mu\text{m}$  drops between -37 and -38  $^{\circ}\text{C}$  following cooling at 2.5  $^{\circ}\text{C}/\text{minute}$  using a similar technique.[112] This is lower than the peak freezing temperatures of -34 to -36  $^{\circ}\text{C}$  observed here, but this may be expected as the drops here are larger and cooled at a slower rate.

Assuming homogeneous nucleation, the rate can be quantified. Taking the results shown in Figure 7.16a as a typical example, at the peak freezing rate at -35.1  $^{\circ}\text{C}$ , the nucleation rate is estimated at  $1.6 \times 10^6 \text{ cm}^{-3}\text{s}^{-1}$ , assuming a hemispherical shape. Murray et al. plots homogeneous nucleation rates from numerous studies in this temperature range,[112] and this value is within the scatter of results, although above the trend line which predicts a rate of  $5 \times 10^4 \text{ cm}^{-3}\text{s}^{-1}$  at this temperature.

Carvalho et al. have discriminated experimentally between homogeneous and heterogeneous freezing in drop populations.[116, 117] They observed the freezing of polymer drops of various sizes on the same substrates, which were binned by size and the nucleation rate calculated for each size range. By studying the dependence of the drop nucleation rate  $J$  on the drop radius  $r$ , it was found that

$$J \propto r^n \quad (7.2)$$

where the value of  $n$  is indicative of homogeneous or heterogeneous nucleation. For various nucleation modes,  $n$  would be expected to vary as follows:

- homogeneous nucleation would lead to  $n = 3$ ;
- heterogeneous nucleation on either the substrate or the oil-water interface would lead to  $n = 2$ ;
- nucleation along the oil-water-substrate contact line would lead to  $n = 1$ .

In these experiments it was not possible to use multiple-sized drops on one substrate. However by comparing nucleation rates between substrates with differently-sized drops, the nature of nucleation could in theory be determined.

## 7.6.2 Procedure

Substrates were prepared exactly as described in Section 7.4.3, without any roughening of any of the surfaces. Arrays were produced with drop diameters of 50, 30 and 20  $\mu\text{m}$ , condensed as usual and trapped under oil. After sealing the cell, the substrate was taken

down to a temperature of  $-34.5\text{ }^{\circ}\text{C}$  (as measured, corresponding to estimated substrate temperatures of  $-34.0$ ,  $-33.8$  and  $-34.0\text{ }^{\circ}\text{C}$  for silicon, glass and mica respectively) and left at that temperature until most droplets had frozen or until many drops had extended fingers of ice into each other.

Analysis was performed by, for each drop, finding the image in which it froze, if it did freeze, or the image in which it was compromised by a neighbouring drop extending a finger into its vicinity. For each pair of consecutive images, each liquid drop which froze of its own accord over that time period was considered a positive event, and each one that remained liquid a negative event. Drops which froze with help from their neighbours contributed negative events for each pair of images up to the point when the origin of a freezing event would be considered ambiguous, and were not considered thereafter. Drop behaviour prior to the temperature stabilising at  $-34.5\text{ }^{\circ}\text{C}$  was not considered, this allowed contaminated drops which would tend to freeze early to do so without affecting results.

Across all images, the probability  $p$  of any one drop freezing in any one time period could be calculated, with an error, by considering the total number of positive and negative events recorded across the sequence. The ratio of positive to negative events gives  $p$ , and from binomial statistics the error in  $p$  is given by [122]

$$\Delta p = \sqrt{\frac{p(1-p)}{N}} \quad (7.3)$$

where  $N$  is the total number of events. The nucleation rate  $J$ , the number of nucleation events per drop per second, can then be found from

$$1 - p = e^{-J\Delta t} \quad (7.4)$$

where  $\Delta t$  is the time interval between images.

Drop diameters were not assumed to match those of the photomask patterns, but were measured directly. For each substrate a mean diameter was found by taking a sample of twelve random drops and measuring their diameters.

### 7.6.3 Results

The number of unfrozen drops was found to decrease approximately exponentially, as evidenced by the linear decrease in the logarithm of the unfrozen fraction with time, shown for silicon substrates in Figure 7.23. Results for other substrates were found to

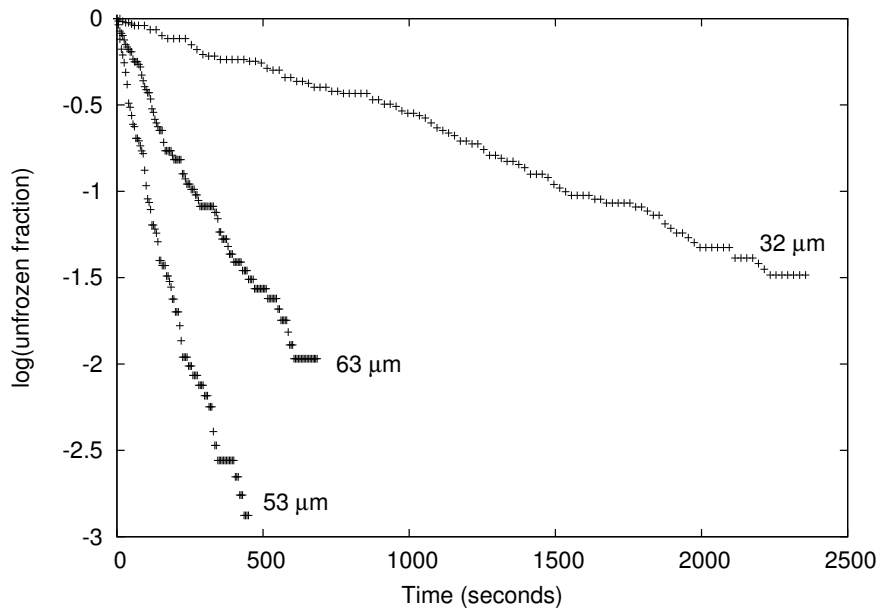


FIGURE 7.23: Graph showing the logarithm of the fraction of unfrozen droplets with time for three populations on silicon substrates. Each line is labelled with the mean drop diameter. The linear decay is evidence of a well defined constant nucleation rate.

be similarly linear. This indicates that the nucleation rate is approximately constant with time, validating the approach of Equation 7.4.

Figures 7.24, 7.25 and 7.26 plot results for silicon, glass and mica respectively. The nucleation rate for each substrate is plotted against the droplet diameter, alongside lines showing a gradient corresponding to  $n = 2$  (heterogeneous nucleation) and  $n = 3$  (homogeneous nucleation).

It can be seen that there is a significant scatter in points, making firm conclusions difficult. For mica, there appears to be no trend at all; the reasons for this are unknown. The explanation for the scatter, significantly above error, could be twofold: firstly, very small changes in the substrate temperature could lead to significant changes in the nucleation rate, and secondly the contact angle and hence volume of droplets is not well controlled and hence likely varies considerably between arrays. If (and only if) nucleation is homogeneous, this would produce a scatter in nucleation rates.

On silicon, there is a weak trend, and homogeneous nucleation fits the limited data slightly better than heterogeneous nucleation. On glass, there is a stronger trend, and homogeneous nucleation fits the points quite well.

This system does not appear to be well-suited to identifying the dominant mode of nucleation. As different droplet sizes are studied independently, there is opportunity for temperature variation between substrates, and as the contact angle cannot be controlled, the droplet volume is never exactly known. The results here cannot be

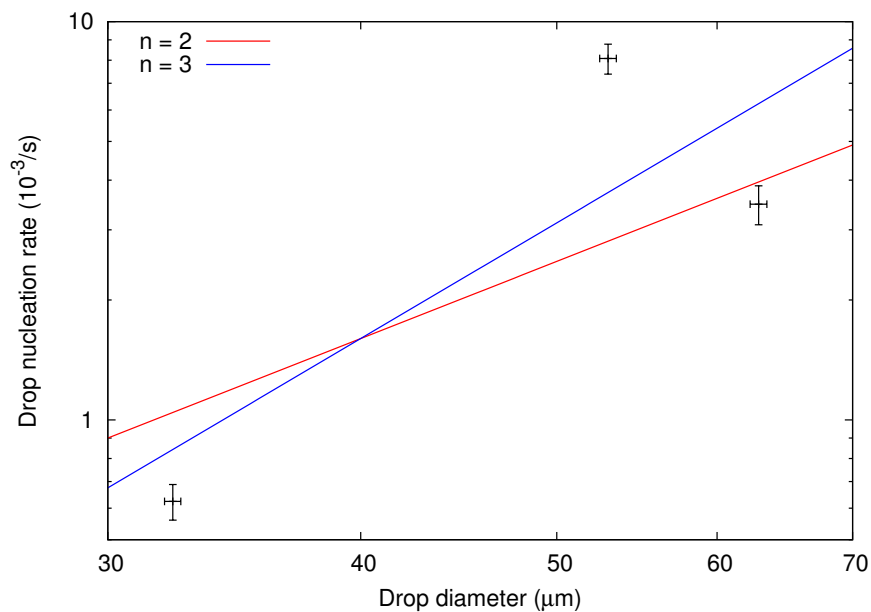


FIGURE 7.24: Graph showing the droplet nucleation rate and mean diameter on three silicon substrates. The red and blue lines show the gradients expected for heterogeneous and homogeneous nucleation respectively.

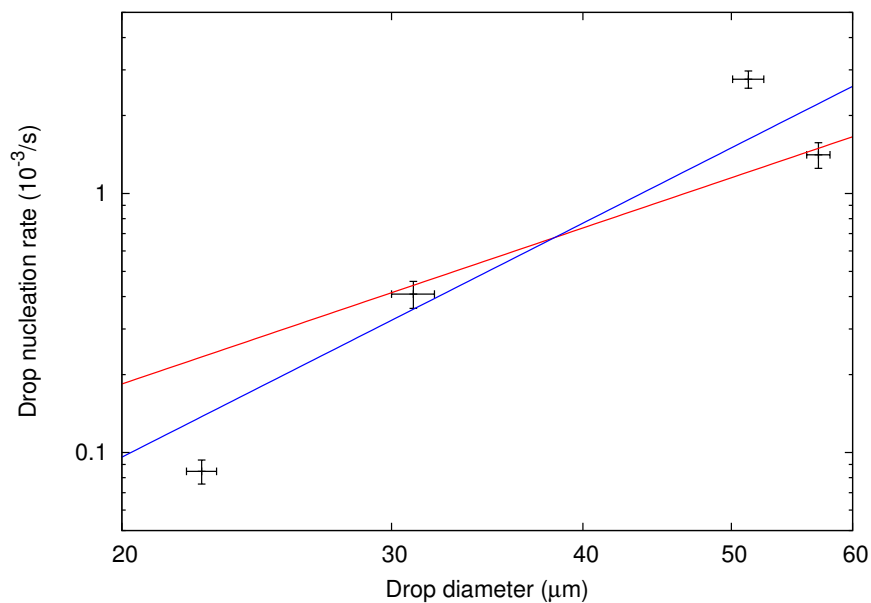


FIGURE 7.25: Graph showing the droplet nucleation rate and mean diameter on four glass substrates. The red and blue lines show the gradients expected for heterogeneous and homogeneous nucleation respectively.



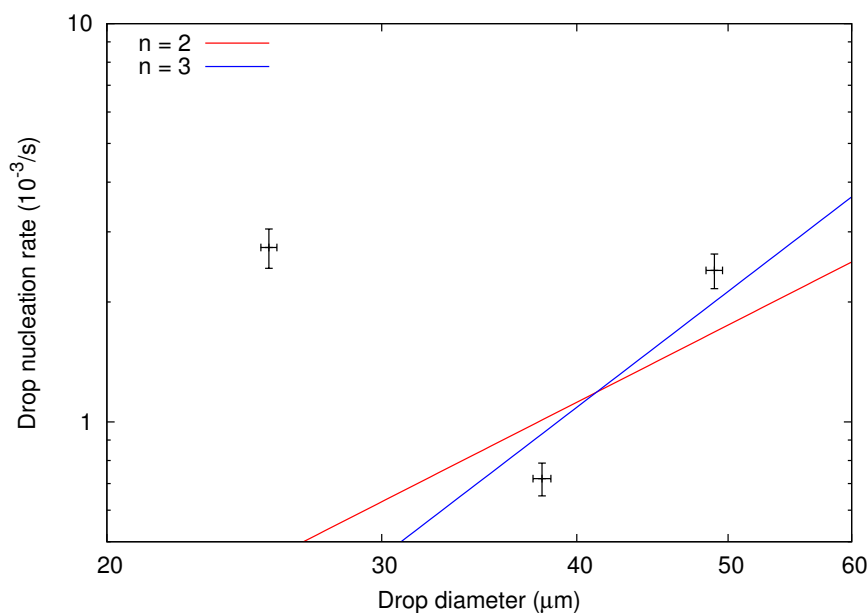


FIGURE 7.26: Graph showing the droplet nucleation rate and mean diameter on three mica substrates. The red and blue lines show the gradients expected for heterogeneous and homogeneous nucleation respectively.

considered conclusive, however the trends evident and the large scatter are suggestive of homogeneous nucleation.

## 7.7 Extension to other liquids

The surface patterning technique was found to be effective at forming arrays of several other liquids. Figure 7.27 shows arrays of dimethyl sulphoxide, glycerol and formamide on silicon, formed by immersing the substrate in the liquid and withdrawing rapidly. These liquids all have extremely low vapour pressures at room temperature, and so the arrays could be handled in atmosphere for a short period without evaporating.

Glycerol was not used for freezing experiments as it supercools to an extreme extent. Triethylene glycol also formed good quality arrays, although no photographs exist, and was cooled as with water arrays to initiate freezing, but the drops still appeared to be liquid at  $-75\text{ }^{\circ}\text{C}$ , at which point the surrounding silicone oil was rapidly freezing.

Dimethyl sulphoxide and formamide, however, were both observed to freeze under the microscope. These both have an advantage over water/ice in that the crystals are brilliantly visible between crossed polarisers, making unambiguous identification of freezing events very simple.

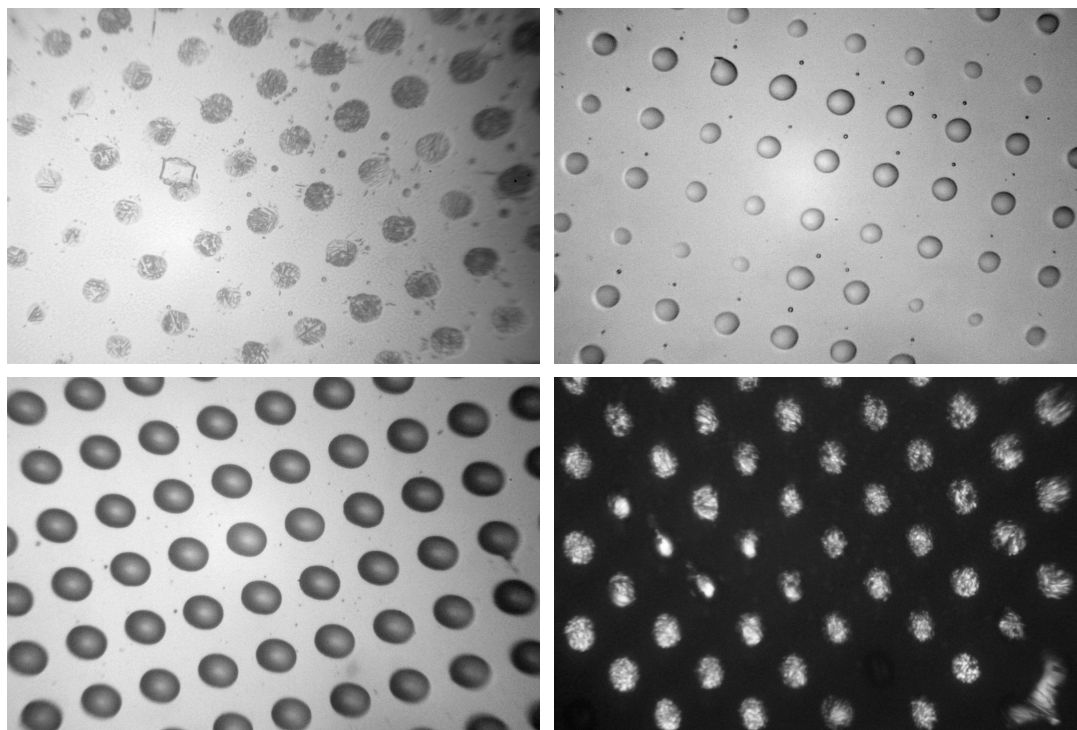


FIGURE 7.27: Optical micrographs showing  $50\ \mu\text{m}$  arrays of: (top left) frozen dimethyl sulphoxide; (top right) liquid glycerol; (bottom left) liquid formamide; (bottom right) mostly frozen formamide between crossed polarisers.

### 7.7.1 Dimethyl sulphoxide

Dimethyl sulphoxide arrays were formed on patterned smooth silicon by drawing from bulk liquid in atmosphere and then quickly trapping under a layer of silicone oil. Unfortunately, the liquid proved to be slightly soluble in the oil, and the droplets shrank and disappeared in a matter of minutes. To prevent this, silicone oil was saturated with dimethyl sulphoxide by leaving 1 mL of oil standing over 1 mL of dimethyl sulphoxide for 24 hours. After coating an array in this saturated oil, the substrate was quickly sealed inside the cell (which also contained a reservoir of dimethyl sulphoxide to keep the air saturated) to prevent evaporation.

As seen in Figure 7.27, the array formed was highly uneven, with a large change in droplet volume from one side of the view to the other. Figure 7.28 shows the freezing temperatures, demonstrating a very strong dependence upon droplet size. This is tentatively ascribed to significant water absorption; water would be at higher concentration in smaller droplets, and would reduce the melting point of the mixture. Upon reheating, melting was observed at around  $-15\ ^\circ\text{C}$ , about  $30\ ^\circ\text{C}$  below the melting point, implying a large amount of absorbed water.

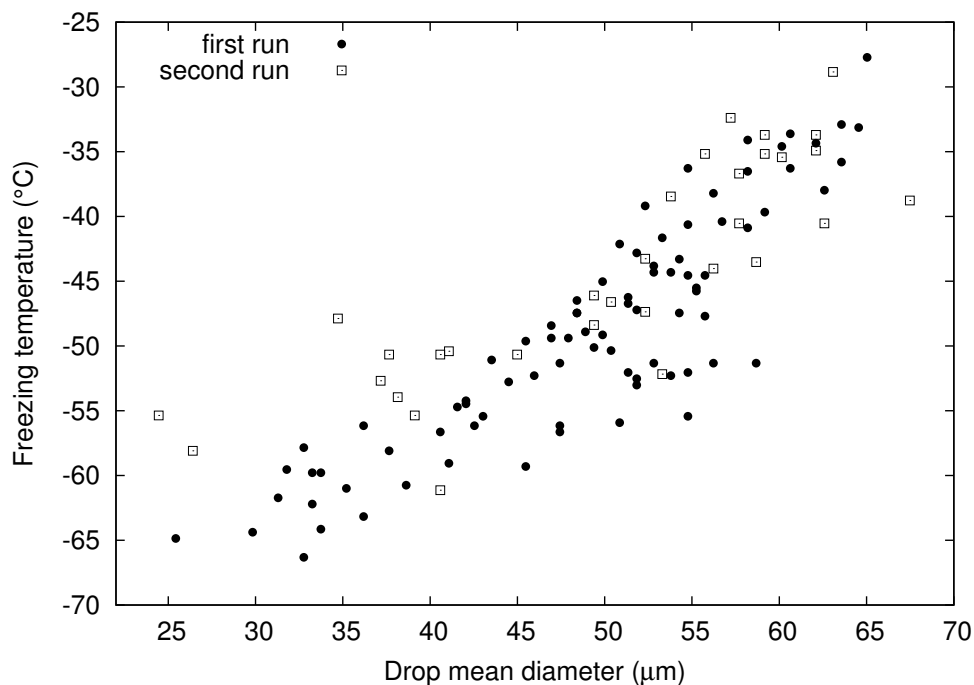


FIGURE 7.28: Graph showing the freezing temperatures of droplets of dimethyl sulphoxide on silicon as a function of size. Two consecutive runs were performed.

### 7.7.2 Formamide

Formamide arrays were initially trapped under silicone oil after formation. An experiment to freeze droplets in this way on silicon found them to freeze between  $-75$  and  $-85$  °C, unfortunately this was simultaneous with the freezing of the oil. Melting was seen upon reheating at  $-20$  °C, about  $20$  °C below the melting point of pure formamide.

As the vapour pressure of formamide is extremely low, considerably lower than that of dimethyl sulphoxide, it was found that arrays could be used without oil. One array on smooth silicon froze between  $-50$  and  $-65$  °C, with droplets melting slightly below  $0$  °C upon reheat. Another on silicon scratched with " $< 1$  μm" diamond powder froze at  $-90$  to  $-100$  °C, with melting observed at  $-46$  °C upon reheat. This difference is unlikely to be related to the change in surface topography, but rather to a difference in array preparation technique leading to a very different amount of absorbed water vapour.

## 7.8 Summary

Previous results had suggested that picolitre water droplets froze at higher temperatures on rougher silicon surfaces, but this was shown to be an artifact of faster frost spread on scratched surfaces. To see if there was a real effect on nucleation, smooth and roughened

surfaces of silicon, glass and mica were patterned with a hydrophobic monolayer which allowed the condensation of a regular array of picolitre water droplets.

Freezing temperatures of drops were compared between smooth and scratched surfaces, and in all cases nucleation occurred at about  $-35\text{ }^{\circ}\text{C}$ , just above the homogeneous nucleation temperature. Allowing for a small error in temperature between runs, all results were within coincidence of equivalent smooth results with three exceptions. First was mica scratched with “40–60  $\mu\text{m}$ ” diamond powder, but here apparently higher freezing temperatures were seen to be an artifact of freezing events spreading between drops. The second was silicon scratched with “ $< 1\ \mu\text{m}$ ” diamond powder where the population was heterogeneous, with about 20% freezing at an elevated temperature, although whether this was due to contamination or to topographically favourable sites under a minority of drops could not be determined. The final exception was chemically etched mica, where water appeared to freeze about  $0.5\text{ }^{\circ}\text{C}$  higher on the etched substrate. This difference is likely to be significant, although it is not quite large enough to firmly rule out temperature discrepancies between runs, and if it is accepted then we cannot know whether to attribute it to topographical or chemical changes.

Attempts to diagnose heterogeneous or homogeneous nucleation were inconclusive. Attempts to use other liquids than water were unsuccessful.

## Chapter 8

# On the nucleation of calcium carbonate from solution

### 8.1 Introduction

#### 8.1.1 On calcium carbonate

Calcium carbonate ( $\text{CaCO}_3$ ) is a mineral of considerable geological importance, being the principal component of both chalk and limestone. It is a widely-studied compound in biomineralisation, being the main compound making up eggshells, pearls and many invertebrate shells. Its crystallisation is widely observed as the formation of limescale on surfaces exposed to hard water.

It has three crystal anhydrous polymorphs: calcite (the most stable), aragonite and vaterite. Calcite has a trigonal crystal structure and tends to form rhombohedral crystals with flat faces on the {104} planes. Aragonite has an orthorhombic structure, and in the conditions typical in these experiments tends to form long prismatic needles, often bunched together to give a “wheat sheaf” appearance. Vaterite, the least stable polymorph, has a hexagonal crystal structure and usually appears as round spherulitic structures.

There is also a highly metastable amorphous phase, which unlike aragonite and vaterite is never seen to grow to large sizes. Estimates of solubility vary wildly and are highly dependent on pH, temperature and other factors; the tendency of the carbonate concentration to slowly reach an equilibrium with atmospheric carbon dioxide further complicates matters. One set of typical estimates are given in Table 8.1. Note that some estimates of amorphous solubility are as high as 1.7 mM.[123]

Polymorph	solubility (mM)
amorphous	0.66
vaterite	0.02
aragonite	0.008
calcite	0.005

TABLE 8.1: Table showing the estimated solubility of each polymorph of calcium carbonate at 25 °C. Values are from Gal et al.,[124] based on data from Plummer et al.[125]

### 8.1.2 On the nucleation of calcium carbonate

There has been much work to suggest that calcium carbonate crystals often form via a metastable amorphous phase, particularly in a biological context.[126–130] An amorphous phase can be expected to have a lower interfacial energy with the solution than a crystalline phase, hence it will likely have a lower nucleation free energy barrier and be the first to form. These amorphous phases then grow and at some point may transform into calcite or another polymorph. Once there are crystals in the solution, the concentration will drop below the amorphous solubility and the remaining amorphous material will dissolve.

The existence of an amorphous phase has great impact on heterogeneous nucleation. The transition from supersaturated solution to amorphous phase to crystal can be seen as thermodynamically analogous to the transition from supersaturated vapour to supercooled liquid to solid. As such, we might expect similar phenomena as discussed in Chapter 6, with acute features stabilising amorphous condensates, which may then grow and crystallise.

Stephens et al. grew calcium carbonate in an acute annular wedge formed between two crossed cylinders of mica coated with a thiol monolayer.[131] They observed stable amorphous condensates at surface separations below 1  $\mu\text{m}$ . Loste et al. observed crystallisation in micrometre pores consistent with the filling of the pores with amorphous calcium carbonate followed by crystallisation.[132]

Several studies have reported the observation of aggregated clusters of molecules, smaller than a critical nucleus, stable for several minutes, in calcium carbonate solutions.[42, 133, 134] It is hypothesised that these “pre-nucleation clusters” aggregate to form amorphous nuclei, although the extent of their role in nucleation, if indeed they have one, is disputed.

### 8.1.3 On calcium carbonate and mica

Stephens et al. reported the epitaxial growth of calcite on mica, with crystals oriented with a {001} plane in contact with the substrate.[135] They noted that this was only seen after “weathering” of the mica: leaving it exposed to atmospheric air for a period of hours to days. Very high humidity levels, or the immersion of the substrate in water, were found to prevent epitaxial growth. As such, it was hypothesised that the epitaxy is dependent on the formation of small potassium carbonate crystals on the mica surface, which act to anchor amorphous particles which then transform to epitaxial calcite due to a close lattice match.

I have myself found a second orientation of epitaxial growth on mica, as shown in Figure 8.1. This is less commonly observed, and the precise conditions required to form it remain unknown. The example shown here was obtained using 5 mM solution at 45 °C on mica weathered for one hour. The plane which this orientation presents to the surface has not been identified.

## 8.2 Techniques

Glass and silicon substrates were cleaned as described in Section 3.1.5. Mica and other mineral substrates were cleaved in a laminar flow cabinet, such that both sides of the substrate were newly-cleaved surfaces, and then cut to size with scissors. Substrates designated as “fresh” were transferred to solution within minutes of cleavage. Those designated as “weathered” were left propped in the laminar flow cabinet with both sides in contact with the atmosphere for a variable amount of time, typically an hour unless otherwise stated, before being transferred to solution. Those designated as “immersed” were placed in 50 mL of deionised water in which they were left for a variable period, typically an hour unless otherwise stated. Immersed samples were transferred to solution without drying; i.e. taken from the water and immersed in solution without allowing time for the film of water on the surface to rupture.

Equimolar calcium chloride and sodium carbonate solutions were prepared and left in contact with the atmosphere for at least 24 hours to achieve equilibrium with atmospheric carbon dioxide. To prepare a calcium carbonate solution of  $x$  mM, component solutions of  $2x$  mM of equal volumes were poured simultaneously into a 50 mL plastic tube (although less than 50 mL of solution was often used, usually just enough to cover the substrate). The tube was quickly sealed and shaken to ensure good mixing, and then the substrate was dropped in and the tube resealed. The design of the tubes ensured

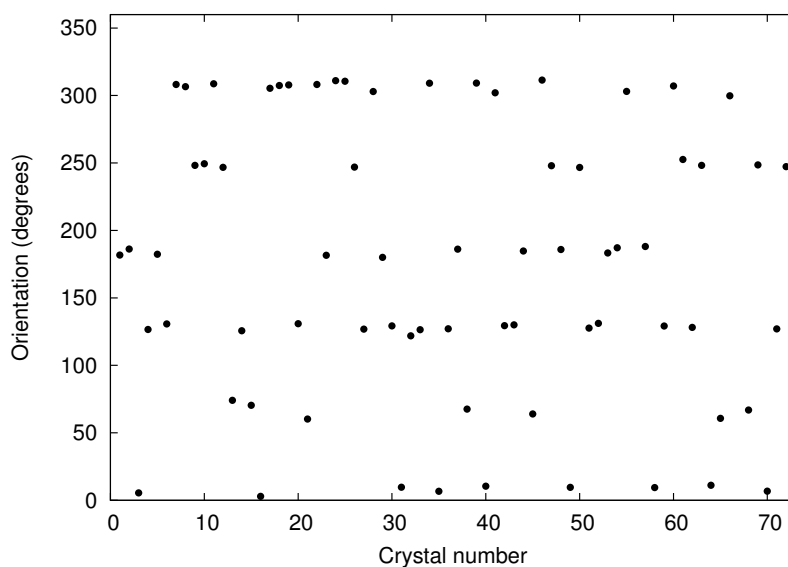
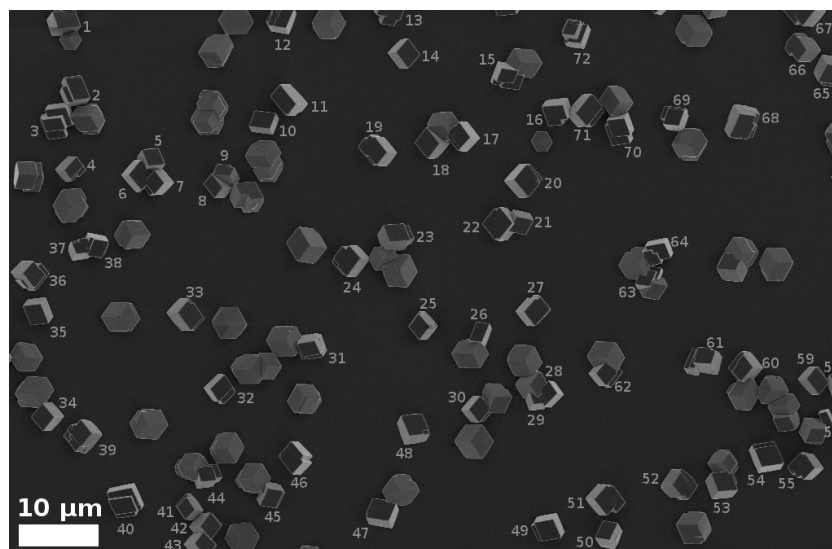


FIGURE 8.1: (Top) electron micrograph showing oriented calcite crystals on mica, in both the  $\{001\}$  orientation (unnumbered) and the unknown orientation (numbered); (bottom) graph showing the measured orientation of each numbered crystal above, measured relative to an arbitrary fixed orientation. There are clear  $60^\circ$  intervals between orientations, demonstrating alignment to the sixfold symmetry of the mica lattice.

that substrates roughly 1" wide would be held nearly vertical, to avoid excessive settling of crystals from solution onto the surface, and that both sides were symmetrically placed in the solution.

Substrates were left for as long as needed for the solution to be exhausted (several hours for 4 mM or higher, twenty-four hours for lower concentrations). They were then withdrawn from solution, rinsed in water and ethanol and dried in a nitrogen stream.



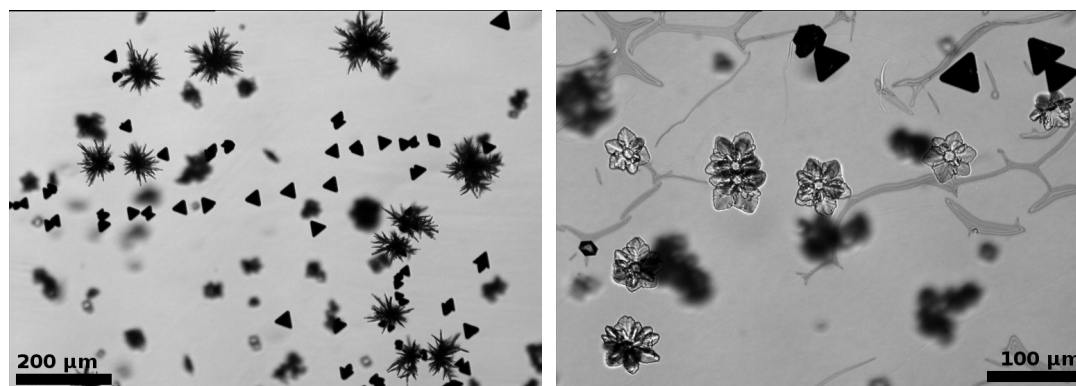


FIGURE 8.2: Optical micrographs showing crystals grown on mica at 60 °C: (left) aragonite and epitaxial calcite; (right) vaterite and epitaxial calcite.

### 8.3 General observations

Across all substrates, crystals observed were mostly calcite, often with significant amounts of vaterite, and more rarely aragonite.

Higher temperatures were typically associated with higher nucleation densities, and larger fractions of vaterite and especially aragonite. Figure 8.2 shows two micrographs, taken from the same sample, from 5 mM solution grown on fresh mica at 60 °C. All three polymorphs are clearly visible.

Nucleation was often (but not always) uneven in its distribution across different areas of a substrate, and especially between two different sides of a substrate. Efforts to keep both sides equivalent by symmetrical weathering and a perfectly vertical position during growth did not succeed in reducing the degree of variation between the two sides, especially with mica substrates. The cause of this variation remains unknown. Figure 8.3 shows an example of qualitatively different growth on two sides of the same area of a piece of mica.

Calcium carbonate growth is extremely sensitive to even slight contamination on surfaces, leading to much variation in nucleation behaviour across a substrate if it is not kept perfectly clean. Figure 8.4 shows an extreme example where the surface has been touched with the finger of a clean nitrile glove. For this reason substrates were always held by the edges, and observations were always made in the untouched regions away from the edges.

#### 8.3.1 Substrate pretreatment

Figure 8.5 shows a typical example of the effects of varying mica pretreatment. Immersed mica typically has a low nucleation density and no epitaxial growth. It is more

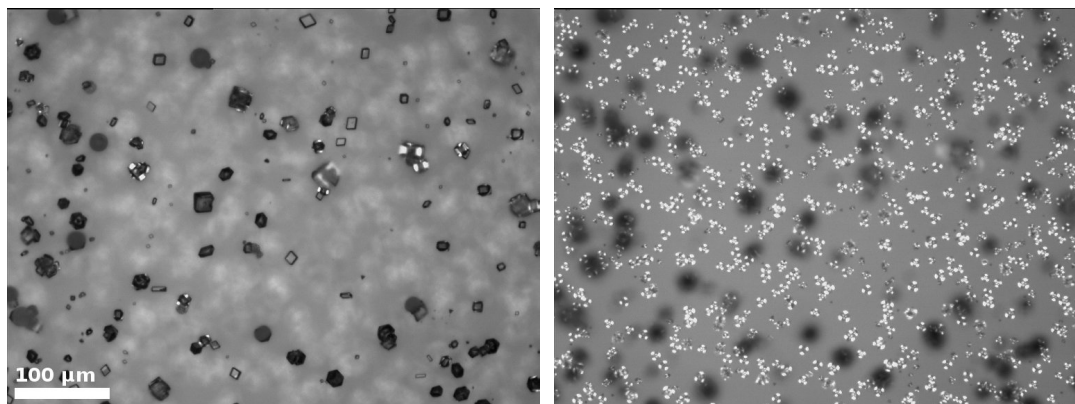


FIGURE 8.3: Optical micrographs showing calcite crystals grown on two sides of the same region of a piece of weathered mica: (left) disordered calcite; (right) dense epitaxial calcite. Growth was from 5 mM solution.

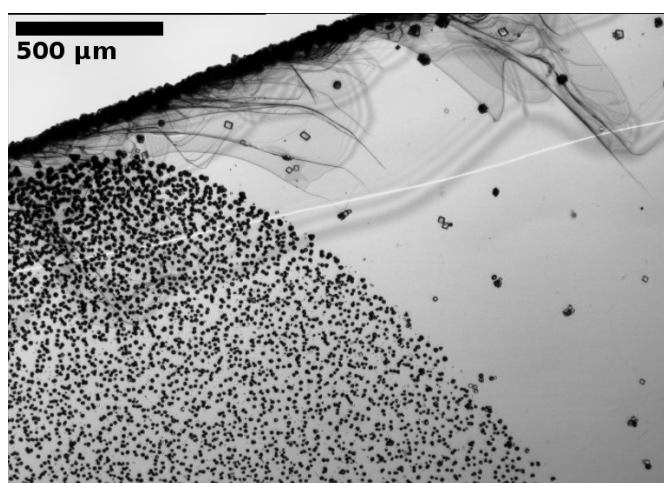


FIGURE 8.4: Optical micrograph showing highly inhomogeneous calcite growth on weathered mica, the bottom left of which has been touched by a clean nitrile glove. Growth from 5 mM solution.

likely to have crystals forming aggregates, indicative of crystals settling out of solution rather than nucleating on the surface (see next section).

Weathered mica typically has a high density of epitaxial calcite. This is not always the case; the weathering process appears to be highly dependent upon the ambient humidity, which in our setting was not controllable, and so results were not always reproducible.

Fresh mica often also promotes epitaxial calcite, but less reliably and in lower proportions than weathered mica. These substrates are more likely to feature disordered calcite growth, and generally have nucleation densities in-between those for immersed and weathered mica.

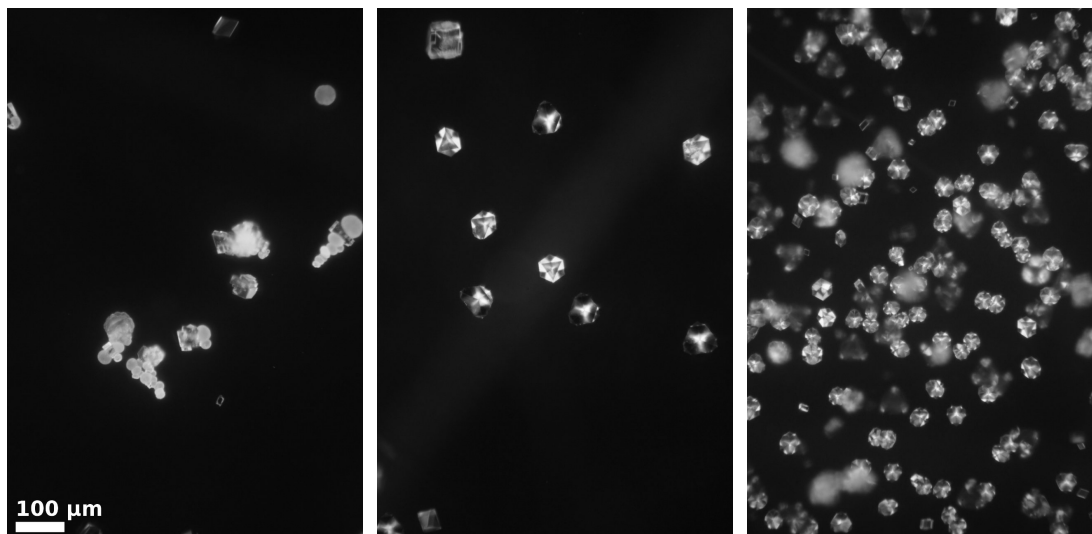


FIGURE 8.5: Optical micrographs showing calcium carbonate growth from 4 mM solutions on mica with differing pretreatment: (left) immersed in water; (centre) fresh; (right) weathered.

### 8.3.2 Concentration

Experiments were performed between 0.5 and 5 mM. The nucleation density depends strongly on concentration, with lower concentrations producing less but larger crystals. There appears to be a higher occurrence of vaterite and particularly aragonite at lower concentrations, but this has not been systematically investigated.

Concentration has a great effect on the occurrence of epitaxy. Figure 8.6 shows crystals grown on three pieces of similarly weathered mica at three different concentrations. Besides a change in nucleation density, no epitaxy is seen at low concentrations: typically it is not seen below about 2 mM. A similar dependence is seen with fresh mica.

At higher concentrations, crystals are often seen to aggregate, for example see the left image of Figure 8.5. The size of these aggregates increases with concentration, and they are not observed at concentrations below about 2 mM. These are attributed to crystals attaching to the surface from solution. It is notable that epitaxial crystals, which must have nucleated on the surface, are never seen to aggregate in this way.

It remains unclear whether these crystals aggregate in solution and then attach to the surface, or whether they attach one at a time, being most likely to make contact with an existing aggregate when drifting towards the surface. Figure 8.7 shows an example of a large aggregate found upon evaporation of a sample of 10 mM  $\text{CaCO}_3$  solution, resembling fractal formations produced by diffusion-limited aggregation.[136, 137].

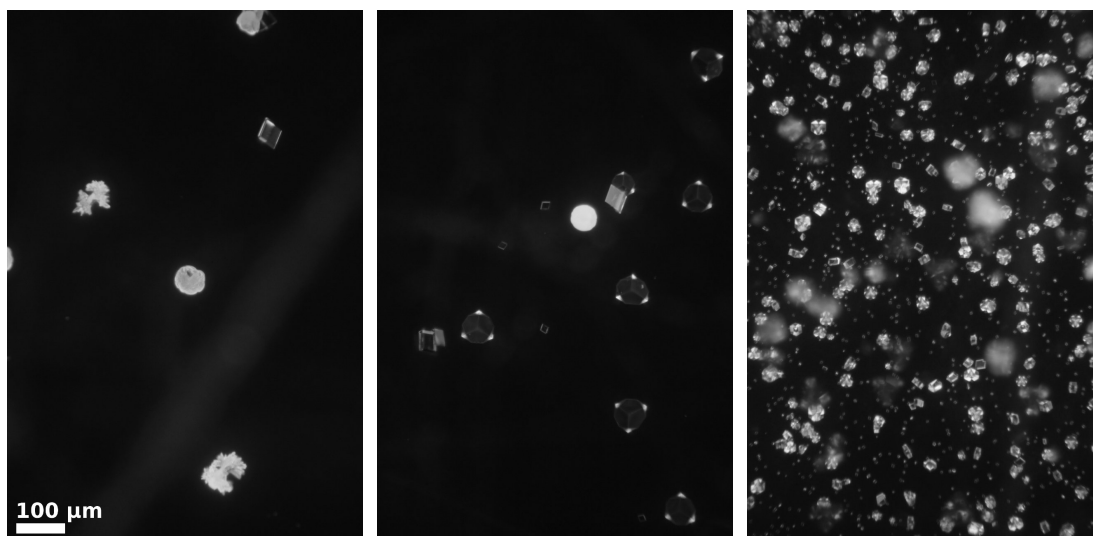


FIGURE 8.6: Optical micrographs showing calcium carbonate growth on weathered mica from solutions with differing concentrations: (left) 1 mM; (centre) 2 mM; (right) 4 mM.

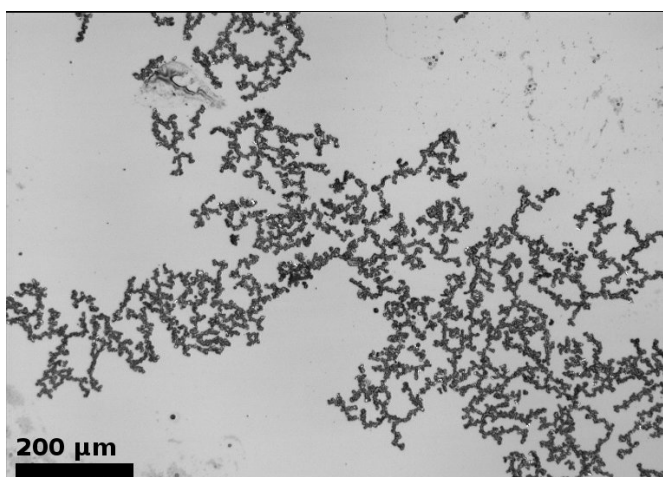


FIGURE 8.7: Optical micrograph showing large fractal aggregate extracted from 10 mM solution.

### 8.3.3 Crystal rings

I was initially perplexed by the presence of well-defined circles of epitaxial crystal growth on weathered mica substrates. These were found to be the result of water droplets condensing or landing on the surface and evaporating prior to crystal growth. An experiment was performed in which small water droplets were sprayed over a fresh mica surface, flicked from the bristles of a clean bottle brush using a gloved finger. The result was a large number of rings like those shown in Figure 8.8, with disordered calcite in the centre and dense epitaxial calcite around the edge.

The rings are hypothesised to be due to the water drops dissolving the potassium

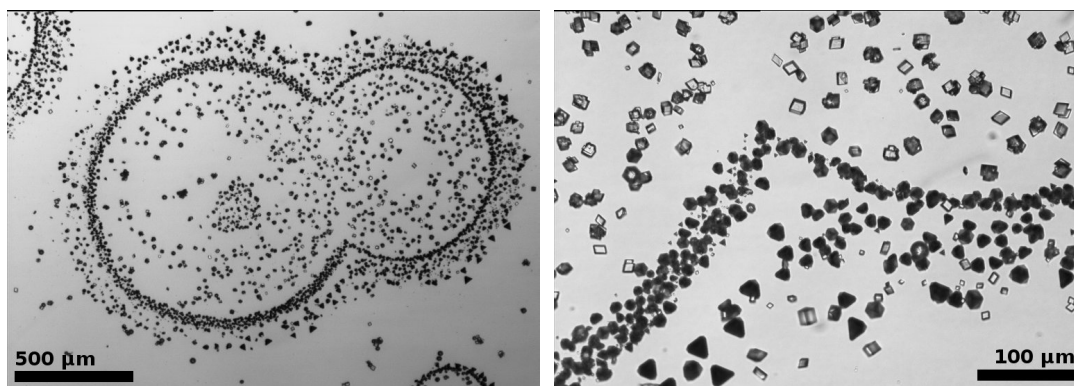


FIGURE 8.8: Optical micrographs showing: (left) rings of calcite crystals; (right) magnification showing epitaxial border with disordered interior. Growth from 5 mM solutions.

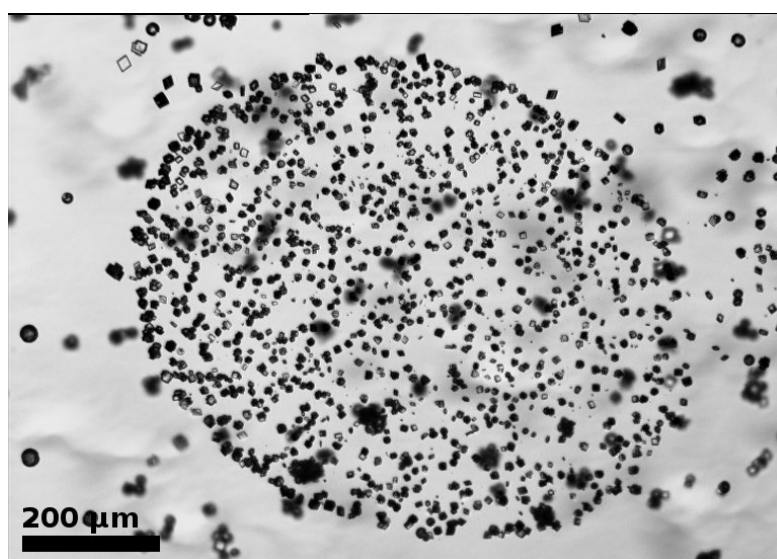


FIGURE 8.9: Optical micrograph showing ring of disordered calcite crystals grown from 5 mM solution on immersed mica sprayed with water droplets.

carbonate on the mica surface and redepositing it around their perimeter as they dry. To test this, similar experiments were performed on mica immersed and then dried in a nitrogen stream, before being sprayed with water droplets. The surface potassium should have been removed by the water immersion. The result was a series of rings like those in Figure 8.9, with disordered crystals and no dense border of epitaxy.

The disordered growth is presumed to arise from contamination from impure water. Water droplets were condensed on fresh mica by leaving it inside a sealed container with a dish of warm water; these droplets, being condensed rather than deposited, should have been much purer. The mica was then removed and left to weather for an hour. Upon growth of calcium carbonate, many rings were seen, having dense epitaxial borders but nearly no disordered calcite growth. An example is shown in Figure 8.10.

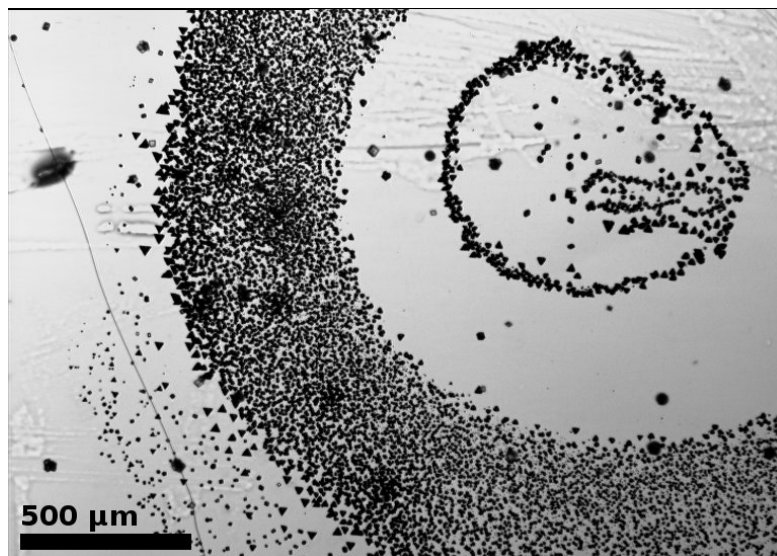


FIGURE 8.10: Optical micrograph showing a double ring of calcite crystals grown from 5 mM solution on mica after condensation and evaporation of water droplets. Nearly all crystals in this image are epitaxial calcite.

## 8.4 Growth on smooth and scratched surfaces

### 8.4.1 Diamond powder scratching

#### Silicon

Calcium carbonate growth on smooth silicon substrates was compared to that on those scratched with each grade of diamond powder, as described in Section 3.1.6. Substrates were sized 2 cm × 1 cm, and after scratching (or not) were cleaned as described in Section 3.1.5 followed by plasma cleaning in an air plasma for two minutes. Growth was from 1 mM solutions. The experiment was repeated once, giving two substrates for each surface treatment.

Twelve sample images were taken across each surface using an optical microscope, each image viewing a 1.02 mm<sup>2</sup> area. The number of crystals in each image was counted. Figure 8.11 shows the mean nucleation density for each substrate. Although it appears that the nucleation density may be higher on the “< 1 μm” scratched substrate, this is by no means unambiguous. Poor repeatability is seen between the two experiments, and the large error bars are due to a significant variation in nucleation density across each surface.

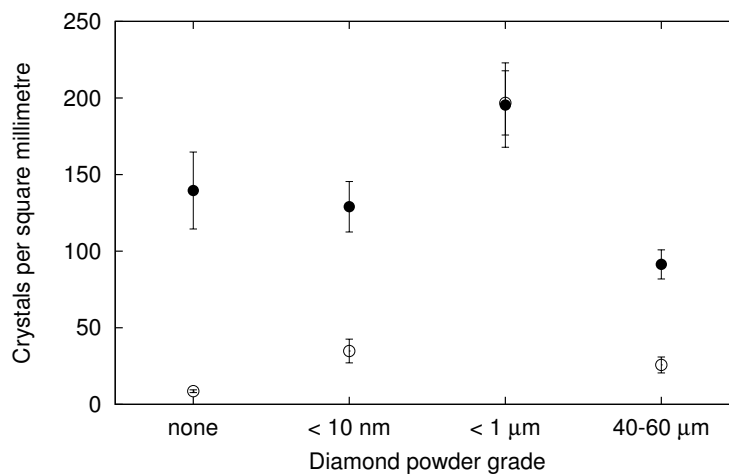


FIGURE 8.11: Graph showing mean calcium carbonate nucleation density on smooth and scratched silicon substrates: (○) first experiment; (●) second experiment. Error bars represent the sample standard deviation divided by  $\sqrt{12}$ .

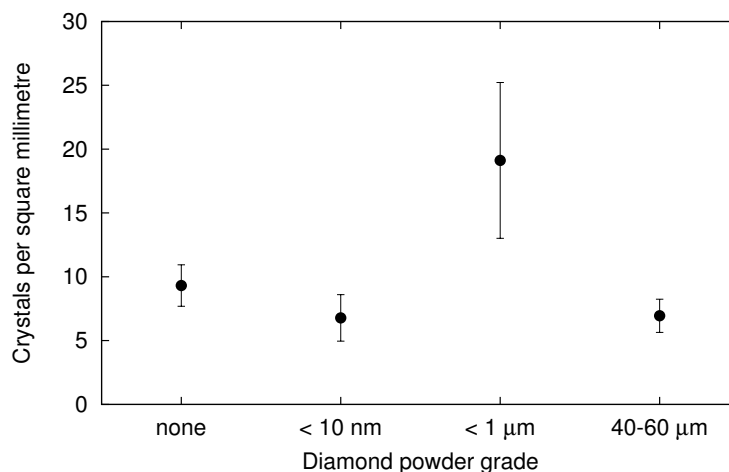


FIGURE 8.12: Graph showing mean calcium carbonate nucleation density on smooth and scratched mica substrates. Error bars represent the sample standard deviation divided by  $\sqrt{12}$ .

### Mica

Experiments with mica substrates were performed similarly to those on silicon. Substrates were sized 6 cm × 2 cm, and after scratching were rinsed in water and ethanol. Only a single substrate was used per surface treatment. Analysis was done as with silicon above. Figure 8.12 shows the results.

Again, large error bars are indicative of a large variation in nucleation density across each substrate, making any difference between surface treatments impossible to conclusively identify.

## Glass

Variations in nucleation density across a surface must be assumed to arise from variations in the surface itself (e.g. surface chemistry, topography, level of contamination) or from variations in the solution (e.g. local concentration, temperature, convection currents). A new experimental procedure was devised to eliminate the latter case.

To compare nucleation between two glass surfaces, two glass slides were sandwiched face-to-face, with plastic spacers ( $< 200 \mu\text{m}$  thick) in between to leave a narrow gap. These were dipped into a supersaturated solution, which was drawn into the gap by capillary action. These sandwiches were left vertically for 24 hours to allow crystals to form. They were then placed under an optical microscope without opening, and sample images could be taken across the two surfaces. At each point, both facing surfaces could be imaged just by changing the focus. When comparing two images such as these, they may be assumed to have been exposed to exactly equivalent growth conditions due to their close proximity.

Substrates were sized  $3'' \times 1''$ , and cleaned as for silicon substrates above. Growth was from 3 mM solutions. Sandwiches were formed between a smooth slide and a scratched slide, with smooth-smooth sandwiches used as controls. Twelve pairs of images were taken across each sandwich, with each image viewing an area of  $0.95 \text{ mm}^2$ .

Figure 8.13 shows results for one growth in sandwiches featuring each scratching type. Each data point plots the nucleation density on two closely separated facing surfaces, and each plot represents a single pair of substrates. The " $40\text{--}60 \mu\text{m}$ " substrate shows no difference to its smooth counterpart. The " $< 1 \mu\text{m}$ " substrate shows slightly increased nucleation on the scratched surface, and the " $< 10 \text{ nm}$ " substrate shows much higher nucleation densities on the smooth substrate. However, it can be seen that the scatter of points is in all cases large. There remains an enormous variation in nucleation densities across surfaces, including smooth surfaces, and this does not appear to correlate between different areas of the two surfaces. Hence the variation must be due to variations in the surfaces, rather than the solutions.

This makes finding useful information from these experiments essentially impossible. A repeat was performed, and the heterogeneous distribution of nucleation densities across surfaces was seen to be even worse. The apparent result that scratching with " $< 10 \text{ nm}$ " diamond powder reduced the nucleation density was not seen to be repeatable, as shown in Figure 8.14.



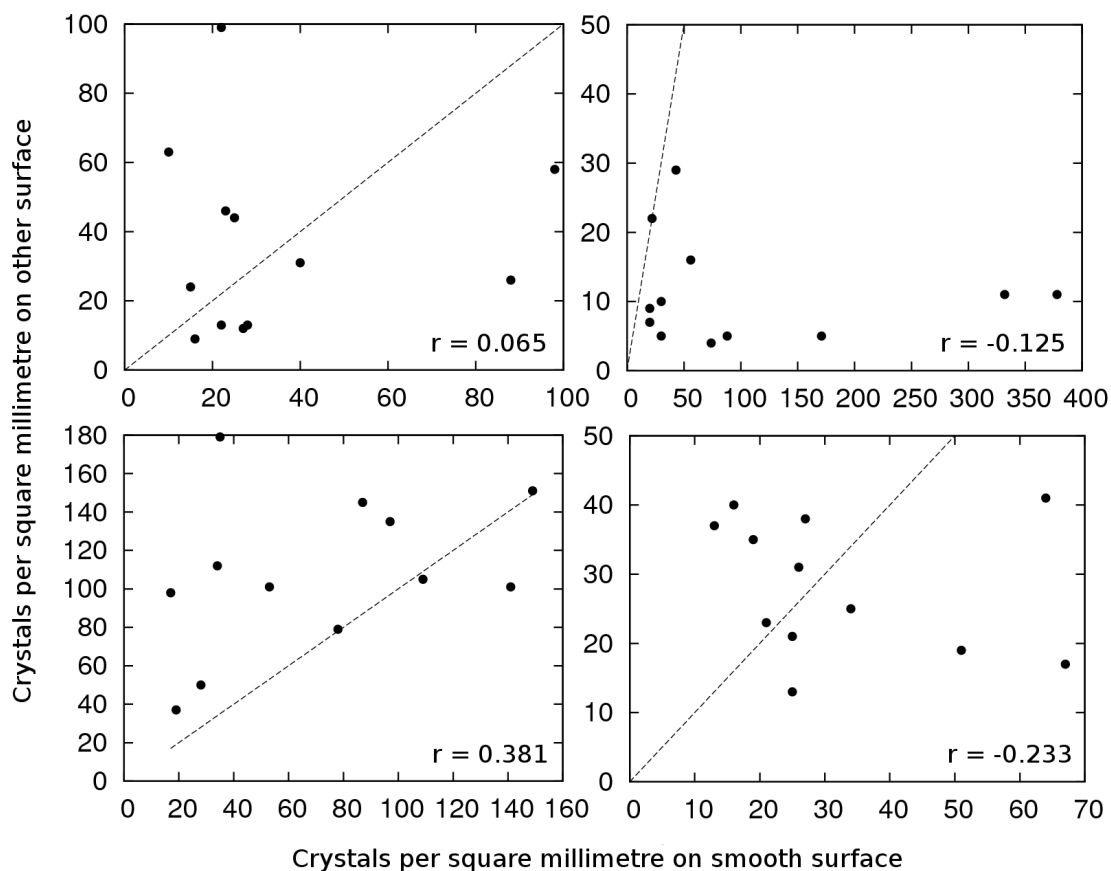


FIGURE 8.13: Graph showing nucleation densities on smooth and scratched glass surfaces plotted against the density on a facing smooth surface. Dashed lines indicate the lines of equal nucleation density. Surfaces were scratched with the following grades of diamond powder: (top left) none; (top right) " $< 10\text{ nm}</math>"; (bottom left) " $< 1\ \mu\text{m}</math>"; (bottom right) " $40\text{--}60\ \mu\text{m}</math>". Numbers in the bottom-right of each plot are the Pearson correlation coefficients, showing little to no correlation.$$$

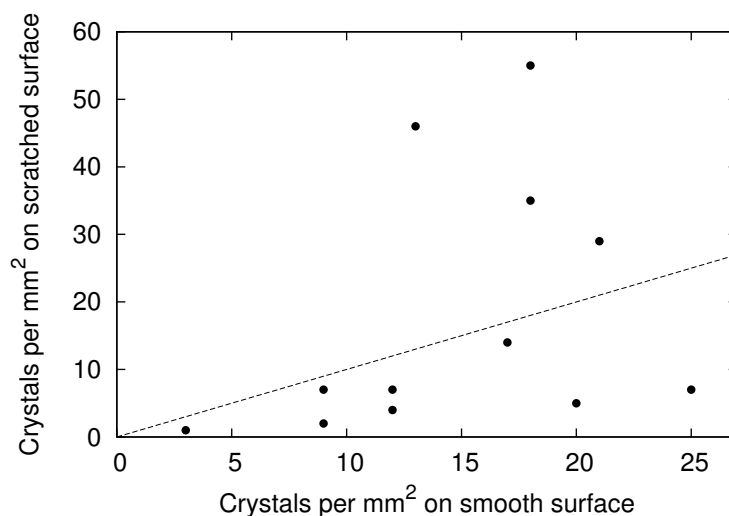


FIGURE 8.14: Graph showing nucleation densities on " $< 10\text{ nm}</math>"-scratched glass surfaces plotted against the density on a facing smooth surface. The dashed line indicates the lines of equal nucleation density. This experiment was identical in all regards to that producing data shown in the top right of Figure 8.13.$

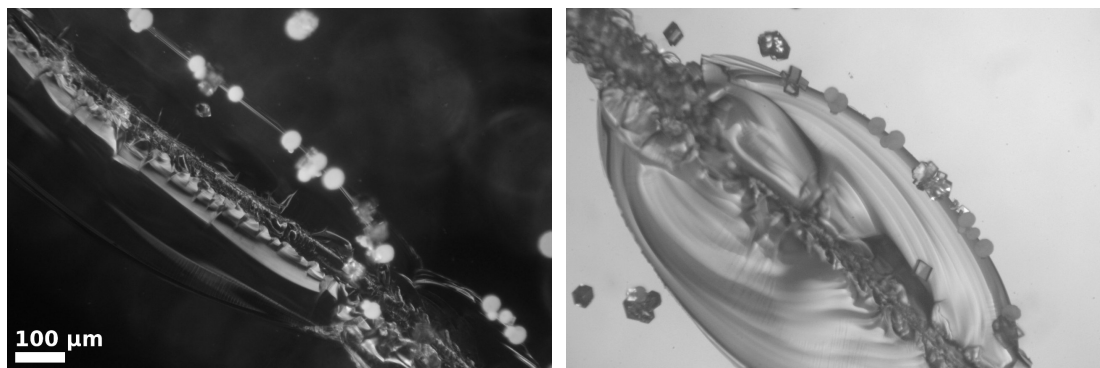


FIGURE 8.15: Optical micrographs showing calcite and vaterite growing on chip edges of glass scratches. Both images are from 4 mM growths.

### 8.4.2 Crude scratches

#### Glass

Crude scratches were made on glass slides by scoring with a diamond-tipped pen. Substrates were then cleaned as in Section 3.1.5. Three glass scratches were used in solutions of each of 0.5, 1, 2, 3 and 4 mM.

Glass scratches appear to consist of a groove with a rough bottom and smooth sides where the glass has chipped away. Calcite and vaterite crystals were seen growing along the scratches, but rather than growing in the rough bottoms, as seen when growing camphor in a similar scratch (Section 4.6.1), calcium carbonate grew primarily along the very edges of the chipped sides, as shown in Figure 8.15. This behaviour was not evident at 0.5 and 1 mM as the nucleation density was too low to make any strong statements about preferential nucleation sites. It was visible at all higher concentrations and most evident at 4 mM.

This behaviour is surprising as the chip edges are presumed to form sharp *convex* surface geometries, as opposed to the concave geometries expected to act as preferential nucleation sites from classical nucleation theory. Figure 8.16 shows electron micrographs of crystals growing along such a feature, and a magnified view of the chip edge between them. The resolution here is not high, but it appears there may be small chips along the edge, and possibly fine cracks running up the sides. These could possibly provide small-scale confined geometries, favourable to nucleation, although this has not been confirmed.

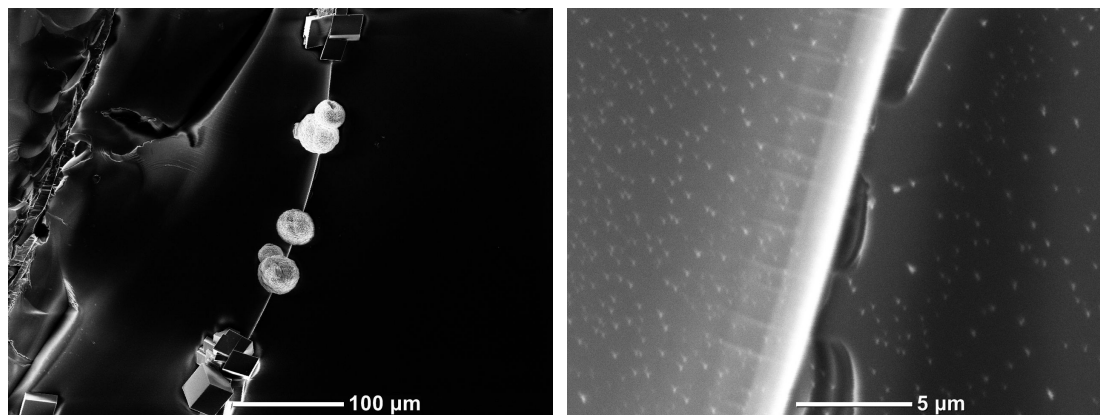


FIGURE 8.16: Electron micrographs showing: (left) calcite and vaterite on a glass chip edge; (right) magnification of chip edge between two crystals.

### Mica

A clean scalpel blade was used to make scratches on freshly cleaved mica surfaces in two different ways. Firstly, the blade was *scraped* across the surface, scoring the mica, and secondly it was *crushed* down firmly into the mica without pulling it along the surface. Both promoted the growth of calcium carbonate, but in qualitatively different ways.

Figures 8.17 and 8.18 show growth on scraped and crushed scratches respectively. Growth was performed on immersed, fresh and weathered mica, at each of 1, 2 and 4 mM.

Crystal growth was seen on scraped scratches in all conditions except for 1 mM/immersed mica. For this type of scratch, the scalpel is usually seen to remove layers of mica, leaving a trough with a relatively flat bottom. This may explain why crystals are generally seen at the edges of the scratches, rather than in the middle. For 4 mM growth on weathered mica, growth is seen to take the form of a dense region of epitaxial growth either side of—but not in or immediately adjacent to—the scratch. The reasons for this are not clear. On immersed mica, crystals are seen as aggregates extending from one side of the scratch, this is particularly clear at 4 mM. This is strongly suggestive of crystals joining the surface from solution, which the scratch edge acts to snag as they drift past.

Crystal growth was also seen on crushed scratches in all conditions except for 1 mM/immersed mica. Here the scratch does not appear to have a flat bottom, as no material has been dragged away. For immersed mica, the effect is very similar to that for a scraped scratch, with crystal aggregates extending in one direction from the scratch, most likely

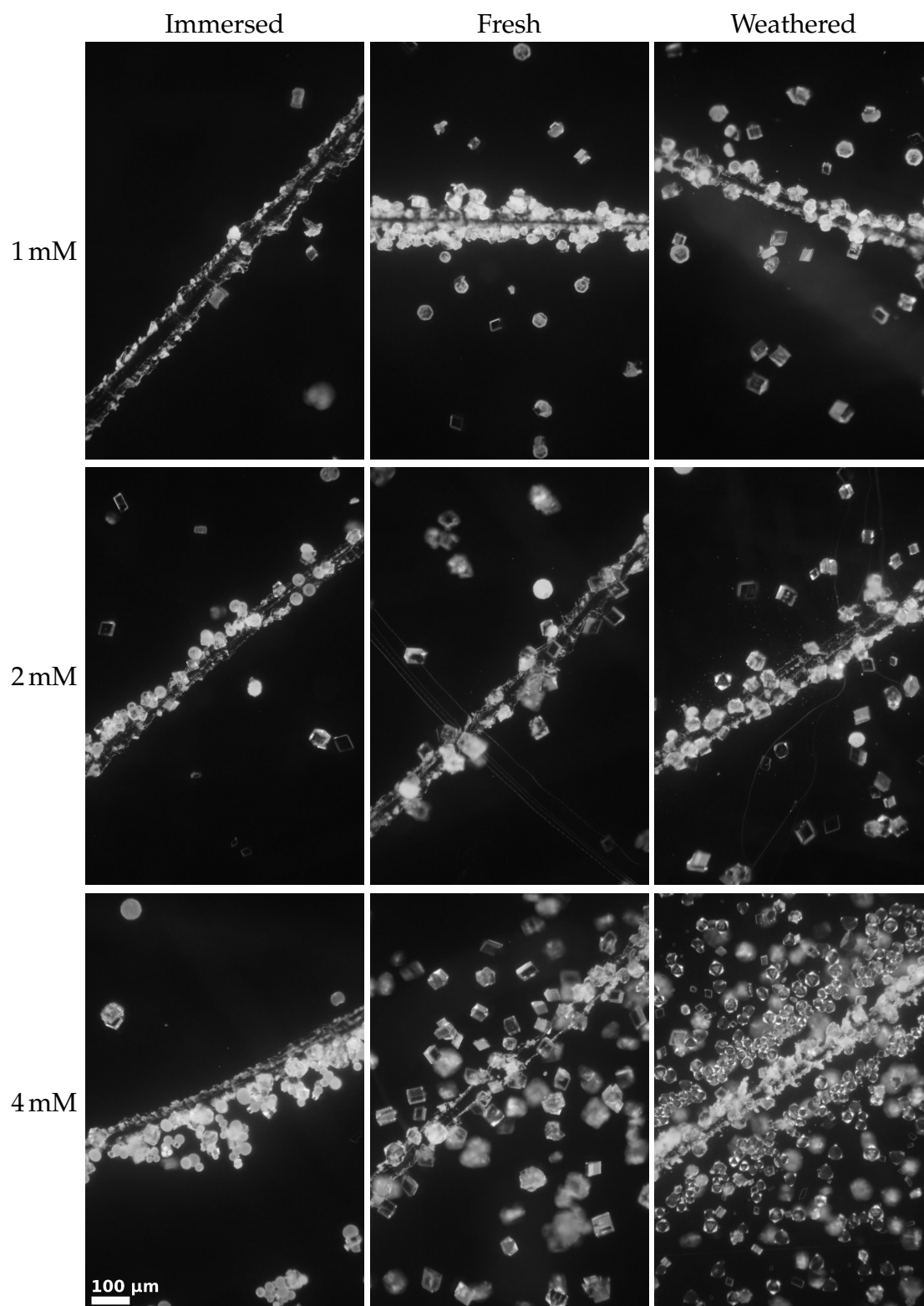


FIGURE 8.17: Optical micrographs showing growth of calcium carbonate on scraped scratches on mica for several concentrations and surface pretreatments.

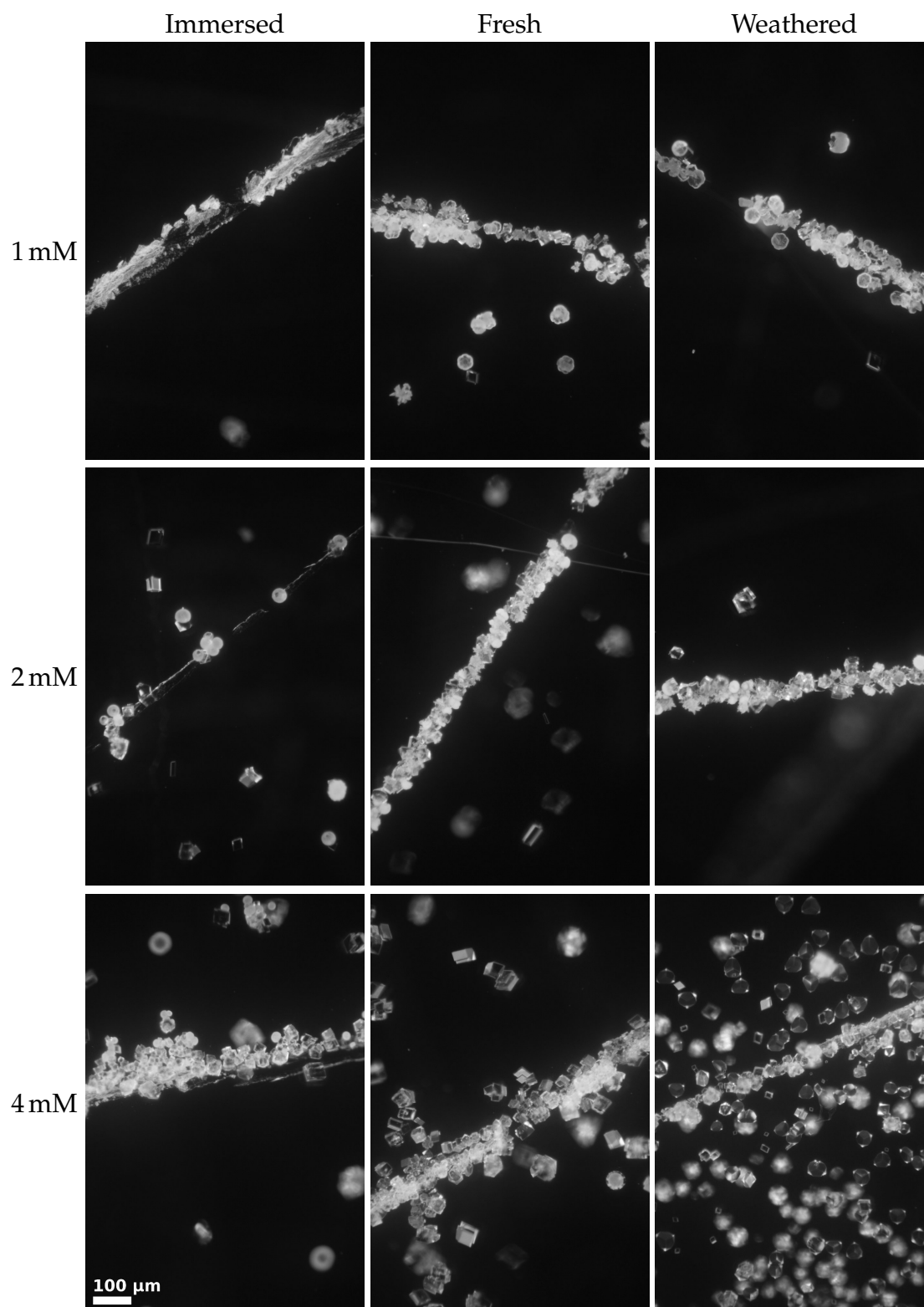


FIGURE 8.18: Optical micrographs showing growth of calcium carbonate on crushed scratches on mica for several concentrations and surface pretreatments.

aggregated from solution. For other mica pretreatments, the scratch is almost completely obscured by dense crystal growth, even at 1 mM. There is still a border of denser epitaxial growth around the scratch at 4 mM on weathered mica, but it is much less dense or distinct than for scraped scratches.

## 8.5 Growth on mica defects

Calcium carbonate is often seen to grow preferentially along cleavage defects on mica. Unfortunately, the random nature of defects makes it difficult to perform controlled tests in varying conditions. Figure 8.19 shows the results of calcium carbonate growth at 1, 2 and 4 mM on immersed, fresh and weathered mica substrates all containing defects. Growth was seen along defects in all conditions, although the presence of crystals over defects on 1 mM/immersed could easily be coincidental. At 4 mM, growth on immersed mica is again seen as aggregates to one side of the feature, suggesting attachment from solution.

Growth on mica defects appears to be highly defect-dependent: even on a single substrate, one defect may promote heavy growth whilst another similar-looking defect promotes no growth at all. Where crystals are growing epitaxially on flat mica, growth along defects may be either disordered or epitaxial. An example of epitaxial growth along a defect is shown in Figure 8.20.

### 8.5.1 Pocket features

An investigation was performed to find if calcium carbonate nucleation showed any preference for the pocket features found to be so effective for crystals nucleating from vapour in Chapter 5. Nine mica substrates containing pocket features were used. Immediately after cleavage, each substrate was photographed through an optical microscope within a laminar flow cabinet, using reflected light to identify and locate one or more pockets. Substrates were then put straight into solution, left to weather or immersed in water. Calcium carbonate was grown from 1, 2 and 4 mM solutions for each substrate pretreatment. The previously-photographed area of mica could then be relocated and photographed to identify any coincidence of calcium carbonate and pocket locations.

On most substrates, there was no evidence of calcium carbonate growth in or around pockets. Three substrates out of the nine, however, showed possible growth from pockets. The conditions for these three substrates were extremely varied. They are presented in Figure 8.21.

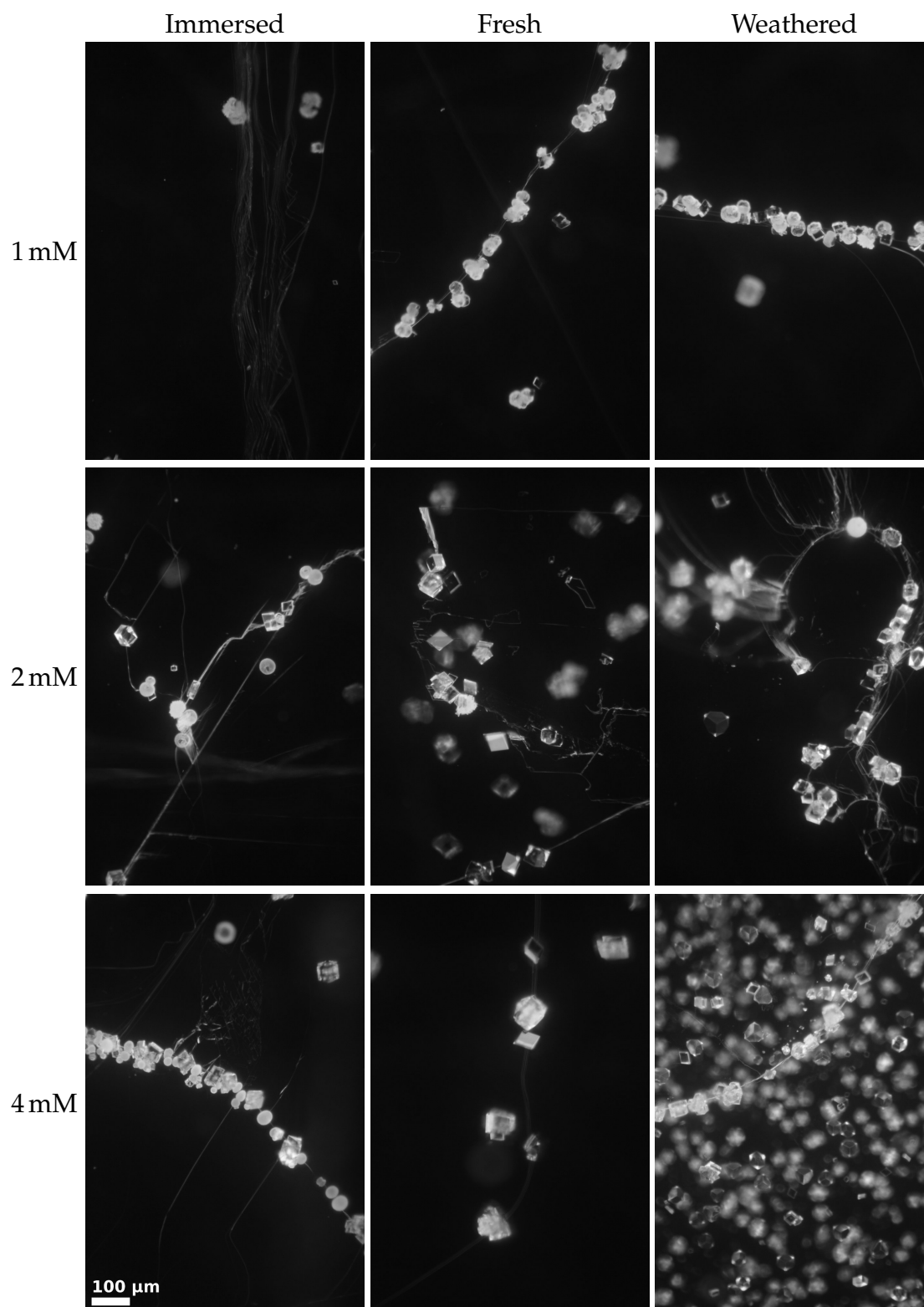


FIGURE 8.19: Optical micrographs showing growth of calcium carbonate on mica defects for several concentrations and surface pretreatments.

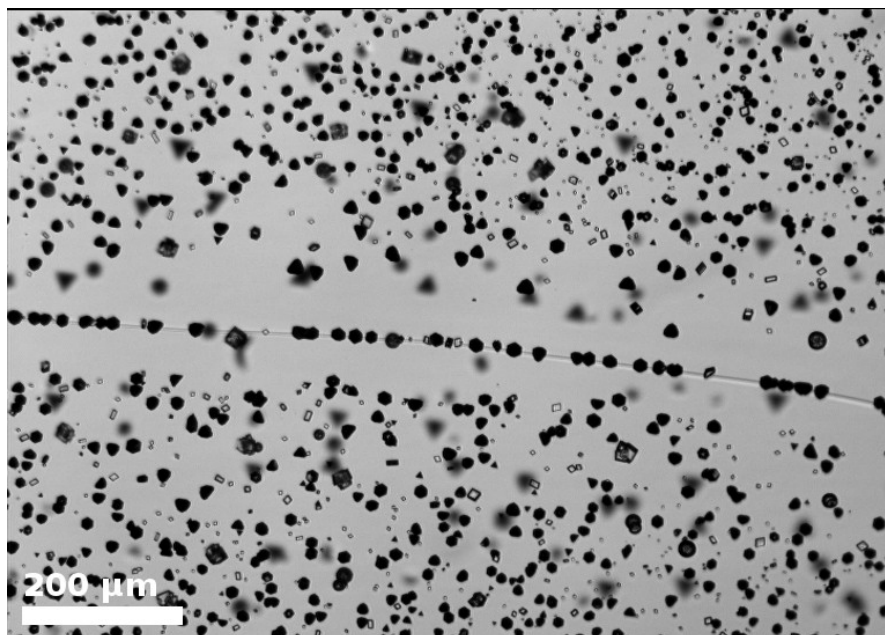


FIGURE 8.20: Optical micrograph showing epitaxy of calcite on a mica defect.

It was noticed that the positions of pockets before growth did not always correspond to their positions after growth: these features are apparently able to translate across the surface if mechanically disturbed. It is not clear if this disturbance arose from immersion of the substrate in solution, or drying in a nitrogen stream, or both.

There is no evidence of the characteristic growth pattern of crystals forming from vapour in pockets: that of two crystals growing from the pocket corners. It seems likely, therefore, that if pockets do promote calcium carbonate nucleation, they do so by a quite different mechanism.

## 8.6 Other substrates and compounds

### 8.6.1 Calcium fluoride

Calcium fluoride ( $\text{CaF}_2$ ) was used to provide a comparison with calcium carbonate. It has a low aqueous solubility of 0.20 mM at 25 °C.[100] Its crystal system is much simpler, forming a single polymorph, fluorspar, which has a cubic structure and habit.

Supersaturated solutions of calcium fluoride at concentrations of  $x$  mM were prepared by mixing equal volumes of solutions of sodium fluoride at  $4x$  mM and calcium chloride at  $2x$  mM. Experiments were performed identically to those with calcium carbonate. Immersed mica substrates were used, and crystals were left to grow for 24 hours before removing substrates.



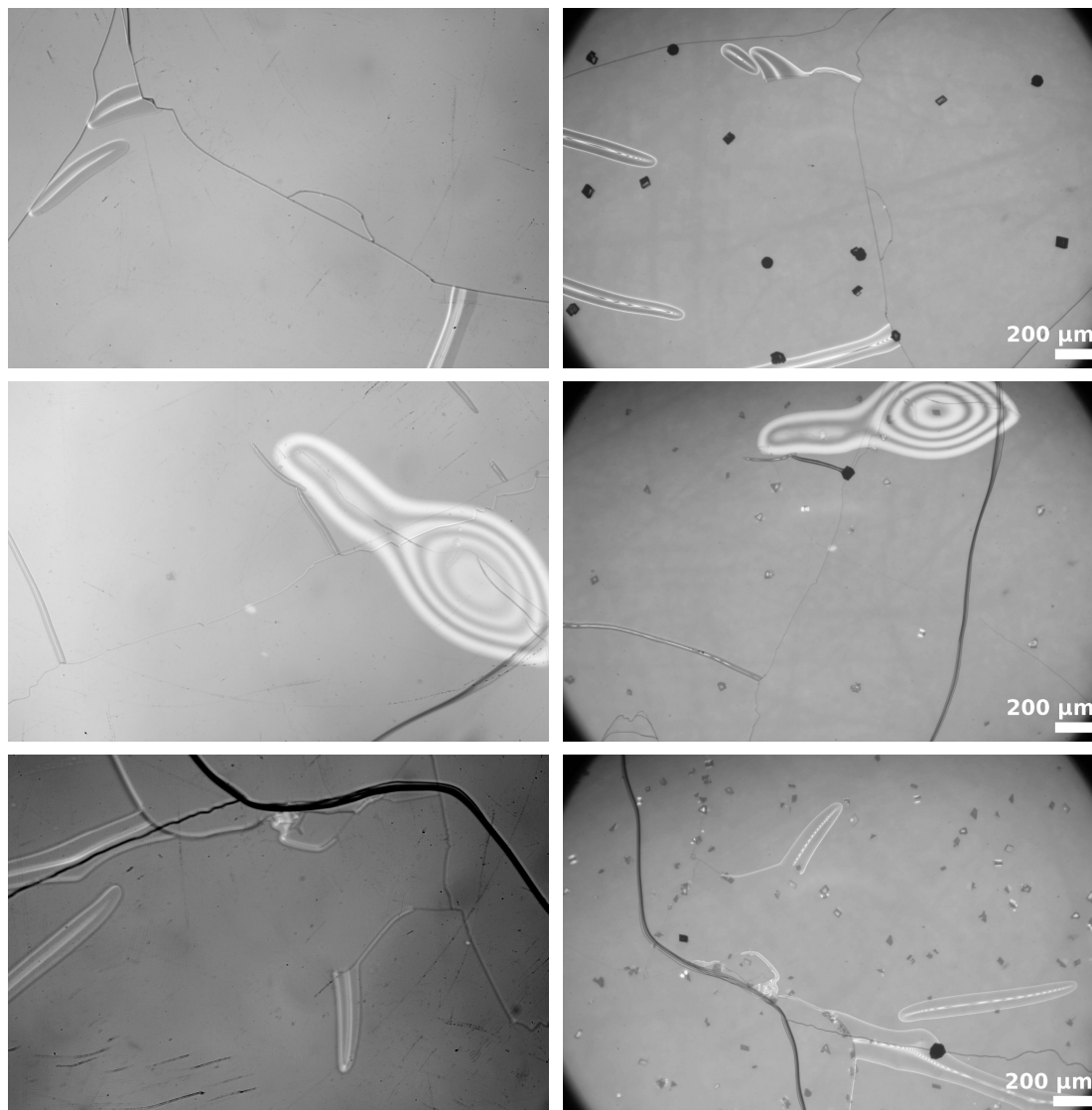


FIGURE 8.21: Optical micrographs showing pocket-rich mica before (left) and after (right) possible calcium carbonate growth. Conditions were, from top to bottom: 1 mM/immersed; 4 mM/weathered; 2 mM/fresh. A magnified view of the pocket in the bottom-right image is given in Figure 8.22.

The nucleation density was found to progress from zero to a very high number over a very small concentration range, between 1.2 and 1.5 mM, with no crystals forming at 1.2 mM or below. Figure 8.23 shows examples of growth across this range. At 1.3 mM, some defects are seen to aggregate crystals, although the majority show no apparent effect on nucleation. At 1.4 mM and above, no tendency to grow along defects is observed.

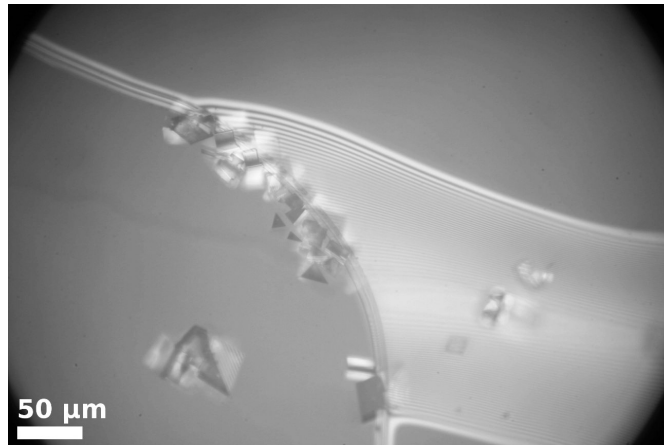


FIGURE 8.22: Optical micrograph showing a high-magnification view of the pocket in the final image of Figure 8.21. Growth was at 2 mM on fresh mica.

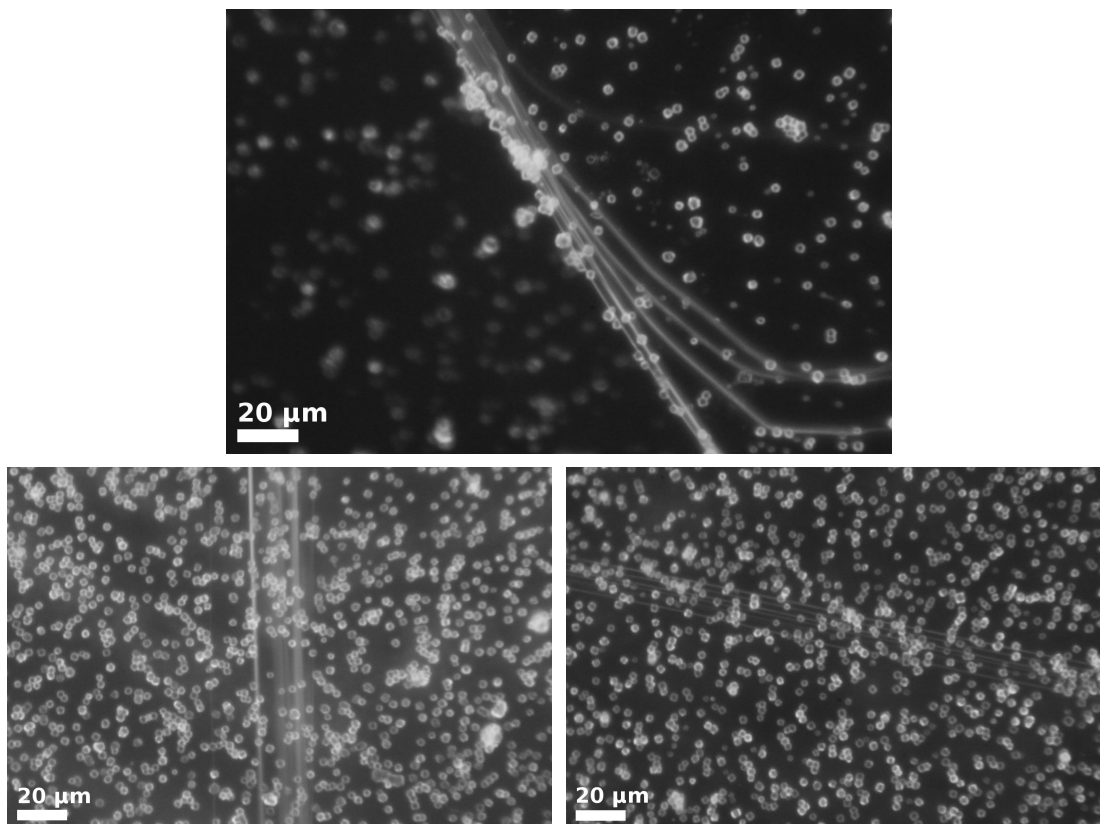


FIGURE 8.23: Optical micrographs showing fluorspar growth on mica, from concentrations: (top) 1.3 mM; (bottom left) 1.4 mM; (bottom right) 1.5 mM.

### 8.6.2 Other layered minerals

Calcium carbonate was grown on substrates of cleaved lepidolite, biotite and vermiculite to compare to results on mica. Experiments were performed exactly as with mica substrates, and all growth was performed at 3 mM concentration.

All three substrates gave qualitatively similar results. On none was there any notable dependence on substrate pretreatment. All substrates exhibited high nucleation density and large amounts of epitaxial growth compared to those typical on mica at a similar concentration, suggesting that these substrates are preferable to mica for heterogeneous nucleation. Epitaxy on calcite's {001} planes was seen on all substrates, even immersed substrates. It was in no case the exclusive mode of growth, with most substrates exhibiting regions of disordered calcite growth. Vermiculite substrates appeared to give the highest nucleation densities and the highest proportions of epitaxial growth, although this was not quantitatively studied. Figure 8.24 shows an example of epitaxial growth for each mineral and substrate pretreatment.

It appears that the dependence on substrate pretreatment of calcite epitaxy seen with mica is not shared by other aluminosilicates. This implies that for lepidolite, biotite and vermiculite the soluble surface ions exposed by cleavage are of no importance in the process; this despite lepidolite and biotite having interlayer potassium ions, as mica does, whereas vermiculite has magnesium ions between its layers.

Preferential growth along defects was observed for all minerals and substrate pretreatments. On no substrates was this behaviour universal, and defects with no crystal overgrowth were common. It is not known what causes certain defects to promote growth when others do not, and defect geometries on these minerals have not been characterised. Figure 8.25 shows an example of defect overgrowth for each mineral and substrate pretreatment.

Across all three minerals and for different substrate pretreatments, crystals were observed to sometimes grow in well-defined lines, as though along a linear feature, but no feature was visible. Figure 8.26 shows an example.

## 8.7 Summary

Calcium carbonate growing from solution has been seen to be affected by topography on various substrates, often growing preferentially along scratches and defects. However the properties of a good nucleation site that make it favourable remain unknown; pocket geometries in particular, highly effective at promoting nucleation from vapour,

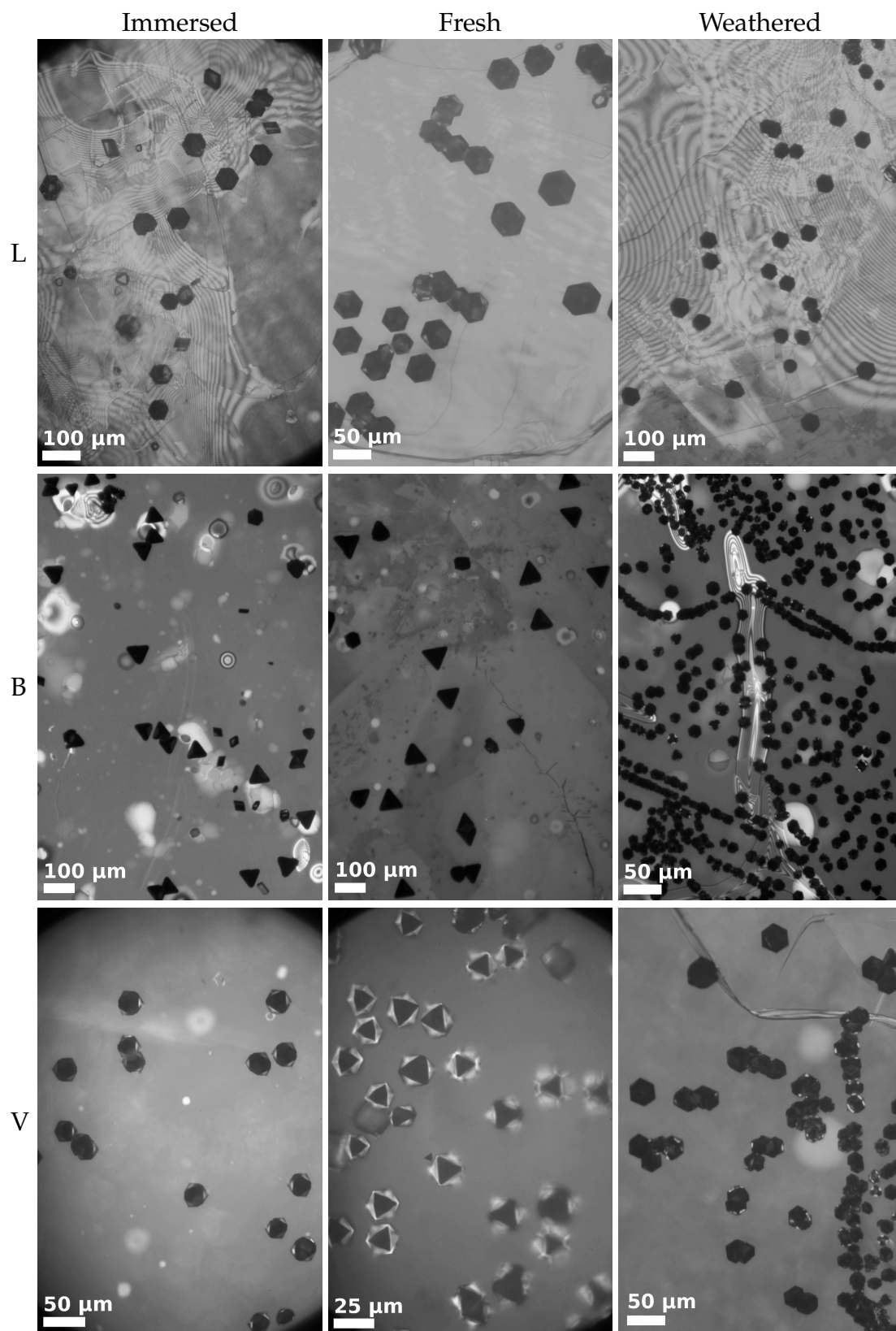


FIGURE 8.24: Optical micrographs showing epitaxy of calcium carbonate grown from 3 mM solutions on lepidolite (L), biotite (B) and vermiculite (V) for varying substrate pretreatments.

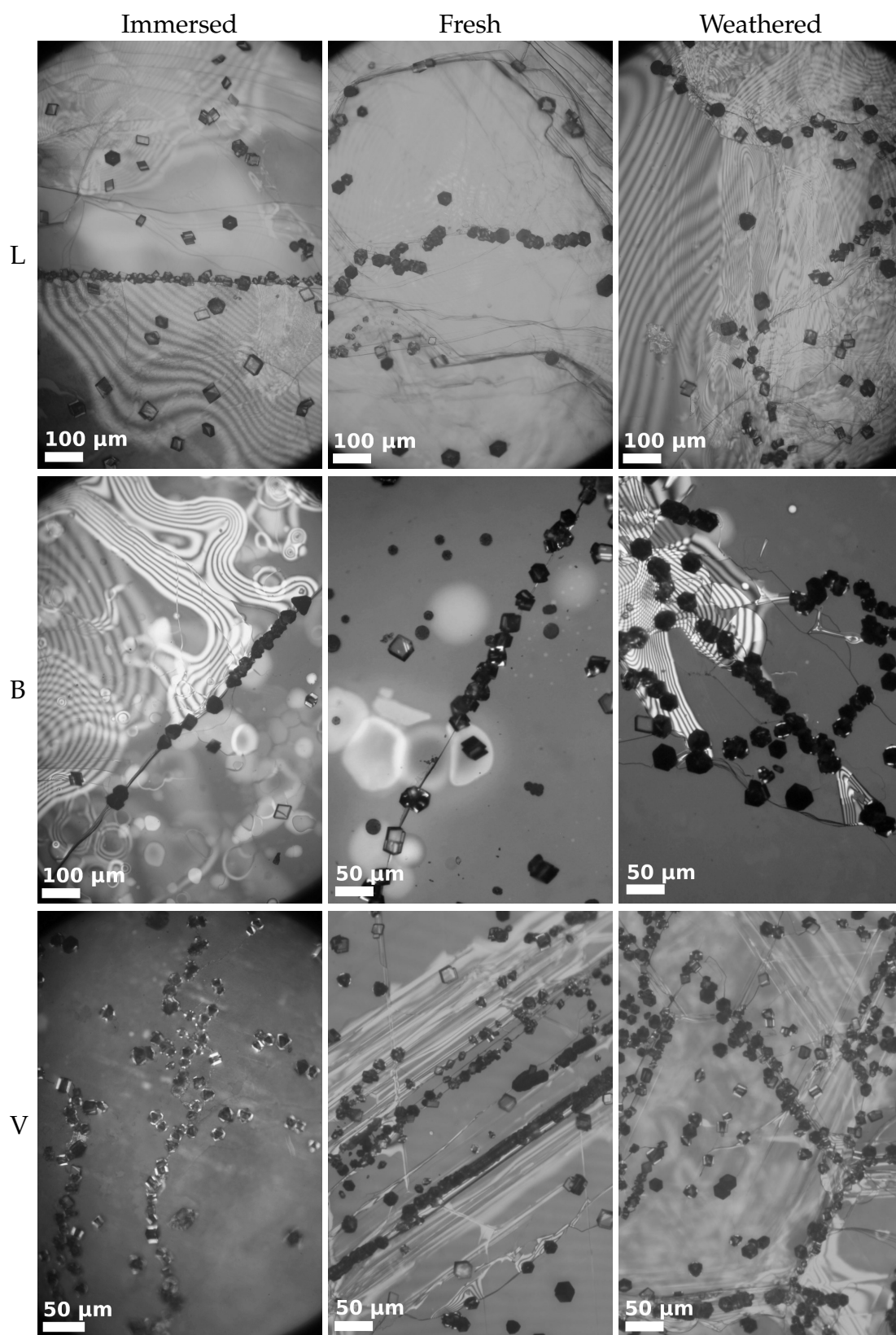


FIGURE 8.25: Optical micrographs showing calcium carbonate grown from 3 mM solutions on lepidolite (L), biotite (B) and vermiculite (V) defects for varying substrate pretreatments.

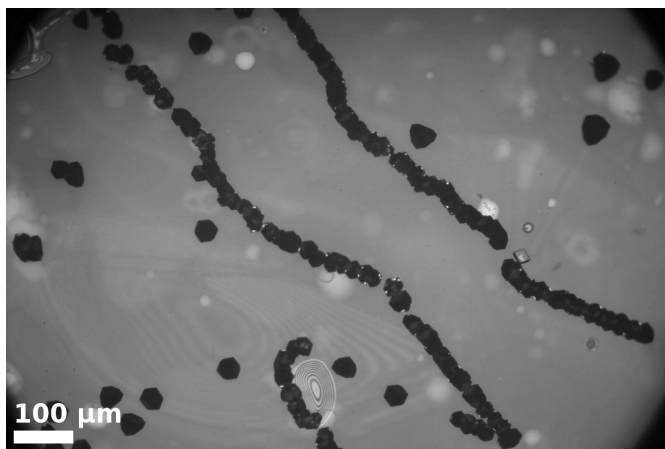


FIGURE 8.26: Optical micrograph showing calcite nucleation along an invisible feature, here on immersed biotite from 3 mM solution.

are not seen to be generally effective here. Attempts to quantify differences in nucleation density between smooth and scratched surfaces were unsuccessful, due to a high sensitivity to slight differences across even apparently clean surfaces.

The ability of a mica scratch or defect to promote calcium carbonate growth is seen to be dependent on surface history, with surfaces that have been immersed in water between cleavage and crystal growth generally displaying little preference for such sites compared to those that have been used fresh or left to weather in atmospheric conditions. However, mica appears to be unrepresentative even of its own family of layered aluminosilicates: other similar minerals showed no dependence on surface history and much more consistent occurrence of epitaxy.

## Chapter 9

# Conclusions

It was demonstrated, at the start of this thesis, that there is theoretical support for preferential nucleation in concave surface features, whether by direct nucleation or by the intermediary of a capillary condensate or analogous phase. Throughout the last five chapters, I have presented numerous experiments which have attempted to achieve the following:

- to contribute to the existing body of evidence supporting (or contradicting) this phenomenon;
- to probe the range of systems in which these effects are important;
- to use well-defined geometries to identify the key criteria for an effective nucleation site;
- to probe the microscopic mechanics of nucleation in favourable geometries.

In all of these regards I have to a greater or lesser extent succeeded. The following sections summarise the findings of each of the three major areas of work.

### 9.1 Nucleation from vapour

Research in this area began with findings that surfaces significantly roughened with diamond powder appeared to nucleate crystals more readily than corresponding smooth surfaces. Looking at the nucleation of ice and numerous organic compounds, it soon became evident that crystals had a strong preference for growing along scratches on a smooth surface, and along defects on a mica surface. Further, it was noticed that

nucleation is rarely well described by considering the properties of a surface as a whole, but rather nucleation is entirely dominated by a small number of the most favourable sites.

Attempts were made to mill well-defined features into silicon substrates, with increasing success. Ice was found to show a strong preference for nucleation along these small milled features in every case, but as the features became closer to geometric perfection, nucleation tended to be dominated by a small number of sites, suggesting that it is imperfections, rather than the 100 nm features themselves, that aid nucleation.

Four organic compounds were selected for a series of experiments aiming to identify preferential nucleation site geometries on mica surfaces. In each case, it was seen that step edges, although plentiful, were generally ineffective, and most nucleation occurred at sites where there were likely to be acute wedge geometries, often resulting from delaminated sheets of mica. More limited results for ice suggested a similar preference.

Large pockets on mica surfaces were found to provide ideal systems for studying nucleation in acute wedges. Many compounds were seen to grow preferentially from these features, and in a distinctive manner highly diagnostic of the presence of a condensate along the line of the wedge prior to nucleation of a bulk crystal. These condensates were observed for several compounds, ice being a notable exception, although the fact that ice follows the same distinctive growth pattern as other compounds is suggestive of it forming by the same mechanism. In some cases the condensate growth with increasing saturation could be plotted, revealing a steady growth, with norbornane exhibiting a discontinuity in growth rate potentially corresponding to a phase transition. Further experiments are required to unambiguously identify the nature of these condensates, although it appears highly likely that they are solid prior to emergence of a bulk crystal, with growth into a bulk phase hindered by the narrow opening of the pocket.

## 9.2 Nucleation from the melt

Starting from previous experiments which appeared to show higher freezing temperatures of water drops on roughened surfaces, I first discovered that these were a mere artifact of faster frost spreading on a rough surface. Subsequently I developed a method for producing a large array of regular picolitre droplets condensed from the air, using a patterned hydrophobic monolayer which could be applied to several different surfaces.

Using this method, the freezing of water on smooth and roughened silicon, glass and mica surfaces was compared. In each case, freezing occurred at the same well-defined



temperature, close to the value expected for homogeneous nucleation, with three exceptions: silicon scratched with " $< 1 \mu\text{m}$ " diamond powder, on which about 20% of droplets froze at higher temperatures; mica scratched with "40–60  $\mu\text{m}$ " diamond powder, on which many drops froze at higher temperatures due to freezing events spreading from drop to drop; and chemically etched mica, on which drops froze at about 0.5 °C higher than on smooth mica. The first of these owed to a heterogeneity in the drop population (either due to a small number of topographically favourable sites or significant contamination), the latter could possibly have been an effect of chemical alteration of the surface rather than topography. Attempts were made to identify whether nucleation was homogeneous, heterogeneous or occurred at the contact line; results were highly ambiguous.

It was attempted to apply the technique to other liquids, and although several were found to produce high quality droplet arrays, technical difficulties prevented any usable results from being obtained.

### 9.3 Nucleation from solution

It was known that calcium carbonate often showed a preference for nucleation along scratches and defects on mica surfaces. I have confirmed this, and done work to characterise the effect of concentration and substrate pretreatment on this phenomenon. Surface history was shown to be critically important for mica substrates, whereas for other layered minerals growth was seen along defects but was apparently quite unaffected by substrate history.

It was noticed that nucleation behaviour was often qualitatively different from that from vapour, with for example pocket geometries having little discernible effect. Attempts to quantify the nucleating abilities of different surfaces were not successful.

### 9.4 Grand conclusion

The role of topography is seen to be very different in each system. From vapour, topography is a critical factor, and highly acute geometries are effective nucleation sites for a broad range of compounds. From solution, the nucleation of calcium carbonate appears to involve quite specific surface interactions, and although surface topography seems to be important, its role is far from understood. From the melt, ice nucleation has not been conclusively seen to be affected by topography at all for the three substrates studied.

With regards to nucleation from vapour, surface topography engineering has been shown to be an effective way to direct nucleation. The ability of highly acute features to promote nucleation by stabilising a condensate has been unambiguously demonstrated. For such systems, and likely for others, it seems likely that surface geometry is a critical factor which must be considered if we are to understand nucleation phenomena.

## Appendix A

# Nucleation free energy barrier in a conical pit

To calculate the free energy barrier to nucleation in any given geometry, it seems necessary to calculate both the volume of the nucleus and the surface area of each interface, multiply these by  $\Delta G_V$  and the appropriate  $\gamma$  respectively and add these together to get the total. However, Lee and Aaronson have demonstrated that for a broad range of possible geometries, the nucleation free energy barrier scales in proportion to the nucleus volume, and hence only the volume of the nucleus needs to be calculated.[138, 139]

For the calculations involved here, it is sufficient to say that the conditions for a nucleus are as follows:

1. its interface may everywhere make the equilibrium contact angle  $\theta$  with the substrate as defined in Equation 2.11;
2. it may scale in radius without necessitating a change in shape.

This includes a broad range of geometries, including a flat plane, a wedge formed between two flat planes, a corner where three or more planes meet, a conical pit, a pyramidal pit or the inverse (convex) forms of any of these geometries. Where two or three planes meet, there is no requirement for the nucleus to make the same contact angle with each. Geometries where these conditions do not hold include most curved surfaces and straight confined pores.

More precisely, by the first condition I mean that the centre of the nucleus lies at a normal distance  $d$  from each substrate plane, such that

$$d = -R \cos \theta = R \frac{\gamma_{sl} - \gamma_{sv}}{\gamma_{lv}} \quad (\text{A.1})$$

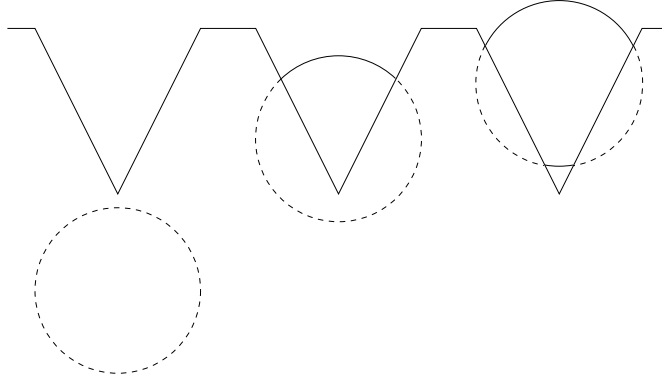


FIGURE A.1: Illustration of the shape of a nucleus when: (left)  $\theta \leq 90^\circ - \frac{\varphi}{2}$ ; (centre)  $90^\circ - \frac{\varphi}{2} < \theta < 90^\circ + \frac{\varphi}{2}$ ; (right)  $\theta \geq 90^\circ + \frac{\varphi}{2}$ .

where  $R$  is the radius, and  $\gamma_{sl}$ ,  $\gamma_{sv}$  and  $\gamma_{lv}$  the interfacial energies of the substrate-nucleus, substrate-medium and nucleus-medium interfaces respectively. Geometry shows that this condition is equivalent to Equation 2.11 holding at the edge of the contact zone, and the shape for which this condition holds for every substrate plane represents the most energetically favourable shape for a nucleus; this can be considered a simple extension of the Gibbs-Wulff theorem for the equilibrium shape of crystals, with the interfacial energies dictated by substrate geometry rather than crystal anisotropy.[140] This approach is useful as it applies equally to non-spherical nuclei, where the contact angle is not well defined.

For the specific case of a conical pit, it therefore is necessary only to find the volume of the truncated sphere having a centre position everywhere satisfying Equation A.1. If  $\theta \leq 90^\circ - \frac{\varphi}{2}$ , then the calculation is trivial: the centre of the sphere is so far below the tip of the pit that no part of it protrudes, and the volume is zero. Figure A.1 shows the situation for this and the other two scenarios.

When  $90^\circ - \frac{\varphi}{2} < \theta < 90^\circ + \frac{\varphi}{2}$ , the volume is the sum of a cone and a spherical cap. The cap has a radius of curvature  $R$  (the critical radius of the sphere) and makes an angle of  $\theta + \frac{\varphi}{2} - 90^\circ$  at its edge, from geometrical considerations. The volume of a spherical cap  $V_{\text{cap}}$  can be expressed as

$$V_{\text{cap}}(r, \omega) = \frac{1}{3}\pi r^3(2 + \cos \omega)(1 - \cos \omega)^2 \quad (\text{A.2})$$

where  $r$  is the radius of curvature and  $\omega$  the edge angle. The cone, from further geometrical considerations, has a base radius  $r_{\text{cone}}$  of  $-R \cos\left(\theta + \frac{\varphi}{2}\right)$  and a height of  $r_{\text{cone}} \tan\left(90^\circ - \frac{\varphi}{2}\right)$ . As the volume of a sphere is given by  $\frac{1}{3}\pi r^2 h$ , this gives a volume for the conical part of

$$V_{\text{cone}} = -\frac{\pi}{3}R^3 \cos^3\left(\theta + \frac{\varphi}{2}\right) \tan\left(90^\circ - \frac{\varphi}{2}\right). \quad (\text{A.3})$$

Summing these two contributions together and dividing by  $\frac{4}{3}\pi R^3$  we find the total volume relative to a full sphere to be

$$V_{\text{relative}}(\theta, \varphi) = Q\left(\theta + \frac{\varphi}{2} - 90^\circ\right) - \frac{1}{4} \cos^3\left(\theta + \frac{\varphi}{2}\right) \tan\left(90^\circ - \frac{\varphi}{2}\right) \quad (\text{A.4})$$

where

$$Q(\omega) = \frac{V_{\text{cap}}(R, \omega)}{\frac{4}{3}\pi R^3}. \quad (\text{A.5})$$

In the case where  $\theta \geq 90^\circ + \frac{\varphi}{2}$ , the volume is the sum of that of two spherical caps and a truncated cone. The outer cap has an edge angle of  $\theta + \frac{\varphi}{2} - 90^\circ$  (as with the previous case), but the inner cap has a lower edge angle of  $\theta - \frac{\varphi}{2} - 90^\circ$ . Both have a radius of curvature of  $R$ .

The truncated cone has an outer radius  $r_{\text{cone}}$  of  $-R \cos\left(\theta + \frac{\varphi}{2}\right)$  and an inner radius  $r'_{\text{cone}}$  of  $-R \cos\left(\theta - \frac{\varphi}{2}\right)$ . The volume therefore is equal to that for the conical part of the previous case, minus the volume of a cone similar in shape but of dimensions reduced by a factor  $\frac{r'_{\text{cone}}}{r_{\text{cone}}}$ . Therefore:

$$V_{\text{cone}} = \left\{ -\frac{\pi}{3} R^3 \cos^3\left(\theta + \frac{\varphi}{2}\right) \tan\left(90^\circ - \frac{\varphi}{2}\right) \right\} \left( 1 - \left(\frac{r'_{\text{cone}}}{r_{\text{cone}}}\right)^3 \right) \quad (\text{A.6})$$

and hence

$$V_{\text{cone}} = -\frac{\pi}{3} R^3 \cos^3\left(\theta + \frac{\varphi}{2}\right) \tan\left(90^\circ - \frac{\varphi}{2}\right) \left( 1 - \left(\frac{\cos\left(\theta - \frac{\varphi}{2}\right)}{\cos\left(\theta + \frac{\varphi}{2}\right)}\right)^3 \right). \quad (\text{A.7})$$

Adding the contributions from the two spherical caps and dividing by  $\frac{4}{3}\pi R^3$ , we find

$$V_{\text{relative}}(\theta, \varphi) = Q\left(\theta + \frac{\varphi}{2} - 90^\circ\right) + Q\left(\theta - \frac{\varphi}{2} - 90^\circ\right) - \frac{1}{4} \cos^3\left(\theta + \frac{\varphi}{2}\right) \tan\left(90^\circ - \frac{\varphi}{2}\right) \left( 1 - \left(\frac{\cos\left(\theta - \frac{\varphi}{2}\right)}{\cos\left(\theta + \frac{\varphi}{2}\right)}\right)^3 \right). \quad (\text{A.8})$$



# Bibliography

- [1] Y. A. Cengel and M. A. Boles. *Thermodynamics: an engineering approach*. McGraw-Hill Higher Education, 2006.
- [2] P. W. Atkins and J. De Paula. *Physical chemistry*. Oxford University Press, sixth edition, 1998.
- [3] D. Kashchiev. *Nucleation: basic theory with applications*. Butterworth-Heinemann, 2000.
- [4] I. V. Markov. *Crystal growth for beginners: fundamentals of nucleation, crystal growth and epitaxy*. World Scientific Singapore, 2003.
- [5] R. von Helmholtz. Untersuchungen über Dämpfe und Nebel, besonders über solche von Lösungen. *Annalen der Physik*, 263(4):508–543, 1886.
- [6] M. Volmer. *Kinetik der Phasenbildung*. Dresden und Leipzig, 1939.
- [7] J. W. Gibbs, H. A. Bumstead, and W. R. Longley. *The collected works of J. Willard Gibbs*, volume 1. Longmans, Green and Company, 1928.
- [8] J. N. Israelachvili. *Intermolecular and surface forces*. Academic Press, third edition, 2011.
- [9] B. K. Chakraverty and G. M. Pound. Heterogeneous nucleation at macroscopic steps. *Acta Metall.*, 12(8):851–860, 1964.
- [10] C. A. Sholl and N. H. Fletcher. Decoration criteria for surface steps. *Acta Metall.*, 18(10):1083–1086, 1970.
- [11] N. H. Fletcher. Active sites and ice crystal nucleation. *J. Atmos. Sci.*, 26(6):1266–1271, 1969.
- [12] M. V. Massa and K. Dalnoki-Veress. Homogeneous crystallization of poly(ethylene oxide) confined to droplets: The dependence of the crystal nucleation rate on length scale and temperature. *Phys. Rev. Lett.*, 92(25), 2004.
- [13] K. L. Mittal. *Contact angle, wettability and adhesion*, volume 4. CRC Press, 2006.
- [14] J. Drelich, E. Chibowski, D. D. Meng, and K. Terpilowski. Hydrophilic and superhydrophilic surfaces and materials. *Soft Matter*, 7(21):9804–9828, 2011.
- [15] Y. Yang, M. Asta, and B. B. Laird. Solid-liquid interfacial premelting. *Phys. Rev. Lett.*, 110(9):096102, 2013.

- [16] S. Engemann, H. Reichert, H. Dosch, J. Bilgram, V. Honkimäki, and A. Snigirev. Interfacial melting of ice in contact with SiO<sub>2</sub>. *Phys. Rev. Lett.*, 92(20):205701, 2004.
- [17] S. J. Bonafede and M. D. Ward. Selective nucleation and growth of an organic polymorph by ledge-directed epitaxy on a molecular crystal substrate. *J. Am. Chem. Soc.*, 117(30):7853–7861, 1995.
- [18] C. A. Mitchell, L. Yu, and M. D. Ward. Selective nucleation and discovery of organic polymorphs through epitaxy with single crystal substrates. *J. Am. Chem. Soc.*, 123(44):10830–10839, 2001.
- [19] V. López-Mejías, A. S. Myerson, and B. L. Trout. Geometric design of heterogeneous nucleation sites on biocompatible surfaces. *Cryst. Growth Des.*, 13(8):3835–3841, 2013.
- [20] R. Shaw, A. Durant, and Y. Mi. Heterogeneous surface crystallization observed in undercooled water. *J. Phys. Chem. B*, 109(20):9865–9868, 2005.
- [21] A. J. Durant and R. A. Shaw. Evaporation freezing by contact nucleation inside-out. *Geophys. Res. Lett.*, 32(20):L20814, 2005.
- [22] S. Suzuki, A. Nakajima, N. Yoshida, M. Sakai, A. Hashimoto, Y. Kameshima, and K. Okada. Freezing of water droplets on silicon surfaces coated with various silanes. *Chem. Phys. Lett.*, 445(1-3):37–41, 2007.
- [23] A. P. Fornea, S. D. Brooks, J. B. Dooley, and A. Saha. Heterogeneous freezing of ice on atmospheric aerosols containing ash, soot, and soil. *J. Geophys. Res.: Atmospheres*, 114(D13):201, 2009.
- [24] L. Ladino, O. Stetzer, F. Lüönd, A. Welti, and U. Lohmann. Contact freezing experiments of kaolinite particles with cloud droplets. *J. Geophys. Res.: Atmospheres*, 116(D22):202, 2011.
- [25] L. A. Ladino Moreno, O. Stetzer, and U. Lohmann. Contact freezing: a review of experimental studies. *Atmos. Chem. Phys.*, 13(19):9745–9769, 2013.
- [26] R. P. Sear. Nucleation at contact lines where fluid-fluid interfaces meet solid surfaces. *J. Phys.: Condens. Matter*, 19(46):466106, 2007.
- [27] Y. S. Djikaev and E. Ruckenstein. Thermodynamics of heterogeneous crystal nucleation in contact and immersion modes. *J. Phys. Chem. A*, 112(46):11677–11687, 2008.
- [28] C. Gurganus, A. B. Kostinski, and R. A. Shaw. Fast imaging of freezing drops: No preference for nucleation at the contact line. *J. Phys. Chem. Lett.*, 2(12):1449–1454, 2011.
- [29] C. Gurganus, A. B. Kostinski, and R. A. Shaw. High-speed imaging of freezing drops: Still no preference for the contact line. *J. Phys. Chem. C*, 117(12):6195–6200, 2013.
- [30] K. Iland, J. Wölk, R. Strey, and D. Kashchiev. Argon nucleation in a cryogenic nucleation pulse chamber. *J. Chem. Phys.*, 127(15):154506, 2007.
- [31] M. Sharaf and R. Dobbins. A comparison of measured nucleation rates with the predictions of several theories of homogeneous nucleation. *J. Chem. Phys.*, 77(3):1517–1526, 1982.



- [32] T. Zykova-Timan, C. Valeriani, E. Sanz, D. Frenkel, and E. Tosatti. Irreducible finite-size effects in the surface free energy of NaCl crystals from crystal-nucleation data. *Phys. Rev. Lett.*, 100:036103, 2008.
- [33] S. Prestipino, A. Laio, and E. Tosatti. Systematic improvement of classical nucleation theory. *Phys. Rev. Lett.*, 108:225701, 2012.
- [34] D. Reguera. How far is classical nucleation theory from predicting nucleation rates accurately? In *AIP Conf. Proc.*, volume 1527, page 9, 2013.
- [35] L. Filion, M. Hermes, R. Ni, and M. Dijkstra. Crystal nucleation of hard spheres using molecular dynamics, umbrella sampling, and forward flux sampling: A comparison of simulation techniques. *J. Chem. Phys.*, 133(24):244115, 2010.
- [36] D.W. Oxtoby. Density functional methods in the statistical mechanics of materials. *Ann. Rev. Mater. Res.*, 32(1):39–52, 2002.
- [37] S. Ghosh and S. K. Ghosh. Homogeneous nucleation in vapor-liquid phase transition of lennard-jones fluids: A density functional theory approach. *J. Chem. Phys.*, 134:024502, 2011.
- [38] A. B. Nadykto, F. Yu, M. V. Jakovleva, J. Herb, and Y. Xu. Amines in the Earth’s atmosphere: a density functional theory study of the thermochemistry of pre-nucleation clusters. *Entropy*, 13(2):554–569, 2011.
- [39] D. Winter, P. Virnau, and K. Binder. Heterogeneous nucleation at a wall near a wetting transition: a Monte Carlo test of the classical theory. *J. Phys.: Condens. Matter*, 21(46):464118, 2009.
- [40] S. Punnathanam and P. A. Monson. Crystal nucleation in binary hard sphere mixtures: A Monte Carlo simulation study. *J. Chem. Phys.*, 125(2):024508–024508, 2006.
- [41] L. B. Gower. Biomimetic model systems for investigating the amorphous precursor pathway and its role in biomineralization. *Chem. Revs.*, 108(11):4551–4627, 2008.
- [42] F. C. Meldrum and R. P. Sear. Now you see them. *Science*, 322(5909):1802–1803, 2008.
- [43] D. Erdemir, A. Lee, and A. Myerson. Nucleation of Crystals from Solution: Classical and Two-Step Models. *Acc. Chem. Res.*, 42(5):621–629, 2009.
- [44] D. Gebauer and H. Cölfen. Prenucleation clusters and non-classical nucleation. *Nano Today*, 6(6):564–584, 2011.
- [45] R. P. Sear. The non-classical nucleation of crystals: microscopic mechanisms and applications to molecular crystals, ice and calcium carbonate. *Int. Mater. Rev.*, 57(6):329, 2012.
- [46] W. Ostwald. Studien über die Umwandlung und Bildung fester Körper. *Eitschrift Phys. Chem*, 22:289, 1897.

- [47] T. Threlfall. Structural and thermodynamic explanations of Ostwald's rule. *Org. Proc. Res. & Dev.*, 7(6):1017–1027, 2003.
- [48] S. V. Dorozhkin. Amorphous calcium (ortho) phosphates. *Acta biomater.*, 6(12):4457–4475, 2010.
- [49] Y-W. Wang, Y-Y. Kim, H. K. Christenson, and F. C. Meldrum. A new precipitation pathway for calcium sulfate dihydrate (gypsum) via amorphous and hemihydrate intermediates. *Chem. Comm.*, 48(4):504–506, 2012.
- [50] D. Nowak, M. Heuberger, M. Zach, and H. K. Christenson. Thermodynamic and kinetic supercooling of liquid in a wedge pore. *J. Chem. Phys.*, 129(15):154509, 2008.
- [51] D. Nowak and H. K. Christenson. Capillary condensation of water between mica surfaces above and below zero-effect of surface ions. *Langmuir*, 25(17):9908–9912, 2009.
- [52] H-J. Butt and M. Kappl. Normal capillary forces. *Adv. Colloid Interface Sci.*, 146(1):48–60, 2009.
- [53] A. O. Parry, A. J. Wood, and C. Rascón. Wedge filling, cone filling and the strong-fluctuation regime. *J. Phys.: Condens. Matter*, 13(21):4591, 2001.
- [54] M. J. Greenall, A. O. Parry, and J. M. Romero-Enrique. Three-dimensional wedge filling in ordered and disordered systems. *J. Physics: Condens. Matter*, 16(15):2515, 2004.
- [55] A. Milchev, M. Müller, K. Binder, and D. P. Landau. Wedge filling and interface delocalization in finite Ising lattices with antisymmetric surface fields. *Phys. Rev. E*, 68(3):031601, 2003.
- [56] D. Turnbull. Kinetics of Heterogeneous Nucleation. *J. Chem. Phys.*, 18(2):198–203, 1950.
- [57] B. Sandnes. The physics and the chemistry of the heat pad. *Am. J. Phys.*, 76(6):546–550, 2008.
- [58] K. Higuchi and S. Noda. Selected area diamond deposition by control of the nucleation sites. *Diam. Relat. Mater.*, 1(2):220–229, 1992.
- [59] P. Ascarelli and S. Fontana. Dissimilar grit-size dependence of the diamond nucleation density on substrate surface pretreatments. *Appl. Surf. Sci.*, 64(4):307–311, 1993.
- [60] J. G. Buijnsters, L. Vázquez, and J. J. ter Meulen. Substrate pre-treatment by ultrasonication with diamond powder mixtures for nucleation enhancement in diamond film growth. *Diam. Relat. Mater.*, 18(10):1239 – 1246, 2009.
- [61] N. H. Lin, W. Y. Shih, E. Lyster, and Y. Cohen. Crystallization of calcium sulfate on polymeric surfaces. *J. Colloid Interface Sci.*, 356(2):790–797, 2011.
- [62] Y. Diao, A. S. Myerson, T. A. Hatton, and B. L. Trout. Surface design for controlled crystallization: The role of surface chemistry and nanoscale pores in heterogeneous nucleation. *Langmuir*, 27(9):5324–5334, 2011.

- [63] G. Di Profio, E. Fontananova, E. Curcio, and E. Drioli. From tailored supports to controlled nucleation: Exploring material chemistry, surface nanostructure, and wetting regime effects in heterogeneous nucleation of organic molecules. *Cryst. Growth Des.*, 12(7):3749–3757, 2012.
- [64] A. Sengupta Ghatak and A. Ghatak. Disordered nanowrinkle substrates for inducing crystallization over a wide range of concentration of protein and precipitant. *Langmuir*, 29(13):4373–4380, 2013.
- [65] M. Järn, S. Areva, V. Pore, J. Peltonen, and M. Linden. Topography and surface energy dependent calcium phosphate formation on sol-gel derived TiO<sub>2</sub> coatings. *Langmuir*, 22(19):8209–8213, 2006.
- [66] S. Keysar, R. Semiat, D. Hasson, and J. Yahalom. Effect of surface roughness on the morphology of calcite crystallizing on mild steel. *J. Colloid Interface Sci.*, 162(2):311–319, 1994.
- [67] C. Mu, J. Pang, Q. Lu, and T. Liu. Effects of surface topography of material on nucleation site density of dropwise condensation. *Chem. Eng. Sci.*, 63(4):874–880, 2008.
- [68] P. Conrad, G. Ewing, R. Karlinsey, and V. Sadtschenko. Ice nucleation on BaF<sub>2</sub>(111). *J. Chem. Phys.*, 122(6):064709, 2005.
- [69] P. Asanithi. Surface porosity and roughness of micrographite film for nucleation of hydroxyapatite. *J. Biomed. Mater. Res. Part A*, 2013. doi: 10.1002/jbm.a.34930.
- [70] V. Raiko, R. Spitzl, J. Engemann, V. Borisenko, and V. Bondarenko. MPCVD diamond deposition on porous silicon pretreated with the bias method. *Diam. Relat. Mater.*, 5(10):1063–1069, 1996.
- [71] N. E. Chayen, E. Saridakis, R. El-Bahar, and Y. Nemirovsky. Porous silicon: an effective nucleation-inducing material for protein crystallization. *J. Molec. Bio.*, 312(4):591–595, 2001.
- [72] N. E. Chayen, E. Saridakis, and R. P. Sear. Experiment and theory for heterogeneous nucleation of protein crystals in a porous medium. *Proc. Nat. Acad. Sci. USA*, 103(3):597–601, 2006.
- [73] U. V. Shah, D. R. Williams, and J. Y. Y. Heng. Selective crystallization of proteins using engineered nanonucleants. *Cryst. Growth Des.*, 12(3):1362–1369, 2012.
- [74] J. M. Ha, J. H. Wolf, M. A. Hillmyer, and M. D. Ward. Polymorph selectivity under nanoscopic confinement. *J. Am. Chem. Soc.*, 126(11):3382–3383, 2004.
- [75] Y. Diao, K. E. Whaley, M. E. Helgeson, M. A. Woldeyes, P. S. Doyle, A. S. Myerson, T. A. Hatton, and B. L. Trout. Gel-induced selective crystallization of polymorphs. *J. Am. Chem. Soc.*, 134(1):673–684, 2011.

- [76] B. Cantaert, E. Beniash, and F. C. Meldrum. Nanoscale confinement controls the crystallization of calcium phosphate: Relevance to bone formation. *Chemistry—A European Journal*, 19(44):14918–14924, 2013.
- [77] A. Portavoce, M. Kammler, R. Hull, M. C. Reuter, and F. M. Ross. Mechanism of the nanoscale localization of Ge quantum dot nucleation on focused ion beam templated Si (001) surfaces. *Nanotechnology*, 17:4451, 2006.
- [78] Y. Diao, T. Harada, A. S. Myerson, T. A. Hatton, and B. L. Trout. The role of nanopore shape in surface-induced crystallization. *Nat. Mater.*, 10(11):867–871, 2011.
- [79] P. A. Dennig and D. A. Stevenson. Influence of substrate topography on the nucleation of diamond thin films. *Appl. Phys. Lett.*, 59(13):1562–1564, 1991.
- [80] L. Jiang, X. Lu, Y. Leng, S. Qu, B. Feng, and J. Weng. Micropatterned TiO<sub>2</sub> effects on calcium phosphate mineralization. *Mater. Sci. Eng. C*, 29(8):2355–2359, 2009.
- [81] D. G. Georgieva, M. E. Kuil, T. H. Oosterkamp, H. W. Zandbergen, and J. P. Abrahams. Heterogeneous nucleation of three-dimensional protein nanocrystals. *Acta Crystallogr. D*, 63(5):564–570, 2007.
- [82] I. Nederlof, R. Hosseini, D. Georgieva, J. Luo, D. Li, and J. P. Abrahams. A straightforward and robust method for introducing human hair as a nucleant into high throughput crystallization trials. *Cryst. Growth Des.*, 11(4):1170–1176, 2011.
- [83] T. Kovács, F. C. Meldrum, and H. K. Christenson. Crystal nucleation without supersaturation. *J. Phys. Chem. Lett.*, 3(12):1602–1606, 2012.
- [84] H. K. Christenson and T. Kovács. A two-step mechanism for crystal nucleation without supersaturation. *Faraday Discuss.*, 159:123–138, 2012.
- [85] C. Marcolli. Deposition nucleation viewed as homogeneous or immersion freezing in pores and cavities. *Atmos. Chem. Phys. Disc.*, 13(6):16367–16456, 2013.
- [86] A. Welti, Z. A. Kanji, F. Lüönd, O. Stetzer, and U. Lohmann. Exploring the mechanisms of ice nucleation on kaolinite: From deposition nucleation to condensation freezing. *J. Atmos. Sci.*, 71(1):16–36, 2014.
- [87] A. J. Page and R. P. Sear. Heterogeneous nucleation in and out of pores. *Phys. Rev. Lett.*, 97(6):065701, 2006.
- [88] L. O. Hedges and S. Whitelam. Patterning a surface so as to speed nucleation from solution. *Soft Matter*, 8(33):8624–8635, 2012.
- [89] L. O. Hedges and S. Whitelam. Selective nucleation in porous media. *Soft Matter*, 9(41):9763–9766, 2013.
- [90] A. J. Page and R. P. Sear. Crystallization controlled by the geometry of a surface. *J. Am. Chem. Soc.*, 131(48):17550–17551, 2009.

- [91] J. A. van Meel, R. P. Sear, and D. Frenkel. Design principles for broad-spectrum protein-crystal nucleants with nanoscale pits. *Phys. Rev. Lett.*, 105(20):205501, 2010.
- [92] S. Tolansky. The topography of crystal faces. II. The topography of cleavage faces of mica and selenite. *Proc. Roy. Soc. London, Series A*, 184(996):51–63, 1945.
- [93] D. Hull. The geometry of cracks and blisters in mica. *Acta mater.*, 45(1):233–244, 1997.
- [94] H. K. Christenson and J. N. Israelachvili. Growth of ionic crystallites on exposed surfaces. *J. Colloid Interface Sci.*, 117(2):576–577, 1987.
- [95] F. Ostendorf, C. Schmitz, S. Hirth, A. Kühnle, J. J. Kolodziej, and M. Reichling. Evidence for potassium carbonate crystallites on air-cleaved mica surfaces. *Langmuir*, 25(18):10764–10767, 2009.
- [96] F. Ostendorf, C. Schmitz, S. Hirth, A. Kühnle, J. J. Kolodziej, and M. Reichling. How flat is an air-cleaved mica surface? *Nanotechnology*, 19(30):305705, 2008.
- [97] H. K. Christenson. Adhesion and surface energy of mica in air and water. *J. Phys. Chem.*, 97(46):12034–12041, 1993.
- [98] P. A. Campbell, L. J. Sinnamon, C. E. Thompson, and D. G. Walmsley. Atomic force microscopy evidence for K<sup>+</sup> domains on freshly cleaved mica. *Surface science*, 410(2):L768–L772, 1998.
- [99] N. Bano and A. K. Jonscher. Dielectric properties of humid mica surfaces. *J. Mater. Sci.*, 27(6):1672–1682, 1992.
- [100] D. R. Lide, editor. *Handbook of chemistry and physics*. CRC, 2006-2007.
- [101] C. L. Yaws and C. Gabbula. *Yaws' Handbook of Thermodynamic and Physical Properties of Chemical Compounds*. Knovel, 2003.
- [102] R. S. Bradley and T. Drury. The vapour pressure and lattice energy of carbon tetrabromide. *Trans. Faraday Soc.*, 55(0):1844–1847, 1959.
- [103] W. V. Steele. The standard enthalpies of formation of bicyclic compounds III. 1,7,7-trimethylbicyclo[2.2.1]heptan-2-one. *J. Chem. Thermodyn.*, 9(4):311–314, 1977.
- [104] S. P. Verevkin and V. N. Emel'yanenko. Enthalpy of formation and strain of norbornane from thermochemical measurements and from ab initio calculations. *J. Phys. Chem. A*, 108(31):6575–6580, 2004.
- [105] J. S. Chickos and W. E. Acree Jr. Enthalpies of sublimation of organic and organometallic compounds. *J. Phys. Chem. Ref. Data*, 31(2):537, 2002.
- [106] J. L. Holbrough, J. M. Campbell, F. C. Meldrum, and H. K. Christenson. Topographical control of crystal nucleation. *Cryst. Growth Des.*, 12(2):750–755, 2012.
- [107] J. M. Campbell, F. C. Meldrum, and H. K. Christenson. Characterization of preferred crystal nucleation sites on mica surfaces. *Cryst. Growth Des.*, 13(5):1915–1925, 2013.

- [108] P-G. De Gennes, F. Brochard-Wyart, and D. Quere. *Capillarity and Wetting Phenomena*. Springer, 2008.
- [109] B. Vonnegut. The nucleation of ice formation by silver iodide. *J. Appl. Phys.*, 18(7):593–595, 1947.
- [110] B. J. Murray, S. L. Broadley, T. W. Wilson, J. D. Atkinson, and R. H. Wills. Heterogeneous freezing of water droplets containing kaolinite particles. *Atmos. Chem. Phys.*, 11(9):4191–4207, 2011.
- [111] J. D. Atkinson, B. J. Murray, M. T. Woodhouse, T. F. Whale, K. J. Baustian, K. S. Carslaw, S. Dobbie, D. OSullivan, and T. L. Malkin. The importance of feldspar for ice nucleation by mineral dust in mixed-phase clouds. *Nature*, 498(7454):355–358, 2013.
- [112] B. J. Murray, S. L. Broadley, T. W. Wilson, S. J. Bull, R. H. Wills, H. K. Christenson, and E. J. Murray. Kinetics of the homogeneous freezing of water. *Phys. Chem. Chem. Phys.*, 12(35):10380–10387, 2010.
- [113] E. Sanz, C. Vega, J. R. Espinosa, R. Caballero-Bernal, J. L. F. Abascal, and C. Valeriani. Homogeneous ice nucleation at moderate supercooling from molecular simulation. *J. Am. Chem. Soc.*, 135(40):15008–15017, 2013.
- [114] B. Vonnegut. Variation with temperature of the nucleation rate of supercooled liquid tin and water drops. *J. Colloid Sci.*, 3(6):563–569, 1948.
- [115] G. M. Pound and V. K. La Mer. Kinetics of crystalline nucleus formation in supercooled liquid tin. *J. Am. Chem. Soc.*, 74(9):2323–2332, 1952.
- [116] J. L. Carvalho and K. Dalnoki-Veress. Homogeneous bulk, surface, and edge nucleation in crystalline nanodroplets. *Phys. Rev. Lett.*, 105(23):237801, 2010.
- [117] J. L. Carvalho and K. Dalnoki-Veress. Surface nucleation in the crystallisation of polyethylene droplets. *Euro. Phys. J. E*, 34(1):1–6, 2011.
- [118] P. Laval, A. Crombez, and J. Salmon. Microfluidic droplet method for nucleation kinetics measurements. *Langmuir*, 25(3):1836–1841, 2009.
- [119] C. J. Stephens, Y-Y. Kim, S. D. Evans, F. C. Meldrum, and H. K. Christenson. Early stages of crystallization of calcium carbonate revealed in picoliter droplets. *J. Am. Chem. Soc.*, 133(14):5210–5213, 2011.
- [120] J. Parker, P. Claesson, D. Cho, A. Ahlberg, J. Tidblad, and E. Blomberg. Plasma modification of mica. *J. Colloid Interface Sci.*, 134(2):449–458, 1990.
- [121] W. T. Eadie, D. Drijard, F. E. James, M. Roos, and B. Sadoulet. *Statistical methods in experimental physics*. North-Holland, Amsterdam, 1971.
- [122] R. E. Walpole, R. H. Myers, S. L. Myers, and K. Ye. *Probability and statistics for engineers and scientists*, volume 5. Macmillan New York, 1993.

- [123] L. Brečević and A. E. Nielsen. Solubility of amorphous calcium carbonate. *J. Cryst. Growth*, 98(3):504–510, 1989.
- [124] J-Y. Gal, J-C. Bollinger, H. Tolosa, and N. Gache. Calcium carbonate solubility: a reappraisal of scale formation and inhibition. *Talanta*, 43(9):1497–1509, 1996.
- [125] L. N. Plummer and E. Busenberg. The solubilities of calcite, aragonite and vaterite in CO<sub>2</sub>-H<sub>2</sub>O solutions between 0 and 90°C, and an evaluation of the aqueous model for the system CaCO<sub>3</sub>-CO<sub>2</sub>-H<sub>2</sub>O. *Geochim. Cosmochim. Acta*, 46(6):1011–1040, 1982.
- [126] Y-W. Wang, Y-Y. Kim, C. J. Stephens, F. C. Meldrum, and H. K. Christenson. In situ study of the precipitation and crystallization of amorphous calcium carbonate (ACC). *Cryst. Growth Des.*, 12(3):1212–1217, 2012.
- [127] L. Addadi, S. Raz, and S. Weiner. Taking advantage of disorder: amorphous calcium carbonate and its roles in biomineralization. *Adv. Mater.*, 15(12):959–970, 2003.
- [128] Stephens, C. *On the transformation of amorphous calcium carbonate into calcite*. PhD thesis, School of Physics & Astronomy, University of Leeds, 2010.
- [129] Y. Politi, T. Arad, E. Klein, S. Weiner, and L. Addadi. Sea urchin spine calcite forms via a transient amorphous calcium carbonate phase. *Science*, 306(5699):1161–1164, 2004.
- [130] X. Xu, J. T. Han, and K. Cho. Formation of amorphous calcium carbonate thin films and their role in biomineralization. *Chemistry of materials*, 16(9):1740–1746, 2004.
- [131] C. J. Stephens, S. F. Ladden, F. C. Meldrum, and H. K. Christenson. Amorphous calcium carbonate is stabilized in confinement. *Adv. Func. Mater.*, 20(13):2108–2115, 2010.
- [132] E. Loste, R. J. Park, J. Warren, and F. C. Meldrum. Precipitation of calcium carbonate in confinement. *Adv. Func. Mater.*, 14(12):1211–1220, 2004.
- [133] D. Gebauer, A. Völkel, and H. Cölfen. Stable prenucleation calcium carbonate clusters. *Science*, 322(5909):1819–1822, 2008.
- [134] E. M. Pouget, P. H. H. Bomans, J. A. C. M. Goos, P. M. Frederik, N. A. J. M. Sommerdijk, et al. The initial stages of template-controlled CaCO<sub>3</sub> formation revealed by cryo-TEM. *Science*, 323(5920):1455–1458, 2009.
- [135] C. J. Stephens, Y. Mouhamad, F. C. Meldrum, and H. K. Christenson. Epitaxy of calcite on mica. *Cryst. Growth Des.*, 10(2):734–738, 2010.
- [136] T. Vicsek. *Fractal growth phenomena*. World Scientific, 1989.
- [137] S. Hashmi, H. Wickman, and D. Weitz. Tetrahedral calcite crystals facilitate self-assembly at the air-water interface. *Phys. Rev. E*, 72(4):041605, 2005.
- [138] J. K. Lee and H. I. Aaronson. Application of the modified Gibbs-Wulff construction to some problems in the equilibrium shape of crystals at grain boundaries. *Scripta Metallurgica*, 8(12):1451–1460, 1974.

- [139] J. K. Lee and H. I. Aaronson. The equilibrium shape of a particle at macroscopic steps and kinks and the Gibbs-Wulff construction. *Surface Science*, 47(2):692–696, 1975.
- [140] R. Cerf and J. Picard. *The Wulff crystal in Ising and percolation models*, volume 1878. Springer, 2006.